Characterizing the Nonlinear Optical Response of Silicon Vacancy Centers in Diamond and Showcasing the Next Generation of Optical Frequency Combs

by

Matthew Walton Day

A dissertation submitted in partial fulfillment
of the requirements for the degree of
Doctor of Philosophy
(Physics)
in The University of Michigan
2021

Doctoral Committee:

Professor Steven Cundiff, Chair
Professor Jennifer Ogilvie
Associate Professor Kai Sun
Professor Herbert Winful
Assistant Professor Liuyan Zhao

Matthew W. Day

mwday@umich.edu

ORCID iD: 0000-0002-2276-0831

To my family

ACKNOWLEDGEMENTS

Every graduation is the success of a village of people helping to grow and mature the person receiving the degree. I will do my best to thank everyone by name who made this possible. Thank you to Professor Steven Cundiff, who has provided solid intellectual guidance and a tremendous amount of research freedom from the first time I walked into his office as a Freshman in Boulder at JILA. I am ever thankful for your support, advice, and encouragement. I am grateful to those on the committee who have taken their time to read this document and to the Graduate program coordinator Prof. Vanessa Sih and the front-office support of Lauren Segall in Physics for their stewardship of this degree program.

The research presented herein is the culmination of years of hard work, during which I had the distinct pleasure of working with Dr. Christopher Smallwood. A finer research mentor would be incredibly difficult to find. Thank you also to my colleagues (and collaborators) Kelsey Bates, Torben Purz, Rachel Owen, Yiming Gong, Ruixue Zhang, Grace Kerber, Cesar Perez, Blake Hipsley, Drs. Eric Martin, Albert Liu, Jason Shih An Horng, Takeshi Suzuki, Rohan Singh, Galan Moody, Bo Sun, Elizabeth Drueke, Bachana Lomsadze, Mark Dong, Ronald Ulbricht, and Brad Smith for always being inspiring and helpful. Thank you to Professor Dong Sun for providing an introduction to quantum materials, to Professor Liuyan Zhao for your deft scientific and career advice, Professor Herbert Winful for your assistance and skillful guidance of the frequency comb project, and Professors Jennifer Ogilvie and Kai Sun for helpful and exciting research discussions over the years. Thank you to

Professor Christine Aidala for interesting conversations, and for always looking out for interesting intersections between the high- and low-energy worlds.

Of course, no scientific project would get off the ground without the help of the support staff in the LSA Business office and the machinists in the LSA Instrument shop. For your help building our experiments, I'm immensely grateful.

There is also absolute army without whose support I would not have been able to complete this degree. To my parents Drs. Katherine and Warren Day, thank you for demonstrating by example that a career in the pursuit of a better understanding of the world can be rewarding, challenging, and fun. Thank you for the positive direction you've helped me chart. My hilarious sister, Anna Day, has always provided an understanding and kind ear when things get tough, thank you. I am forever grateful to Mark and Cindy Nasky, their son Drew Nasky, and Christian Schureman for their unconditional love and encouragement through graduate school (and my life in general). To my partner, Susan LaMoreaux, thank you for putting up with my stress, odd hours, and for your kind and compassionate encouragement. To my Graduate School friends not listed above, Kara Mattioli, Johnny Jordan, Garrett Merz, Karley Thurston, Eric Gonzales, Shruti Paranjape, Rory Fitzpatrick, Bradley Dice, and Owen Puls, thank you for your support and understanding as we navigate this challenge in parallel. I know you're all off to great things! To my lifelong friends Blake Jackson, Nicole Castagneri, Phil Temple, Ewelena Pena, Alex Reginold, Jordan Mallec, Joel Ayers, Tessa Hennesy, Michel Concannon, Michael Dyer, Lauren Martin, Kevin Andresen, and everyone else, thank you for always being hilarious, kind, and willing to listen to me kvetch about the trials of higher education. You're truly an incredible ensemble.

PREFACE

This is a thesis in two parts. I first began our work on Silicon Vacancy Centers in diamond when I joined the group in 2017, with the hope that we would be able to employ our nonlinear spectroscopy tools to provide a better understanding of the optical properties of these color centers. I believe we were largely successful in this endeavour. The first half of my thesis is a summation of the two results to which my contributions were most substantial.

Simultaneously, Professor Cundiff encouraged me to finish the diode frequency comb project, picking up where a prior graduate student, Dr. Mark Dong had left off. This work is not thematically related to the first half of the thesis. However, it constituted a bulk of the latter half of my dissertation work, and will therefore constitute the latter half of this thesis.

TABLE OF CONTENTS

LIST OF FIGURES

Figure

LIST OF APPENDICES

Appendix

ABSTRACT

This thesis covers two completely different topics: the nonlinear optical properties of Silicon Vacancy Centers in Diamond, and the demonstration of Miniaturized, coherent diode frequency combs. As such, this Abstract will be broken into two abstracts discussing the primary findings within this document for each subject.

The Nonlinear Optical Response of Silicon Vacancy Center in Diamond

-

This work employs multidimensional coherent spectroscopy (MDCS) to show that a previously unknown hidden population of dark silicon-vacancy centers dominates the resonant nonlinear optical response of an ensemble of such centers. We present evidence to support our assertion that this phenomenon is due to strain-induced coupling to a dark state. We posit two mechanisms by which this could occur.

Furthermore, we use a particular version of MDCS sensitive only to excitation dependent interactions between color centers, known as double-quantum spectroscopy, to show that inter-center interactions (causing peak shifts on the order of between 4 and 40 GHz) occur in our sample and are likely electronic dipole-dipole interactions. We demonstrate rudimentary control over the interaction strength between color center pairs by introducing an intense optical pulse and varying the pulse strength. As a function of the pulse field, the double quantum spectra show pairwise Rabi-like oscillations in the peak amplitude, which is a direct signature of varying interaction strength.

Showcasing the Next Generation of Coherent Optical Frequency Combs

-

We showcase a new breed of semiconductor diode-based miniaturized frequency combs. Two dozen of our combs fit within a grain of rice. In this thesis, we characterize the modelocking physics of these frequency combs. We show that these lasers output coherent frequency modulated frequency combs, providing evidence that passive modelocking within the laser cavity occurs to stabilize the comb output.

Beyond demonstrating that these frequency combs are indeed *coherent* combs, we also demonstrate their use in a practical dual-comb spectroscopy application. We acquire a dual-comb absorption spectrum of a gas cell, with a resolution better than 25GHz achieved in only 10μs of data acquisition time. We also show that these frequency combs can be battery powered, and that they are efficient, tunable, and simple. This thesis shows that diode frequency combs are truly portable and capable of providing a platform for practical precision measurement to thrive.

CHAPTER I

An Introduction to Silicon-Vacancy Point Defects in Diamond

1.1 Background

Diamond is an exceptional material. Over the centuries, it has captivated countless generations of scholars, aesthetes, craftspeople, and any number of others [1, 2]. Of the properties possessed by diamond, seminal Roman naturalist Pliny the Elder had much to say:

> The substance that possesses the greatest value, not only among the precious stones, but of all human possessions, is adamas [1] a mineral which, for a long time, was known to kings only, and to very few of them. ...
>
> When, by good fortune, [diamond] does happen to be broken, it divides into fragments so minute as to be almost imperceptible. These particles are held in great request by engravers, who enclose them in iron, and are enabled thereby, with the greatest facility, to cut the very hardest substances known. So great is the antipathy borne by this stone to the magnet, that when placed near, it will not allow of its attracting iron; or if the magnet has already attracted the iron, it will seize the metal

[1] diamond

> and drag it away from the other. Adamas, too, overcomes and neutralizes poisons, dispels delirium, and banishes groundless perturbations of the mind; hence it is that some have given it the name of "ananchites." - Pliny the Elder, *The Natural History*, Book 37, Chapter 15 [3].

Nestled just before obviously untrue the claims of medicinal powers associated with diamond, we find potential observations of two of its unique properties: diamond is incredilby hard (serving as the reference material for the high end of the Mohs scale of hardness) [4], and it is *diamagnetic* [5], meaning that it acts to expel magnetic field lines penetrating the crystalline structure (though Pliny's rigor leaves much to be desired, and it's unlikely that 'antipathy' maps into diagmagnetism per se). These two properties, in addition diamond's brilliant lustre, its natural occurrence in many different colors, and its extraordinarily toughness, have made it the most sought after industrially applicable gem [2]. The twin histories of aesthetic appreciation of diamond and the formal study of its properties can be considered two sides of the same coin, each having nearly as much intrigue as the other. Understanding the behavior of electrons in diamond is just as alluring to modern spectroscopists as its brilliance was to jewelers throughout human history.

After Pliny's documentation of *adamas*, the study of diamond remained a perennially active topic [2]. Particularly, techniques were developed to enhance the cutting properties of the crystal, and geologists strove to find ever larger quantities of diamond for swelling industrial purposes. In 1904, it was found that diamond placed next to Radium, likely being irradiated by electrons shed by the radioactive element, would remain green (and sometimes radioactive) after treatment [6]. This was probably due to the creation of crystallographic *defects* within the structure of the crystal when the electrons would displace carbon atoms from their host sites to create defects within the lattice. A defect occurs when one or more carbon atom of the host crystal is displaced from its location, leaving a vacancy. This discovery, coupled with

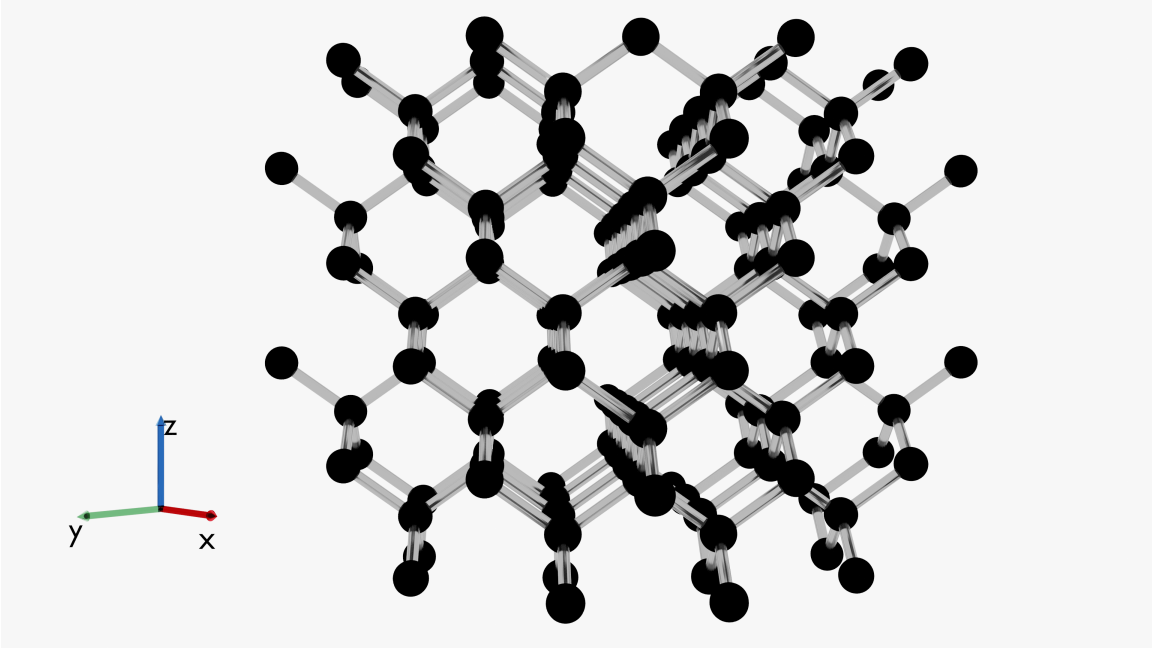

Figure 1.1: The face-centered-cubic structure of the diamond lattice as viewed from the [110] plane. This plane corresponds to the cleavage plane of the sample studied in this work.

a puzzling array of flourescence lines later attributed to defects and atomic inclusions, found by spectroscopists upon ultraviolet irradiation [7]. This, coupled with the characterization of the face-centered cubic diamond crystal structure [8] (as depicted in Figure 1.1), birthed the modern study of structural impurities in diamond using optical spectroscopy.

In 1976, it was found that the most common defect in diamond was associated with nitrogen impurities within the host lattice binding to a nearby lattice defect [9]. Much later, in 1996 [10] the detailed energy level structure and formation mechanism was proposed. It was determined that the nitrogen vacancy center (NV) hosted one nitrogen atom bound covalently to a *vacant* adjacent lattice site. This unique structure allows the energy levels of the nitrogen impurity to mix with the dangling bonds of the host lattice to form an energy level system that is easily accessible at both optical and microwave frequencies. Furthermore, because of the unique properties of the diamond lattice outlined above, NV centers behave almost like naturally

occurring trapped atomic systems within the lattice, obviating the need for experimental overhead associated with confining free atoms. From a quantum measurement and information perspective, they posses boundless application potential [11–13]. NV centers are isolated from the outside environment in large part due to the hardness and diamagnetic nature of the lattice; Pliny's observations are still relevant.

Subsequent to the precise understanding of the optical properties of NV centers, realizations of quantum computation with centers were proposed [11]. These proposals focused on using the split ground state as a qubit (an accessible, manipulable two-level quantum system). Recent work has extended the coherence time of this qubit to roughly 1 second [14], long enough for widescale application. Other possible applications include using NV centers as nanoscopic, sensitive probes of magnetic fields by monitoring subtle shifts in the energy level splittings induced when NV centers are placed in proximity to magnetic field lines [12]. Such sensors have been made that are sensitive to the directionality of the field, and it is becoming more common to use NV centers to image magnetic fields directly generated by interesting transport phenomena in solids [15], or to image magnetic fields with complicated topology with high resolution [16].

NV centers have been shown to be possible candidates for many other applications. In scenarios where quantum information must be stored in a so-called 'quantum-memory' (a qubit or set of qubits with an extended coherence time) before being re-accessed, NV centers have been shown great promise [17]. NV centers have also been shown to be adept at measuring the strain induced in a diamond crystal, with potential application as remotely probed strain gauges [18]. So wide are the potential applications of NV centers [19], that the study of their optical and electronic properties constituted one of the most heavily pursued areas of spectroscopy over the past two decades.

It was not long, however, until it was realized that NV centers do have a few major

flaws in applications requiring optical identicality between emitters and absorbers. For one thing, they are highly polar, meaning that they are uniquely susceptible to static and dynamic lattice fluctuations. This results in a broad phonon sideband over which much of their absorption and fluorescence occurs [20], because the excited state manifold couples efficiently with diamond lattice phonons. This is not desirable when one wants to communicate amongst a number of identical centers with identical photons: if one sends a photon of a certain color into an NV center, there is no guarantee the same color photon will come out, reducing the overall efficiency of a communication or computation channel.

Because of this fact, the search for color centers with more favorable optical properties intensified. Many other defects associated with other ions and dislocations were known. Rapid work was done to enumerate the properties of the group IV color centers (defects associated with atoms which are iso-valent to carbon). Much of this characterization work is ongoing [21], but it was quickly apparent that one point defect in the family of defects associated with the silicon atom could potentially provide an optically accessible system with many of the same features as the NV center (optically accessible energy levels associated with different electron spins, long spin coherence times, long electronic coherence times, ability to generate indistinguishable photons, etc.)[20, 22–25].

1.2 The Physical Structure of the Silicon-Vacancy Center

The silicon-associated defect we study in this work, the negatively charged Silicon-Vacancy center (SiV), has several advantages over the NV center. Due to the spatial similarity between its ground and excited state electron wavefunction owing to its membership in the D_{3d} point group, the SiV center is much less susceptible to linear perturbations than the NV center. This means, primarily, that roughly 70% of the photoluminescence is emitted in the zero phonon line (ZPL) manifold [20], as opposed

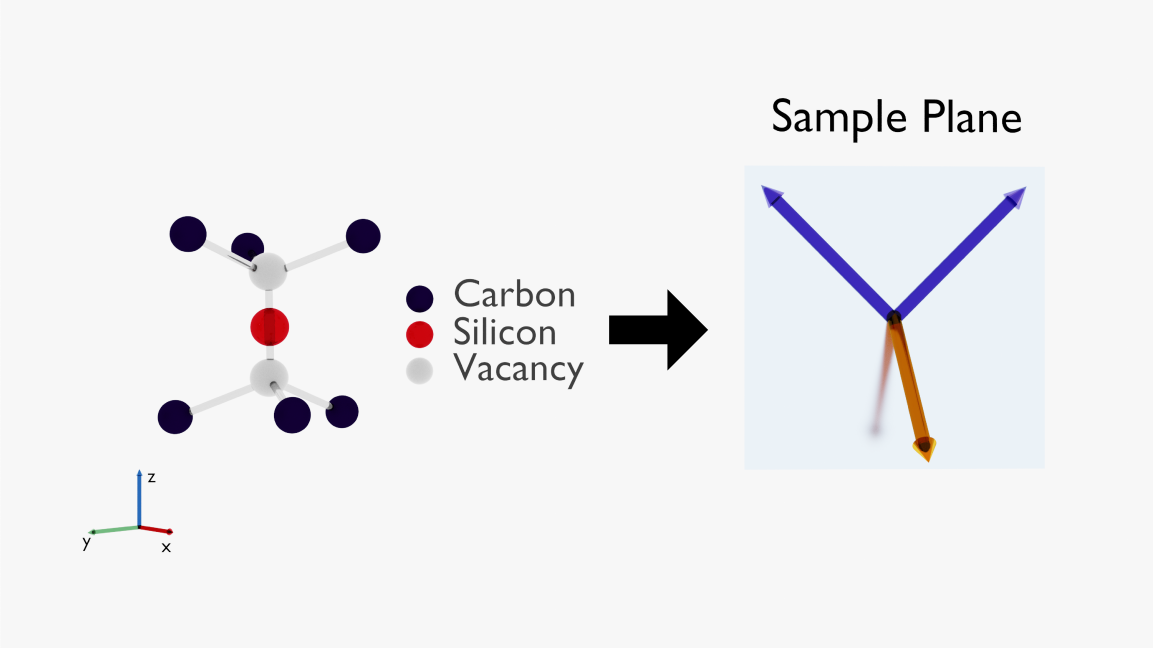

Figure 1.2: The split di-vacancy structure of the SiV color center. This structure leads to four possible orientations within the diamond lattice. Here we depict these orientations with respect to the [110]-oriented face of our lattice. There are two in-plane orientations, and two out-of-plane orientations of the vacancy-Silicon-vacancy axis.

to the large spread of possible emission and absorption energies present in the NV center. This makes the SiV much more favorable for a majority of the aforementioned applications.

This color center is composed of a silicon atom located equidistantly between two carbon vacancies in the diamond lattice [22]. Figure 1.2 is a depiction of this physical structure, along with possible orientations in the diamond lattice. In general, group IV color centers tend to follow this structure and orientation along the $\langle 111 \rangle$ axes of diamond. Indeed, other vacancy centers associated with most remaining atoms in group IV have been discovered and characterized [21, 26–29]. These color centers tend to form in a similar structure to the SiV and each have their own relative merits and demerits with respect to both the SiV center and the NV center. In tandem with the negatively charged silicon-vacancy center, there exist the neutral and doubly negatively charged SiV centers [30].

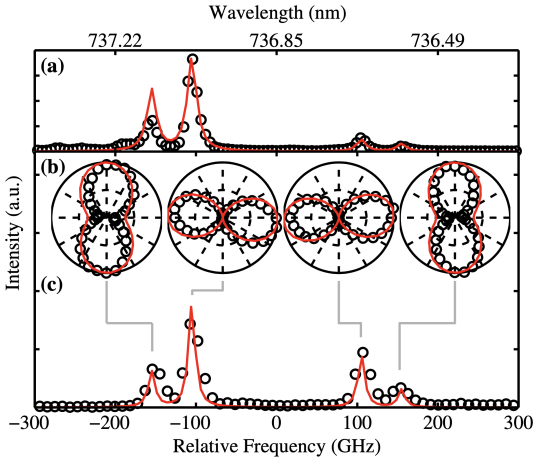

Figure 1.3: As adapted from [31], the four-line structure of the SiV center (a) from a sparse SiV ensemble and (b) from a single color center. The polarization selection rules are linear, with two transitions being excited with vertically polarized light, and two with horizontally polarized light, as depicted in the figure insets.

1.3 The Electronic Structure of the Silicon-Vacancy Center

Upon close experimental and theoretical study of the photoluminescence attributable to the SiV center, it was found that the negatively charged defect had a four zero-phonon line (ZPL) transition manifold [31] which is the set of transition energies at which no phonon is emitted or absorbed along with the optical emission and absorption processes taking place under interaction between the color center and light. This four-line manifold, as first described in Figure 1.3, has four transition energies, with a typical ground-state splitting of 50 GHz and a typical excited state splitting of 250 GHz. Figure 1.4 depicts this electronic structure. Each ground and excited state is doubly degenerate in the spin degree of freedom, allowing for easy optical manipulation of the electron spin by coupling excitation to a weak magnetic field [31].

As stated above, the SiV electronic structure, for both the negatively charged and neutral color center, is favorable for generating indistinguishable photons, and amenable to coherent optical control of electron spin states [20, 25]. Anywhere the NV center has been employed in the past, the SiV center stands to improve its

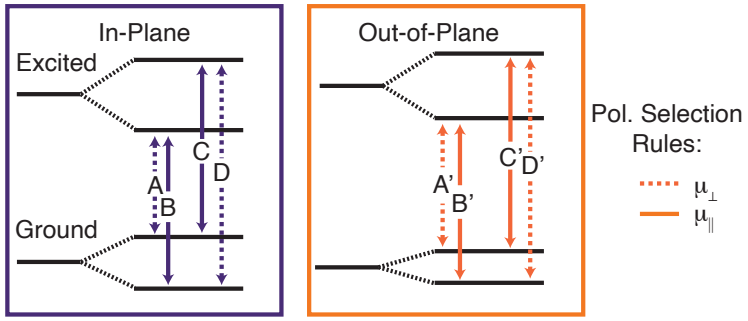

Figure 1.4: The ground- and excited-states of the Silicon-vacancy center are split by spin-orbit coupling to a pair of doubly-degenerate ground and excited states. Four optical transitions can take place amongst these energy levels, with two pairs of orthogonally polarized transitions allowed. The polarization selection rules are denoted with respect to the vacancy-Silicon-vacancy axis.

performance. However, there are several open questions that remain. In this work we attempt to address some of these open questions by characterizing the nonlinear spectroscopic response of SiV centers in diamond to optical excitation.

1.4 Open Questions in the Study of the Silicon-Vacancy Center

Although many of the basic properties of SiV centers in diamond have been investigated, several open questions remain. Primarily, the quantum efficiency (number of outgoing/number of incoming photons) for the SiV is relatively low [32]. In order to form the basis of future quantum-information architecture, this is a phenomenon that must be addressed. There is some evidence that electrons in the higher-lying excited state can couple to a dark state [30], thus opening a nonradiative decay channel for electrons and reducing the quantum efficiency of the color center. Furthermore, a majority of the study carried out so far on silicon vacancy centers in diamond has been either using single centers or sparse ensembles of color centers. Thus, it is not clear that the properties that have been characterized so far are characteristic of a majority of color centers, or if the selection of exceptional centers with favorable properties has

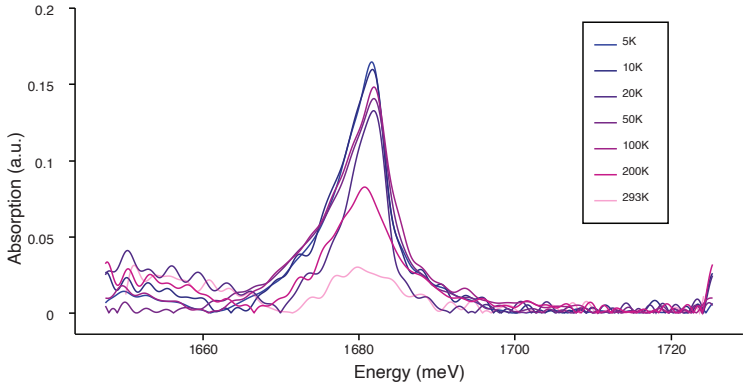

Figure 1.5: An absorption spectrum of an ensemble of silicon vacancy centers in diamond as a function of temperature.

biased the field, increasing engineering headaches in the future. These facts lead to the question: how inhomogeneous are ensembles of color centers; in other words, do their individual ZPL lines vary in energy as a result of differing environments in the diamond lattice? To get a basic idea of how deep this question might lead us, we took a simple absorption spectrum. *This spectrum, in Figure 1.5, is in direct tension with the data measured in Figure 1.3.* We do not see four broad transitions of the ZPL, as canonically measured. Clearly, the single-center results observed so far are not reflective of the collective behavior of our sample. The answer to our first question appears to be complicated.

Furthermore, the effects and possible consequences that center-center interactions have on SiV optical properties have been sparingly investigated. So far, only photonic interactions between pairs of distant centers have been studied [33]. Isolated, bright centers form the bedrock of the characterization efforts so far, yet it may be advantageous to be able to tune interactions between centers to be able to couple or decouple arrays of centers together to transmit information [34]. Understanding the ways in which color centers interact is crucial to tailoring the properties of future SiV-based devices. This leads to the question: do proximate color centers interact, and if so, how?

To answer both of these questions, we will employ collinear multi-dimensional co-

herent spectroscopy (MDCS) to study our dense ensemble of SiV centers in diamond [35–37]. The next chapter will serve to provide a basic primer on MDCS, and we will cover all relevant experimental details in that chapter. To the reader interested in MDCS (but wishing to avoid pages of mathematics), two basic facts about MDCS are important: primarily, by unwrapping optical spectra over multiple frequency axes, MDCS is capable of distinguishing the ensemble-averaged response (the inhomogeneous response) and the intrinsic individual response (the homogeneous response) of systems to optical pulses of light. Additionally, MDCS is uniquely sensitive to few- and many-body interactions between optically active systems. These two facts, in addition to the ability to examine coherent coupling between systems or between systems and dark states, makes MDCS an ideal tool to answer these questions.

In the chapter following the MDCS primer, We discuss the results of comparing MDCS spectra collected using two different detection techniques: one sensitive only to the photoluminescence of excited color centers, and the other sensitive to the full response of color centers to optical driving, including centers that do not emit photons. We use this comparison to investigate the large population of color centers that do not possess the canonical four-line ZPL spectral response upon optical driving, and posit mechanisms by which energy deposited to these these color centers decays through non-radiative channels, solving the tension between our absorption data, and the well-known luminescence profile of the SiV color center. In the final chapter within this half of my thesis, we discuss our work using MDCS to study interactions between color centers. We show that SiV centers in an ensemble *do* interact, and they likely do so through radiative dipole-dipole interactions. Furthermore, we show that these multiple centers can be made to behave as single quantum systems when linked by interactions. These results add to the rich SiV literature, and point the way toward new applications of SiV centers in diamond.

References

(1) Crookes, W., *Diamonds*; Harper Brothers: London, 1909.

(2) Tolansky, S., *The History and Use of Diamond*; Methuen: 1962.

(3) Pliny; Bostock, J.; Riley, H. T.; Mayhoff, K. F. T. The natural history `http://www.perseus.tufts.edu/cgi-bin/ptext?lookup=Plin.+Nat.+toc`.

(4) Mcconnell, R., *Quantitative hardness of irradiated and non-irradiated diamond ; final report.* Ann Arbor; University of Michigan, Mineralogical Laboratory: 1962.

(5) Nikolaev, A. V.; Verberck, B., *Diamagnetism of Diamond and Graphite*; Elsevier B.V.: 2006, pp 245–278.

(6) Crookes, W. *Proceedings of the Royal Society of London* **1904**, *74*, 47–49.

(7) LONSDALE, K. *Nature* **1944**, *153*, 669–672.

(8) BRAGG, W. H.; BRAGG, W. L. *Nature* **1913**, *91*, 557–557.

(9) Davies, G.; Hamer, M. F. *Proceedings of the Royal Society of London. Series A, Mathematical and Physical Sciences* **1976**, *348*, 285–298.

(10) Lenef, A.; Rand, S. *Physical Review B - Condensed Matter and Materials Physics* **1996**, *53*, 13441–13455.

(11) Lukin, M. D.; Hemmer, P. R. *Phys. Rev. Lett.* **2000**, *84*, 2818–2821.

(12) Taylor, J. M.; Cappellaro, P.; Childress, L.; Jiang, L.; Budker, D.; Hemmer, P. R.; Yacoby, A.; Walsworth, R.; Lukin, M. D. *Nature Physics* **2008**, *4*, 810–816.

(13) Schröder, T.; Trusheim, M. E.; Walsh, M.; Li, L.; Zheng, J.; Schukraft, M.; Sipahigil, A.; Evans, R. E.; Sukachev, D. D.; Nguyen, C. T.; Pacheco, J. L.; Camacho, R. M.; Bielejec, E. S.; Lukin, M. D.; Englund, D. *Nature Communications* **2017**, *8*, 1–7.

(14) Abobeih, M. H.; Cramer, J.; Bakker, M. A.; Kalb, N.; Markham, M.; Twitchen, D. J.; Taminiau, T. H. *Nature Communications* **2018**, *9*, 2552.

(15) Ku, M. J. H. et al. *Nature* **2020**, *583*, 537–541.

(16) Lenz, T.; Chatzidrosos, G.; Wang, Z.; Bougas, L.; Dumeige, Y.; Wickenbrock, A.; Kerber, N.; Zázvorka, J.; Kammerbauer, F.; Kläui, M.; Kazi, Z.; Fu, K.-M. C.; Itoh, K. M.; Watanabe, H.; Budker, D. *Phys. Rev. Applied* **2021**, *15*, 024040.

(17) Fuchs, G. D.; Burkard, G.; Klimov, P. V.; Awschalom, D. D. *Nature Physics* **2011**, *7*, 789–793.

(18) Knauer, S.; Hadden, J. P.; Rarity, J. G. *npj Quantum Information* **2020**, *6*, 50.

(19) Schirhagl, R.; Chang, K.; Loretz, M.; Degen, C. L. *Annual Review of Physical Chemistry* **2014**, *65*, PMID: 24274702, 83–105.

(20) Becker, J. N.; Becher, C. *Physica Status Solidi (A) Applications and Materials Science* **2017**, *214*, 1–11.

(21) Bradac, C.; Gao, W.; Forneris, J.; Trusheim, M. E.; Aharonovich, I. *Nature Communications* **2019**, *10*, 5625.

(22) Goss, J.; Jones, R.; Breuer, S.; Briddon, P.; Öberg, S. *Phys. Rev. Lett.* **1996**, *77*, 3041–3044.

(23) Becker, J. N.; Pingault, B.; Groß, D.; Gündo ğan, M.; Kukharchyk, N.; Markham, M.; Edmonds, A.; Atatüre, M.; Bushev, P.; Becher, C. *Phys. Rev. Lett.* **2018**, *120*, 053603.

(24) Sipahigil, A.; Jahnke, K. D.; Rogers, L. J.; Teraji, T.; Isoya, J.; Zibrov, A. S.; Jelezko, F.; Lukin, M. D. *Phys. Rev. Lett.* **2014**, *113*, 1–5.

(25) Sipahigil, A. et al. *Science* **2016**, *354*, 847–850.

(26) Ditalia Tchernij, S. et al. *ACS Photonics* **2018**, *5*, 4864–4871.

(27) Trusheim, M. E.; Wan, N. H.; Chen, K. C.; Ciccarino, C. J.; Flick, J.; Sundararaman, R.; Malladi, G.; Bersin, E.; Walsh, M.; Lienhard, B.; Bakhru, H.; Narang, P.; Englund, D. *Phys. Rev. B* **2019**, *99*, 075430.

(28) Iwasaki, T. et al. *Scientific Reports* **2015**, *5*, 12882.

(29) Rugar, A. E.; Dory, C.; Aghaeimeibodi, S.; Lu, H.; Sun, S.; Mishra, S. D.; Shen, Z.-X.; Melosh, N. A.; Vučković, J. *ACS Photonics* **2020**, *7*, 2356–2361.

(30) Gali, A.; Maze, J. R. *Phys. Rev. B* **2013**, *88*, 235205.

(31) Hepp, C.; Müller, T.; Waselowski, V.; Becker, J. N.; Pingault, B.; Sternschulte, H.; Steinmüller-Nethl, D.; Gali, A.; Maze, J. R.; Atatüre, M.; Becher, C. *Phys. Rev. Lett.* **2014**, *112*, DOI: 10.1103/PhysRevLett.112.036405.

(32) Neu, E.; Agio, M.; Becher, C. *Opt. Express* **2012**, *20*, 19956–19971.

(33) Evans, R. E.; Bhaskar, M. K.; Sukachev, D. D.; Nguyen, C. T.; Sipahigil, A.; Burek, M. J.; Machielse, B.; Zhang, G. H.; Zibrov, A. S.; Bielejec, E.; Park, H.; Lončar, M.; Lukin, M. D. *Science* **2018**, *362*, 662–665.

(34) Zhang, J.; Ditty, M.; Burgarth, D.; Ryan, C. A.; Chandrashekar, C. M.; Laforest, M.; Moussa, O.; Baugh, J.; Laflamme, R. *Physical Review A - Atomic, Molecular, and Optical Physics* **2009**, *80*, 1–5.

(35) Tekavec, P. F.; Lott, G. A.; Marcus, A. H. *Journal of Chemical Physics* **2007**, *127*, 214307.

(36) Nardin, G.; Autry, T. M.; Silverman, K. L.; Cundiff, S. T. *Opt. Express* **2013**, *21*, 28617–27.

(37) Smallwood, C. L.; Cundiff, S. T. *Laser and Photonics Reviews* **2018**, *12*, 1–21.

CHAPTER II

Multidimensional Coherent Spectroscopy: A Short Primer

2.1 Introduction

Optical spectroscopy is one of the most powerful tools we have developed to learn about nature. Spectroscopists study the interaction between matter and light. Information about the microscopic mechanisms governing particles in a material is encoded in the colors of light that an object emits or absorbs. A measurement quantifying the colors of light that an object emits or absorbs is measured as an *optical spectrum*. The object of modern spectroscopy is to tease apart the details of the interactions that govern the broad array of interleaving quantum phenomena giving rise to the macroscopic behavior of systems. There are a panoply of advanced modern spectroscopic experiments, used to investigate anything from the basic quantum mechanics driving photosynthesis [1], or to disentangle the nature of interactions that govern the most basic emergent phenomena, i.e. ferroelectricity and super-conducting behavior, by studying the emission spectra of model systems as the extrinsic environment is tuned [2].

A typical spectroscopy experiment involves shining a laser with some known spectrum at a sample and recording either the photoluminescence (PL) (light re-emitted

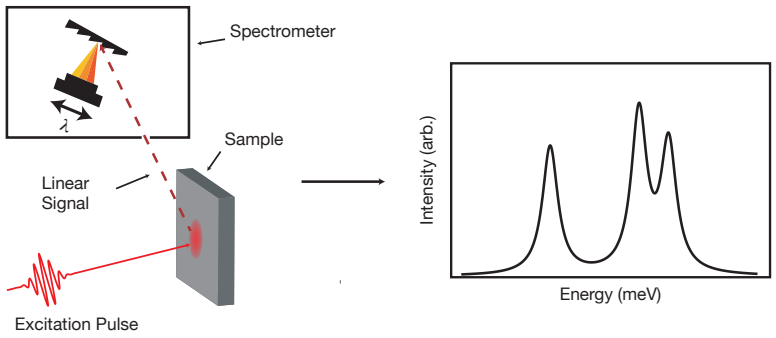

Figure 2.1: A figure summarizing most linear spectroscopy measurements. A laser is directed at a sample one wants to characterize. The interaction of the sample with the laser either causes the sample to emit or absorb light, which is then sent to a spectrometer to resolve the color content of the sample's response, as depicted in the rightmost panel.

upon absorption of the initial laser light) or the absorption (the reduction in intensity of light transmitted through the sample) as a function of frequency. Because we are interested in teasing out the microscopic dynamics of the light-matter interaction upon excitation of our silicon-vacancy centers with light in this thesis, we consider spectroscopy as *the study of the interaction between an open quantum system and ultrafast pulses of light*. We take the phrase *open quantum system* to mean a collection of quantum mechanical states of some system that interact with light and are weakly coupled to their environment.

Spectroscopists often describe the ways in which the quantum mechanical properties of a system determine their spectra using something called the *density matrix formalism*. We will not enumerate all statistical properties that density operators and quantum states posses; that would be a recapitulation of several textbooks worth of material, see for instance Refs. [3–5]. Instead, we will utilize the most relevant results for our work here.

The fundamental conceit behind density matrix formalism is the following: by

treating the electric field interacting with an object as a classical electromagnetic wave that subtly perturbs the system, the statistical response of a material to this perturbation will be determined by adding a term to its Hamiltonian encoding the new electric field interaction. The time evolution of the statistics of the states occupied by an ensemble of objects interacting with each other and their environment, or an *open quantum system* as defined above, can be described using this statistical framework once the Hamiltonian governing the interaction between the system and light is known. This formalism allows us to study what happens, quantum mechanically, when we perturb an open quantum system with light.

This chapter will briefly introduce *coherent spectroscopy* as a way in which to probe the basic quantum mechanical properties of a system. This type of spectroscopy is one in which a series of ultrashort pulses of light (duration <1 ps) are used to interact with a material system. Typically, the unknown information that a spectroscopist is interested in learning amounts to determining the center frequency and lineshape of some spectroscopic resonance. By carefully measuring these two properties under different experimental conditions, a full dynamical picture of the behavior of emitters (electrons, excitons, or other particles or collective modes within a material) often begins to emerge.

This chapter will begin by introducing the basic ideas of coherent, linear two-pulse spectroscopy. We will then discuss the limitations of this type of spectroscopy and introduce a *nonlinear* spectroscopic technique, Multi Dimensional Coherent Spectroscopy (or MDCS), that is designed to overcome these limitations. We will outline the basics of two measurements reported here in subsequent chapters, and show how they will address the the main questions posed in the previous chapter in the Silicon-Vacancy system.

Per reference [4], we have a few options when attempting to describe the dynamics of a quantum system under optical driving. (1) Assuming we have an isolated

system and know the collection of stationary states spanning the space of all possible configurations of a system (known as Hilbert space), we can work directly with the Hamiltonian in the interaction picture and then examine its action on the initial state of the system. (2) If, instead, the total system is actually an *ensemble* of individual identical constituents, but the coupling of the system to its environment is *Markovian* [4, 6, 7], it is advantageous to work with the density operator as opposed to individual eigenstates, and describe the dynamics of this system directly in Hilbert space (the vector space of states spanned by the possible eigenstates a system can occupy). This approach results in the famous Optical Bloch equations [6]. (3) If a system is sufficiently complicated, and its coupling to a bath is nontrivial, one must work in *Liouville Space*: a higher dimensional vector-space spanned by all possible density operators. The goal in this case is to describe the trajectory of the initial density matrix through Liouville space as the system interacts in a complex way with its environment, and only options (2) and (3) are fully extendable to treat a quantized electric field.

From the perspective of capturing the essential properties of systems probed with spectroscopic techniques, we must choose one of the above paths before we start. It is essential that we introduce MDCS with enough theoretical tools at our disposal to analyze the relevant dynamics of SiV centers, but not so much detail that we obscure the main points. We therefore select option (2) from the above.

2.2 Linear Response Theory and Two-Pulse Correlation Spectroscopy

In this section, we will introduce a coherent spectroscopic technique, time-domain, two-pulse correlation spectroscopy, that will help us study the microscopic dynamics of quantum systems. We will emphasize again an important point: when approaching

an unknown system, the spectroscopist is interested in extracting the center frequencies and lineshapes of resonances in some optical range, with the hope that a model of the underlying microscopic dynamics can be successfully applied. Often, as we shall see, there are many ambiguities that remain unsolvable in this type of spectroscopy. However, we will begin introducing the formalism necessary to understand MDCS, illustrate the workings of Fourier transform spectroscopy in general, and link coherent two-pulse correlation spectroscopy with more familiar spectroscopic techniques such as absorption and photoluminescence (PL) techniques. We will build this groundwork here, as it is important to easily understanding MDCS as an extension of basic time-domain spectroscopic techniques.

Suppose we take an 'atom' with two energy levels: a 'ground' and an 'excited' state, with state vectors $|0\rangle$ and $|1\rangle$ respectively. This constitutes the most simple possible quantum-mechanical system. Suppose also that this atom is allowed to interact with its environment. The effect that interactions with the environment will have on an open quantum system are covered in slightly more detail detail in appendix A, but for the sake of simplicity, we will assume we are working in the *Markovian Limit* [4, 8] with a simple system-bath coupling. Strictly speaking this limit results in exponential dephasing of our optical response [4]. Though extensive formalism exists to describe the dynamics of open quantum systems in which this limit does not apply [4, 9], for all results discussed herein, we can safely describe relevant spectral lineshapes as resulting from exponential dephasing of the system. We should be clear here about our goal: we are outlining the ways in which the microscopic quantum dynamics influence the macroscopic spectra we measure with ultrafast laser pulses. To that end, we will simulate the equation of motion of our system under a driving field and show how a two-pulse correlation spectroscopic measurement can help us characterize our system.

Suppose we have a Hilbert space spanned by states $|0\rangle$ and $|1\rangle$. The density matrix

is an operator, defined as

$$\rho = \sum_{n,m} c_n^* c_m \left|n\right\rangle \left\langle m\right| \tag{2.1}$$

with $n, m \in [0, 1]$ indexing the possible eigenstates of the system, and the c_n are complex coefficients such that $\sum_n |c_n|^2 = 1$. Let us suppose that our system has a stationary Hamiltonian H_0 with eigenenergies E_0 and E_1 of states $|0\rangle$ and $|1\rangle$ respectively such that

$$H_0 = \begin{pmatrix} E_0 & 0 \\ 0 & E_1 \end{pmatrix}. \tag{2.2}$$

Now, the time evolution of our density matrix will be given by the Liouville-von Neuman equation

$$\dot{\rho} = \frac{-i}{\hbar}[H, \rho]. \tag{2.3}$$

At this point, our formalism is completely general. We will now, however, assume that the light interacting with our system perturbs it only slightly. This will later allow us to perturbitively expand our dynamics by electric field order. To that end, our Hamiltonian will become

$$H = H_0 + V(t), \tag{2.4}$$

where

$$V(t) = \begin{pmatrix} 0 & -\mu E(t) \\ -\mu E^*(t) & 0 \end{pmatrix} \tag{2.5}$$

is the expression for the driving potential in the dipole approximation such that our system's interaction with light can be described fully by the transition dipole moment $\mu = \langle 0| e\mathbf{r} |1\rangle$ with e the elementary charge of the electron, $E(t)$ the driving field, and $\mathbf{r}$ a spatial coordinate. For some arbitrary state of our system, we can write

$$\rho = \begin{pmatrix} \rho_{00} & \rho_{01} \\ \rho_{01}^* & \rho_{11} \end{pmatrix}. \tag{2.6}$$

Now, inserting this state into the time-evolution equation, we will have the following equation of motion

$$\begin{pmatrix} \dot{\rho}_{00} \\ \dot{\rho}_{01} \\ \dot{\rho}_{10} \\ \dot{\rho}_{11} \end{pmatrix} = \frac{-i}{\hbar} \begin{pmatrix} -\mu E(t)\rho_{10} + \mu E^*(t)\rho_{01} \\ \rho_{01}(E_0 - E_1) + \mu E(t)(\rho_{00} - \rho_{11}) \\ \rho_{10}(E_1 - E_0) + \mu E^*(t)(\rho_{11} - \rho_{00}) \\ \mu E(t)\rho_{10} - \mu E^*(t)\rho_{01} \end{pmatrix}. \tag{2.7}$$

Before simulating this equation of motion for the density matrix of our system, we will introduce two decay mechanisms for this system: the system is allowed to spontaneously emit a photon over the transition from the excited state to the ground state or the excitation is allowed to 'decohere' through fluctuations of the transition energy due to interactions with the environment. We will therefore phenomenologically describe their effect on the density matrix by introducing two decay rates:

$$\Gamma = \frac{1}{T_1} \tag{2.8}$$

is the characteristic decay rate of a population of electrons excited to state $|1\rangle$ while

$$\gamma = \frac{1}{T_2} \tag{2.9}$$

is the characteristic, pure-dephasing timescale (T_2) of fluctuations in the energy of state $|1\rangle$ [4, 6, 10]. This timescale is set by interactions that cause the phase coherence of a state to be lost (inter-center interactions, center-phonon coupling, etc.) without the population in state $|1\rangle$ decaying by the emission of a photon. In general, we will have

$$\gamma = \frac{(\Gamma_{rad} + \Gamma_{nonrad})}{2} + \frac{1}{T_2} \tag{2.10}$$

where Γ_{rad} corresponds to the radiative lifetime of an emitter in the excited state and

Γ_{nonrad} corresponds to the rate of spontaneous decay of an excitation through non-radiative channels, such as phonon emission, or decay into a dark state [3, 4, 11]. All real quantum systems are inherently 'open' to some extent, with their energy levels susceptible to the influence of their surroundings, captured here phenomenologically with γ.

With these modifications, our equations of motion have now become

$$\begin{aligned} \dot{\rho}_{00} &= \tfrac{-i}{\hbar}(-\mu E(t)\rho_{10} + \mu E^*(t)\rho_{01}) + \Gamma\rho_{11} \\ \dot{\rho}_{01} &= \rho_{01}(i\omega_0 + \gamma) - \tfrac{i\mu E(t)}{\hbar}(\rho_{00} - \rho_{11}) \\ \dot{\rho}_{10} &= \rho_{10}(-i\omega_0 + \gamma) + \tfrac{i\mu E(t)}{\hbar}(\rho_{00} - \rho_{11}) \\ \dot{\rho}_{11} &= \tfrac{-i}{\hbar}(-\mu E(t)\rho_{10} + \mu E^*(t)\rho_{01}) - \Gamma\rho_{11} \end{aligned} \quad . \tag{2.11}$$

This is equivalent to the famous Optical Bloch equation describing the dynamics of a two-level system under arbitrary driving field [12]. To learn about our system using light, we will use a laser pulse (though in general the pulse need not be real)

$$E(t) = A_0 \cos(\omega_0 t) e^{-\frac{t^2}{2\sigma^2}}. \tag{2.12}$$

In figure 2.2, we show the solution to these equations with the parameters $\gamma = 1/25 = \Gamma$, $2\sigma^2 = 100$, $E_0 = 0.05$, and $\omega_0 = 1.25$ with arbitrary units. It should be noted that there are two separate quantities that we might be interested in when we say the 'dynamics' of a two-level system interacting with light: we may be interested either in the population decay time, or in the 'coherence' that has been excited by the input pulse. In this case, a *coherence* refers to a nonzero, oscillatory off-diagonal density matrix element. **We are typically interested in this element because it determines the dominant ultrafast response of a system to a driving field**.

How might we measure this density matrix element? When the incident electric

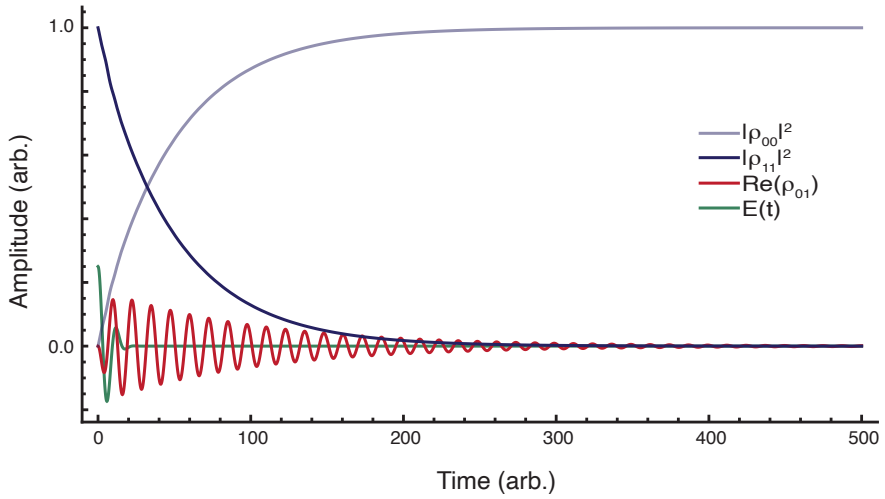

Figure 2.2: A simulation of the dynamics of the various density matrix elements for a two-level system under resonant, pulsed driving by an electric field.

field interacts with the sample, it induces a polarization field.

$$\vec{P}(t) = \mathrm{Tr}(\rho\hat{\mu}) \tag{2.13}$$

where ρ is our density matrix and μ is the transition dipole operator

$$\hat{\mu} = \begin{pmatrix} 0 & \vec{\mu}_{01} \\ \vec{\mu}_{10} & 0 \end{pmatrix}. \tag{2.14}$$

with $\vec{\mu}_{01} = \langle 0| e\mathbf{r} |1\rangle = \vec{\mu}^{\,*}_{10}$ being the familiar transition dipole moment. We can then calculate the induced polarization field, finding

$$\vec{P}(t) = \vec{\mu}_{01}\rho_{10}(t) + \vec{\mu}_{10}\rho_{01}(t). \tag{2.15}$$

It is clear then, that the off-diagonal matrix elements govern our system's linear response to driving with an optical pulse in this case. How then should we measure such an induced polarization field? There are several ways. The most simple characteriza-

tion would be to shine the pulse through the system of interest. The polarization field will destructively interfere with the input pulse, generating an 'absorption' dip in the transmitted spectrum. **This** is the underlying connection between coherent spectroscopic techniques and more traditional absorption measurements. We can write this relation by noting

$$\vec{P}(\omega) = \epsilon_0 \chi \vec{E}(\omega). \tag{2.16}$$

The dip generated by interferometric attenuation of the polarization field by a sample of length l will be governed by the well-known Beer's law [6]

$$I(\omega) = I_0(\omega)^{-\alpha(\omega)l} \tag{2.17}$$

where we can relate the polarization field we calculated above to the observed attenuation due to the emitted polarization field using the relationship [6]

$$\alpha = \frac{\omega}{c}\mathrm{Im}(\chi). \tag{2.18}$$

This type of spectroscopy, however, is an *incoherent* spectroscopy. We cannot get phase information about $\vec{P(t)}$ using a simple absorbtion measurement, and so we do not know if the width of our absorption feature reflects the timescale of the intrinsic dynamics, or if other contributions like the generation of a population or photon scattering play a role in determining the overall spectrum. Getting phase information about $\vec{P(t)}$ allows us to get slightly more information from a one-dimensional spectrum.

To see how, assume that we have an unknown two-level system with γ and Γ (different from the above simulation and unknown) describing its behavior under radiative driving by a pulsed laser. The goal is to characterize the sample's *polarization* as a result of the incoming electric field. We will be attempting to measure $\vec{P}(t)$

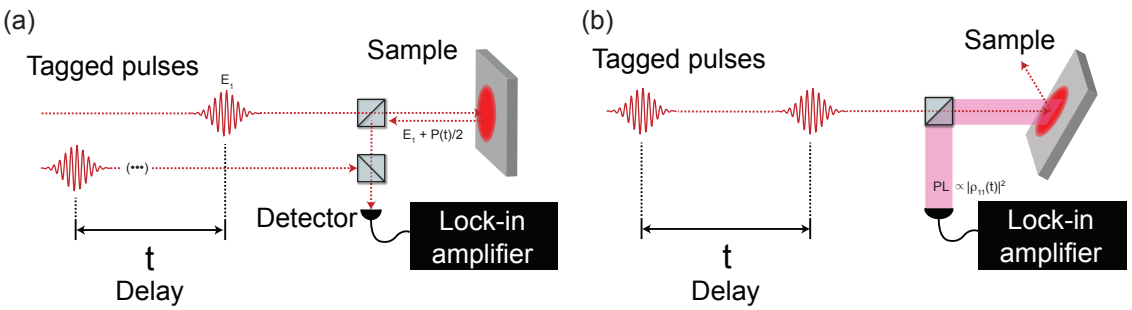

Figure 2.3: A depiction of the practical two different implementations of two-pulse correlation spectroscopy. In case (a), a laser pulse is sent onto a sample, with the reflected (or transmitted) field being characterized by a pulse that does not interact with the sample. In case (b), two laser pulses interact with the sample. The first pulse excites a polarization field ($\vec{P(t)}$), while the second pulse converts the phase and amplitude information of $\vec{P(t)}$ into a modulation of the PL emitted by the sample, reflected in a modulation of the matrix element $\rho(t)_{11}$.

by using one pulse to drive the system, and another to characterize its response by monitoring how the sample's response to the first field changes its response to the second.

There are two ways to do this: we can either send a pulse into the sample and collect the reflected or transmitted light, then interfere the returned pulse with a second pulse as a function of the time delay between them, or we can monitor the modulation of the PL as a function of the delay between pulses. The first method is the generalized version of Fourier Transform Infrared Spectroscopy, while the second method corresponds more closely to a PL-detected absorption spectrum. Figure 2.3 is a summary of the practical implementation of each technique. In a practical implementation of two-pulse correlation spectroscopy, one usually modulates the first pulse with respect to the second in some way, either by chopping the pulse or applying a finite frequency shift with an acousto-optic modulator (AOM). Information on $\vec{P(t)}$ is then collected on a photodiode by monitoring the amplitude and phase of the signal modulated at the beat frequency between the pulse tags with a Lock-In amplifier as a function of the delay between the two tagged pulses, and then Fourier-transformed to yield a frequency-domain spectrum. This collection method adapts

readily to nonlinear spectroscopy [13, 14].

The first collection method (figure 2.3(a)) corresponds to a cross-correlation between the polarization field excited in the system and the electric field field of our laser light source. Figure 2.4 shows the signal yielded by this characterization for a two level system with the pulses as described in equation 2.12. In the second case (figure 2.3(b)), we are converting the phase and amplitude of the off-diagonal matrix elements into a population modulation in the excited state of our system as a function of the delay between our pulses. Figure 2.5 shows the signal measured at a photo detector as a function of the inter-pulse delay for such a measurement.

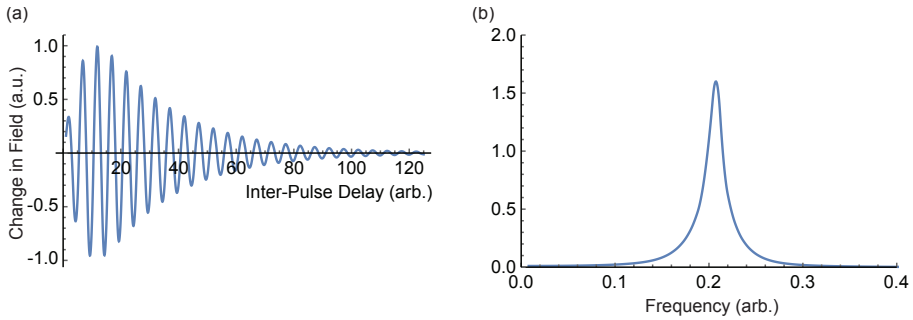

Figure 2.4: The induced polarization field in the (a) time and (b) frequency domains detected by interfering the radiated polarization field with a characterization pulse. The signal initially rises because the excitation pulse has a finite length on the timescale of these dynamics.

The decay of the coherent signal gives us a measurement of γ or Γ (depending on

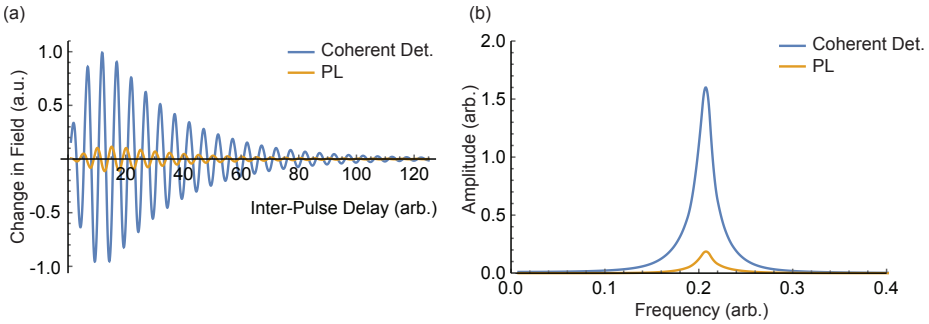

Figure 2.5: A comparison between detecting the induced polarization and detecting the modulated PL as a function of inter-pulse delay in the (a) time and (b) frequency domains.

which is dominant) if we are lucky, but it is typically not the case that the dynamics are this simple [4]. For completeness, we remark that in general it must be the case that $\Gamma \leq \gamma/2$ [6]. There is an important detail that differentiates between these two measurements: there is a clear, fixed, 90° phase difference between them in the time domain, as seen in Figure 2.5. This is due to the fact that exciting a polarization is a 'first-order' effect. Exciting a population is a 'second-order' effect. Though you measure the same qualitative spectrum, there is always a 90° fixed phase between these quantities, resulting from the perturbative expansion in ρ required to understand their relationship. Another important difference that we shall see later on is that the polarization field can be measured between two energy levels *even if* the higher-lying excited state is 'dark' in that it is unlikely to decay via a photon emission. This important phase shift hints at how to generalize these detection methods in a nonlinear, third- or fourth-order spectroscopy technique. More on this in section 2.3.

Figure 2.6 shows how we can diagrammatically represent two-pulse correlation spectroscopy and the action of two pulses on our density matrix. Before the interaction with the first pulse (A), our system is in the ground state. Pulse A transfers some of the weight of that density matrix element to the off-diagonal elements (as indicated by the red arrows). When the second pulse interacts with the sample, some of the weight in the off-diagonal matrix elements is transferred to ρ_{11}. Changes in the Polarization field, $\vec{P(t)}$, and the population ($|\rho_{11}|^2$) upon interaction with the first and second pulses are shown.

Although the interaction of each pulse generates changes in all density matrix elements, our eventual signal depends only on the combined action of each of pulses A and B in Fig. 2.6. To wit: each pulse of light transfers information from one density matrix element to one or more others. The trajectories traced out by these pathways of information transfer can be represented within the framework of *perturbation theory*. In the limit of weak driving fields, each of the 'transfer' steps can be repre-

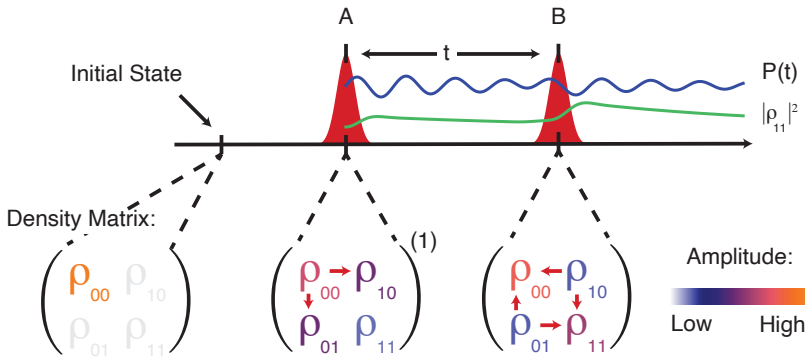

Figure 2.6: This is a depiction of the general response of a two-level system to two pulses of light. The polarization field oscillates as a function of inter-pulse delay, and one measures either the change in the second pulse due to $\vec{P(t)}$ or the modulation of $|\rho_{11}|^2$ as a function of inter-pulse delay. Both measurements give you a proxy for $\vec{P(t)}$ which encodes the sample's response to electromagnetic driving driving. The qualitative behavior of the density matrix at the arrival of each pulse is shown; the red arrows indicate how information constituting the signal pathway of interest is transferred around the matrix elements as each pulse interacts with the sample.

sented as incrementing or decrementing between selected density matrix elements (as represented by following the red arrows in figure 2.6).

The second point is that, amongst the complex transfer of information between density matrix elements, we want to pick out the evolution of selected 'pathways,' which trace the evolution of the density matrix elements as a function of multiple interactions between our sample and our laser field. As can be seen in the simulations of the density matrix dynamics depicted by the solid lines in figure 2.6, one pulse can cause a change in multiple density matrix elements. The key is to trace a specific portion of the information on the sample's interaction with our pulses of light as it is shuffled around the density matrix elements. We typically do that by noting that our driving pulses can be written

$$E(t) = A(t)\mathrm{Exp}(i\mathbf{k}\cdot\mathbf{x} - i\omega t) \tag{2.19}$$

where $A(t)$ is the envelope, where we now use a full, complex representation of the electric field. We can thus 'tag' each and every pulse in a pulse sequence impinging on

a sample by either applying a shift to ω or spatially changing the relative $\mathbf{k}$ between pulses. We can then look for signals at specific combinations of these tags to select out a particular 'pathway' that will reveal the information we aim to garner from a system.

2.2.1 The Limitations of Linear Spectroscopy

When one is attempting to characterize the response of an ensemble to an electromagnetic field, coherent one dimensional spectroscopy yields information about the dynamics of the linear polarization field. Because our goal is to characterize the response of a system to light as thoroughly as possible, coherent linear spectroscopy has a number of shortcomings.

Linear spectra are one-dimensional, so therefore it is inherently impossible to tell if the linewidth of the transitions reflects the homogeneous microscopic dephasing rate $\gamma = 1/T_2$ or if the linewidth of the transitions are broadened by the interplay between sample disorder and the basic fundamental dynamics of the system under scrutiny. If it is the latter, the linewidth of the measured spectrum reflects the distribution of possible transition energies probed by our laser. Figure 2.7 shows this ambiguity.

Furthermore, in a spectrum containing multiple resonances, it is not possible to tell if the different resonances are coupled together. Strictly speaking, **coherent coupling** between resonances occurs when the excitation of one resonance at a particular frequency changes the dynamics of a different resonance at a different frequency. This ambiguity is summarized in figure 2.8.

As a practical consideration in a case where multiple species of some system are present, like in the case of an isotopic mixture of two or more gases [15], or multiple systems are contributing to the spectrum in similar frequency or energy ranges, such as in an unknown mixture of liquids, or in our case different orientations of color centers [16], linear one dimensional spectra may be congested with different resonances

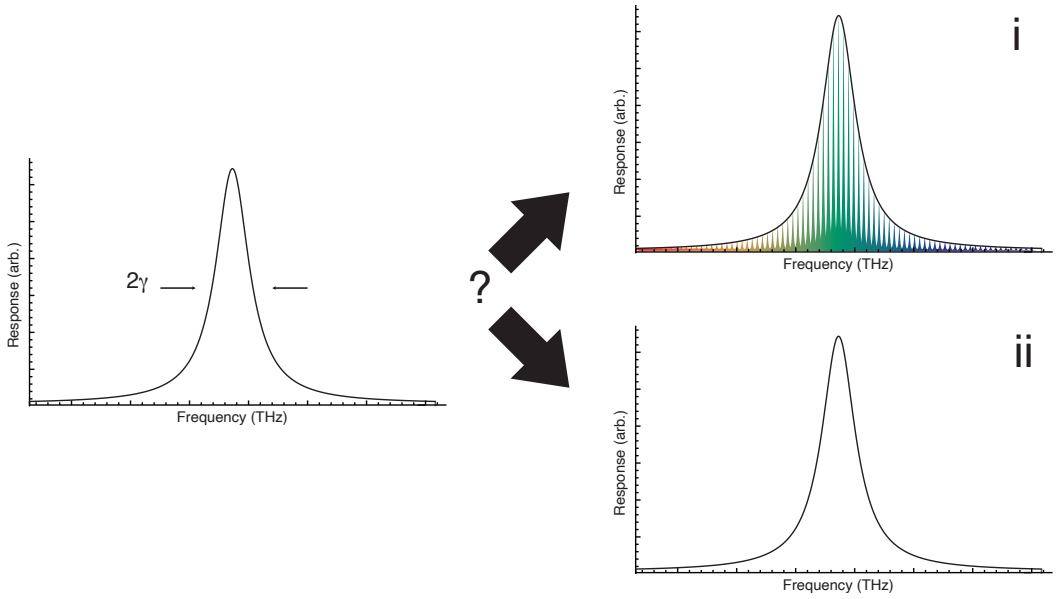

Figure 2.7: A depiction of an ambiguity inherent in a typical one-dimensional spectrum. In panel (i), the transition is composed of a statistical distribution of resonances. In panel (ii), the linewidth of the feature truly reflects the underlying dephasing time of the transition in question. These two situations may result in the same spectrum.

with unknown correlations [17]. In the case where a mixture of two or more species are contributing to the overall response of a sample to optical driving, it would be advantageous to separate out the systems using the fact that the inter-system coherent coupling will be much weaker than intra-system coherent coupling. This ambiguity is illustrated in figure 2.10. Without knowing *a priori* what the exact composition of a mixture is or what species are present in that mixture (whether a solid, liquid, or gas) it is not possible to sort out what peaks belong to which constituent.

We can solve all of these ambiguities at once if we are able to *unfold* a sample's coherent response to optical driving over multiple frequency axes.

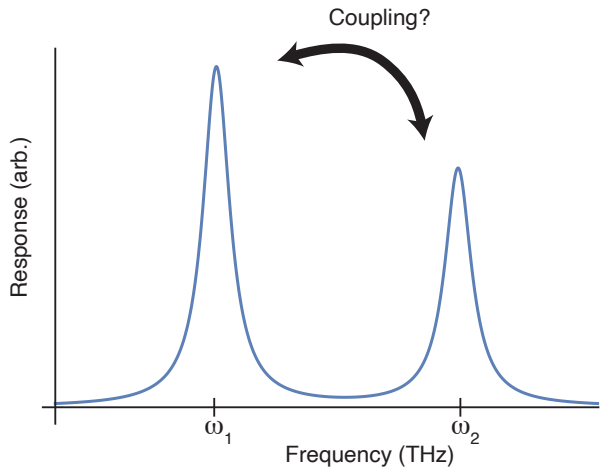

Figure 2.8: A depiction of a different ambiguity inherent in a typical one-dimensional spectrum. Because one-dimensional spectra inherently contain contributions from all signal pathways that contribute to a peak, regardless of their initial excitation energy, you cannot tell if two different resonances influence eachother on an ultrafast timescale.

2.3 The Advantages and Working Principle of Multidimensional Coherent Spectroscopy

Multidimensional coherent spectroscopy is an optical analogue of an older experimental technique, two-dimensional nuclear magnetic resonance spectroscopy. It resolves all prior highlighted ambiguities by correlating a sample's response to multiple driving laser pulses over multiple frequency axes. It was first proposed in 1993 by Tanimura and Mukamel [18]. In the decades since, it has found use nearly everywhere congested spectra or broad peaks obscure the underlying dynamics of the quantum response of a system to an electric field. It has been used to unravel the excitation dynamics of excitons in transition metal dichalcogenides [19], map the ways in which emergent many-body correlations determine the overall optical response of semiconductor systems [17], and even revealed the intricacies of charge transfer in photosynthetic systems [1]. We will first walk through the ways in which MDCS resolves the above outlined ambiguities, and then we will discuss precisely *how* one

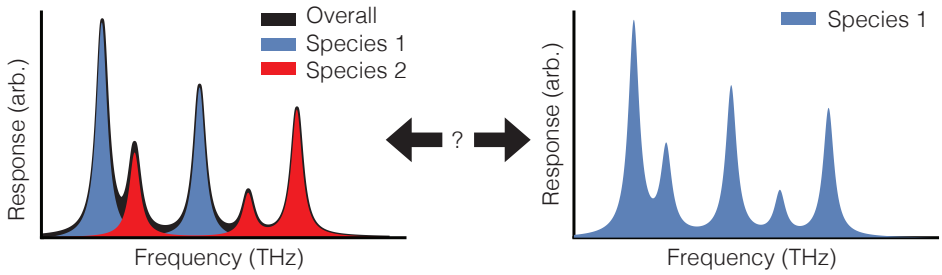

Figure 2.9: A depiction of the case in which multiple systems may be contributing to the same spectrum. Without a prior knowledge of the composition of said mixture, it is not possible to separate out the contributions of multiple species, or weather the whole spectrum is composed of the contributions from just one species.

acquires an MDCS spectrum.

The below spectrum, adapted from ref. [15], demonstrates the resolution of all prior ambiguities. It is an MDCS spectrum correlating absorption and emission frequencies as a function of two polarizations of the excitation pulses in a mixture of two isotopes of Rubidium atoms. This measurement is a type of MDCS that is analogous to coherently correlating the excitation and emission frequencies of some system under study. In this case, the spectrum is congested. However, two different families of resonances (highlighted in the concentric dashed boxes, in Fig. 2.10) are present. The pink dashed circle denotes a cluster of cross-peaks from one isotope that clearly shows that each of these resonances are coherently coupled to most other on-diagonal resonances in the inner box. The two boxes correspond to different isotopes of the Rubidium vapor, and are clearly different species because there are no cross-peaks linking the two. Thus the presence of two species and their contribution to the overall optical response has been resolved. The on-diagonal arrow (red) represents the statistical distribution of center frequencies that contribute to the uppermost on-diagonal resonance, while the orthogonal blue arrows demonstrate the intrinsic linewidth of the peak.

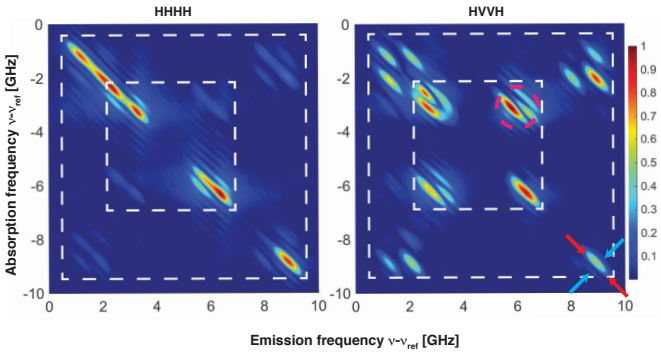

Figure 2.10: An example of an MDCS spectrum resolving all prior-stated ambiguities, adapted from ref. [15].

2.3.1 The Single-Quantum Rephasing Spectra

A single-quantum, rephasing MDCS spectrum is the most common kind of MDCS spectrum reported. It is a Four-Wave Mixing (FWM) spectrum resulting from three pulses interacting within a sample, producing a fourth pulse carrying information detailing the three pulses' effect on the sample. Single-quantum spectra resolve both the statistical distribution of frequencies reflecting an ensemble's optical response (the inhomogeneous linewidth) and the intrinsic linewidth, as well as resolving any possible coherent coupling between resonances in a system. It is termed a one-quantum spectrum because it is resonantly probing the system's response to a single multiple of the frequency of the driving field. This technique answers the question *'If light at some distribution of frequencies interacts with a system, in what ways are the system's absorption and emission processes correlated?'* It is termed a 'rephasing' spectrum because it is the optical analogy to a Hahn echo nuclear-magnetic resonance experiment [20].

To see how a rephasing MDCS spectrum allows one to separate the intrinsic and ensemble-averaged linewidths of the optical response of some system, consider the following. In figure 2.11 (a), we illustrate a simple picture of the one- and two-dimensional nonlinear interactions of this system to light. Its one-dimensional and two-dimensional spectra will be similar, though in the two-dimensional spectrum, its

response will appear as a peak on the equal-frequency diagonal. Suppose there are now two emitters of the same type in a sample, physically separated and existing in slightly different environments such that they emit and absorb light at slightly different frequencies. If there are the only two systems queried by an optical pulse, then their response may be separated in frequency in both one- and multi-dimensional spectra, as in figure 2.11 (b). The key is that each system emits and absorbs light at its natural frequency, thus showing up as on-diagonal peaks, while the cross-diagonal linewidth is the same and reflects the intrinsic linewidth of the optical transition. When a distribution of N such emitters is present, such as in figure 2.11 (c), the on-diagonal linewidth will reflect the statistical distribution of emission and absorption energies to which the sample responds, while the one-dimensonal spectrum is simply broadened by this distribution. However, the cross-diagonal linewidth will remain unaffected by the existence of a statistical distribution of response frequencies. This information is impossible to glean from the corresponding one-dimensional spectrum. As an aside, because the system's first-order interaction with the optical pulses is conjugate to its third-order interaction with the optical pulses, it is customary to mark the absorption axes as negative in frequency.

2.3.2 The Perturbative Understanding and Calculation of MDCS Spectra

As stated in section 2.2, the optical response of a system to driving by pulses of light can be described using the density matrix. MDCS is a technique that aims to study a sample's response to multiple driving pulses. In order to describe the data acquisition process, let's return to the end of our two-pulse correlation discussion. We noted that, when we were coherently detecting the polarization field emitted by our sample, we were detecting the oscillation of the off-diagonal density matrix elements as a function of inter-pulse delay. It must be stated that due to the fact that ultrashort pulses are also by nature quite intense, when we calculate the trajectory of

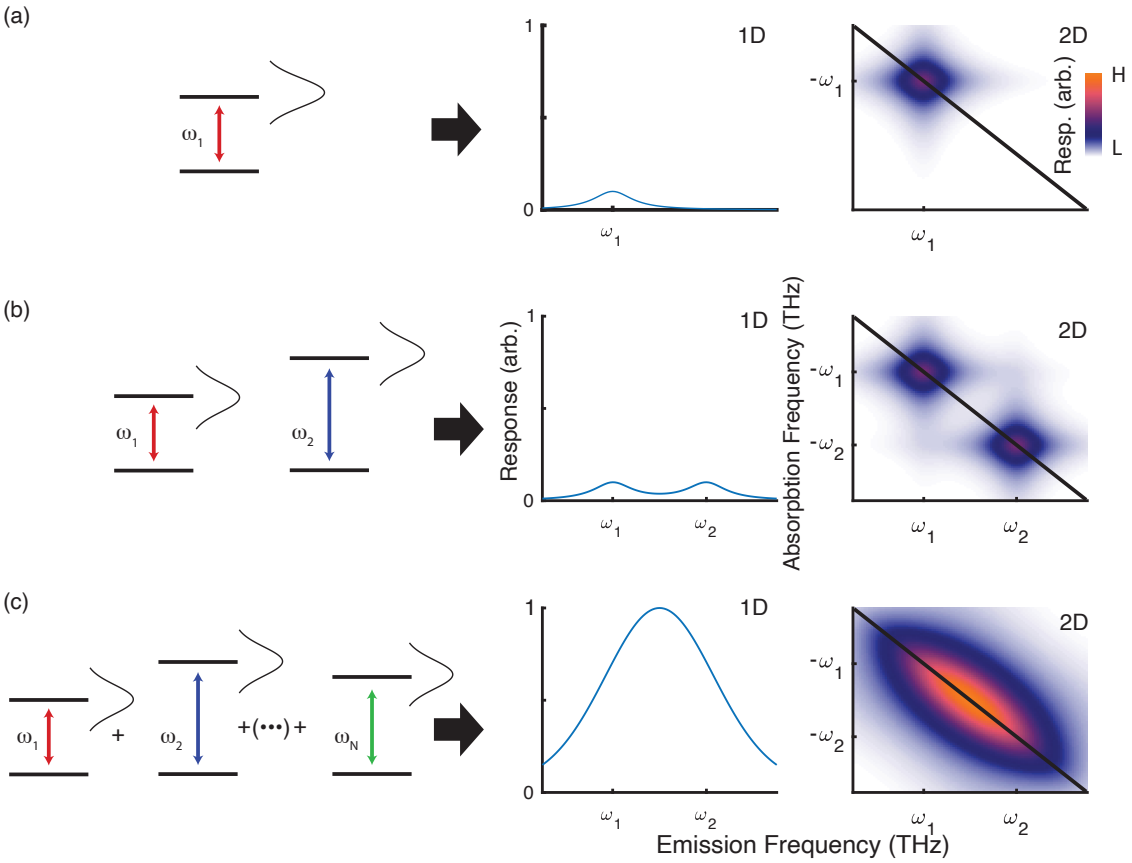

Figure 2.11: This figure depicts the 1D and MDCS spectra of (a) a single two-level system with some intrinsic response linewidth, (b) two such systems, and (c) a statistical distribution of such systems. The contributions from each individual system sum along the equal-frequency diagonal while the anti-diagonal direction retains undisturbed information about the intrinsic response linewidth of the resonances.

the density matrix as a function of time by summing all possible 'signal pathways,' there may be others that don't contribute to our signal that we ignore due to our ability to select the signal of interest. In the perturbative limit, at every interaction between a pulse and the system, information is transferred between density matrix elements in a taxi-cab geometry (either laterally or vertically) [4, 7, 17].

To coherently correlate the sample's absorption and emission behavior in a single-quantum rephasing spectrum, we must correlate the absorption and emission polarization fields. Because each pulse can only increment and decrement information by one horizontal or vertical position in the density matrix, correlating the absorbed polarization field with the emitted polarization field is necessarily a correlation between

a first-order polarization and a third order polarization. We must therefore work to at least third order in our perturbative expansion, and we must measure a four-wave mixing signal (FWM) that corresponds to the third-order polarization emitted as a 'fourth wave' upon nonlinear mixing by our three excitation pulses within the material.

To see how we might represent this process mathematically and diagrammatically, we will expand the density matrix [17]

$$\rho(t) = \rho^{(0)}(t) + \rho^{(1)}(t) + \rho^{(2)}(t) + \rho^{(3)}(t) + \rho^{(4)}(t) + \dots \,. \tag{2.20}$$

Let's suppose that the density matrix is originally in the state $\rho^{(0)}(t)$. The goal is to retrieve the state of the system upon three interactions with three pulses of light. A possible experiment is outlined in figure 2.12. We begin by splitting a single laser pulse into four. We then send all four pulses through four different acousto-optic modulators to shift their center frequencies, by which we 'tag' each pulse. We then use three pulses to interact with the sample and the fourth to either convert the third-order polarization into a population or to characterize the emitted, third order polarization, in an identical manner to the coherently detected two-pulse measurement. In general, by monitoring the signal (either PL or coherently detected field) modulated at a frequency $\omega_{sig} = \pm\omega_A \pm \omega_B \pm \omega_C \pm \omega_D$, we can ensure that the signal we are measuring is from the desired trajectory of ρ. Though this seems complex, all we are doing is correlating a first-order coherence after pulse A interacts with the sample with a third-order coherence after the action of pulse C. We then scan the time delays over which these coherences evolve, termed τ and t, collect the phase and amplitude of the signal modulated at our chosen frequency, and then numerically Fourier transform the data to obtain a two-dimensional spectrum. We leave the exact details to section 2.4.

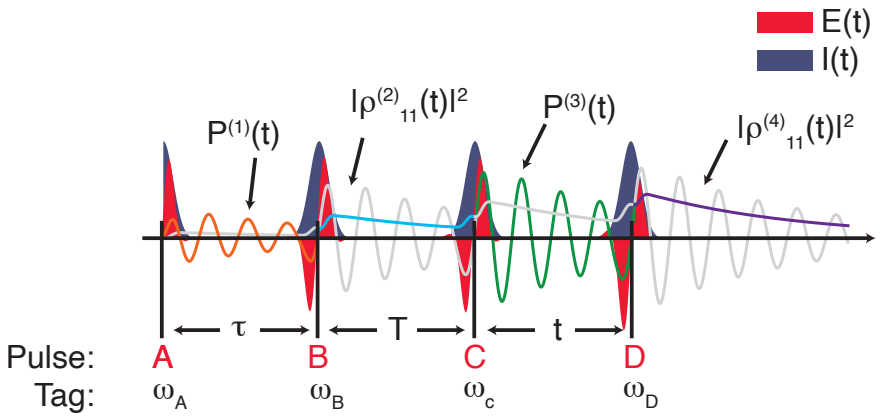

Figure 2.12: This figure summarizes all major theoretical details of an MDCS experiment. We track the evolution of the density matrix against three time delays. The polarization induced by action of the first pulse (orange) is correlated against the polarization induced by action of the third pulse (green).

To calculate the dynamics of the density matrix, we recall

$$\dot{\rho}(t) = -\frac{i}{\hbar}[V(t), \rho] \tag{2.21}$$

where

$$V(t) = -\hat{\mu} \cdot \vec{E}(t) \tag{2.22}$$

is an operator describing the light-matter interaction, with μ is the transition matrix as before, and $\vec{E}(t)$ being the electric field. This equation is straightforward to integrate

$$\rho(t) = \frac{-i}{\hbar} \int_{-\infty}^{t} dt'[V(t'), \rho(t)]. \tag{2.23}$$

However, this is a recursive series, as we are both solving for and integrating for $\rho(t)$. We thus apply the perturbative expansion from equation 2.20 to expand this integral. Taking the first order perturbation induced by the first pulse, and assuming that the

system is initially in the state $\rho^{(0)}$, we have

$$\rho^{(1)}(t) = \frac{-i}{\hbar} \int_{-\infty}^{t} dt' [V(t'), \rho^{(0)}(t)]. \tag{2.24}$$

In fact, by induction, we can generalize this expression to find the density matrix at any order

$$\rho^{(n)}(t) = \int_{-\infty}^{t} dt' \frac{-i}{\hbar} [V(t'), \rho^{(n-1)}(t)]. \tag{2.25}$$

This equation is deceptively compact: at every order in $\rho^{(n)}$, the commutator will depend all lower orders of ρ. Our task is now therefore to find a way to easily solve for $\rho^{(3)}(t)$ knowing $\rho^{(0)}(t)$, and then connect this solution method to the MDCS experiment.

The most common method by which to track the possible contributions to equation 2.25 is by a diagrammatic method known as the double-sided Feynman diagram [4, 6–8]. Each diagram represents the evolution of one specific signal pathway within the experiment, and by summing all diagrams, one can model the experimental data and connect the MDCS spectra to dynamical quantities of interest. There are four possible diagram vertex types [4, 7]:

$$\begin{vmatrix} |i\rangle & \langle l| \\ |i\rangle & \langle j| \end{vmatrix} \nwarrow : \rho_{il}^{(n)} = \frac{-i\mu_{ij}}{2\hbar} \int_{-\infty}^{t} dt' E_n^*(t') e^{-i\Omega_{il}(t-t')} \rho_{ij}^{(n-1)}(t') \tag{2.26}$$

$$\begin{vmatrix} |i\rangle & \langle l| \\ |i\rangle & \langle j| \end{vmatrix} \nearrow : \rho_{il}^{(n)} = \frac{-i\mu_{ij}}{2\hbar} \int_{-\infty}^{t} dt' E_n(t') e^{-i\Omega_{il}(t-t')} \rho_{ij}^{(n-1)}(t') \tag{2.27}$$

$$\nwarrow \begin{vmatrix} |j\rangle & \langle l| \\ |i\rangle & \langle l| \end{vmatrix} : \rho_{jl}^{(n)} = \frac{i\mu_{ij}}{2\hbar} \int_{-\infty}^{t} dt' E_n^*(t') e^{-i\Omega_{jl}(t-t')} \rho_{ij}^{(n-1)}(t') \tag{2.28}$$

$$\nearrow \begin{vmatrix} |j\rangle & \langle l| \\ |i\rangle & \langle l| \end{vmatrix} : \rho_{jl}^{(n)} = \frac{i\mu_{ij}}{2\hbar} \int_{-\infty}^{t} dt' E_n(t') e^{-i\Omega_{jl}(t-t')} \rho_{ij}^{(n-1)}(t') \tag{2.29}$$

where the electric field of each pulse is $E(t) = A(t)\Big(\mathrm{Exp}(ik_n x - i\omega_{n,tag}t) + c.c.\Big)$ is the electric field of the n-th laser pulse with envelope $A(t)$ and frequency $\omega_{n,tag} = \omega_c + \omega_{tag}$ or momentum $\mathbf{k}_n$ used to tag the specific pulse for convenience. The signal pathway of a particular diagram is determined by tracking combinations of $\omega_{n,tag}$ or $\mathbf{k}_n$. Furthermore, $\Omega_{ij} = \omega_{ij} - \gamma_{ij}$ is the frequency evolution of the density matrix element in the Markovian limit with $\omega_{ij} = (E_i - E_j)/\hbar$ the frequency separation between states i and j and γ_{ij} being the homogeneous dephasing rate of the ij-th resonance. More comprehensive information on the diagrammatic formalism, and how it can be used to calculate spectra outside of the Markovian limit is available in refs. [4, 6, 7, 9, 17] among others.

We can use our vertices as enumerated above to track the evolution of $\rho(t)$ by tracking signals that depend on combinations of $\mathbf{k}_n$ or $\omega_{n,tag}$ for different 'signal pathways,' because as the powers of the field multiply together, different combinations of $\mathbf{k}$ or ω_{tag} are possible as the 'order' of the measurement is increased. So far, we have been evasive when speaking about signal pathways. Specifically what we mean when we say signal pathways are specific combinations of pulse-dependant interactions that reveal different information about a system. A discussion of every signal pathway and and its applicability is outside of the scope of this thesis, but the most commonly measured FWM signal pathways are

$$\begin{aligned} S_I &= -k_A + k_B + k_c \text{ or } & S_I &= -\omega_A + \omega_B + \omega_c \\ S_{II} &= +k_A - k_B + k_c \text{ or } & S_{II} &= +\omega_A - \omega_B + \omega_c \\ S_{III} &= +k_A + k_B - k_c \text{ or } & S_{III} &= +\omega_A + \omega_B - \omega_c \end{aligned} \tag{2.30}$$

where we highlight in blue the two measurement pathways we report in this thesis.

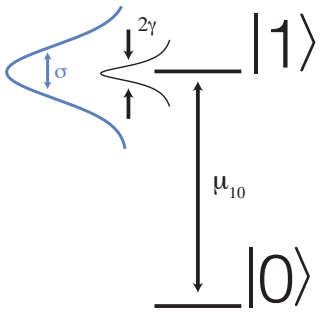

Figure 2.13: A two-level system with inhomogeneity characterized by σ and homogenous dephasing rate γ with lifetime Γ.

S_I corresponds to the aforementioned rephasing, one-quantum signal pathway when time-domain data is taken by varying the first and third time delays. A 'zero quantum spectrum' that quantifies coherences between closely spaced states is also possible by correlating the fluctuation of the third order signal as a function of T and t as well, corresponding to a two-dimensional version of Coherent Anti-Stokes Raman Spectroscopy or CARS, while a 'non-rephasing' spectrum, used to separate closely spaced resonances is taken by monitoring S_{II}, and a double-quantum spectrum (detailed later) is acquired by monitoring S_{III}.

To illustrate how to use the diagrammatic formalism outlined in equation 2.29, let's focus on just one two-level system to start. The process is the following: we must find all possible contributions to our S_I signal, then multiply the integrals outlined above together step-by-step once we have written down the necessary diagrams, then do the full integration to calculate our expected signal. Assume that we have the two-level system depicted in figure 2.13 [4, 6, 8, 17]. There's a simple way to properly multiply the integrals in the formalism outlined in equation 2.29: an in-going arrow corresponds to a $+k_n$ interaction and an out-going arrow corresponds to a $-k_n$ interaction. Now, recalling that our first, second, and third inter-pulse delays are $\tau, T,$ and t respectively we can then then writing down the possible diagrams contributing to $S_I = -k_A + k_B + k_c$, we have the two different diagrams contributing

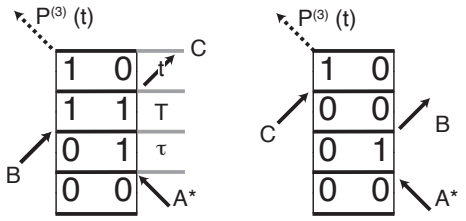

Figure 2.14: The two double-sided Feynman diagrams representing the two pathways contributing to the S_I signal for a two-level system.

to the third-order signal pathway, shown in figure 2.14. In the figure, the bra and ket notation has been dropped for compactness, but each row represents one density matrix element, and every ladder rung represents an interaction with a laser pulse, or in the case of the final rung, the emission of $\vec{P}^{(3)}(t)$. Inter-pulse time delays are marked as ladders on the diagram, and labelled accordingly.

Following the conventions in [7], we multiply the contributions from each vertex detailed in 2.29 as we ascend the latter, keeping careful track of the time arguments. We thus find that the contribution from the diagram on the left is

$$\begin{aligned}\rho_1^{(3)}(\tau,T,t) = \frac{i\mu_{10}^3}{8\hbar^3}\int_{-\infty}^{t} dt''' E_3^*(t''')e^{-i\Omega_{10}(t-t''')} \\ \times \int_{-\infty}^{t'''} dt'' E_2(t''+T)e^{-i\Omega_{11}(t'''-t'')} \\ \times \int_{-\infty}^{t''} dt' E_1(t'+T+\tau)e^{-i\Omega_{01}(t''-t')}.\end{aligned} \tag{2.31}$$

if we take $E_n(t) = \delta(t)$, in the limit of delta-function pulses (which applies in all pertinent situations within this thesis), and taking $\Omega_{10}(t) = \omega_{10} - i\gamma$, $\Omega_{01}(t) = -\omega_{10} - i\gamma$, and $\omega_{11} = -i\Gamma$ to phenomenologically capture population decay and dephasing,we

have

$$\rho_1^{(3)}(\tau,T,t) = \frac{i\mu_{10}^3}{8\hbar^3}\,\mathrm{Exp}\Big(-\Gamma T-\gamma(t+\tau)-i\omega_{10}(t-\tau)\Big) \times \Theta(T)\Theta(\tau)\Theta(t) \tag{2.32}$$

where $\Theta(x)$ is the Heaviside theta function. For the diagram on the right, we go through the same process, except this time we use $\Omega_{00}=0$, so we have

$$\begin{aligned}\rho_2^{(3)}(\tau,T,t) = \frac{i\mu_{10}^3}{8\hbar^3}&\int_{-\infty}^{t} dt''' E_3^*(t''')e^{-i\Omega_{10}(t-t''')} \\ &\times\int_{-\infty}^{t'''} dt'' E_2(t''+T)e^{-i\Omega_{00}(t'''-t'')} \\ &\times\int_{-\infty}^{t''} dt' E_1(t'+T+\tau)e^{-i\Omega_{01}(t''-t')}\end{aligned} \tag{2.33}$$

and therefore

$$\begin{aligned}\rho_2^{(3)}(\tau,T,t) = \frac{i\mu_{10}^3}{8\hbar^3}\,&\mathrm{Exp}\Big(-\gamma(t+\tau)-i\omega_{10}(t-\tau)\Big) \\ &\times\Theta(T)\Theta(\tau)\Theta(t).\end{aligned} \tag{2.34}$$

Our third-order signal with then be the sum of these pathways

$$\begin{aligned}P^{(3)}(t,T,\tau) &= i\mu_{10}\big(\rho_1^{(3)}(\tau,T,t)+\rho_2^{(3)}(\tau,T,t)\big) \\ &= \frac{-\mu_{10}^4}{4\hbar^3}\mathrm{Exp}\Big(-\gamma(t+\tau)-i\omega_{10}(t-\tau)-\Gamma T\Big) \\ &\times\Theta(T)\Theta(\tau)\Theta(t).\end{aligned} \tag{2.35}$$

If we want to include inhomogeneous broadening, we can do that at this point in the process by adding a term to equation 2.35 to reflect the 'slow' fluctuations limit of the Kubo lineshape derived in appendix A. This term comes from assuming that ω_{10} fluctuates in time about some center frequency with a Gaussian distribution, and

then plugging this fluctuation into the integral expansion, but this functional form of the fluctuation need not be the case in general. In fact, the on-diagonal linewidth will simply reflect the statistics of the fluctuations in any resonance center frequency. The time-domain response of our two level system with inhomogeneity captured by σ will be

$$\begin{aligned} P^{(3)}(t,T,\tau) &= i\mu_{10}\big(\rho_1^{(3)}(\tau,T,t) + \rho_2^{(3)}(\tau,T,t)\big) \\ &= \frac{-\mu_{10}^4|E|^3}{4\hbar^3}\mathrm{Exp}\Big(-\gamma(t+\tau) - i\omega_{10}(t-\tau) - \Gamma T - \frac{\sigma^2(t-\tau)}{2}\Big) \\ &\times \Theta(T)\Theta(\tau)\Theta(t). \end{aligned} \tag{2.36}$$

Strictly speaking, we can add in the fluctuations in an energy level in the Ω_{ij} argument in our integrals. Solving the integrals will require a thrice-over repetition of the process in appendix A using a formalism dubbed the 'cumulant expansion' [4]. We do not do this here, because it is not necessary to describe the physics we measure, though for a thorough primer on the form that this perturbative process takes when trying to accurately describe the spectral distribution of lineshape fluctuations, ref. [9] offers good computational details. Figure 2.15 shows a simple, inhomogeneously broadened peak with center frequency $\omega = 1$, frequency distribution $\sigma = 1/2$, and linewidth $\gamma = 1/5$ (all with arbitrary frequency units) to demonstrate a typical time- and frequency-domain one-quantum spectrum.

A one-quantum rephasing spectrum can also yield information about coherent coupling between resonances in a material. To see this, we partially follow the discussion presented in Ref. [21]: consider a three-level system with inhomogeneity like the one depicted in figure 2.16. Fluctuations in the center frequencies ω_{10} and ω_{20} can either be correlated, uncorrelated, or anti-correlated, and we can learn about the effects of the excitation of one state on the dynamics of the other by examining the cross peaks and their shape in the one-quantum spectrum.

First, we will start by looking at the case of uncorrelated fluctuations. We first

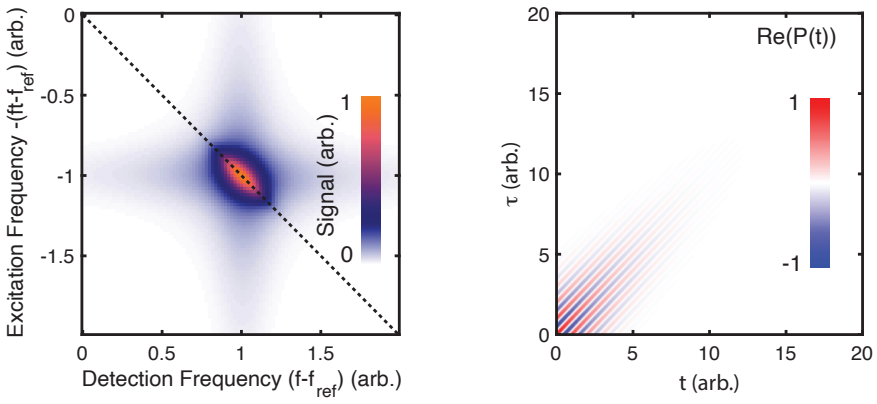

Figure 2.15: A typical one-quantum spectrum of an inhomogeneously broadened peak in the time- and frequency-domains.

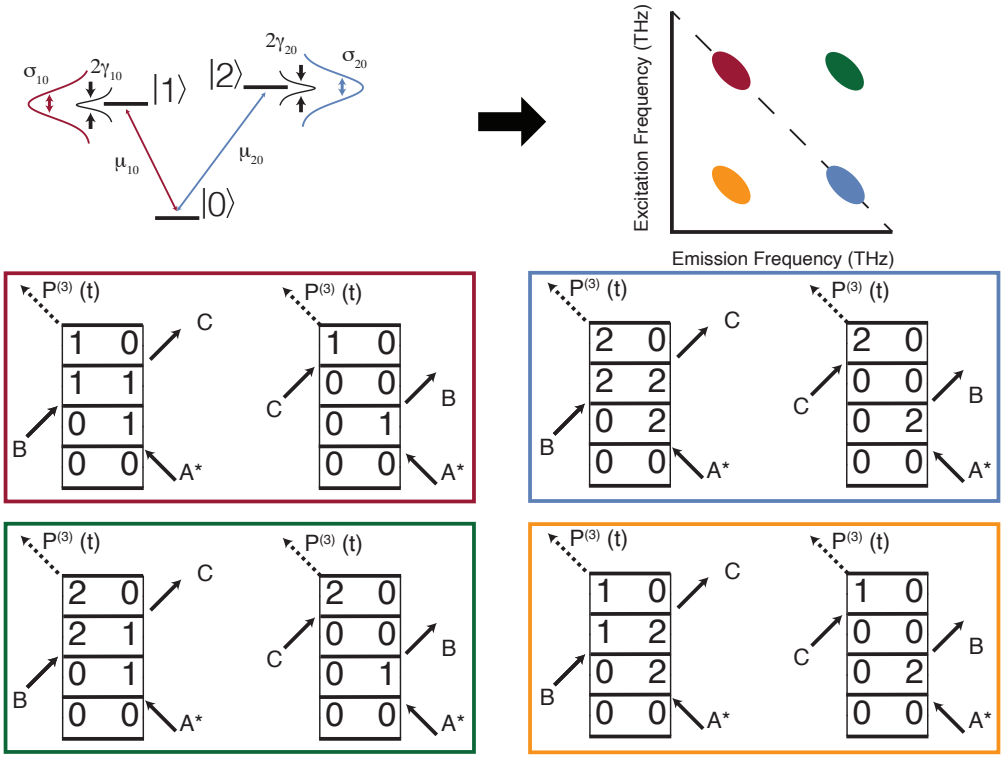

Figure 2.16: A depiction of a simple three-level system with the relevant parameters noted in the top left on the energy level diagram. The schematic of the two-dimensional spectrum is noted in the top right, with peaks color coded to the quantum pathways that contribute to the overall signal as enumerated in the double-sided Feynman diagrams.

outline the possible S_I pathway contributions, detailed in figure 2.16. The on-diagonal peaks, cartooned by blue and red ellipses, will have time-domain responses identical to that in equation 2.35, with the appropriate quantities replaced. Explicitly, their peaks will be given by

$$P_{10}^{(3)}(t,T,\tau) = \frac{-\mu_{10}^4|E|^4}{4\hbar^3}\mathrm{Exp}\Big(-\gamma_{10}(t+\tau) - i\omega_{10}(t-\tau) - \Gamma_{10}T - \frac{\sigma_{10}^2(t-\tau)}{2}\Big) \times \Theta(T)\Theta(\tau)\Theta(t), \tag{2.37}$$

and

$$P_{20}^{(3)}(t,T,\tau) = \frac{-\mu_{20}^4|E|^3}{4\hbar^3}\mathrm{Exp}\Big(-\gamma_{20}(t+\tau) - i\omega_{20}(t-\tau) - \Gamma_{20}T - \frac{\sigma_{20}^2(t-\tau)}{2}\Big) \times \Theta(T)\Theta(\tau)\Theta(t) \tag{2.38}$$

with $\gamma_{ij}, \Gamma_{ij}, \sigma_{ij}, \text{and } \omega_{ij}$ being the pure dephasing rate, the population decay rate, the inhomogeneous linewidth, and the center frequencies for either the $0 \leftrightarrow 1 := 01$ or the $0 \leftrightarrow 2 := 02$ transitions respectively.

For the upper off-diagonal peak, with diagrams depicted in the green box, we have (assuming that the fluctuations in the energy levels are uncorrelated)

$$P_{21}^{(3)}(t,T,\tau) = \frac{-\mu_{10}^2\mu_{20}^2|E|^3}{8\hbar^3}\mathrm{Exp}\Big(i\omega_{10}\tau - \gamma_{10}\tau - i\omega_{20}t - \gamma_{20}t - \frac{\sigma_{20}^2}{2}t^2 - \frac{\sigma_{10}^2}{2}\tau^2\Big) \times \left(1 + \mathrm{Exp}\Big(-i(\omega_{20}-\omega_{10})T - \Gamma_{21}T - \frac{\sigma_{21}^2}{2}T^2\Big)\right)\Theta(T)\Theta(\tau)\Theta(t) \tag{2.39}$$

where σ_{21} is a parameter describing the fluctuations of level $|2\rangle$ with respect to level $|1\rangle$, capturing a phenomenon known as spectral diffusion, and Γ_{21} is the pure dephasing of the coherence between states $|2\rangle$ and $|1\rangle$ as a function of T. For the lower

off-diagonal peak, with diagrams depicted in the yellow box, we have

$$P_{12}^{(3)}(t,T,\tau) = \frac{-\mu_{10}^2\mu_{20}^2|E|^3}{8\hbar^3}\mathrm{Exp}\Big(i\omega_{20}\tau - \gamma_{20}\tau - i\omega_{10}t - \gamma_{10}t - \frac{\sigma_{10}^2}{2}t^2 - \frac{\sigma_{20}^2}{2}\tau^2\Big) \times \left(1 + \mathrm{Exp}\Big(-i(\omega_{10}-\omega_{20})T - \Gamma_{12}T - \frac{\sigma_{12}^2}{2}T^2\Big)\right)\Theta(T)\Theta(\tau)\Theta(t) \tag{2.40}$$

with σ_{12} being a parameter describing the fluctuations of level $|1\rangle$ with respect to level $|2\rangle$, and everything else the same. Figure2.17(a) shows the result of adding these four contributions together, while figure 2.17(b) shows what the spectrum would look like of the fluctuations between energy levels are perfectly correlated.

We include these granular details to point out two facts: first, the coherent coupling peaks can yield more information than just the mere fact that two resonances influence eachother coherently. Their shape can yield crucial information about the nature of correlations between excitations in a material. Furthermore, there *absence* can tell us just as much, as we shall see. When one expects to see coherent coupling peaks in a system with otherwise coupled states, such as in the SiV system where the peaks are not present due to inhomogeneity, it indicates that the local potential landscape is changing the fine splitting in a system, not simply just the center frequency of the collective set of resonances.

2.3.3 Double-Quantum Spectra

The other spectroscopic technique we employ in our study of SiV centers is similar to one-quantum, rephasing spectroscopy, but it is unique in that it is sensitive only to emitters that interact [22]. This spectrum, known as double-quantum 2D or DQ2D, is acquired by monitoring the coherent signal emitted by a sample in the $S_{III} = k_A + k_B - k_C$ direction or modulated at the frequency $\omega_{sig} = \omega_A + \omega_B - \omega_C$ as a function of the second and third time delays. Doing so resolves the coherent behavior

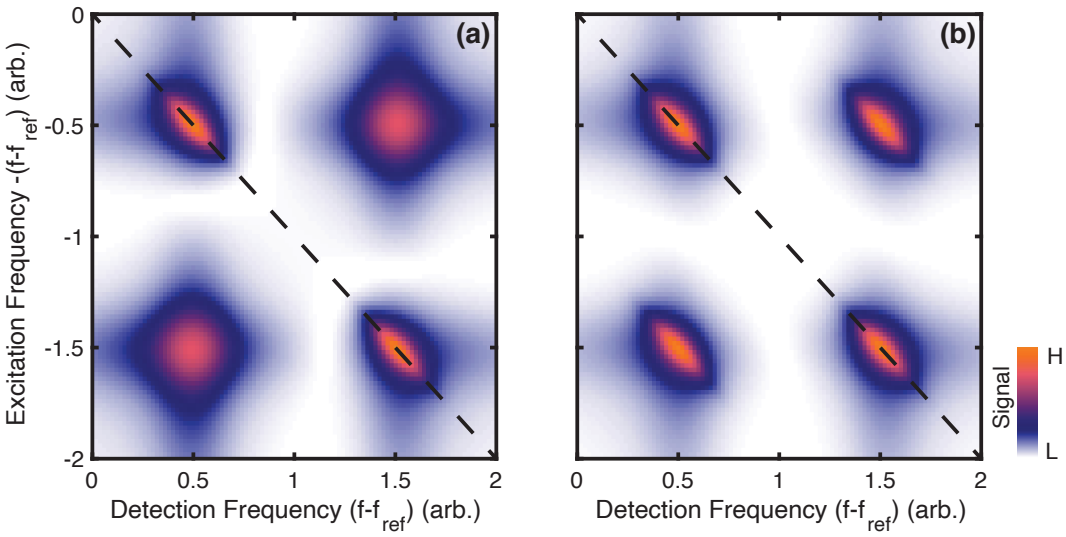

Figure 2.17: A depiction of a one-quantum spectrum resulting from a three level system wherein the energy fluctuations of the two excited states are either (a) uncorrelated or (b) perfectly correlated.

of separate systems that couple together through an excitation-dependent interaction mechanism, such as Pauli blocking or dipole-dipole coupling.

To see how this spectroscopic techniques is sensitive to interactions, consider a pair of identical two-level systems. Their joint behavior can be described by a ladder of three states, $|0\rangle, |1\rangle$ and $|2\rangle$ corresponding to each system in its ground state, one system being in an excited state, and both systems being in their excited states respectively. This corresponds to combining the two singly-excited states in Figure 2.18 into one state with an enhanced transition dipole moment. We can always do this for two systems. However, suppose there are interactions between the two. Then, their joint excited state dynamics, either the center frequency or the dephasing rate, will shift subtly captured in the complex-valued parameter $\Delta = \Delta_s - i\Delta_d$ denoted in figure 2.18. This interaction parameter, Δ captures both Δ_s, corresponding to any shift in the doubly excited state frequency due to interactions, and Δ_d captures the change in dephasing due to interactions between the two systems.

Taking the same conventions as earlier in the chapter, and neglecting any inhomogeneity, we can write the signal resulting from the two pathways shown in the

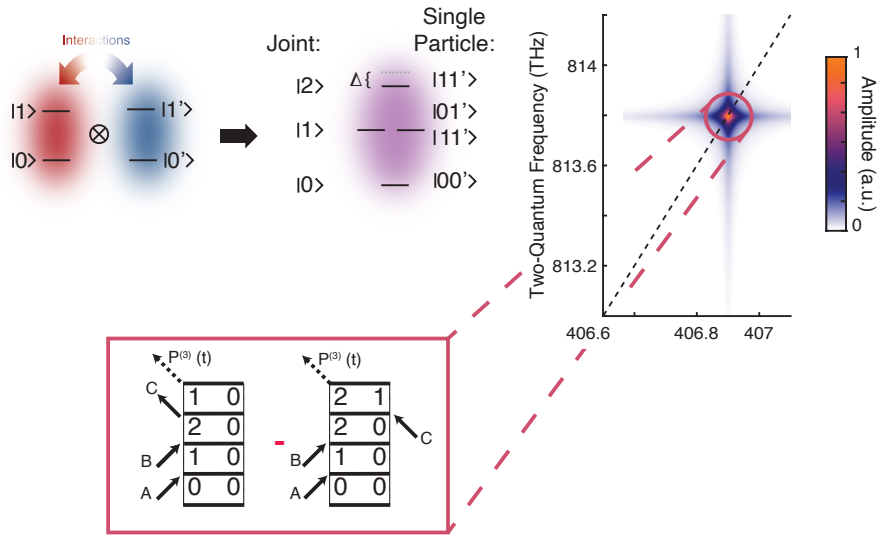

Figure 2.18: A depiction of two two-level systems coupled together by interactions. The interactions can be treated as shifting the center frequency or dephasing rate of the jointly excited state by Δ. A two quantum spectrum resulting from two interacting two-level systems is shown. The diagrams contributing to the on-diagonal peak are shown. Crucially, they have different overall signs, so in the case that $\Delta = 0$, the diagrams cancel. The diagonal represents $f_{DQ} = 2f_{Det}$.

diagrams in figure 2.18 as

$$P^{(3)}(\tau, T, t) = \frac{-\mu_{10}^4}{4\hbar^3}\Bigg(\mathrm{Exp}\Big(i(-\omega_{10}\tau - \omega_{20}T + \omega_{10}t - \gamma_{10}(\tau + t) - \gamma_{20}T\Big) - \\ \mathrm{Exp}\Big(i(-\omega_{10}\tau - \omega_{20}T + \omega_{10}t - \gamma_{10}(\tau + t) - \gamma_{20}T - \Delta\Big)\Bigg)\Theta(\tau)\Theta(t)\Theta(T) \tag{2.41}$$

where ω_{10} is the resonance frequency for the $|0\rangle \leftrightarrow |1\rangle$ transition, $\omega_{20} = 2\omega_{10}$ represents the doubly-excited state coherence frequency and $\gamma_{10} = \gamma_{20}/2$ represent the pure dephasing rates for the coherence in the system. It should be noted that, in the case of two identical two-level systems, the transition dipole moment from the ground to the first excited state doubles in the case of the three-level ladder because one typically cannot distinguish which system is excited, known as the Rabi enhancement [23]. It is clear from equation 2.41 that in the case that $\Delta = 0$ (for no excitation dependent interactions between the two systems), the signal vanishes. This is what is

meant by saying DQ2D is a background-free probe of interactions. In the figure, we took $\omega_{10} = 406.9$ rad.$\cdot$THz$= \omega_{20}/2$, $\gamma_{10} = 0.012 = \gamma_{20}/2$ THz, and $\Delta = 5(1+i)$ GHz to show that even small shifts in the properties of state $|2\rangle$ lead to a DQ2D signal.

Furthermore, in the case of non-identical two level systems, there certainly can still be interactions that drive a DQ2D signal. Take two adjacent, interacting two-level systems. If their excited states are close in energy, but not identical, the two-quantum peak seen on the diagonal in figure 2.41 will split into two peaks that are off of the diagonal because the double-quantum evolution frequency will be the sum of the two different frequencies, while each system will emit the induced polarization field at its natural transition frequency, shown in figure 2.19. One must also treat the system in the four-level diamond when attempting to calculate their spectrum, but the same cancellation that is apparent in equation 2.41 when $\Delta = 0$ will occur. Because the DQ2D signal fundamentally results from a broken cancellation of two signal pathways by a complex-valued interaction parameter, Δ, we can glean information about the inter-system interactions through careful study of the *phase* of these spectra upon changing external environmental parameters, or the initial state of our system. This phase resolution will be crucial to our study of interactions between color centers in diamond.

2.4 Acquiring MDCS Spectra Experimentally

As we have seen, MDCS spectra can be quite useful in disentangling the subtleties of a system's response to light. The MDCS experiment used to collect the data presented in this thesis is a four-pulse, collinear geometry MDCS experiment we term CONS (Coherent Optical Nonlinear Spectrometer). It is collinear in the sense that we do not use the k-vector selection alluded to above, so our pulses can co-propagate through the experiment and into the cryostat, resulting in the ability to achieve diffraction limited spatial resolution at the sample. One advantage of this is

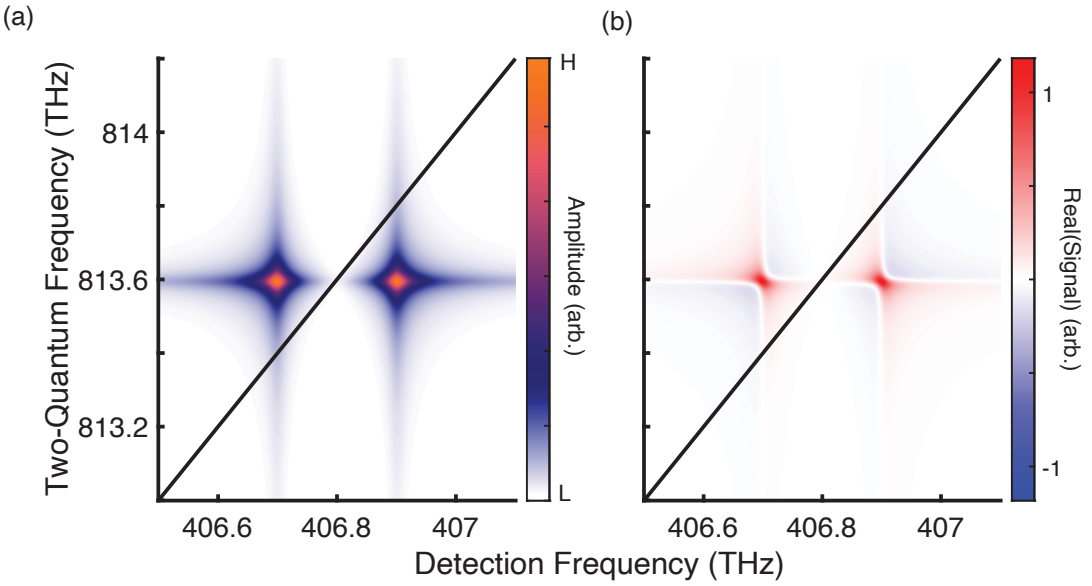

Figure 2.19: (a) A DQ2D spectrum of two two-level systems that are coupled by interactions. (b) The real part of the spectrum can yield crucial information about the nature of interactions coupling the two systems together because it can allow you to extract the interaction parameter Δ.

that we can easily choose to detect either the coherent polarization emitted by the sample or the modulated PL to compare MDCS spectra sensitive to contributions from dark states (coherently detected MDCS spectra) to those which are not (PL-detected MDCS spectra).

We derive our laser pulses from a titanium:sapphire (Ti:Sapph) oscillator with repetition rate 75.5 MHz, pulse duration 200 fs FWHM, and variable center wavelength, which we choose to be 737 nm to study SiV color centers. We route this laser through three nested Mach-Zehnder interferometers and three delay stages to generate four pulses with three controllable time delays between them. We use the first three pulses to generate a FWM signal, and the fourth to characterize this signal. We can choose to send either three or four pulses to the sample, depending on the required measurement configuration.

There are two key challenges when attempting to acquire MDCS spectra. Primarily, one must isolate the perturbative signal that comes from the third-order FWM

pathway, arising from the combined action of the three excitation pulses. As stated before, there are two ways to do this. One can either cross a sequence of beams in a known geometry, and then look for the emission of the signal in the desired direction [24, 25], or one can apply a finite frequency offset to each individual pulse as it propagates through the experiment, and the signal 'direction' will be converted to a signal modulation frequency at the appropriate FWM signal frequency, depending on the pathway chosen [26]. In general, all implementations use a nested interferometer configuration to generate four phase-stable pulses and then either acousto-optic modulators are used to frequency tag each pulse, or the pulses are propagated in some geometry that allows the signal to retrieved in a known direction [7, 25].

In general, a path length stability of better than $\lambda/100$ is required to retrieve the phase and amplitude of the FWM signal [25]. This translates to a distance uncertainty, for a laser centered at 737nm to roughly ± 7 nm over the meters-long experiment. In non-collinear techniques, maintaining this level of phase stability is incredibly challenging, requiring sensitive path-length stabilization [25]. In the collinear geometry, this is much more straightforward. We propagate a continuous wave laser through the experiment, and record the change in the interference patterns between the different interferometers (REF 1 and REF 2 in figure 2.20) by detecting a beatnote at the difference frequency between the AOM modulation frequencies of either pulses A and B or C and D. Then any fluctuations in the interferometers will be recorded as very slight Doppler shifts in the difference frequencies seen at REF 1 and REF 2. The difference frequencies at REF 1 and REF 2 are then mixed in a custom, field-programmable gate array-based single-sideband modulator. The mixed frequency encodes path length fluctuations in an overall frequency shift $\delta\omega(t)$ that varies in time with the fluctuations of the experiment, applied to the reference frequency $\omega_{sig}(t) = \pm\omega_A \pm \omega_B \pm \omega_C \pm \omega_D + \delta\omega(t)$. We use a lock-in amplifier to demodulate the signal retrieved from our sample at $\omega_{sig}(t)$, thereby sampling passive

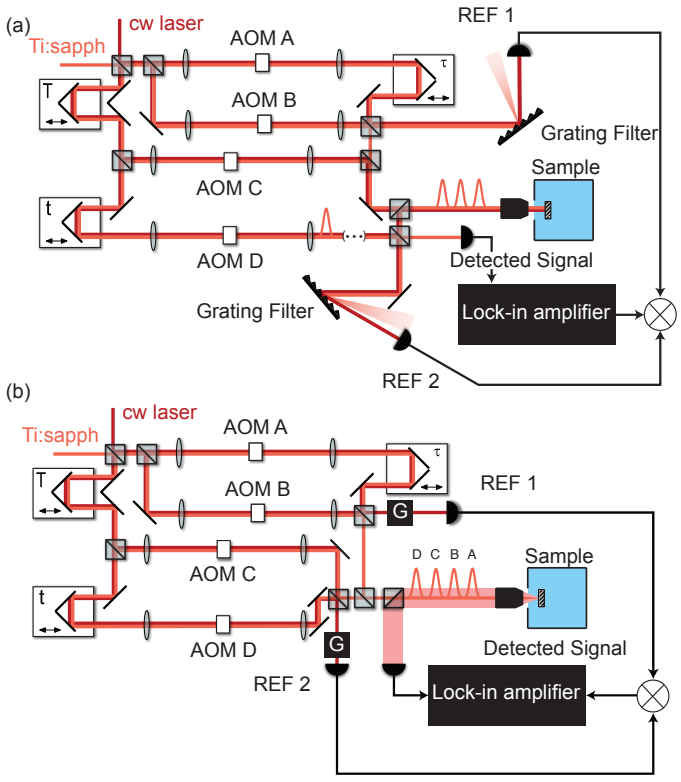

Figure 2.20: The full MDCS experiment used to probe the nonlinear optical response of the SiV centers in diamond. (a)The coherently detected version of the experiment where pulse D was routed around the sample and recombined with the signal downstream of the cryostat and (b) the PL-detected version of the experiment, where all four pulses were sent to the sample and the PL emission was collected. The CW reference laser was propagated through the experiment with a slight spatial offset from the Ti:Sapph pulses to enhance its separation from the pulses, and the beating of the A,B frequency offsets was detected in detector REF 1, while the beating of the C,D frequency offsets was detected in REF 2. For compactness, the grating filters have been replaced with boxed Gs in panel (b).

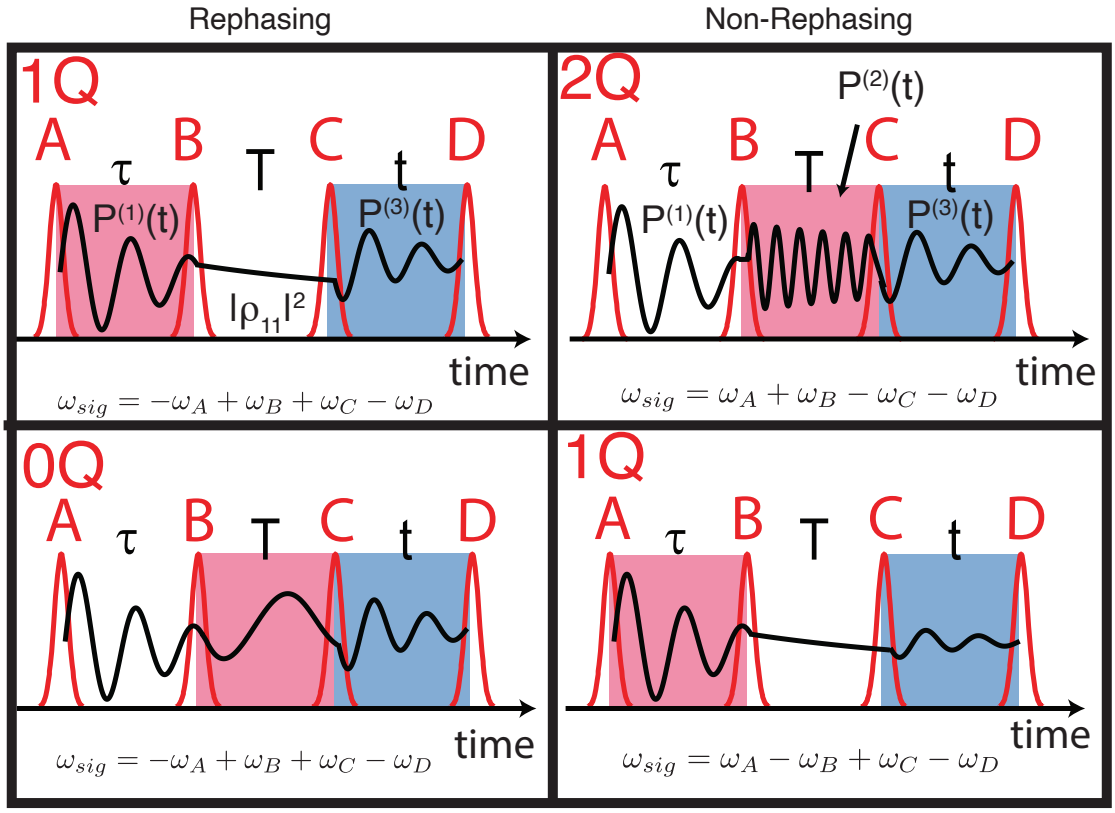

Figure 2.21: A depiction of all possible signal pathways measured in a collinear MDCS spectrum. The black lines depict a typical signal trajectory for each measurement, while the red and blue boxes denote the axes which are scanned during the data acquisition process. The enlarged, red labels for the upper two panels correspond to the experiments conducted within this thesis. We have detailed the specific coherences and populations we track, along with the signal frequency used to select the final FWM pathway.

phase fluctuations due to environmental noise. Figure 2.21 depicts the typical signal pathways outlined in equation 2.30 along with a typical signal trajectory measured (in the black lines) for the three-level system like the one depicted in figure 2.16.

We now get into the exact details distinguishing a coherently detected MDCS spectrum from a PL-detected MDCS spectrum. Figure 2.20(a) is a depiction of the 'coherently detected' MDCS experiment, while figure 2.20(b) shows how this experiment was modified to detect the emitted, modulated PL from the sample [13]. In either case, we are looking for a FWM signal modulated at the correct frequency,

outlined in the 'pathways summary' above. In the case of PL detection, we send all four beams onto the sample, which we tilt slightly to reject any back-scatter from the laser. In the case of coherent detection, we only use three pulses to interact with the sample and route the fourth pulse around the sample to interfere with the third-order signal at the detector. Crucially, the continuous-wave laser that propagates along with pulse C bounces off the sample and then is interfered with its counterpart, co-propogating with pulse D, to sample and passively correct for any fluctuations between the sample and the detector.

We acquire MDCS data at the detector as a function of any combination of our time delays. Phase information about the third-order signal is encoded in the in-phase and in-quadrature modulation of the signal upon demodulation by the lock-in. We assume, for the purposes of this thesis, that the phase of the FWM signal is zero when all four pulses are overlapped. We can make this assumption because our pulse duration is two orders of magnitude below the coherence time of the silicon-vacancy transitions, but it can be more challenging in general to retrieve this absolute optical phase.

2.5 Conclusion

In this chapter, we have walked through all details necessary to understand MDCS and the distinction between PL-detected and coherently detected spectra. We started by summarizing time-domain, linear coherent spectroscopy, and generalized that understanding to MDCS. We illustrated the drawbacks of linear coherent spectroscopy, and we showed how MDCS overcomes those drawbacks by coherently correlating a sample's response to a sequence of ultrafast pulses over multiple frequency axes. In the latter two chapters in this half of the thesis, we will demonstrate how MDCS allows us to build a more complex understanding of SiV physics.

References

(1) Cao, J. et al. *Science Advances* **2020**, *6*, 1–12.

(2) Tang, Y.; Li, L.; Li, T.; Xu, Y.; Liu, S.; Barmak, K.; Watanabe, K.; Taniguchi, T.; MacDonald, A. H.; Shan, J.; Mak, K. F. *Nature* **2020**, *579*, 353–358.

(3) Sakurai, J. J.; Napolitano, J. **2017**, DOI: 10.1017/9781108499996.

(4) Mukamel, S., *Principles of nonlinear optical spectroscopy*; Oxford series in optical and imaging sciences; Oxford University Press: New York, 1995.

(5) Kardar, M., *Statistical Physics of Particles*, 2007.

(6) Boyd Robert W., 1., *Nonlinear optics*; Academic Press: Boston :; Boston : 1992.

(7) Smallwood, C.; Autry, T.; Cundiff, S. *Journal of the Optical Society of America B* **2016**, *34*, DOI: 10.1364/JOSAB.34.000419.

(8) Hamm Peter, 1.; Zanni, M. T., *Concepts and methods of 2D infrared spectroscopy*; Cambridge University Press: Cambridge ; New York :; Cambridge ; New York : 2011.

(9) Abramavicius, D.; Palmieri, B.; Voronine, D. V.; Šanda, F.; Mukamel, S. *Chemical Reviews* **2009**, *109*, 2350–2408.

(10) Chavhan, G. B.; Babyn, P. S.; Thomas, B.; Shroff, M. M.; Mark Haacke, E. *Radiographics* **2009**, *29*, 1433–1449.

(11) Smallwood, C. L.; Ulbricht, R.; Day, M. W.; Schröder, T.; Bates, K. M.; Autry, T. M.; Diederich, G.; Bielejec, E.; Siemens, M. E.; Cundiff, S. T. *Phys. Rev. Lett.* **2021**, *126*, 213601.

(12) Hertel, I. V.; Schulz, C.-P. In *Atoms, Molecules and Optical Physics 2: Molecules and Photons - Spectroscopy and Collisions*; Springer Berlin Heidelberg: Berlin, Heidelberg, 2015, pp 625–666.

(13) Tekavec, P. F.; Lott, G. A.; Marcus, A. H. *Journal of Chemical Physics* **2007**, *127*, 214307.

(14) Martin, E. W.; Cundiff, S. T. *Phys. Rev. B* **2018**, *97*, 081301.

(15) Lomsadze, B.; Cundiff, S. T. *Science* **2017**, *357*, 1389–1391.

(16) Bates, K. M.; Day, M. W.; Smallwood, C. L.; Owen, R. C.; Ulbricht, R.; Schröder, T.; Bielejec, E.; Cundiff, S. T. **2021**.

(17) Smallwood, C. L.; Cundiff, S. T. *Laser and Photonics Reviews* **2018**, *12*, 1–21.

(18) Cundiff, S. T.; Mukamel, S. *Physics Today* **2013**, *66*, 44–49.

(19) Hao, K.; Specht, J. F.; Nagler, P.; Xu, L.; Tran, K.; Singh, A.; Dass, C. K.; Schüller, C.; Korn, T.; Richter, M.; Knorr, A.; Li, X.; Moody, G. *Nature Communications* **2017**, *8*, 1–7.

(20) Hahn, E. L. *Physical Review* **1950**, *80*, 580–594.

(21) Singh, R. Excitons in Semiconductor Quantum Wells Studied Using Two-Dimensional Coherent Spectroscopy, Ph.D. Thesis, 2015.

(22) Kim, J.; Mukamel, S.; Scholes, G. D. *Accounts of chemical research* **2009**, *42*, 1375–1384.

(23) Dudin, Y. O.; Li, L.; Bariani, F.; Kuzmich, A. *Nature Physics* **2012**, *8*, 790–794.

(24) Tian, P.; Keusters, D.; Suzaki, Y.; Warren, W. S. **2003**, *300*, 1553–1556.

(25) Bristow, A. D.; Karaiskaj, D.; Dai, X.; Zhang, T.; Carlsson, C.; Hagen, K. R.; Jimenez, R.; Cundiff, S. T. *Review of Scientific Instruments* **2009**, *80*, 073108.

(26) Nardin, G.; Autry, T. M.; Silverman, K. L.; Cundiff, S. T. *Opt. Express* **2013**, *21*, 28617–27.

CHAPTER III

Hidden Silicon Vacancy Centers in Diamond Revealed With Multidimensional Spectroscopy

3.1 Introduction

In chapter I, we posed the following question: how inhomogeneous are ensembles of Silicon-vacancy centers in general? Revealing part of this answer is important to future applications of SiV centers. The reason for this is twofold. Primarily, because recent work has demonstrated that SiV centers can be controllably implanted with some repeatability and reliability [1], it is important to understand if the 'bright' centers the implantation produces are typical of implanted color centers, or if they are outliers with particularly favorable properties. Additionally, the quantum efficiency of SiV color centers is relatively low [2, 3], meaning one may have to repeat a single-photon operation several times to get a single result. In the quantum information community, this is a challenge that must be overcome.

MDCS is an ideal tool with which to peer into the ensemble average physics of color centers in diamond in general [4, 5] and SiV color centers in particular [6–8]. In our study, we will examine an ensemble of color centers using two different detection techniques, both elaborated upon in chapter II. By comparing the coherently detected MDCS spectra [9] with their PL-detected counterparts [10, 11], we hope to gain

insight into the tension between the absorption and PL spectra which we measure in this sample, as reported in chapter I and to pin down the ensemble-averaged SiV optical properties to better inform application development in the future.

3.2 Revealing Hidden Color Centers by Comparing MDCS Detection Methods

The primary advantage of using a collinear, frequency-tagged MDCS experiment to probe the optical physics of some given system is that one can irradiate a sample with a diffraction-limited spotsize [9, 11–13]. This allows us, as mentioned in chapter II, to acquire spectra using either coherent detection or PL-detection. The reason to compare these two detection methods is simple: often when energy is deposited to an open quantum system, e.g. an electron within a solid, many mechanisms exist for the electron to dissipate that energy. A photon can be re-emitted, or a series of phonons (lattice vibrations) can be emitted as the electron loses energy, etc. Often, decay channels of electrons or excitons upon the absorption of a photon terminate in a 'dark' state, or one in which the direct transition rate between the 'dark' state and the ground state of the system is forbidden in some way. A spectrum which results from the overall nonlinear polarization excited after a sequence of laser pulses can be compared to one acquired using only the photons emitted after excitation to illuminate the possible mechanisms that may cause increased or decreased coupling to 'dark' states in a material. Dark states are so named because one can pump electrons (or excitons, or some other quasi-particle) into a dark state and never retrieve any photons for their trouble. This is obviously a detriment for a system in which one wants to reliably store and shuffle information around electronic states with photons, as in the case of the SiV system. Coupling between an excited state and a dark state could *also* cause the discrepancy we were seeing between the traditional PL and

absorption spectra data acquired from our sample.

To briefly see how this may occur, suppose we have an electron in some excited state $|e\rangle$ within a material, then we can write its transition rate from the excited state back to the ground state (denoted $|g\rangle$) of the system using Fermi's golden rule (elaborated upon in chapter V) [14]:

$$\Gamma(\omega) = \frac{2\pi e^2}{\hbar} |\langle e| H'(t) |g\rangle|^2 \delta(\omega - \omega_{eg}), \tag{3.1}$$

where $H'(t)$ is the interaction Hamiltonian describing either stimulated emission (in the presence of a driving field) or spontaneous emission and $\omega_{eg} = (E_g - E_e)/\hbar$ as the transition frequency. Suppose also that this excited state can couple to a dark state $|d\rangle$ from which emission to the ground state is forbidden, then the transition rate between the excited state and the dark state is

$$\Gamma_d(\omega) = \frac{2\pi e^2}{\hbar} |\langle e| H'(t) |d\rangle|^2 \delta(\omega - \omega_{ed}) \tag{3.2}$$

with $\omega_{ed} = (E_e - E_d)/\hbar$ is the transition frequency between the excited state and the dark state.

If $\Gamma_d >> \Gamma$, then the photons absorbed by state $|e\rangle$ will not be remitted. *However*, the original polarization between the ground and a higher-lying excited state can still be excited and detected in an MDCS spectrum [15], because the dipole moment between the ground and excited state is not zero.

To acquire coherently-detected spectra, as mentioned in chapter II, we irradiate the sample with three pulses. We then route the fourth pulse around the sample and interfere it with the third-order polarization field emitted from the sample. We take the resulting interference and retrieve the four-wave mixing (FWM) component of the signal at $\omega_{sig} = -\omega_A + \omega_B + \omega_C - \omega_D$ by using a lock-in amplifier to demodulate the total signal at the photodetector. Subsequently, we vary the first and third time

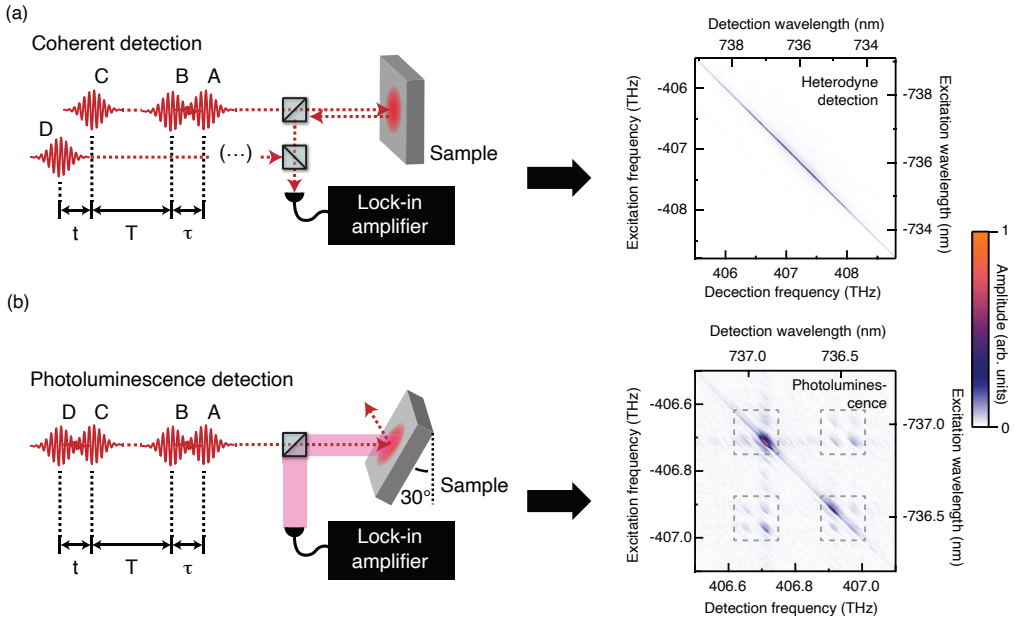

Figure 3.1: (a) A depiction of the coherently-detected MDCS experiment and the spectrum which it yields when conducted on the SiV color center ensemble, included again here for convenience. (b) The PL-detected spectrum and the MDCS spectrum it generates. Though the excitation spectrum of the laser does not change, the two detection methods yield spectra that are wildly different. The sample was tilted 30° relative to the input beams to reject coherent scatter.

delays, and collect the phase and amplitude of the FWM signal as a function of those time delays. To acquire the PL-detected spectra, instead of routing the fourth pulse around the sample, we irradiate the sample with it as well. In this way, the FWM signal will be encoded in the PL modulated at a frequency $\omega_{sig} = -\omega_A + \omega_B + \omega_C - \omega_D$. We then use the same lock-in to demodulate the signal and acquire the FWM phase and amplitude over the first and third time delays as before.

The coherently-detected and PL-detected MDCS spectra are shown in figure 3.1. As can be seen, the two detection methods yield dramatically different spectra. The PL spectrum shows sixteen peaks (within the dotted grey boxes) which are roughly in-line with the expected spectrum if PL were the main mechanism by which the color centers relaxed. The coherently-detected spectrum, however, looks markedly different. It is simply a wide inhomogeneous distribution of transition frequencies on

the equal-frequency diagonal.

The vast difference between the two spectra taken from the same sample under the same conditions (sample held at a temperature of 10 K) using the same laser (pulse center wavelength 737nm, repetition rate 76MHz) beg a microscopic explanation. First, the inhomogeneous linewidth is *so* broad that we must establish that the large inhomogeneous distribution is centered roughly around the SiV color centers, and not the result of some other color center or another defect or nonlinear effect in the crystal. We can then establish a mechanism by which this inhomogeneous distribution of color centers can occur which simultaneously explains the existence of the *bright* and *dark* centers as well as this broad lineshape.

The only other known defect line that could contribute at this energy is the GR1 center, consisting of a bare, neutral vacancy with no adjacent paired impurities [16]. To establish that this defect is not the primary cause of our broad, inhomogeneous distribution, we took coherently detected MDCS spectra with different excitation spectra. This series of spectra, shown in figure 3.2 clearly demonstrates that the signal is centered around the SiV zero-phonon line, though there is some limited overlap with the GR1 center.

To get a sense of just *how* different the two spectra are, we first compare a projection of the PL-detected MDCS to a traditional PL spectrum collected using a grating spectrometer to confirm that the PL-detected MDCS spectrum is accurately reflecting the extant literature on the SiV ZPL spectrum. This spectrum is shown in figure 3.3, and is taken by projecting the full MDCS spectrum down onto the detection axis, corresponding to an integrated FWM spectrum. The traditional PL spectrum was resolution limited by the grating spectrometer we used, with a resolution of roughly 28GHz at this frequency. The PL-detected MDCS inhomogeneous linewidth was (taken from fitting a peak in the projected MDCS spectrum) 28 ± 2 GHz. Although this is broader than the typically reported linewidths [17–19], there is likely residual

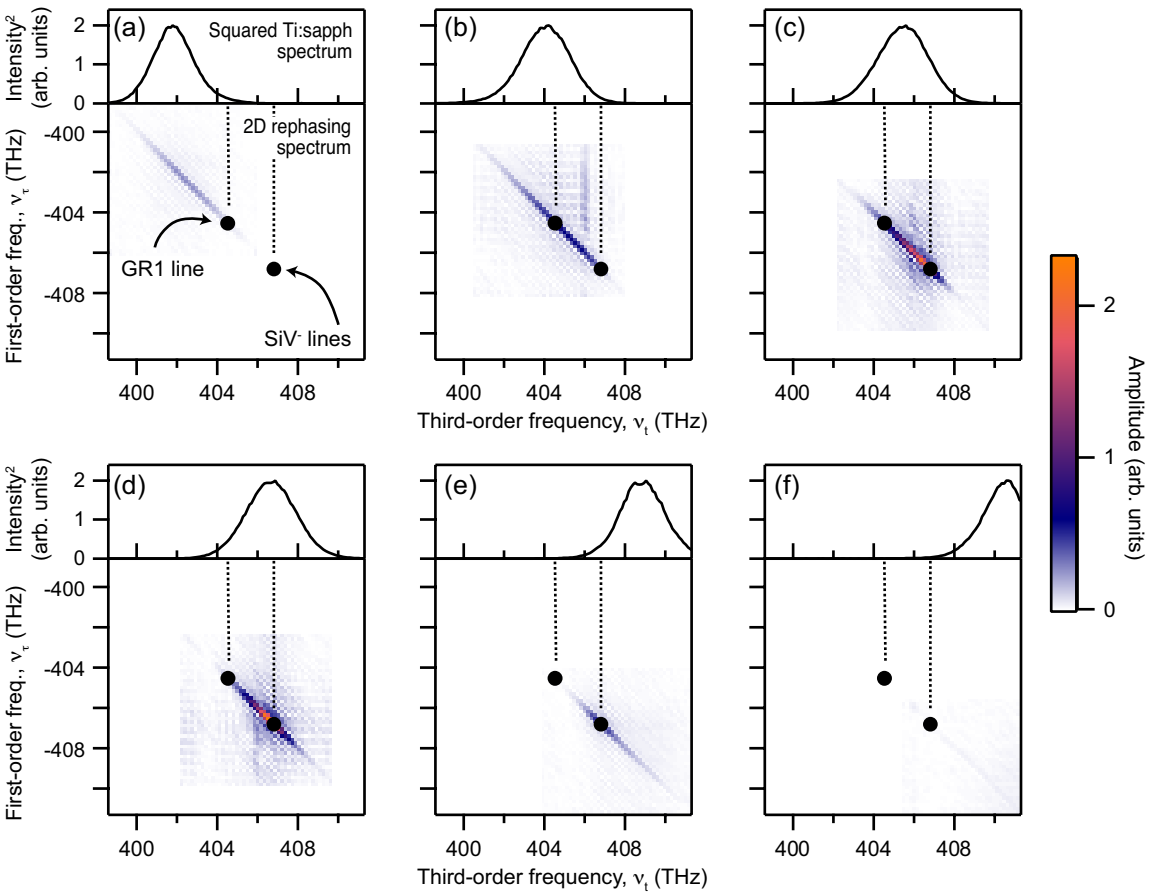

Figure 3.2: (a)-(f) A collection of MDCS spectra acquired using different laser center frequencies. This series demonstrates clearly that the MDCS signal is centered around the SiV zero-phonon line. The top panel of each plot shows the $(\text{Intensity})^2$ spectrum of the laser, corresponding to the maximum possible FWM bandwidth if the signal. The bottom panel of each plot shows the corresponding MDCS spectra acquired with each different laser center energy.

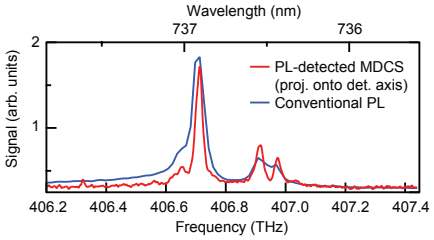

Figure 3.3: A comparison between the MDCS spectrum and the traditionally-detected PL spectrum, showing that the MDCS measurement accurately reflects the PL spectrum taken traditionally by exciting the SiV centers using our pulsed laser, and then resolving the spectrum using a grating spectrometer.

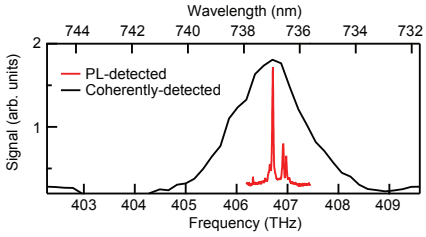

Figure 3.4: A comparison between projections of the coherently-detected MDCS spectrum and the PL-detected spectrum onto the detection axis. As can be seen, the inhomogeneous linewidths of both measurements are orders of magnitude different.

inhomogeneity in our sample due to interactions (see chapter IV) and inhomogeneity in the overall strain tensor (see ref. [7]).

We next compare the PL-detected MDCS linewidths to those in the coherently-detected MDCS spectrum, reported in figure 3.4. The coherently detected MDCS spectrum has an inhomogeneous linewidth of 1.84 ± 0.02 THz as extracted by fitting this spectrum to the finite-bandwidth model presented in ref. [20]. In other words, the coherently detected spectrum has a linewidth that is roughly 65 times that of the PL-detected spectrum. Furthermore, it is notable that there is not a prominent peak at the ZPL growing out of the inhomogeneous pedestal, and the coherently-detected spectrum lacks any semblance of the crosspeaks present in the PL-detected spectrum. These two facts may be clues to the microscopic mechanism behind the broad inhomogeneous linewidth we witness.

First, the lack of crosspeaks means that the states constituting the ZPL manifold

have both inhomogeneous center energies *and* inhomogeneous splittings. If this were not the case, the cross-peaks would appear as broad stripes to either side of the diagonal of the coherently detected spectrum. These are not present above the noise floor of our measurement. Furthermore, if the four ZPL peaks were to prominently tower out of the inhomogeneous pedestal, we could make the case that *on average*, the SiV centers implanted in the sample were of the type emitting PL, as seen from the PL-detected spectrum and from the traditionally collected PL. This is not the case.

3.3 A Possible Model Describing the Dramatic Difference in MDCS Spectra

The sum total of this data is that there must be a mechanism responsible for the reduction in PL that can also account for changing the splitting of the states that constitute the ZPL manifold. From literature, we know that strain in the system can shift the splittings and center frequencies of the SiV ZPL states [21]. Furthermore, our observation is consistent with recent photon echo measurements of SiVs in nanodiamonds, a system in which strain is expected to be even more prevalent [22]. Coupling these observations with the fact that SiV centers have both a low quantum yield [2, 3] and are likely to have a dark state in the vicinity of the ZPL states, as posited in the theory literature [23], makes strain-enhanced coupling between the excited states and one or more nearby 'dark' states the most likely explanation.

In order to show how this phenomenon could 'filter' the broad inhomogeneous spectrum detected in the coherently-detected measurement such that only narrow PL linewidths survive, my colleague Dr. Christopher Smallwood developed a model incorporating two possible scenarios to explain our data. In this model, we consider a three-level system where the highest-lying excited state can couple to a nearby dark

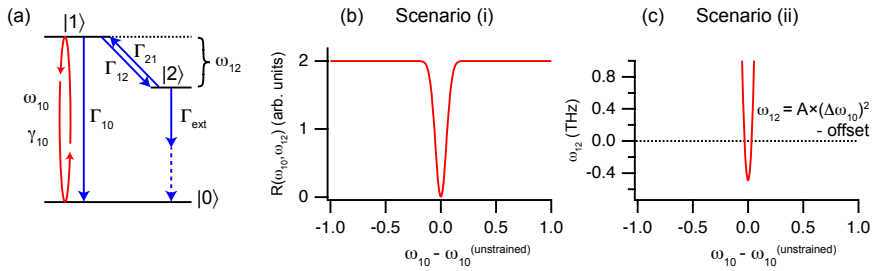

Figure 3.5: (a) The three level system under consideration, with ground state $|0\rangle$, excited state $|1\rangle$, and dark state $|2\rangle$. (b) A depiction of the electron-phonon coupling function $R(\omega_{10}, \omega_{12})$ under the assumptions of scenario (i). (c) A depiction of the relative energy difference between states $|2\rangle$ and $|1\rangle$ under the assumptions of scenario (ii).

state. We assume that there is strong strain inhomogeneity due to the high density of color center implantation in our sample, leading to a broad distribution in the transition frequency between state $|0\rangle$ and $|1\rangle$. We then consider two scenarios under which strain can enhance the coupling between state $|1\rangle$ and $|2\rangle$, leading to a broad inhomogeneous peak in the coherently-detected spectrum, but a narrow PL linewidth. Figure 3.5 summarizes the level system and the two possible scenarios we consider. We assume that the $|1\rangle \Longleftrightarrow |0\rangle$ transition is bright, with transition frequency ω_{10}, population decay rate Γ_{10}, and dephasing rate γ_{10}. We assume that electrons can decay from (be pumped into) state $|1\rangle$ to state $|2\rangle$ (from $|2\rangle$ to $|1\rangle$) at a rate Γ_{12} (Γ_{21}) from which they can further decay (nonradiatively) at a rate Γ_{ext}.

In scenario (i), we consider the possibility that the electron-phonon coupling function $R(\omega_{10}, \omega_{12})$ is suppressed when little or no strain is present, but enhanced in the presence of strain. This can occur if the transition between the bright state $|1\rangle$ and the dark state $|2\rangle$ is symmetry-forbidden. In the case of nonzero strain, the symmetry of some given center may be broken, both shifting the resonance frequency ω_{10} and opening a normally symmetry-forbidden decay channel from state $|1\rangle$ to state $|2\rangle$.

For scenario (ii), we consider the case in which strain shifts the energy levels of each vacancy center such that ω_{10} and ω_{12} shift in the same direction. Suppose that, in the unstrained case, the eigenenergy of state $|2\rangle$ is slightly greater than, but nearly

commensurate with that of $|1\rangle$. Under this scenario, it could be the case that, when strain shifts $|1\rangle$ down in energy, $|2\rangle$ shifts below $|1\rangle$ and a spontaneous decay channel from $|1\rangle \rightarrow |2\rangle$ opens.

We begin by examining the rate equations detailing the behavior of the density matrix describing our system:

$$\dot{\rho}_{10} = -(i\omega_{10} + \gamma_{10})\rho_{10} + \frac{i}{\hbar}V_{10}\left(\rho_{11} - \rho_{00}\right) \tag{3.3}$$

$$\dot{\rho}_{11} = -\Gamma_{10}\rho_{11} - \Gamma_{12}\rho_{11} + \Gamma_{21}\rho_{22} - \frac{i}{\hbar}\left(V_{10}\rho_{01} - \rho_{10}V_{01}\right) \tag{3.4}$$

$$\dot{\rho}_{22} = -\Gamma_{ext}\rho_{22} + \Gamma_{12}\rho_{11} - \Gamma_{21}\rho_{22} \tag{3.5}$$

$$\dot{\rho}_{00} = \Gamma_{10}\rho_{11} + \Gamma_{ext}\rho_{22} + \frac{i}{\hbar}\left(V_{10}\rho_{01} - \rho_{10}V_{01}\right) \tag{3.6}$$

where $V_{10} = -\mu_{10} \cdot \vec{E}(t) = V_{01}^*$ is the interaction Hamiltonian describing the coupling between our system and light. The phonon bath coupling to state $|2\rangle$ will behave in a way reflective of the Bose-Einstein distribution $n(\omega_{12}) = 1/(e^{\beta\hbar\omega_{12}} - 1)$. Furthermore, we know that in the SiV sample we measure, $T_2 << 2T_1$ so we can assume that the decoherence is dominated by the 'pure' electronic dephasing rate (γ_p) [24] with

$$\gamma_{10} = \frac{\Gamma_{10} + \Gamma_{12}}{2} + \gamma_p. \tag{3.7}$$

We will then have that the transfer rates between states $|1\rangle$ and $|2\rangle$ are

$$\Gamma_{12}(\omega_{10}, \omega_{12}) = R(\omega_{10}, \omega_{12})\left[n(\omega_{12}) + 1\right]\mathrm{sgn}(\omega_{12}) \tag{3.8}$$

$$\Gamma_{21}(\omega_{10}, \omega_{12}) = R(\omega_{10}, \omega_{12})n(\omega_{12})\mathrm{sgn}(\omega_{12}) \tag{3.9}$$

with $R(\omega_{10}, \omega_{12})$ the electron-phonon coupling.

We now calculate the expected MDCS spectra for each detection scenario, and then discuss how scenarios (i) and (ii) could act to filter the total third order po-

larization excited from a distribution of three level systems with a set of transition frequencies $\{\omega_{10}\}$ centered about $\omega_{10}^{(\text{unstrained})}$ normally distributed according to

$$G\left(\omega_{10}-\omega_{10}^{(\text{unstrained})}\right)=\frac{N}{\sigma\sqrt{2\pi}}\exp\left(\frac{-\left(\omega_{10}-\omega_{10}^{(\text{unstrained})}\right)^2}{2\sigma^2}\right) \tag{3.10}$$

with $\omega_{10}^{(\text{unstrained})}=1$ and $\sigma=0.2$ in arbitrary frequency units.

Following the conventions of Chapter II and refs. [20, 24], we can calculate the signal due to the third-order correction to the density matrix in the frequency domain for each individual system in both the coherently detected and PL-detected scenarios.

Coherently Detected Signal for one Emitter

In the coherently-detected case, the intensity of the one-emitter signal will be

$$I(\omega_\tau,\omega_t)\propto\frac{-i\mu^3}{8\hbar^3}E_D^*(-\omega_t)\Big(\frac{i}{\omega_t-\omega_{10}+i\gamma_{10}}\frac{i}{\omega_\tau-\omega_{10}+i\gamma_{10}}\Big) \tag{3.11}$$

where $E_D^*(-\omega_t)$ is the field of pulse D after routing around the sample. The signal integrated over all possible center frequencies will then be

$$\begin{aligned}I(\omega_\tau,\omega_t)\propto E_D^*(-\omega_t)\int_{-\infty}^{\infty}d\omega'_{10}\;G(\omega'_{10}-\omega_{10}^{\text{unstrained}})\\ \times\frac{\mu^4}{8\hbar^3}\Big(\frac{i}{\omega_t-\omega'_{10}+i\gamma_{10}}\frac{i}{\omega_\tau-\omega'_{10}+i\gamma_{10}}\Big).\end{aligned} \tag{3.12}$$

PL-Detected Signal for one Emitter

In the PL-detected case, the intensity of the one-emitter signal will be

$$I(\omega_\tau,\omega_t)\propto B(\omega_{10},\omega_{12})\frac{\mu^4}{16\hbar^4}\Big(\frac{i}{\omega_t-\omega_{10}+i\gamma_{10}}\frac{i}{\omega_\tau-\omega_{10}+i\gamma_{10}}\Big) \tag{3.13}$$

where $B(\omega_{10},\omega_{12})$ is the branching ratio describing the portion of centers which emit PL after the fourth pulse interacts with the sample. The final PL-detected signal,

integrating over the whole distribution of center frequencies $G\left(\omega_{10} - \omega_{10}^{(\text{unstrained})}\right)$ is then

$$\begin{aligned} I_{PL}(\omega_\tau, \omega_t) \propto & \int_{-\infty}^{\infty} d\omega'_{10} B(\omega'_{10}, \omega_{12}) G(\omega'_{10} - \omega_{10}^{\text{unstrained}}) \\ & \times \frac{\mu^4}{16\hbar^4} \Big(\frac{i}{\omega_t - \omega'_{10} + i\gamma_{10}} \frac{i}{\omega_\tau - \omega'_{10} + i\gamma_{10}} \Big). \end{aligned} \tag{3.14}$$

The difference between the two measurements is encoded in the branching ratio describing the portion of the signal that will be generated by radiative decay from state $|1\rangle$ as opposed to the portion of the signal that will decay nonradiatively through the dark state $|2\rangle$. This is to describe the fact that the same third-order polarization will be generated in both cases, but the PL-only detection filters the portion of that polarization which can decay radiatively. In the limit that $\gamma_{10} >> 1/T_1$ (which applies in this case), the coherent measurement probes the set of all color centers whereas the branching ratio acts as a filter in the frequency domain for the PL-detected measurement. The branching ratio in either case is

$$B(\omega_{10}, \omega_{12}) = \frac{\Gamma_{10}}{\Gamma_{10} + \Gamma_{12}(\omega_{10}, \omega_{12})}. \tag{3.15}$$

In scenario (i), we can approximate that $R(\omega_{10}, \omega_{12})$ behaves according to the ansatz in figure 3.5(b), i.e. it vanishes about the central frequency $\omega_{10}^{(\text{unstrained})}$, but then goes to some finite value outside of this window. If we set ω_{12} to be a large, positive number such that population flow from $|2\rangle$ to $|1\rangle$ is largely suppressed, then $\Gamma_{12}(\omega_{10}, \omega_{12}) \approx R(\omega_{10}, \omega_{12})$ and

$$B(\omega_{10}, \omega_{12}) \approx \frac{\Gamma_{10}}{\Gamma_{10} + R(\omega_{10}, \omega_{12})}, \tag{3.16}$$

because $\Gamma_{21}(\omega_1 0, \omega_1 2)$ will be suppressed by the Bose-Einstein distribution, meaning

that the phonon bath is unlikely to have enough extra energy to support population transfer back from the dark state after an electron has decayed into it.

In scenario (ii), there are two limits possible. In the case that non-radiative decay from state $|2\rangle$ dominates over re-pumping of state $|1\rangle$ from state $|2\rangle$, then feedback from state $|2\rangle$ to the PL signal will be supressed and

$$B(\omega_{10}, \omega_{12}) = \frac{\Gamma_{10}}{\Gamma_{10} + \Gamma_{12}(\omega_{10}, \omega_{12})}. \tag{3.17}$$

In the opposite limit, where $\Gamma_{10} << \Gamma_{21}$ and $\Gamma_{21} >> \Gamma_{ext}$, then state $|1\rangle$ and $|2\rangle$ will establish a quasi-static thermal equilibrium over time. In this case, the population in states $|1\rangle$ and $|2\rangle$ will be related by the Boltzmann factor between their on-diagonal density matrix elements, $\rho_{11}/\rho_{22} = e^{-\beta\hbar\omega_{12}}$. In this case, $\Gamma_{12}(\omega_{10}, \omega_{12}) \approx \Gamma_{ext}e^{-\beta\hbar\omega_{12}}$ so

$$B(\omega_{10}, \omega_{12}) = \frac{\Gamma_{10}}{\Gamma_{10} + \Gamma_{ext}e^{-\beta\hbar\omega_{12}}}. \tag{3.18}$$

We then simulate the resulting PL spectra in a variety of cases for each scenario. For case (i), presented in figure 3.6 (c)-(h), we vary the ratio between R/Γ_{10} from 0.1 to 10, where the ratio is calculated in the $(\omega_{10} - \omega_{10}^{\text{unstrained}}) \rightarrow \infty$ limit. In all cases, $\gamma_{10} = 0.05\sigma$. For case (ii), we let $\omega_{12} = A(\omega_{10} - \omega_{10}^{unstrained})^2 - c$ where $c = 0.4$, and A $= 5, 50, or 500 \times 10^{12}$ THz$/\omega_{10}^2$. In the limit that $\Gamma_{ext} >> \Gamma_{21}$, we let $R(\omega_{10}, \omega_{12}) = R(\omega_{12} \propto \omega_{12}^2$ when calculating $\Gamma_{12}(\omega_{10}, \omega_{12})$, whereas in the limit $\Gamma_{ext}, \Gamma_{10} << \Gamma_{21}$, we simply calculate $B(\Gamma_{ext} >> \Gamma_{21})$ according to equation 3.18.

The upshot of these simulations is simple. As the the coupling between the phonon bath and our ensemble of three level systems is increased, or as the degree to which the energy of state $|2\rangle$ fluctuates with strain is increased, the PL-detected signal will be filtered relative to the coherently-detected spectrum in a way consistent with our MDCS data. This means that, in a sample where a large degree of strain is present, much of the energy sent into a SiV ensemble will not be re-emitted due to coupling

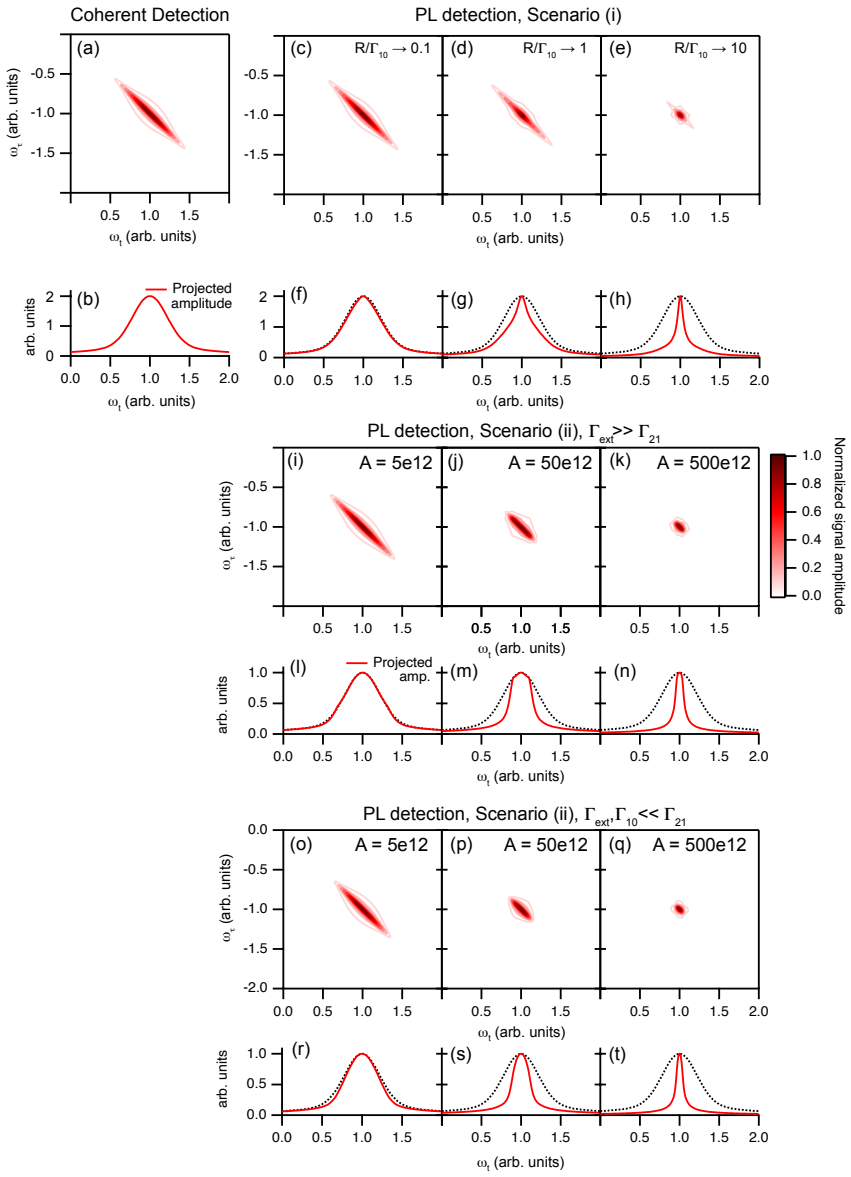

Figure 3.6: The summary of our simulations under scenario (i)(corresponding to panels(c)-(h)) and scenario (ii)(corresponding to panels(i)-(t)). Each one-dimensional panel corresponds to a projection of the above MDCS spectrum onto the ω_t axis for direct comparison to the spectrum in panels (a) and (b). In all cases, as either the coupling to the phonon bath increases with strain (corresponding to increasing R/Γ_{10}) or the degree to which state $|2\rangle$ fluctuates in energy with changing strain increases (corresponding to increasing A as defined above), the PL spectrum is filtered relative to the coherently detected spectrum, matching our results qualitatively.

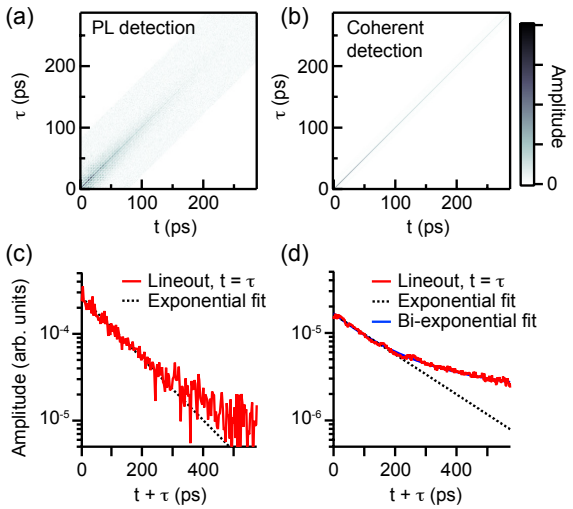

Figure 3.7: A comparison between the time domain MDCS spectra from the (a) PL-detected measurement and the (b) coherently detected measurement. Lineouts along $t = \tau$ from each spectrum are shown in panels (c) and (d).

between color centers and strain.

Our data show definitively that there is a large population SiV color centers which do not emit PL upon resonant excitation. This is the sense in which this population is 'hidden,' because, heretofore, explorations of SiV physics were primarily conducted by closely studying the optical properties of *emitted* light. It may then be natural to ask: are there other significant differences between these populations? To get a sense of the answer to this question, we take advantage of another of MDCS' strengths: the ability to resolve the intrinsic dephasing rate in the presence of inhomogeneity. This is enormously helpful to us, as there is obviously an extreme degree of inhomogeneity in the hidden centers. To do so, we extract a line-out from the time-domain MDCS data, along the line $t = \tau$. This corresponds to extracting the homogeneous dephasing rate of the ensemble. The results of doing so are presented in figure 3.7.

Here, too, the MDCS spectra taken using the two different detection methods show stark differences. In the case of the PL-detected spectrum, the photon echo decays into the noise background when $t + \tau = 500$, whereas the coherently detected signal remains above the noise background throught the entire measurement, and still

remains roughly 20 times the background even when $t + \tau = 600$ps.

Furthermore, the decay of the PL-detected photon echo, shown in figure 3.7(c), fits well to a mono-exponential decay, yielding $T_2 = 122 \pm 7$ ps. The decay of the coherently-detected photon echo on the other hand is clearly multi-exponential. We fit this decay to a bi-exponential decay, yielding two decay constants $T_{2a} = 120 \pm 5$ps and $T_{2b} = 990 \pm 180$ ps, consistent with other photon echo measurements [22]. We note that it is highly likely that the coherently-detected photon echo is a multi-exponential decay, given that there could be more than one class of 'hidden' center in our sample. The difference in dephasing times is not captured with our qualitative model, but the fact that the hidden centers have a longer dephasing time than the PL centers suggests that strain could also impact the dephasing times of each SiV center.

3.4 Conclusion and Future Directions

In this chapter, we have revealed a large population of previously hidden color centers using coherently detected MDCS. By comparing these measurements against the PL-detected spectra, which reflect what we would expect to see given the traditional ZPL emission profile, we have shown that the hidden centers are likely hidden by increased coupling to strain. Furthermore, the fact that these color centers have longer dephasing times than 'bright' centers suggests a potential way to control the electronic dephasing of SiV centers in a sample through the dynamic variation of strain within the sample, potentially possible by flexing and un-flexing a cantilever like the one in Ref. [21]. Further understanding of the interface between strain and the electronic dephasing properties of the SiV ZPL could potentially inform better device manufacture protocols and help to overcome the low quantum efficiency of these emitters, enhancing already proven photonic platforms for quantum information processing or sensing [25].

References

(1) Schröder, T.; Trusheim, M. E.; Walsh, M.; Li, L.; Zheng, J.; Schukraft, M.; Sipahigil, A.; Evans, R. E.; Sukachev, D. D.; Nguyen, C. T.; Pacheco, J. L.; Camacho, R. M.; Bielejec, E. S.; Lukin, M. D.; Englund, D. *Nature Communications* **2017**, *8*, 1–7.

(2) Turukhin, A. V.; Liu, C.-H.; Gorokhovsky, A. A.; Alfano, R. R.; Phillips, W. *Phys. Rev. B* **1996**, *54*, 16448–16451.

(3) Neu, E.; Agio, M.; Becher, C. *Opt. Express* **2012**, *20*, 19956–19971.

(4) Liu, A.; Cundiff, S. T. *Phys. Rev. Mat.* **2020**, *4*, 55202.

(5) Huxter, V. M.; Oliver, T. A. A.; Budker, D.; Fleming, G. R. *Nature Physics* **2013**, *9*, 744–749.

(6) Smallwood, C. L.; Ulbricht, R.; Day, M. W.; Schröder, T.; Bates, K. M.; Autry, T. M.; Diederich, G.; Bielejec, E.; Siemens, M. E.; Cundiff, S. T. *Phys. Rev. Lett.* **2021**, *126*, 213601.

(7) Bates, K. M.; Day, M. W.; Smallwood, C. L.; Owen, R. C.; Ulbricht, R.; Schröder, T.; Bielejec, E.; Cundiff, S. T. **2021**.

(8) Day, M. W.; Bates, K. M.; Smallwood, C. L.; Owen, R. C.; Schröder, T.; Bielejec, E.; Ulbricht, R.; Cundiff, S. T. *arXiV:2105.01103* **2021**.

(9) Martin, E. W.; Cundiff, S. T. *Phys. Rev. B* **2018**, *97*, 081301.

(10) Nardin, G.; Autry, T. M.; Silverman, K. L.; Cundiff, S. T. *Opt. Express* **2013**, *21*, 28617–27.

(11) Tekavec, P. F.; Lott, G. A.; Marcus, A. H. *Journal of Chemical Physics* **2007**, *127*, 214307.

(12) Tian, P.; Keusters, D.; Suzaki, Y.; Warren, W. S. **2003**, *300*, 1553–1556.

(13) Langbein, W.; Patton, B. *Opt. Lett.* **2006**, *31*, 1151–1153.

(14) Sakurai, J. J.; Napolitano, J. **2017**, DOI: 10.1017/9781108499996.

(15) Tollerud, J. O.; Cundiff, S. T.; Davis, J. A. *Phys. Rev. Lett.* **2016**, *117*, 097401.

(16) Stoneham, A. M.; Division, T. P. *Solid State Communications* **1977**, *21*, 339–341.

(17) Arend, C.; Becker, J. N.; Sternschulte, H.; Steinmüller-Nethl, D.; Becher, C. *Phys. Rev. B* **2016**, *94*, 045203.

(18) Becker, J. N.; Görlitz, J.; Arend, C.; Markham, M.; Becher, C. *Nat. Commun.* **2016**, *7*, 13512.

(19) Zhang, J. L.; Lagoudakis, K. G.; Tzeng, Y.-K.; Dory, C.; Radulaski, M.; Kelaita, Y.; Fischer, K. A.; Sun, S.; Shen, Z.-X.; Melosh, N. A.; Chu, S.; Vučković, J. *Optica* **2017**, *4*, 1317–1321.

(20) Smallwood, C.; Autry, T.; Cundiff, S. *Journal of the Optical Society of America B* **2016**, *34*, DOI: 10.1364/JOSAB.34.000419.

(21) Meesala, S. et al. *Phys. Rev. B* **2018**, *97*, DOI: 10.1103/PhysRevB.97.205444.

(22) Lindner, S.; Bommer, A.; Muzha, A.; Krueger, A.; Gines, L.; Mandal, S.; Williams, O.; Londero, E.; Gali, A.; Becher, C. *New J. Phys.* **2018**, *20*, 115002.

(23) Gali, A.; Maze, J. R. *Phys. Rev. B* **2013**, *88*, 235205.

(24) Mukamel, S., *Principles of nonlinear optical spectroscopy*; Oxford series in optical and imaging sciences; Oxford University Press: New York, 1995.

(25) Wan, N. H.; Lu, T. J.; Chen, K. C.; Walsh, M. P.; Trusheim, M. E.; De Santis, L.; Bersin, E. A.; Harris, I. B.; Mouradian, S. L.; Christen, I. R.; Bielejec, E. S.; Englund, D. *Nature* **2020**, *583*, 226–231.

CHAPTER IV

The Existence and Control of Coherent Coupling Between Quantum Emitters in Diamond

4.1 Introduction

4.1.1 Why Study Interactions Between Color Centers?

In the universe of quantum computing and information technology, any quantum mechanical two-level system that can be manipulated easily is referred to a qubit (quantum bit). There are two 'resources' that quantum information architecture relies on: the 'coherence' of a two level system, in other words the time it takes for a qubit to lose the information transferred to it in some way (exactly the same 'coherence' we discussed in the prior chapter), and 'entanglement,' or the ability to link two (or more) quibits together such that their joint state is what is known as an 'Entangled State,' where by measuring the state of one or more qubit, one will know the state of the full system [1–4]. Both concepts, of course, are fields of studies alone, so detailed discussions about the nature of either 'decoherence' processes (which we've only barely brushed with in this Thesis) [5–7], and the weird and wild world of quantum entanglement [2, 3, 8] are well outside the scope of this document. However, studying interactions between SiVs will help us better understand how to control quantum interactions between systems in the future and could inform new ways of

entangling and exchanging information between qubits.

4.1.2 Entanglement through Dipole-Dipole Interactions

Qubits can come in a variety of forms. The most popular qubits fall mainly into three categories: superconducting qubits [9], ionic/atomic qubits [10], and defect qubits [11], of which SiV centers are a member [12–14]. As stated in chapter I, SiV centers have the advantage over other qubit candidates that they are stationary and can be easily interacted with photonically. Thus far, the only sense in which direct inter-center interactions have been studied is in machined diamond cavities where two centers were allowed to exchange photons [15, 16]. However, direct photonic entanglement is not the only way by which color centers interact. In fact, it would be extremely useful to be able to take advantage of dipole-dipole interactions, which have the favorable properties that they are 1) 'always on' between two objects (yet can still be potentially controlled), 2) not as 'directional' as photon-mediated entanglement protocols, and 3) the new eigenstates formed by two interacting color centers through dipole-dipole coupling are Bell states, requiring no preparation to generate entanglement. To see this, we note that the dipole-dipole interaction between two objects is

$$H_{dd} = \frac{J_{12}}{2}(\sigma_x^{(1)}\sigma_x^{(2)} + \sigma_y^{(1)}\sigma_y^{(2)}) \tag{4.1}$$

from reference [17], where J_{12} is the dipole-coupling strength given by

$$J_{ij} = \frac{1}{2\pi\epsilon_0\epsilon_r}\Big[\frac{\vec{\mu_i}\cdot\vec{\mu_j}}{R_{ij}^3} - \frac{3(\vec{\mu_i}\cdot\vec{R}_{ij})(\vec{\mu_j}\cdot\vec{R}_{ij})}{R_{ij}^5}\Big], \tag{4.2}$$

with μ_i, μ_j are the dipole moments for centers i and j, $\epsilon_0\epsilon_r$ is the diamond lattice permeability, $R_{ij} = \mathbf{r}_i - \mathbf{r}_j$ the inter-center distance, and σ_x, σ_y the Pauli x and y spin matrices [3] where we have modified J_{ij} from its form in ref. [17] to include the full interaction, not just the nearfield interaction.

Now, suppose we bring two color centers close together such that these interactions are reasonably strong, ($J \sim$ 1-10GHz). Our two-center system will now be stationary states of their interaction Hamiltonian [17]. Diagonalizing $H_{tot} = H_0 + H_{dd}$, we find that it has stationary states (in the rotating frame of the natural two-level system frequency ω_0, and up to arbitrary phases)

$$\begin{aligned} |\Phi_1\rangle &= |g_1, g_2\rangle \\ |\Phi_2\rangle &= \tfrac{1}{\sqrt{2}}\Big(|g_1, e_2\rangle - |g_1, e_2\rangle \Big) \\ |\Phi_3\rangle &= \tfrac{1}{\sqrt{2}}\Big(|g_1, e_2\rangle + |g_1, e_2\rangle \Big) \\ |\Phi_4\rangle &= |e_1, e_2\rangle \end{aligned} \tag{4.3}$$

with $|g_i\rangle$ and $|e_i\rangle$ being the ground and excited states of the original separate two-level systems. States $|\Phi_2\rangle$ and $|\Phi_3\rangle$ are Bell states, while states $|\Phi_1\rangle$ and $|\Phi_4\rangle$ can be superposed to create an entangled state. The implication of this is that **if we bring two dipole-dipole interacting systems into close proximity, the interactions yield a new basis set of states that are entangled states of the first two systems separately**, not just simple superpositions of the original basis states. This is important because it suggests a simpler way to generate entanglement between systems than the typical (see for instance refs. [18, 19]) heralded entanglement protocols: bring two systems together and allow them to interact through dipole-dipole interactions. Et voilà, entanglement! However, one still must be able to isolate the entangled states from each other. It is thus advantageous to either be able to tune the strength of interaction-induced splittings by moving systems closer together, or by using nearly-resonant systems instead of perfectly indistinguishable states (see Section 4.3.3). This will be the case for our work.

4.1.3 The Role of the Nonlinear Spectroscopist

In general, traditional nonlinear spectroscopy is a semi-classical technique and is therefore not a suitable tool for probing entanglement; our role in this picture, however, is simple: we are going to determine *if* and *by what mechanism* color centers interact, and if they do we will answer the question: *can these interactions be controlled*? We will do so using a nonlinear spectroscopic technique, known as double-quantum two-dimensional spectroscopy (DQ2D), that yields a signal *only* in the presence of excitation-level dependent interactions between separate quantum objects [20].

In many quantum information processing schemes, the difficulty lies not in generating the entanglement, but in having exquisite control over pairs of centers/qubits with the ability to bring them into close proximity [17, 21] and necessitating the ability to *control* inter-center interactions such that the information that entangled centers carry is not lost due to increased decoherence that may come about as a result of the interactions. Techniques to controllably implant SiV centers have been developed [22], and could be employed to construct quantum logic gates built of pairs or groups of interacting centers. These multi-center complexes could be then used as an entanglement resource for storing or manipulating quantum information as a part of a larger quantum information architecture, or as multi-quibit quantum sensors in precision sensing applications where the entanglement between multiple qubits is necessary to surpass the standard shot-noise measurement limit [23].

4.2 A Brief Note on Methodology

The methodoligical flow used in this investigation is as follows: we first use PL-detected DQ2D spectroscopy to show that SiV centers in diamond *do* have excitation-dependent interactions. We then identify dipole-dipole coupling as a likely interaction

mechanism and show that the inhomogeneous linewidths our PL-detected linear spectra could be accounted for entirely with inter-center interactions. Finally, to show that these excitation-dependent interactions could be controllable, we employ a variable-power pulse 1 ns prior to our DQ2D pulses to demonstrate that modifying the initial excitation fraction of SiV centers can be used to change and control their interaction strength.

For completeness, we will mention one other detail pertinent to the DQ2D measurements. Because we are looking for the PL signal modulated at $\omega_{sig} = \omega_A + \omega_B - \omega_C - \omega_D$, we change our AOM frequencies to $\omega_A = 81$ MHz, $\omega_B = 79.135$ MHz, $\omega_C = 81.085$ MHz, and $\omega_D = 79$ MHz. Though our FWM frequency remains constant, we need to look at the beatnote between beams C and A, then between B and D as opposed to the prior situations where we were looking for the beatnotes between A and B, then C and D to retrieve our FWM signal frequency with the CW reference. We then collect the CW beatnotes all on one reference detector, as opposed to the two detailed prior to this chapter in the experimental diagram.

4.3 Results and Discussion

We measure a finite DQ2D signal, which is direct evidence of excitation-dependant interactions. Figure 4.1 shows two DQ2D spectra taken using 3 mW total power for our MDCS pulses, for X and Y polarized excitation light. The linear, two-pulse PL detected spectra corresponding to the same spot on the sample are plotted above the DQ2D spectra, taken using roughly 14 mW of total power, to increase signal to noise of the linear data, though very slight additional broadening was observed at these high powers, the origins of which will be discussed later. Both the linear data and the DQ2D data show a zoo of peaks contributing to the overall signal. This was because, as my colleague and I showed in ref. [24], the nonzero local strain splits the four ZPL transitions into up to twelve separate peaks depending on the orientation of the SiV

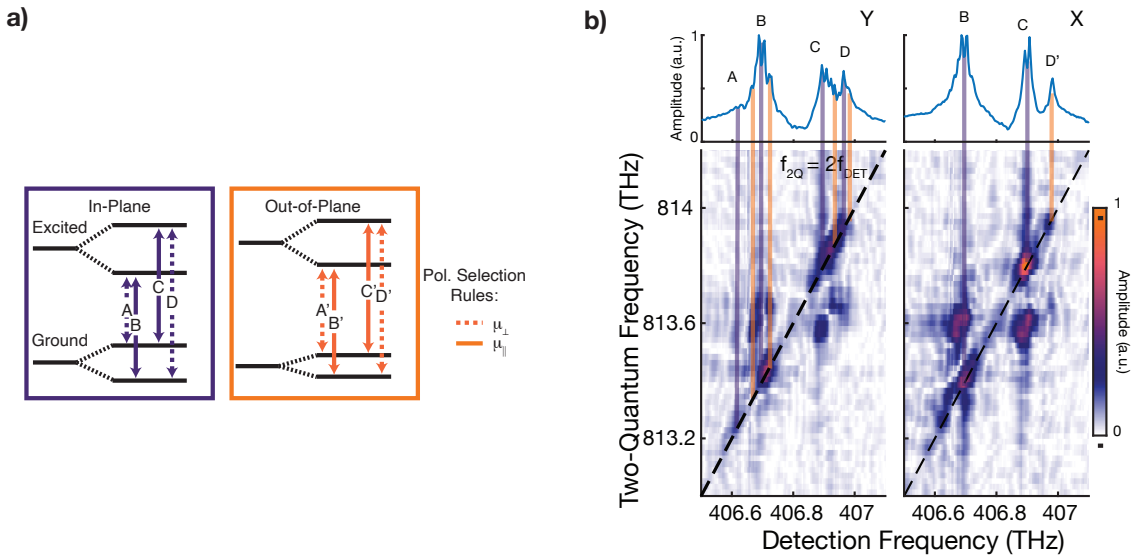

Figure 4.1: (a) The level-scheme for the SiV centers queried in the spectra in (b). (b) DQ2D spectra (with linear spectra plotted above) showing a panoply of resonant and nonresonant interactions contributing to the overall signal. Lines are drawn to approximate the positions of all peaks corresponding to the level systems detailed in (a). Furthermore, the peak labels (for example peak 'B') in the left-hand linear spectra should be construed as composed of peaks from all different orientations, that is 'B' contains both peaks B and B'. The X-polarized data has only the transitions that contribute to the DQ2D spectrum highlighted.

center due to local strain.

This zoo of peaks is not the main finding of this work. Rather, our main result is that excitation dependent interactions between centers happen, regardless of weather or not the interacting states are in resonance, given that both on- and off-diagonal peaks exist. Furthermore, because we have explored the origins of the extra peaks elsewhere, we will instead be focusing on the interactions themselves from here on out. However, the array of peaks makes the initial analysis of the spectra in figure 4.1 challenging; we must sort out all quantum pathways contributing to the spectrum and then we must arrive at a model for interactions that explains our data.

4.3.1 Quantum Pathways that Contribute to a DQ2D Signal

Now that we have determined *that* color centers interact, we need unravel the tangle of quantum pathways that could contribute to a DQ2D spectrum and then work to establish the mechanism by which they interact. To sort out the assembly of pathways, will focus on the X-polarized spectra, because their peak structure is more simple and will be a straightforward place in which to start our analysis. We will first write down our Feynman diagrams to account for all signal pathways, and then assign each diagram a two-dimensional lineshape (which we will write explicitly following the accounting process).

We begin by considering the transitions responsible for our signal, which are the B, C, and D' transitions in the X-polarized spectra. We are fortuitous, because the Feynman diagrams contributing to this signal will be from interleaved but not inter-dependant level systems. Therefore, in modelling our interactions and their effect on the phase and amplitude of the DQ2D spectrum, we can take the picture that every peak in the DQ2D spectrum comes from an independent four-level diamond due to the polarization selection rules that we and others have studied in detail [25], cutting down on the potential complexity of our analysis significantly. This fact is summarized

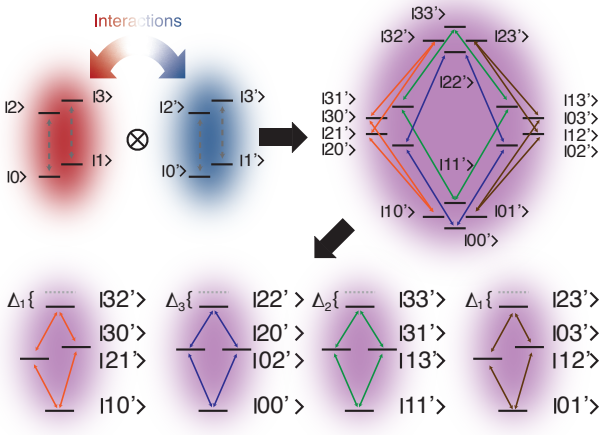

Figure 4.2: A depiction of the level system of two coupled in-plane oriented SiV centers excited with X-polarized light, each with two independent two-level systems corresponding to the B and C transitions in the in-plane centers. The different possible pathways giving rise to a DQ2D signal are color-coded, and the interleaved systems are disentangled accordingly. There are three interaction parameters, $\Delta_1, \Delta_2, and \Delta_3$ corresponding to the three independent sets of pathways, with the non-resonant pathways being doubly degenerate.

in figure 4.2 where we demonstrate that the nested diamond level systems can only have transitions within themselves and not between each other. Furthermore, we will primarily focus on the color centers oriented in-plane, giving rise to transitions B and C, because any coupling these between pathways and those that give rise to peak D' (from the out-of-plane oriented centers) are either not present or not strong enough to yield crosspeaks between peaks B or C and D' above the noise floor of the DQ2D measurement.

We can then write down all twelve Feynman diagrams contributing to one peak within our DQ2D signal, as depicted in figure 4.3. We note that, since we are using a PL detection method, valid signal pathways that end on the doubly excited state contribute to the signal as well, emitting two photons each. That is accounted for by the factor of two in front of the diagrams in the right-hand column of diagrams in figure 4.3.

The X-polarized DQ2D spectra has four such level systems contributing to the

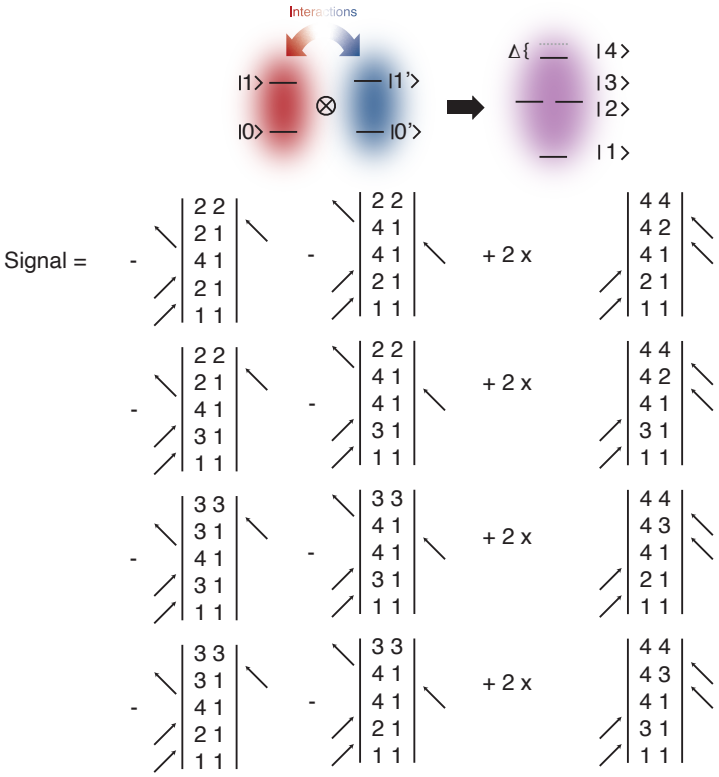

Figure 4.3: The twelve diagrams that contribute to each DQ2D peak in our spectrum; levels 2 and 3 need not be degenerate. We have relabeled the four levels within our coupled diamond system as $1 \rightarrow 4$ to make the diagrams less visually cluttered.

peaks resulting from the B and C transitions, each yielding twelve separate diagrams, so the whole peak system is the sum of 48 such pathways. As argued above, because the four separate peaks are independent, it is enough to simply total up the twelve diagrams corresponding to the twelve signal pathways contributing one peak, assuming as usual that our doubly-excited state has an excitation dependent shift Δ to describe inter-center interactions. Doing so, under the assumption that our pulses are delta functions on the timescale of the dynamics, and noting that we are in the Markovian limit (yielding Lorentzian lineshapes) [7, 26], the DQ2D signal for one independent diamond system is

$$\begin{aligned} S^{(3)}(\tau,\omega_T,\omega_t) = \frac{\mu_{21}^2\mu_{31}^2}{8\hbar^3}\frac{e^{-i\Omega_{21}\tau}+e^{-i\Omega_{31}\tau}}{\omega_T-\Omega_{41}-\Delta} \\ \times\Big(\frac{1}{\omega_t-\Omega_{31}}-\frac{1}{\omega_t-\Omega_{43}-\Delta}+ \\ \frac{1}{\omega_t-\Omega_{21}}-\frac{1}{\omega_t-\Omega_{42}-\Delta}\Big) \end{aligned} \tag{4.4}$$

where ω_T and ω_t are the frequency axes corresponding to the Fourier transform of T and t, μ_{21} and μ_{31} are the transition dipole moments, Δ is our complex-valued, excitation dependent interaction parameter, and $\Omega_{ij} = \omega_{ij} - i\gamma_{ij}$ is the center frequency and dephasing rate for the $i \leftrightarrow j$ optical transition. We note that, because $\Omega_{43} = \Omega_{21}$ and $\Omega_{42} = \Omega_{31}$, when our interaction parameter Δ is zero (i.e. there are no excitation dependent interactions), our signal vanishes as expected.

4.3.2 Likely Mechanism for Inter-Center Interactions

Now that we have identified *that* our color centers interact, we must understand *what mechanism* is most likely to lead to inter-center interactions. Given that color centers are charged, one might be tempted to think that static Coulomb interactions would be responsible for the DQ2D signal that we see. However, this is not possible for two reasons. First, this interaction would not be excitation-dependent; it would

simply be static and therefore it would likely renormalize the ground state energy. Second, even if it were the dominant inter-center interaction, for a pair of centers 6 nm apart, it would cause inhomogeneity on the order of the interaction shift, which would be ∼60 THz, *extremely* broad relative to the linewidths we measure.

The second mechanism one might expect to cause interactions could be wavefunction overlap of adjacent electrons in adjacent color centers causing a spin-flip, known as Dexter coupling [19]. Again this possibility can be ruled out for two reasons. Primarily, the centers are roughly 10nm apart on average, while the wavefunction of each electron is likely confined within roughly one unit cell, within 1/10th the distance to the nearest color center [27] making wavefunction overlap unlikely. Secondarily, Dexter coupling in this system would lead to hybridization of the wavefunctions of the electrons confined to each SiV, and not necessarily directly cause a DQ2D signal, as has been noted in asymmetric quantum wells where spatial wavefunction overlap is more likely [28].

One may also expect Pauli blocking between adjacently excited electronic states could cause excitation-dependent interactions, but this is also unlikely to be the case. For this to be a strong effect, excited electrons in color centers must again have some spatial wavefunction overlap between center pairs [3], and as stated before this is unlikely. Furthermore, each excited state in the ZPL manifold is doubly degenerate in the spin degree of freedom [12, 25, 27], so even if two excited adjacent electrons did experience wavefunction overlap, they could each inhabit one spin state an not experience Pauli pressure.

This leaves the most likely interaction mechanism to be resonant dipole-dipole coupling between color centers. This has been seen to give rise to DQ2D signals frequently in atomic systems [29] and in semiconductor quantum wells [28, 30]. To show that this is likely the cause of inter-center interactions in our sample, we will attempt to simulate the inhomogeneous linewidths in our linear spectra, depicted in

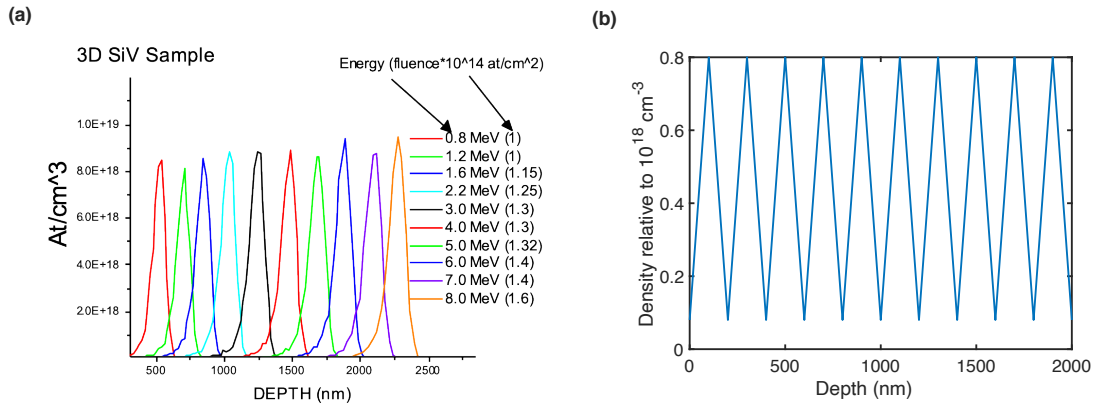

Figure 4.4: (a) The implantation density data for this sample, indicating the flux of Si atoms as a function of depth. (b) An approximation of the density profile in (a) used to calculate the interaction strength in our simulations.

4.1 in the upper right corner of panel (b). We do this because, though the DQ2D signal is sensitive to interactions, the interactions can cause the center frequency or the dephasing rate to either increase or decrease; in other words, the excitation-induced shift (Re(Δ)) and the excitation-induced dephasing (Im(Δ)) can be either negative or positive, which can cause a fitting ambiguity in the lineshape of a DQ2D peak. To simulate the linear spectrum, we numerically populate a cube of 50 nm on each side, containing a number color centers with random orientations along the four allowed direction, determined by the density of successfully implatned centers. We then make the ansatz that $\sim 10\%$ of the color centers are implanted successfully, leading to a maximum density of 0.8×10^{18} centers/cm^3 taken from the data in figure 4.4 (a). This is our only adjustable parameter. We then sample this distribution at each maximum and minimum density site, indicated by our estimated profile in figure 4.4 (b). We use the inter-center dipole-dipole energy, detailed earlier in the chapter, to rediagonalize the static Hamiltonian of each color center:

$$H_{int,ij} = \frac{1}{4\pi\epsilon_0\epsilon_r}\left[\frac{\vec{\mu_i}\cdot\vec{\mu_j}}{|R_{ij}|^3} - \frac{3(\vec{\mu_i}\cdot\vec{R}_{ij})(\vec{\mu_j}\cdot\vec{R}_{ij})}{|R_{ij}|^5}\right] \tag{4.5}$$

where μ is taken to be 14.3 Debye, (scaled to the appropriate peak height in the linear

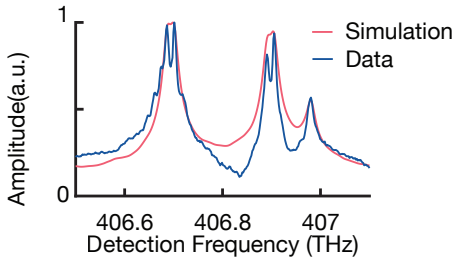

Figure 4.5: A comparison between the linear, PL detected absorption spectrum and the simulation incorporating only interaction-induced inhomogeneous broadening. The simulation qualitatively captures the lineshape of the linear data, demonstrating that dipole-dipole interactions could contribute at the correct strength to both cause a DQ2D signal and in the overall response of the SiV ensemble.

data) from literature, and $\vec{R}_{ij} = \vec{r}_j - \vec{r}_i$ as before with $\epsilon_0\epsilon_r$ the relative permeability of the diamond lattice. We take these new center energies for each center as the center frequency for a Lorentzian emission profile, taking the homogeneous linewidth to be $T_2 = 120$ ps, as measured by myself and my colleagues in this sample [31]. Finally, we add a weak, interacting Gaussian pedestal of the same density, with initial center frequencies distributed over 1.8 THz, to match the weak, but broad inhomogeneous linewidth we see in the one-quantum PL-detected spectrum and the pedestal underlying two-pulse correlation data.

The result of this simple simulation is rather surprising: interactions alone, ranging in strength between 4 and 40 GHz in strength, can cause the broadening present in our linear spectra. Figure 4.5 is a summary of this result. The point of the simulation is not to assert that dipole-dipole interactions are the only cause of inhomogeneity in the sample. This is, in fact, almost certainly not the case [31]. Instead, inter-center interactions could contribute at the correct order of magnitude in strength to both cause a DQ2D signal and inhomogeneous broadening as would be expected in an ensemble of randomly distributed, interacting objects.

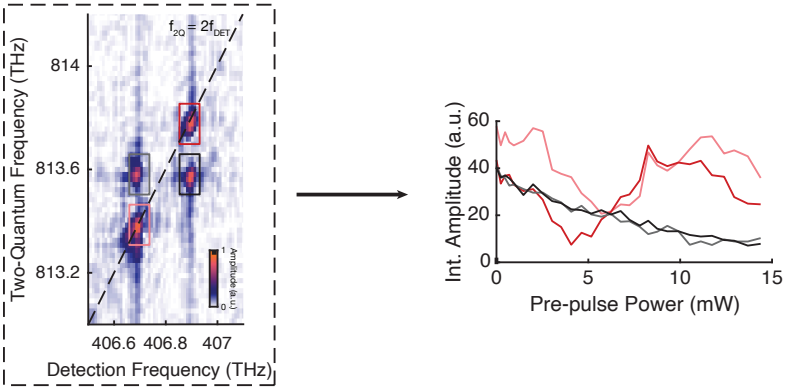

Figure 4.6: A summary of the pre-pulse dependent DQ2D peaks, integrated over the boxes depicted in the spectrum. As the pre-pulse power changes, the on-diagonal peaks (red, pink) undergo an oscillation in amplitude, whereas the off-diagonal peaks (grey,black) do not.

4.3.3 Control over Excitation-Dependent Interactions

Now that we have established that SiV centers interact and established the likely mechanism by which interactions occur, the next logical question to ask is: *can we control the interactions between the centers?* To this end, we add a variable-strength laser pulse 1 ns prior to our FWM pulse sequence, called a 'pre-pulse,' spatially overlapped with the FWM pulses at the sample. The idea is to probe the behavior of inter-center interactions using the DQ2D spectra as we control the initial state of the system. We set the delay between the pre-pulse and the FWM pulses to 1 ns to allow coherent effects to dephase (over the timescale of 120 ps [31]) prior to the arrival of the FWM pulses, such that we are only modifying the population state of the system. Successfully establishing control over the inter-center interactions will be marked by the ability to change the DQ2D spectra with the pre-pulse power.

When the pre-pulse power is varied, the on-diagonal peaks (corresponding to the DQ2D signal dominated by pairs of SiV centers) coherently oscillate, while the off-diagonal peaks saturate and decrease. This is evidence of Rabi-like behavior *only for the resonant center pairs*. The right hand plot of 4.6 summarizes this phenomenon.

What might be happening? Well, we can look back to our dipole-dipole Hamilto-

nian for clues. We will recall that

$$H_{tot} = H_0 + H_{dd} \tag{4.6}$$

where

$$H_0 = \delta_1 \left|e_1, g_2\right\rangle \left\langle e_1, g_2\right| + \delta_2 \left|g_1, e_2\right\rangle \left\langle g_1, e_2\right| \tag{4.7}$$

and from above

$$H_{dd} = \frac{J_{12}}{2}\left(\sigma_x^{(1)}\sigma_x^{(2)} + \sigma_y^{(1)}\sigma_y^{(2)}\right) \tag{4.8}$$

where J_{12} is the interaction strength between centers 1 and 2, and $|g_1, g_2\rangle := |g_1\rangle \bigotimes |g_2\rangle$, $|e_1, g_2\rangle := |e_1\rangle \bigotimes |g_2\rangle$, etc. are the new states in the two-system product basis, $\delta_1 = \hbar\omega_1, \delta_2 = \hbar\omega_2$ are the eigenenergies for the excited states of centers 1 and 2 respectively, and $|g_i\rangle, |e_i\rangle$ are the ground and excited states for systems $i = 1, 2$. We can diagonalize the full Hamiltonian to yield new eigenstates

$$\begin{aligned} |\phi_1\rangle &= |g_1, g_2\rangle \\ |\phi_2\rangle &= \tfrac{1}{\sqrt{b_-^2+1}}(b_- |e_1, g_2\rangle + |g_1, e_2\rangle) \\ |\phi_3\rangle &= \tfrac{1}{\sqrt{b_+^2+1}}(b_+ |e_1, g_2\rangle + |g_1, e_2\rangle) \\ |\phi_4\rangle &= |e_1, e_2\rangle \end{aligned} \tag{4.9}$$

where

$$b_\pm = \frac{-\delta_1 - \delta_2 \pm \sqrt{16a^4 + \delta_1^2 + \delta_2^2 - 2\delta_1\delta_2}}{4a^2} \tag{4.10}$$

with $a = |J_{12}|/2$ being the interaction strength. In the case that $\delta_1 = \delta_2$, then $b_\pm = \pm 1$, recovering the states from the introduction. The reason that our nonresonant interactions saturate is that they *decohere* prior to the arrival of the FWM pulses: because J$\propto \mu_1^2(\omega)\mu_2^2(\omega)$, the out-of resonant centers will both have increased dephasing and reduced interaction strengths relative to the resonant centers. **This means that the resonant centers are likely to form long-lived pair-wise**

addressable four-level systems with naturally entangled eigenstates.

With this in mind, we develop a model to explain the Rabi-like behavior of the on-diagonal peaks. We'll use our four new eigenstates and write

$$H_{EM} = \begin{pmatrix} \epsilon_1 & -\vec{\mu}\cdot\vec{E}(t) & -\vec{\mu}\cdot\vec{E}(t) & 0 \\ -\vec{\mu}\cdot\vec{E}(t) & \epsilon_2 & 0 & -\vec{\mu}\cdot\vec{E}(t) \\ -\vec{\mu}\cdot\vec{E}(t) & 0 & \epsilon_3 & -\vec{\mu}\cdot\vec{E}(t) \\ 0 & -\vec{\mu}\cdot\vec{E}(t) & -\vec{\mu}\cdot\vec{E}(t) & \epsilon_4 \end{pmatrix} \tag{4.11}$$

as the interaction Hamiltonian between our joint system and a driving electric field in the dipole approximation. We assume that $\epsilon_1 = 0$, $\epsilon_2 = \epsilon_3 = \hbar\omega_1 = \delta_1$ (and that $\delta_1 = \delta_2$), $\epsilon_4 = 2\hbar\omega_1 = 2\delta_1$, and $\vec{E}(t) = \vec{E}_0\cos(\omega t)$ where ω is the driving frequency of the field. We neglect the fact that $\epsilon_2 = \delta_1 - (|J_{12}|^2/2)$ and $\epsilon_3 = \delta_1 + (|J_{12}|^2/2)$ differ slightly from the central energy value because these differences (1-10 GHz) are negligible on the scale of the $\sim$ 406.7 THz transition frequency of the SiV centers and anyways won't significantly change our model when we drive the system resonantly (which we do). Using the time-dependant Schrödinger equation, we have the coupled set of differential equations for the time evolution of the system (where c_i are the complex weighting coefficients for each state)

$$i\dot{c_1}(t) = -\vec{\mu}\cdot\vec{E}_0(c_2(t) + c_3(t))\cos(\omega t) \tag{4.12}$$

$$i\dot{c_2}(t) = -\vec{\mu}\cdot\vec{E}_0(c_0(t) + c_4(t))\cos(\omega t) + \hbar\omega_1 c_2(t) \tag{4.13}$$

$$i\dot{c_3}(t) = -\vec{\mu}\cdot\vec{E}_0(c_0(t) + c_4(t))\cos(\omega t) + \hbar\omega_1 c_3(t) \tag{4.14}$$

$$i\dot{c_4}(t) = -\vec{\mu}\cdot\vec{E}_0(c_2(t) + c_3(t))\cos(\omega t) + 2\hbar\omega_1 c_4(t). \tag{4.15}$$

The rotating wave approximation consists of making the substitution $d_1(t) = c_1(t)$, $d_2(t) = c_2(t)e^{i\omega t}$, $d_3(t) = c_3(t)e^{i\omega t}$, and $d_4(t) = c_4(t)e^{2i\omega t}$ and afterward disregarding terms evolving at 2ω because they evolve too quickly to affect the dynamics and will

average to zero on the timescale we are interested in studying. Under this approximation, the above set of differential equations becomes

$$i\dot{d_1}(t) = -\frac{\Omega}{2}(d_2(t) + d_3(t)) \tag{4.16}$$

$$i\dot{d_2}(t) = -\frac{\Omega}{2}(d_1(t) + d_4(t)) + \hbar(\omega - \omega_1)d_2(t) \tag{4.17}$$

$$i\dot{d_3}(t) = -\frac{\Omega}{2}(d_1(t) + d_4(t)) + \hbar(\omega - \omega_1)d_3(t) \tag{4.18}$$

$$i\dot{d_4}(t) = -\frac{\Omega}{2}(d_2(t) + d_3(t)) + 2\hbar(\omega - \omega_1)d_4(t) \tag{4.19}$$

where Ω is the Rabi frequency $\Omega = \vec{\mu} \cdot \vec{E}/\hbar$. If we drive our system resonantly such that $\omega = \omega_1$, then the coefficients for the time-evolution of the four states are

$$d_1(t) = \cos^2(\frac{\Omega t}{2}) \tag{4.20}$$

$$d_2(t) = d_3(t) = \frac{i}{2}\sin(\Omega t) \tag{4.21}$$

$$d_4(t) = -\sin^2(\frac{\Omega t}{2}). \tag{4.22}$$

we then have that, for N resonant systems,

$$\rho_{11} = N\cos^4(\frac{\Omega t}{2}) \tag{4.23}$$

and

$$\rho_{44} = N\sin^4(\frac{\Omega t}{2}). \tag{4.24}$$

This is the core of our model. We let the signal strength depend on the ground state population and the interaction strength (Δ) depend on the doubly excited state

population (to yield a DQ2D signal). We will then have

$$S^{(3)}(\tau,\omega_T,\omega_t) \propto \frac{\cos^4(E/E_\pi)\mu_{21}^2\mu_{31}^2}{8\hbar^3}\frac{e^{-i\Omega_{21}\tau}+e^{-i\Omega_{31}\tau}}{\omega_T-\Omega_{41}-\Delta(E)} \times\Big(\frac{1}{\omega_t-\Omega_{31}}-\frac{1}{\omega_t-\Omega_{43}-\Delta(E)}+ \frac{1}{\omega_t-\Omega_{21}}-\frac{1}{\omega_t-\Omega_{42}-\Delta(E)}\Big) \tag{4.25}$$

where we scale the population argument such that $E/E_\pi = \pi/2$ for an electric field E corresponding to a canonical 'pi-pulse,' and we approximate that the interactions depend linearly on the excitation fraction such that $\Delta(E) = \Delta_{s,0} - i\Delta_{d,0} + sin^4(E/E_{pi})(\Delta_{s,1} - i\Delta_{d,1})$ where $\Delta_{s,0}$ and $\Delta_{d,0}$ are the zero pre-pulse excitation-induced shift and excitation-induced dephasing giving rise to the DQ2D signal respectively, and $\Delta_{s,1}, \Delta_{d,1}$ are the changes of these quantities as a linear function of excitation fraction.

Because $\Delta(E)$ is complex, we must fit both the amplitude and the phase of the DQ2D data to see if our model is realistic. We do this by focusing on the peak with the best signal-to-noise ratio, the on-diagonal peak in the red box. We take a line-out across the peak of the spectrum as a function of the square-root of the prepulse power (which is proportional to the prepulse field), retaining both the amplitude and phase of the data. We input the linewidths in the ω_t and ω_T axes $\gamma_t = 12$ GHz and $\gamma_T = 22$ GHz, measured from the 2Q spectrum. Figure 4.7 is a summary of the output of this process. The fit returns the values in table 4.1.

Fit Parameter	Fit Value (GHz)
$\Delta_{d,0}$	2
$\Delta_{s,0}$	6
$\Delta_{d,1}$	50
$\Delta_{s,1}$	-200

Table 4.1: The best-fit values for fitting the model to the behavior of the upper on-diagonal DQ2D peak.

This simple model is a reasonable reproduction of the qualitative behavior of the

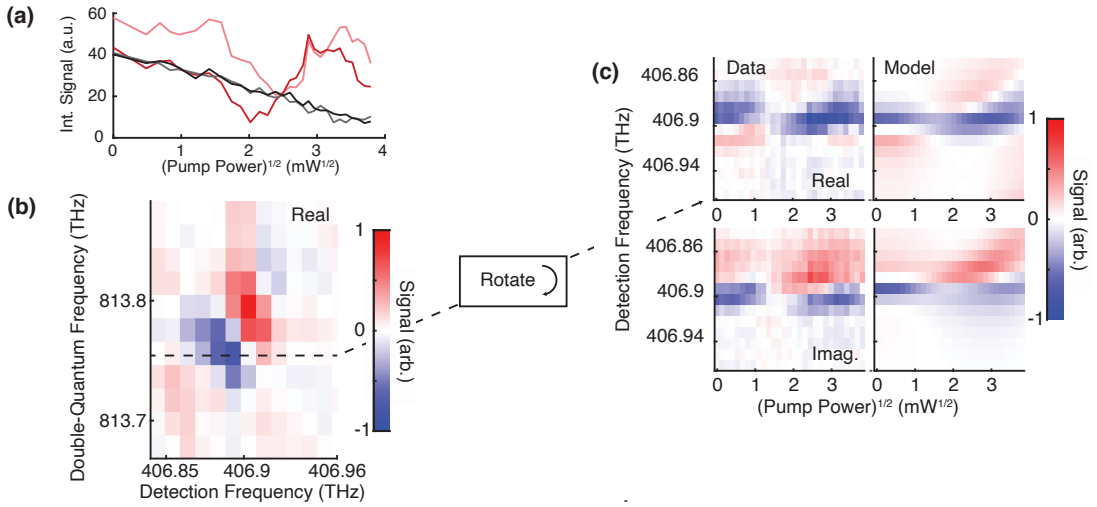

Figure 4.7: (a) The peak oscillations of the four DQ2D peaks we are considering, still color coded according to figure 4.6 but scaled to the square root of the the pre-pulse power. (b) The real part of the upper on-diagonal peak. We take slices of this peak and fit them in (c).

data, as can be seen in the comparison in figure 4.7 (c). We reproduce both the phase oscillation and the amplitude oscillation as a function of pre-pulse power, even though the underlying picture is likely to be complicated by the fact that the ensemble contains three- and four- center complexes contributing to the overall DQ2D signal as well.

We perform two checks on the fit to show that our model captures the important physics well. First, the estimate for $\Delta_{s,0} = 6$ GHz agrees well with the static 4-40 GHz interaction peak shifts induced calculated by the lineshape simulation. Second, we can recover the pi-pulse power required to Rabi-flop just one center from this fit which we can compare to the value calculated using the dipole moment known from literature [13].

Before comparing our fit π-pulse power, $P_{\pi,exp}$, to the theoretical π-pulse power, $P_{\pi,thy}$, we must take care of two details. When accounting for the spatial variation of our Rabi oscillations due to the fact that the pre-pulse and FWM beams have roughly the same spotsize, we must apply a slight correction factor to our dipole moment $\mu_r = \mu\sqrt{(2)}b$ where b = 0.81, and the factor of $\sqrt{2}$ comes from the relative

45° orientation of the in-plane dipoles to the electric field (accounting for the dot product in the calculation of the Rabi frequency). The correction factor b is derived in detail in Appendix B.

We can now compare our fit to the literature-derived π-pulse power. We calculate the peak power required to Rabi-flop a single center into the excited state, given a Gaussian electric field of waist w_0, using our corrected value μ_r. Because the details of the calculation matter, we will step through this basic but crucial derivation below. We start with the electric field of a Gaussian spot

$$E(r,\theta) = E_0 \; e^{\frac{-r^2}{w_0^2}}. \tag{4.26}$$

Furthermore, assuming a Gaussian time-domain pulse profile, we get that the field of a pi-pulse is

$$E_\pi = \frac{\hbar\pi}{\sqrt{2\pi}\mu_r\sigma} \tag{4.27}$$

We take $\sigma = 87$ fs for our measured pulse width, extracted from an auto-correlation of the FWM pulses. We then have that

$$P_{\pi,thy,peak} = \int_0^\infty \int_0^{2\pi} r \; d\theta \; dr \frac{c\epsilon(E_\pi)^2}{2} e^{\frac{-2r^2}{w_0}} \tag{4.28}$$

and thus

$$P_{\pi,thy,peak} = \frac{\pi^2 c\epsilon\hbar^2 w_0^2}{8\mu_r^2\sigma^2}. \tag{4.29}$$

When evaluated, we find that $P_{\pi,thy,peak} = 711$ W which, accounting for a pulse FWHM duration of 200 fs, and a repetition of 75.5 MHz yields $P_{\pi,thy} = 11.4$ mW. One final detail is that, to calculate $P_{\pi,exp}$, we take the fit value and correct it for the index of refraction difference between vacuum and the diamond lattice, and the same 45° angle between the dipole moment and the effective field inside the diamond such that $P_{\pi,exp} = (0.5667/\sqrt{2})P_{\pi,fit} = 9.6$ mW. This is in good agreement with $P_{\pi,thy}$,

showing that our model is a resaonable qualitative explanation of the phenomena giving rise to both the DQ2D signal and the coherent oscillations we observe.

4.4 Conclusion

This chapter summarizes the results obtained through investigating the SiV ensemble using DQ2D spectroscopy. We have shown that the color centers interact in an excitation-dependent way, giving rise to the DQ2D spectrum. We further show that dipole-dipole coupling betwen centers is likely, and that these interactions can explain the we observe in other measurements. Finally, we demonstrate that the interactions can be controlled by varying the initial state of the SiV ensemble. Though MDCS is a largely semi-classical technique, and we certainly do not claim to directly observe quantum entanglement between centers, if we are correct about the mechanism by which color centers couple together, long-range entanglement mediated by the dipole-dipole coupling *is* occurring when we interact with the ensemble optically.

This result has a number of implications. Primarily, because color centers can be deterministically placed [22], one might imagine instantiating an array of a discrete number of color centers that are within 10-100 nm of each other, which automatically entangle. This could potentially be an easy way to entangle qubits; a necessity for quantum memory [32], sensing [23], or quantum telecommunications and cryptography applications [33].

Furthermore, these arrays of color centers could provide an alternative to devices currently relying on trapped ions [10] or complex photonic manufacture [15, 34] to generate arrays of entangleable qubits. One could use the tunability of inter-center interactions to implement a new quantum computing scheme with deterministic 'interaction' phases when all of the SiV qubits are allowed to couple and exchange information, much like what is currently done with superconducting qubits [9]. Also, because the single-center linewidth is often not lifetime limited, yet the

Bell $|\Phi\rangle = (2^{-1/2})(|\phi_4\rangle + |\phi_1\rangle)$ may have an enhanced coherence time $> T_2 = 120$ ps already measured in this sample because we observe coherent oscillations even after a waiting time of 1 ns in this system.

Finally, studying excitation-dependent interactions is incredibly useful from a basic physics point of view. SiVs could potentially be model systems in which to generate and manipulate many-body states using an ensemble of SiV centers. When placed close to a surface and queried with an optical technique possessing high spatial resolution, for instance DQ2D combined with the tip of an atomic force microscope, ensembles of small numbers of SiV centers in close proximity could be used to understand how few-body wavefunctions hybridize to become many-body, extended states, a fundamental question in condensed matter physics [35].

References

(1) Ladd, T. D.; Jelezko, F.; Laflamme, R.; Nakamura, Y.; Monroe, C.; O'Brien, J. L. *Nature* **2010**, *464*, 45–53.

(2) Horodecki, R.; Horodecki, P.; Horodecki, M.; Horodecki, K. *Reviews of Modern Physics* **2009**, *81*, 865–942.

(3) Sakurai, J. J.; Napolitano, J. **2017**, DOI: 10.1017/9781108499996.

(4) Lukin, M. D.; Hemmer, P. R. *Phys. Rev. Lett.* **2000**, *84*, 2818–2821.

(5) Abramavicius, D.; Palmieri, B.; Voronine, D. V.; Šanda, F.; Mukamel, S. *Chemical Reviews* **2009**, *109*, 2350–2408.

(6) Boyd Robert W., 1., *Nonlinear optics*; Academic Press: Boston :; Boston : 1992.

(7) Mukamel, S., *Principles of nonlinear optical spectroscopy*; Oxford series in optical and imaging sciences; Oxford University Press: New York, 1995.

(8) BELL, J. S. *Physics* **1964**, *1*, 195–200.

(9) Krantz, P.; Kjaergaard, M.; Yan, F.; Orlando, T. P.; Gustavsson, S.; Oliver, W. D. *Applied Physics Reviews* **2019**, *6*, DOI: 10.1063/1.5089550.

(10) Bruzewicz, C. D.; Chiaverini, J.; McConnell, R.; Sage, J. M. *Applied Physics Reviews* **2019**, *6*, DOI: 10.1063/1.5088164.

(11) Zhang, G.; Cheng, Y.; Chou, J. P.; Gali, A. *Applied Physics Reviews* **2020**, *7*, DOI: 10.1063/5.0006075.

(12) Pingault, B.; Jarausch, D. D.; Hepp, C.; Klintberg, L.; Becker, J. N.; Markham, M.; Becher, C.; Atatüre, M. *Nature Communications* **2017**, *8*, DOI: 10.1038/ncomms15579.

(13) Becker, J. N.; Becher, C. *Physica Status Solidi (A) Applications and Materials Science* **2017**, *214*, 1–11.

(14) Becker, J. N.; Pingault, B.; Groß, D.; Gündo ğan, M.; Kukharchyk, N.; Markham, M.; Edmonds, A.; Atatüre, M.; Bushev, P.; Becher, C. *Phys. Rev. Lett.* **2018**, *120*, 053603.

(15) Evans, R. E.; Bhaskar, M. K.; Sukachev, D. D.; Nguyen, C. T.; Sipahigil, A.; Burek, M. J.; Machielse, B.; Zhang, G. H.; Zibrov, A. S.; Bielejec, E.; Park, H.; Lončar, M.; Lukin, M. D. *Science* **2018**, *362*, 662–665.

(16) Sipahigil, A. et al. *Science* **2016**, *354*, 847–850.

(17) Hudson, E. R.; Campbell, W. C. *Phys. Rev. A* **2018**, *98*, 040302.

(18) Laurat, J.; Choi, K. S.; Deng, H.; Chou, C. W.; Kimble, H. J. *Phys. Rev. Lett.* **2007**, *99*, 7–10.

(19) Bernien, H.; Hensen, B.; Pfaff, W.; Koolstra, G.; Blok, M. S.; Robledo, L.; Taminiau, T. H.; Markham, M.; Twitchen, D. J.; Childress, L.; Hanson, R. *Nature* **2013**, *497*, 86–90.

(20) Kim, J.; Mukamel, S.; Scholes, G. D. *Accounts of chemical research* **2009**, *42*, 1375–1384.

(21) Campbell, W. C.; Hudson, E. R. *Phys. Rev. Lett.* **2020**, *125*, 120501.

(22) Schröder, T.; Trusheim, M. E.; Walsh, M.; Li, L.; Zheng, J.; Schukraft, M.; Sipahigil, A.; Evans, R. E.; Sukachev, D. D.; Nguyen, C. T.; Pacheco, J. L.; Camacho, R. M.; Bielejec, E. S.; Lukin, M. D.; Englund, D. *Nature Communications* **2017**, *8*, 1–7.

(23) Degen, C. L.; Reinhard, F.; Cappellaro, P. *Rev. Mod. Phys.* **2017**, *89*, 1–39.

(24) Bates, K. M.; Day, M. W.; Smallwood, C. L.; Owen, R. C.; Ulbricht, R.; Schröder, T.; Bielejec, E.; Cundiff, S. T. **2021**.

(25) Hepp, C.; Müller, T.; Waselowski, V.; Becker, J. N.; Pingault, B.; Sternschulte, H.; Steinmüller-Nethl, D.; Gali, A.; Maze, J. R.; Atatüre, M.; Becher, C. *Phys. Rev. Lett.* **2014**, *112*, DOI: 10.1103/PhysRevLett.112.036405.

(26) Smallwood, C.; Autry, T.; Cundiff, S. *Journal of the Optical Society of America B* **2016**, *34*, DOI: 10.1364/JOSAB.34.000419.

(27) Gali, A.; Maze, J. R. *Phys. Rev. B* **2013**, *88*, 235205.

(28) Nardin, G.; Moody, G.; Singh, R.; Autry, T. M.; Li, H.; Morier-Genoud, F.; Cundiff, S. T. *Phys. Rev. Lett.* **2014**, *112*, 046402.

(29) Lomsadze, B.; Cundiff, S. T. *Phys. Rev. Lett.* **2018**, *120*, 233401.

(30) Stone, K. W.; Gundogdu, K.; Turner, D. B.; Li, X.; Cundiff, S. T.; Nelson, K. a. *Science* **2009**, *324*, 1169–1174.

(31) Smallwood, C. L.; Ulbricht, R.; Day, M. W.; Schröder, T.; Bates, K. M.; Autry, T. M.; Diederich, G.; Bielejec, E.; Siemens, M. E.; Cundiff, S. T. *Phys. Rev. Lett.* **2021**, *126*, 213601.

(32) Bradac, C.; Gao, W.; Forneris, J.; Trusheim, M. E.; Aharonovich, I. *Nature Communications* **2019**, *10*, 5625.

(33) Pirandola, S. et al. *arXiv* **2019**, 1–118.

(34) Wan, N. H.; Lu, T. J.; Chen, K. C.; Walsh, M. P.; Trusheim, M. E.; De Santis, L.; Bersin, E. A.; Harris, I. B.; Mouradian, S. L.; Christen, I. R.; Bielejec, E. S.; Englund, D. *Nature* **2020**, *583*, 226–231.

(35) Schlosser, F.; Knorr, A.; Mukamel, S.; Richter, M. *New Journal of Physics* **2013**, DOI: 10.1088/1367-2630/15/2/025004.

CHAPTER V

An Introduction to Frequency Comb Physics

5.1 Background

Optical frequency combs are repetitive time domain electric field wave-forms such that, in the frequency domain, their spectra consist of a dense forest of discrete optical frequencies (or teeth) separated by a characteristic frequency corresponding to the periodicity of the output electric field, resembling a comb one would use to maintain their hair. The term 'optical frequency comb' was first coined to refer to the spectra which fit this description but has since expanded to refer to the lasers outputting combs. Figure 5.1 depicts the traditional realization of a frequency comb: a train of ultrashort (duration <1ps) pulses of light output by a femtosecond modelocked laser. The spectrum of a frequency comb is defined by just two frequencies: the repetition rate ($f_{rep} = 1/T_{rep}$) of the laser's output waveform and a carrier-envelope offset frequency (f_{ceo}) that is set by the dispersion of the laser cavity. Strictly speaking, the frequency of the n-th tooth output by a frequency comb can be expressed as

$$f_n = n\ f_{rep} + f_{ceo}. \tag{5.1}$$

This relationship will be elaborated upon later. However, for this relationship to be true of a laser, the electric fields of each of its output modes must be 'coherent' with

one another, meaning there is a fixed phase relationship between each electric field mode. The concept of coherence between a comb's output frequencies is simple, but it underlies nearly every use of optical combs because f_{rep} and f_{ceo} are typically in the radio-frequency (RF) domain of the electromagnetic spectrum. Frequency combs can therefore be used to connect optical frequencies to RF measurement, control, and characterization techniques. Because the RF and optical domains of the electromagnetic spectrum are roughly six orders of magnitude apart in frequency, this task was previously nearly impossible, requiring a plethora of linked oscillators and a bevy of stabilization electronics to accomplish [1–3].

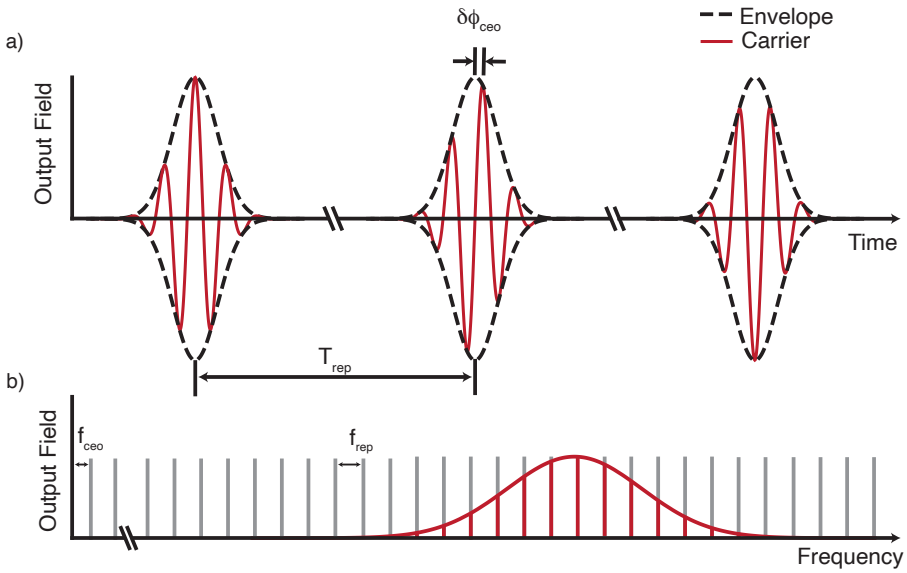

Figure 5.1: (a) The time-domain output of a femtosecond laser showing three successive optical pulses separated by T_{rep} with a pulse-to-pulse carrier-envelope phase slip $\delta\phi_{ceo}$. (b) The frequency-domain spectrum of a frequency comb, showing a number of 'teeth' in spaced by the repetition rate of the laser's waveform, and offset from zero frequency by the offset frequency.

The development of the optical frequency comb represented a paradigm shift for spectroscopists investigating the interactions between light and matter [1]. This is due to the fact that RF frequencies are relatively easy to measure with great precision, while directly characterizing an optical frequency yields at best a precision of one part in a million. By connecting the RF and optical domains of the electromag-

netic spectrum, using a frequency comb to reference optical spectra to the standard definition of the second became possible [1, 4]. Since atomic clocks with precision of one part in 10^{18} to a few parts in 10^{19} [5] are now the state of the art, it would be relatively straightforward to apply this level of precision to optical measurements through the use of a frequency comb.

Subsequent to the first realizations of frequency combs, techniques to self-reference and stabilize their output led to an explosion of their use in precision optical frequency synthesis and measurement [6, 7], the birth of direct precision comb spectroscopy [8, 9], and the invention of the optical atomic clock [10]. Roughly a decade after combs first arrived on the scene, interest in frequency comb spectroscopy has been reignited by the realization that multiple combs can be used to acquire optical spectra with a combination of resolution and acquisition speed currently setting the gold standard in spectroscopy[11, 12]. These techniques use two or more frequency combs to interact with a sample of interest, after which the spectroscopic information is encoded in the amplitude of individual teeth from each comb. This information will then be transformed into the RF domain through the surjective mapping of beatnotes between pairs (or triplets) of comb teeth [11, 13] into individual RF comb teeth.

Multi-comb spectroscopic techniques, in particular dual-comb spectroscopy (DCS), are an attractive alternative to many time-domain spectroscopies because they require far fewer moving parts and no dispersive elements, and thus the actual spectroscopy measurement apparatus can be simplified to just two combs and a fast photodiode [11]. This dramatic simplification of DCS spectroscopy relative to other spectroscopic techniques has opened a new frontier in technique development. The quixotic goal pursued by a vast array of researchers is the development of miniature, portable comb-based spectrometers. Such an advancement would allow for real-time monitoring of atmospheric gas concentrations [12] greenhouse gas emissions, or trace toxic gas detection. Figure 5.2 depicts a possible realization of this scheme. Developing

comb-based real-time precision atmospheric gas assay technologies would represent a disruptive advance in our ability to quantify and thus control gaseous emissions at sites of interest. No other sensing technology exists with the combination of sensing precision and acquisition speed provided by DCS.

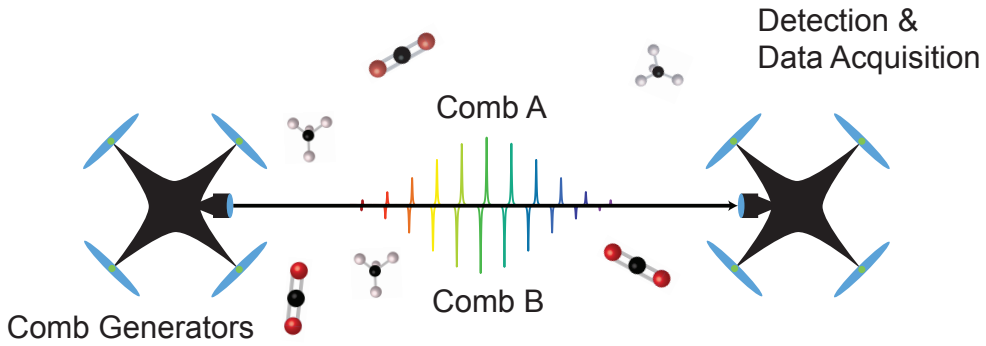

Figure 5.2: A possible realization of real-time atmospheric gas monitoring using two drones. The drone on the left contains two frequency combs which are beamed through open air to the drone on the right. Gasses in the middle impart absorption features onto the comb spectra which are then measured in the RF dual-comb spectrum seen by the drone on the right. The extent to which light is absorbed between drones thus can be mapped to the local concentration of a trace gas.

The bottleneck stunting the growth of such technologies is the current size of the most common frequency comb light sources. Combs today are typically table-based oscillators that consume the same quantity of energy as several running refrigerators and are far too bulky to provide the platform for the next generation of miniaturized dual-comb spectrometers. To be truly portable, a frequency comb must meet five criteria: (1) its output must be coherent, it must be (2) compact, (3) battery operable, (4) tunable, and have (5) demonstrated use in dual-comb spectroscopy measurements.

Frequency combs using microscopic rings of silicon or fused silica, pumped by high-powered lasers into the comb output regime, are the most well-studied alternative to table-based combs. Micro-ring resonator combs rely on driving the resonators so hard with light that nonlinear Kerr effect produces a periodic output electric field, and thus a frequency comb. While these light sources are well-characterized, and have been used in demonstrations of DCS [14], their pump lasers are often bulky and power

hungry, and their spectra are difficult to tune, posing a problem for true portability.

It is therefore a very attractive solution to generate the frequency comb directly in the laser diode. Several diode frequency comb (DFC) technologies exist. Commonly, quantum dots [15] or quantum dashes [16] are used as the gain medium, but quantum well DFCs offer the advantage of larger gain coefficients and thus more flexible operating parameters. In this half of my thesis, we present our work characterizing the output spectra of a truly portable semiconductor quantum well-based DFC. We show data that demonstrates DFCs fulfill all requirements for true portability, and a first-of-its kind DCS measurement of a HCN gas calibration cell, clearly illustrating the fact that DFCs can be used to acquire rapid spectra of gasses. The sum total of this work is to show that DFCs are capable of providing a platform to launch ubiquitous, miniature, rapid, and precision gas spectrometers into a new era.

The above background serves as sufficient introduction to the lay reader for understanding the context of the results presented in this thesis. The rest of the chapter is going to dive into the basics of frequency comb physics to discuss how frequency combs are typically generated with in-phase modelocking, and how they are generated in semiconductor lasers with frequency-modulated (FM) modelocking. In the chapters that follow, characterizing the electric field of our DFC sources will be discussed. They are coherent combs that show the 'smoking gun' signatures of being frequency-modulated modelocked combs as expected. Following this, the demonstration of dual comb spectroscopy with diode frequency combs will show that DFCs are practical miniaturized comb sources ready for wide deployment to diverse applications. Finally, a detailed theoretical discussion of the meaning of coherence between field lines within a frequency comb and the implications thereof for experiments will be shown.

5.2 The Basics of Comb Physics

This introduction is not meant to cover *all* details of comb generation, but we will enumerate the basic requirements for a frequency comb in very broad terms, and will spend some time in subsequent subsections discussing the details of modelocking in various different types of frequency combs. We begin with a sketch covering the basics of laser operation. The treatment of laser physics in this thesis loosely follows that of Andrew Weiner's Ultrafast Optics text [17] and that of Pedrotti, Pedrotti, and Pedrotti [18] adapted for our needs here.

First, a definition: a laser is simply a device in which a gain medium (a material capable of emitting photons through stimulated emission when appropriately excited) is placed within a cavity (two or more mirrors arranged such that light is confined to circulate between them) and pumped into a population inversion such that light amplification by stimulated emission can occur. Light Amplification by the Stimulation of Emission (LASEing) occurs when a photon (either spontaneously emitted, or seeded into the cavity) stimulates the emission of a deluge of photons from the population of electrons excited into a higher lying, 'lasing' state of the gain medium.

A frequency comb is a (1) cavity confining a (2) gain medium which supports multiple lasing modes (a wide gain bandwidth) and a (3) mechanism to enforce a phase relationship between these modes. We will devote time to discussing the necessity of each of these three requirements in turn and demonstrate how one cannot get a true frequency comb without modelocking to ensure the mutual coherence between electric field modes.

5.2.1 Laser Cavities

For most practical laser applications, there is a laser cavity configuration which will be tailor-able to suit [17]. Because this thesis centers on my work characterizing diode-based frequency combs, we will confine ourselves to discussing perhaps the

most ubiquitous laser cavity design: the Fabry-Pérot cavity. This cavity consists of two highly reflective mirrors aligned parallel to one another such that light circulates between them. Figure 5.3 is a basic depiction of such a laser cavity. A typical laser cavity will have an end mirror with a very high reflectivity, typically recirculating in excess of 99% of the field, with an output coupler to extract the light from the cavity with a typical reflectivity of about 95%. Diode lasers are nearly always co-planar Fabry-Pérot cavities due to their small size relative to the output beam and the relative ease of creating parallel surfaces during the cleaving process.

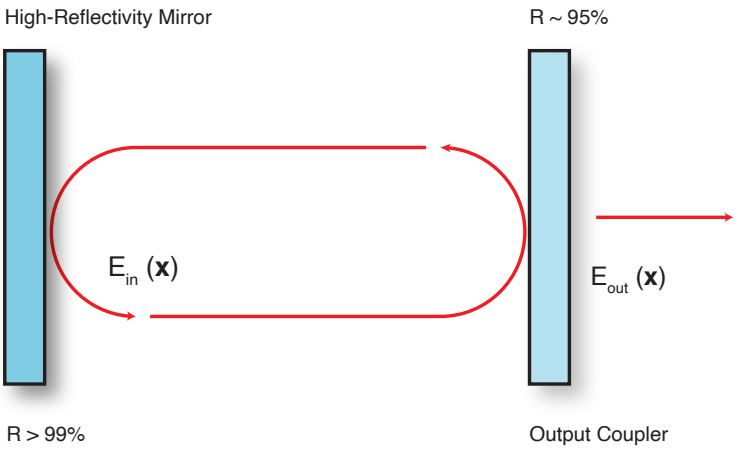

Figure 5.3: A basic Fabry-Pérot cavity confining an electric field circulating within. A typical cavity for a laser has a 'high-reflectively' mirror and an 'output coupler' as the main cavity mirrors.

To confine an electric field wave within the cavity, the net phase accumulation by the field over one round trip in the cavity must be zero. The length of the cavity is therefore an integer multiple of half the allowed field wavelengths:

$$\lambda = \frac{2L}{m}. \tag{5.2}$$

The spacing, in frequency, between allowed modes is thus

$$\Delta f = \frac{c}{2L}. \tag{5.3}$$

This quantity is known as the free-spectral range, and sets the repetition frequency of an optical frequency comb.

5.2.2 Wide Gain Bandwidth Media

Now that we have a cavity to confine light, we must have a gain medium in which to amplify the photons we place in the cavity. A gain medium is simply a collection of ions, crystalline defects, an active section of a semiconductor, or a gas of atoms in which a population inversion (a larger number of electrons in an excited state than in the ground state) can be supported. There are many ways of pumping electrons into the higher-lying states in materials, but the important aspect of the so-called 'lasing' states in gain media is that they have long electron lifetimes such that light amplification can occur in the medium when a resonant photon stimulates emission from the lasing state.

To see this, we will consider a concrete example. Suppose we have a three-level system acting as our gain medium, as depicted in Figure 5.4. In this material, we have electron decay times τ_{23} describing the decay of electrons from state $|2\rangle$ to state $|3\rangle$, and τ_{31} describing the decay of electrons from state $|3\rangle$ to state $|1\rangle$. For the lasing process to occur, we want our electrons to be 'stuck' in state $|3\rangle$. For this to happen, we need $\tau_{31} > \tau_{23}$.

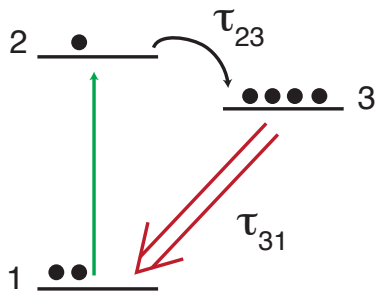

Figure 5.4: A depiction of a three-level system for use as a laser gain medium with the pump transition shown in green and the lasing transition shown in red. The circles represent electrons. A population inversion has been built up in state 3.

Now, supposing we have N atoms, pump rate P (atoms/sec) and stimulated emission rate R (photons/sec) in our laser, we can write down rate equations describing the operation of the laser. We need that $N_1 + N_2 + N_3 = N$ (where N is the total number of electrons), and thus

$$\dot{N_1} = -P(N_1 - N_2) + N_3/\tau_{31} + R(N_3 - N_1) \tag{5.4}$$

$$\dot{N_2} = P(N_2 - N_1) - N_2/\tau_{23} \tag{5.5}$$

$$\dot{N_3} = -R(N_3 - N_1) - N_3/\tau_{31} + N_2/\tau_{23}. \tag{5.6}$$

Now, the *small signal gain* provided by stimulated emission the gain medium for either a spontaneously emitted photon, or a seed photon, is proportional to the population inversion, and is

$$g_s = \sigma_{em}(N_3 - N_1)L_{gain} \tag{5.7}$$

where σ_{em} is the emission cross section for an electron in state 3 and L_{gain} is the length of the gain medium. As the pump rate P is increased, either by changing the intensity of a laser pumping transition $|1\rangle \rightarrow |2\rangle$ or in the case of a diode laser by increasing the injection current, the gain available will saturate above a value known as the threshold gain, and the output power of our laser will increase linearly with pump power. The solution to equations 5.4-5.6 under steady-state operation are plotted in Figure 5.5 with the assumption that $\tau_{23} = \tau_{31}/100$. Though the saturation dynamics of this particular system and other such details are outside of the scope of this introduction, what should be clear is that in order to maintain a population inversion, one requires a gain medium with at least one meta-stable state into which electrons are allowed to decay.

What is critical in the case of a frequency comb is the *gain bandwidth* of this gain medium as compared to the free spectral range of the laser cavity, because by

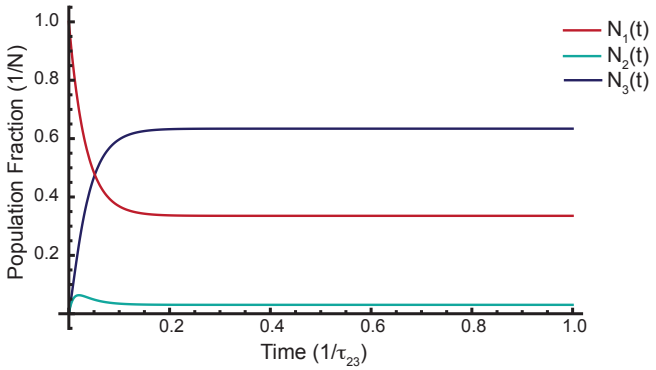

Figure 5.5: The solutions to the rate equations for a three-level system under steady-state operation plotted as a fraction of total number of electrons. Population inversion for state $|3\rangle$ over state $|1\rangle$ is achieved after startup if the decay time for electrons pumped into state $|2\rangle$ is rapid as compared to the lifetime of state $|3\rangle$.

definition a frequency comb must support multiple lasing modes. Suppose we have the three-level system as depicted in Figure 5.4. In frequency space, the gain available to modes within the laser is

$$g_s(\omega) = \sigma_{em}(\omega)(N_3 - N_1)L_{gain} \tag{5.8}$$

where $\sigma_{em}(\omega)$ is the frequency-dependent emission cross-section of our gain medium.

Each gain medium will have a specific spectrum of frequencies for which the emission cross-section is nonzero, and a specific saturation power. In our system, let's assume that $\tau_{23} << \tau_{31}$ such that when analyzing the emission dynamics of the system, we can assume that it's effectively a two-level system. We can therefore conduct a simple derivation using Fermi's Golden rule (FGR) (see for instance ref. [19]) to see two ways wide-bandwidth gain can arise within a gain medium.

By definition, the emission cross-section is

$$\sigma_{em} = \frac{\text{Energy/time emitted by an atom}}{\text{Energy flux of the radiation field}}. \tag{5.9}$$

We can write the transition rate for an atom in state $|3\rangle$ to state $|1\rangle$ by spontaneously emitting a photon in the presence of radiation using

$$\Gamma^{(t)}(\omega)_{3\to 1} = \frac{2\pi}{\hbar} |\langle 2| V_{31} |1\rangle|^2 \rho(E) \tag{5.10}$$

where $\rho(E)$ is taken to mean the transition energy density of states within some interval E to $E + dE$ such that

$$\int_0^\infty \mathrm{dE}\ \rho(E) = 1. \tag{5.11}$$

Combining these two facts, we can write

$$\sigma_{em}(\omega) = \frac{2\hbar\omega\pi |E_0\mu_{31}|^2 \rho(E)}{\hbar c\ U_{field}} \tag{5.12}$$

where U_{field} is the energy density of the transverse electromagnetic field in the cavity with amplitude E_0 and $\mu_{31} = \langle 3| e\mathbf{r} |1\rangle$ is the transition dipole moment between states 3 and 1 and c is the vacuum speed of light. Since

$$U_{field} = \frac{1}{2}\epsilon_0 |E_0|^2 = \frac{\pi e^2 |E_0|^2}{2\alpha\hbar c} \tag{5.13}$$

with e being the elementary electron charge and α the fine structure constant, we can rewrite equation 5.12

$$\sigma_{em}(\omega) = \frac{4\alpha\omega\hbar}{e^2} |\mu_{31}|^2 \rho(E). \tag{5.14}$$

As promised, there are two ways in the above expression for a broad gain spectrum to arise. The first is if the transition from state $|3\rangle$ to $|1\rangle$ is a *homogeneously broadened* transition where all electrons in state $|3\rangle$ emit photons at the same central frequency during their transition, but the lifetime of the transition is incredibly short. Typically, $\rho(E) = \delta(E_3 - E_1 - \hbar\omega)$ is used for calculating a transition rate when the transition

lifetime is extremely short relative to the dynamics under study. Since this is not the case in a laser, we recall that $\delta(E_3 - E_1 - \hbar\omega)$ can be rewritten as

$$\delta(E_3 - E_1 - \hbar\omega) = \lim_{\gamma \to 0} \frac{\hbar\gamma}{2\pi((\omega - \omega_{31}) + (\gamma/2)^2)} \tag{5.15}$$

where $\gamma = 1/\tau_{31}$ is the transition lifetime and $\omega_{31} = (E_3 - E_1)/\hbar$. This finite transition rate will then broaden the avialiable gain spectrum such that we have

$$g_s(\omega) = \frac{2\alpha\omega\hbar^2|\mu_{31}|^2}{\pi e^2} \frac{\gamma}{(\omega - \omega_{31}) + (\gamma/2)^2} \; (N_3 - N_1) \; L_{gain}. \tag{5.16}$$

Multi-mode lasers employing only homogeneously broadened gain media are not common because the whole gain spectrum saturates at once, leading to gain competition amongst cavity modes, and single-mode lasing.

The other way in which a broad gain spectrum can be supported within the medium is if different electrons in state $|3\rangle$ (or $|1\rangle$) experience different local environments within the medium and thus the transitions from state $|3\rangle$ to $|1\rangle$ have some finite frequency-space distribution depending on the local potential to which each electron is subjected. In this case, the lasing transition is said to be *inhomogeneously broadened* and $\rho(E)$ will reflect a broad distribution of possible energies for the excited state electrons. While the particulars of $\rho(E)$ are specific to each gain medium, we will take the approximation that the transition energies are normally distributed about a central frequency ω_{31} with a width σ such that

$$\rho(E) = \hbar\rho(\omega_{31}) = \frac{\hbar}{\sqrt{2\pi}\sigma} e^{-(\omega - \omega_{31})^2/(2\sigma^2)} \tag{5.17}$$

and therefore

$$g_s(\omega) = \frac{2\alpha\omega\hbar^2}{\pi e^2} \frac{e^{-(\omega - \omega_{31})^2/(2\sigma^2)}}{\sqrt{2\pi}\sigma} \; (N_3 - N_1) \; L_{gain}. \tag{5.18}$$

The intensity spectrum of the laser will be proportional to the frequency-domain

convolution between the cavity modes and the available gain spectrum

$$I(\omega) \propto g_s(\omega)T(\omega) \tag{5.19}$$

where $T(\omega)$ is the transfer function of the cavity so that we can write

$$I(\omega) = I_{sat}(\frac{g_s(\omega)}{g_{th}} - 1)T(\omega) \tag{5.20}$$

where I_{sat} is the saturation intensity of the gain medium at which the gain becomes clamped to a finite value g_{sat}. In the case of an inhomogeneously broadened gain medium with width σ

$$I(\omega) = I_{sat}\Big[\Big(\frac{2\alpha\omega\hbar^2|\mu_{31}|^2}{g_{th}\pi e^2}\frac{e^{-(\omega-\omega_{31})^2/(2\sigma^2)}}{\sqrt{2\pi}\sigma}\ (N_3 - N_1)\ L_{gain}\Big) - 1\Big]T(\omega), \tag{5.21}$$

where in the homogeneously broadened case we have

$$I(\omega) = I_{sat}\Big[\Big(\frac{2\alpha\omega\hbar^2|\mu_{31}|^2}{g_{th}\pi e^2}\frac{\gamma}{(\omega-\omega_{31}) + (\gamma/2)^2}\ (N_3 - N_1)\ L_{gain}\Big) - 1\Big]T(\omega). \tag{5.22}$$

5.2.3 A gain Medium within a Cavity

If we want our laser to actually achieve lasing, we must confine our gain medium within a cavity such that emitted photons from the gain medium are allowed to circulate within the cavity to stimulate the emission of ever more photons. In a cavity with mode spacing Δf_m and half-width, half-maximum linewidth Γ (given by the finesse of the cavity [18]), we will have that, for the m-th cavity mode

$$T_m(\omega) = \frac{\Gamma}{2\pi}\frac{1}{(\Gamma/2)^2 + (\omega - \omega_m)^2}. \tag{5.23}$$

Now, putting together our large-bandwidth gain medium with our cavity, we have for the inhomogeneous case

$$I(\omega) = I_{sat} \sum_m \left[\left(\frac{2\alpha\omega\hbar^2|\mu_{31}|^2}{g_{th}\pi e^2} \frac{e^{-(\omega-\omega_{31})^2/(2\sigma^2)}}{\sqrt{2\pi}\sigma} \left(N_3 - N_1\right) L_{gain} \right) - 1 \right] \times \frac{\Gamma}{2\pi} \frac{1}{(\Gamma/2)^2 + (\omega - \omega_m)^2}. \quad (5.24)$$

In the frequency domain, this corresponds to the spectra depicted in Figure 5.6.

Although the intensity spectrum of our laser looks comb-like, **a multi-mode, broadband laser is not necessarily a frequency comb**. The reasons for this will be discussed in great detail in the chapter discussing the coherence properties of a frequency comb. In order for a broadband laser to be a frequency comb, it must *modelocked* in that the adjacent fields for each of the cavity modes must have a fixed phase relationship between them. The two most prominent types of modelocking will be discussed presently, however a detailed discussion on the nature of coherence in a frequency comb will be discussed in its dedicated chapter, Chapter VII.

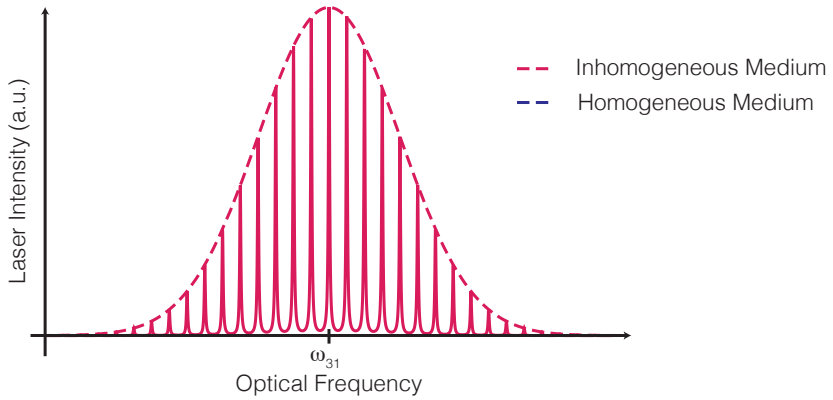

Figure 5.6: The output spectra of a multi-mode lasers with an inhomogeneously broadened medium. The dotted line represents the gain availability in either medium while the solid lines are the laser output modes.

One final remark must also be made at this point. In a real gain medium within a real laser cavity, the modes undergoing amplification will also experience dispersion

because, typically, the phase and group velocities for an electric field within a gain medium are different. The effects that this has on the overall spectrum of the laser will be discussed along with the details of modelocking our laser, but the point is that this dispersion will apply a finite frequency shift to the comb spectrum once modelocking has been achieved, determining f_{ceo} [1].

5.3 Frequency Combs Generated by In-Phase Modelocking

In the prior sections, we discussed the necessity for a broadband gain medium confined within a cavity to the generation of a frequency comb. However, the combination of these two things is not enough to make sure that our laser is a frequency comb. We assiduously avoided discussing the electric field output directly to avoid getting bogged down into distinctions between modelocking types and discussions of the precise nature of how one enforces a coherent relationship between each of the electric field modes. Now we will explicitly discuss the intra-cavity field; in addition, we will bring in the properties of real, noisy, dispersive cavities into the discussion where appropriate. For the sake of clarity, let's assume that we have a gain medium with a step-function net gain envelope centered around ω_{31} such that

$$A(\omega) = \begin{cases} 0 & \omega < -2 \text{ THz} \\ 1 & -2 \text{ THz} < \omega < 2\text{THz} \\ 0 & \omega > 2 \text{ THz} \end{cases} \tag{5.25}$$

where we use THz as an arbitrary reference unit for our frequency axis. In the time-domain, the electric field within our cavity will be

$$E_{cav}(t) = \sum_n A_n(t) e^{-i\omega_n t + \phi_n(t)} \tag{5.26}$$

where $\phi_n(t)$ is some stochastically varying, time-dependant phase, and $A_n(t)$ is the time-domain amplitude of the n-th mode, given by the inverse Fourier-transform of equation 5.25.

This is not necessarily the field of a frequency comb. If all of the $\phi_n(t)$ are unrelated for each mode, the laser will simply output a comb-like spectrum in the frequency domain without any time-domain coherence. To see this, we generate two different output fields with the exact same frequency-domain amplitude spectrum

$$E_{comb}(t) = \sum_n A(t) e^{-i\omega_n t + \phi_{n,comb}(t)} \tag{5.27}$$

and

$$E_{cav}(t) = \sum_n A(t) e^{-i\omega_n t + \phi_{n,noise}(t)}. \tag{5.28}$$

If we have that, in the frequency domain, all modes share the exact same phase (in-phase modelocking), then our time-domain spectrum will be that of a pulsed laser. If, instead all modes share no phase information, the output of the random field will just be noise in the time-domain, despite the fact that the frequency domain power spectra are the same. In our amplitude spectrum, we incorporate the effects of a slightly noisy laser cavity by allowing our admitted electric field modes to have a finite frequency-domain width, in this case corresponding to a stochastic repetition rate jitter of ± 1 GHz in the time domain with $\omega_{rep} = 500$ GHz to make numerical simulation convenient.

In one case, we 'lock' all phases together by forcing all modes to be in-phase with each other at a certain point in time (equivalent to $\phi_{n,comb}(\omega) = 0 \ \forall \ \omega$). In the other case, we do no such modelocking. Rather we set $\phi_{n,noise}(\omega) = 2\pi r$ with r a uniformly distributed random number within the interval $r \in [0, 1]$. In the in-phase modelocking case, we see that our time-domain laser output is a series of pulses separated by the repetition rate of the laser. In the randomly-phased case, we see that

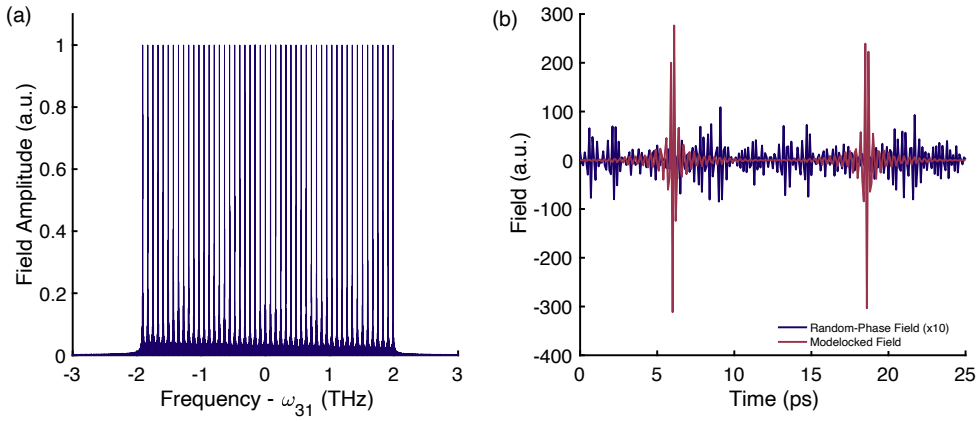

Figure 5.7: (a) The frequency-domain spectrum used in both cases. (b) The output fields of a modelocked and an un-modelocked, multi-mode light source. In the latter case, no pulse structure is observed, and the output field is essentially just noise.

the field is simply noise in the time domain. Figure 5.7 contains the results of this simple demonstration. In the noise case, there is no relationship between the modes emitted by the lightsource, thereby nullifying the usefulness of the un-modelocked multi-mode laser. We will elaborate on the cause and implications of this fact in our detailed discussion of mutual coherence between the comb teeth. However, it is plain that in the absence of phase locking between the modes, knowing all information possible about one particular mode in the cavity does not tell you anything about the other modes. Most frequency comb applications rely on the fact that one *does* have shared information between modes, which is the case when the different modes *do* share a phase relationship (in this case, they are forced to be in-phase).

We can now make an operationally strict definition of *mutual coherence* at this point. Though it is not exhaustive, and a more concrete mathematical description (and its implications) of mutual coherence will be discussed in great detail in Chapter VII, we can make the following statement. **A multi-mode laser is a frequency comb if and only if there is a fixed phase relationship its electric field modes.**

If a multi-mode light source meets this criterion, it can be described with the total

electric field

$$E_{comb}(t) = \sum_n A_n(t) e^{-i\omega_n t + \phi_n(t)}, \tag{5.29}$$

because the phases of each mode have a strict phase relationship between them; $\phi_n(t)$ will take the form

$$\phi_n(t) = \omega_{ceo} t + \Phi(t) \tag{5.30}$$

where $\Phi(t)$ is a phase noise term capturing the variations of the phase of each mode as a function of time. We've introduced the 'carrier-envelope offset frequency' ω_{ceo} to quantify the phase slip between the 'carrier' and the 'envelope' from pulse-to-pulse. The origin of this frequency shift is the difference between the phase and group velocities of all modes within the cavity, and its effect is to shift all cavity modes slightly in the frequency domain. Explicitly,

$$\omega_{ceo} = 2L\omega_c \Big(\frac{1}{v_g} - \frac{1}{v_p} \Big) \omega_{rep}, \tag{5.31}$$

or if the pulse-to-pulse phase shift is large, then we have

$$\omega_{ceo} = \mathrm{mod}\big(2L\omega_c (\frac{1}{v_g} - \frac{1}{v_p}) \omega_{rep}, \omega_{rep}\big). \tag{5.32}$$

where ω_c is the carrier frequency of the frequency comb (the geometric mean frequency of the comb) with $v_g = d\omega/dk$ and $v_p = \omega/k$ being the group and phase velocities respectively in a cavity of length L. Furthermore, because all of the modes share a strict phase relationship, there will be just two kinds of noise that can occur in the laser: noise shared mutually by all modes and noise in their relative spacing. This fact allows us to write

$$\Phi(t) = n\psi(t) + \phi(t) \tag{5.33}$$

where $\psi(t)$ parameterizes the noise present in the spacing between the modes, and

$\phi(t)$ quantifies the phase noise common to all modes. Now, if we let $\omega_n = n\omega_{rep}$, we can write

$$E_{comb}(t) = \sum_n A_n(t) e^{-i(n\omega_{rep}+\omega_{ceo})t + n\psi(t) + \phi(t)} \tag{5.34}$$

As we shall see, the particular form of $\Phi(t)$ yields an important consequence: in most applications, the noise in the comb spectrum can be measured and corrected, for example by correcting fluctuations in the length of the cavity or noise in the number of photons within the cavity. This yields the centrally useful fact: frequency combs can be used to noiselessly up- (and down-)convert radio frequencies (optical frequencies) into the optical (radio-frequency) domains. This dual-direction 'frequency conversion gear' underlies nearly all precision frequency and distance measurement, and is the major reason that the drive to miniaturize frequency comb technology for application outside the lab is so intense [2, 12].

How might one modelock a multi-mode laser? There are several methods by which this is done, typically segmented into two groups termed *active* or *passive* modelocking, depending on the degree to which some aspect of the laser cavity (for example reflectively, length, or loss) is modulated actively by the user. Passive modelocking refers to any method of locking the phases of the cavity modes together by passive elements of the cavity design to ensure it is more favorable to pulsed operation than to continuous wave operation. A text could be devoted to the various kinds of modelocking [17], but here we will discuss the most common case: that of the titanium sapphire oscillator. To modelock a titanium sapphire oscillator, one takes advantage of the nonlinear Kerr lensing effect in the gain medium. For real media, the index of refraction can be expanded perturbatively.

$$n = n_0 + n_2 I(t) + ... \tag{5.35}$$

where n_o is the zero-intensity index of refraction within a material, n_2 is termed

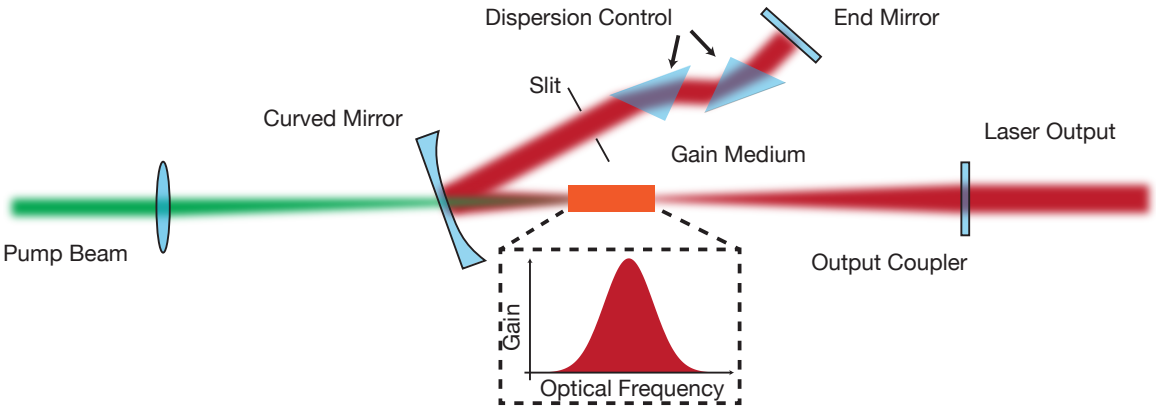

Figure 5.8: A depiction of a possible mode-locked laser cavity. The slit blocks part of the spatially larger continuous wave spatial mode, making pulsed lasing much more favorable.

the *nonlinear* refractive index, and $I(t)$ is the intensity of the field within the laser cavity. Clearly, as the intensity of the light within the cavity is increased, the index of refraction of the gain medium will increase if $n_2 > 0$. This phenomena will cause self-focusing of intense light within the cavity, and a self-steepening of the phase gradient of an electric field within the medium [20]. Given that pulses in a laser cavity are typically $10^2 - 10^4$ times more intense than the equivalent continuous-wave average power would suggest, one can take advantage of the fact pulses will be self-focused within the gain medium, with the result being that the spot-size of the pulsed modes circulating within the laser cavity will be smaller than that of the equivalent continuous-wave modes. A diagram of a possible modelocked cavity design is shown in Figure 5.8. Because the index of refraction $n_2(\omega)$ is typically frequency dependant, one must compensate carefully for the dispersion induced by the self-focusing and reflections off in-cavity mirrors by including a prism pair to ensure that all modes are still in phase with each other at the gain medium.

The master equation governing the formation of pulses within a laser cavity was described three decades ago by Hermann Haus and reproduced for our discussion below [21]. Suppose we have a time-varying electric field envelope $E(t)$ propagating

within our laser cavity. Our cavity will have a round-trip loss l due to imperfect reflections off of any mirrors or other dissipation that occurs in the cavity. Furthermore, our cavity will experience a round-trip gain

$$\Delta E(t + t_{rep}) = g(1 + \frac{1}{\Gamma_g^2}\frac{d^2}{dt^2})E(t) \tag{5.36}$$

where Γ_g is a parameter describing the curvatue of the gain spectrum, and g is the small-signal gain of the gain medium, equivalent to g_s above. The gain medium and all mirrors will introduce dispersion (the difference between phase and group velocities) into the propagation of all modes within the cavity, which is quantified by the parameter D and can be measured for most physical cavities. This has the effect of changing the phase of all modes within the pulse envelope each cavity round-trip such that

$$\Delta E(t + t_{rep}) = iD\frac{d^2}{dt^2}E(t). \tag{5.37}$$

Furthermore, the dispersion introduced by a saturable Kerr gain medium of length d that obeys Equation 5.35 will also introduce a phase modulation proportional to the intensity $I(t)$

$$\Delta E(t + t_{rep}) = (-i\frac{\omega_o n_2 d}{cA}I(t) + \gamma)|E(t)|^2 \tag{5.38}$$

where A is the mode cross-section, n_2 is the nonlinear index of refraction, γ describes the loss reduction as a result of saturating the gain medium, and ω_0 is the laser center frequency. Summing all of these effects together yields

$$\Big[g\big(1 + \frac{1}{\Gamma_g^2}\frac{d^2}{dt^2}E(t)\big) - l + iD\frac{d^2}{dt^2} + (\gamma - i\frac{\omega_o n_2 d}{cA}|E(t)|^2)\Big] = 0 \tag{5.39}$$

where we are implicitly assuming that the cavity is operating at steady state by setting the sum of these effects to zero. This equation admits short-pulsed solutions and was key to the discovery of the frequency comb, with a typical frequency comb

spectrum being

$$E(t) \propto \sum_n \mathrm{Exp}(-i\frac{(t-nT_{rep})^2}{2\sigma^2})(\mathrm{Exp}(-i\omega_0 t - \phi_{ceo}t) + c.c.) \tag{5.40}$$

with σ_n and ω_0 being the pulse duration (set by the convolution between the gain bandwidth and the cavity bandwidth) and carrier frequency (set by the central frequency admitted by the cavity) respectively.

In the case of the Titanium sapphire oscillator, the gain medium itself is responsible for locking all of the phases together through the balance between the cavity dispersion term (equation 5.37) and the action of the phase modulation provided by the Kerr effect, captured in equation 5.38. This balance is how a frequency comb is generated in an in-phase modelocked laser.

5.4 Frequency Combs Generated using Frequency-Modulated Modelocking

In-phase modelocking constitutes the most common form of frequency-comb generation. It was the original way in which experimentalists attempted to generate frequency combs from semiconductor laser diodes. However, the gain dynamics in semiconductor combs are not amenable to in-phase modelocking. Because of the high amount of gain available within a relatively short distance, in-phase modelocked semiconductor lasers often face a trade off between pump efficiency and pulse duration, which is a showstopper in the case that one wants a portable, efficient frequency comb. Thus, the community used semiconductor saturable absorbers abutted to the diode structure in an attempt to generate a practical in-phase modelocked comb [22]. While this approach is successful, it is still not the most efficient possible way in which to generate a frequency comb within a semiconducting diode laser because it does not take advantage of *all* the available gain bandwidth within the diode and

requires the added complication of manufacturing a sensitive multi-section device, something that is not desirable in field-based frequency comb applications. To make the most efficient use of all gain available in a semiconducting structure, one must rely on frequency-modulated modelocking to ensure that the in-cavity modes are out of phase[23–25].

To understand why this is, one must consider the interplay between the cavity and the gain medium in the case that the gain medium and the cavity are provided by the same structure, as in semiconductor laser diodes. Exhaustive prior work on this topic is discussed in Dr. Mark Dong's thesis [23], and in recent theory developments [23, 25, 26], but we will synthesize the main points of these results here to illustrate *why* frequency-modulated modelocking must be used to lock the phases together in a semiconductor frequency comb. The main point is that **in order to take advantage of all available gain within a diode structure, one must have the fields be out of phase with one another.** This fact is a result of a phenomenon known as spatial hole burning and is the method by which several lasing modes can be supported in a laser diode, described numerically in Reference [23] and analytically in Reference [25]. If your electric fields are out of phase with each other, the inter-mode phases will passively modelock to maintain steady-state operation [23]. To see how this may happen, we will sketch the basic physics of spatial hole burning in a diode laser and then discuss how this naturally leads to frequency-modulated modelocking between the multiple modes within the laser cavity.

A typical diode laser consists of an active layer incorporated into a p-n junction semiconductor diode. At the junction between the p- and n-doped substrates, one grows a gain structure which consists of a number of deep quantum wells within a very large, shallow confinement structure to confine the electric field within the active layer. Electrons are electrically injected into the structure, and fall down the energy level ladder depicted in Figure 5.9. Here we are not concerned here with

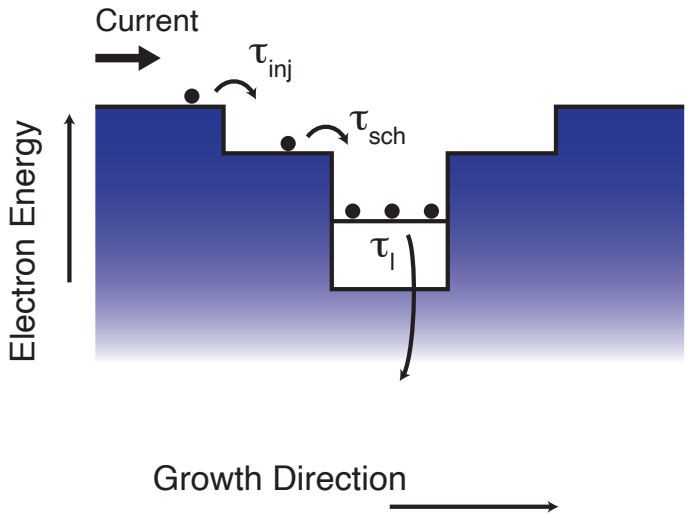

Figure 5.9: The electron-only view of the energy level scheme present in a semiconductor diode. Electrons are injected directly into the excited state by running a current through the diode structure. They fall into the spatial confinement heterostructure (SCH), then the quantum wells where they radiate their energy into the lasing mode before being drawn out of the structure.

a detailed discussion of the band structure of semiconductor materials, the nature of electrons confined within semiconductor quantum well potentials, or the physics of quantum confinement. The main point is that, in a semiconducting crystal, one can replace one of the atomic constituents with another possessing slightly different electronic properties [27]. Either injecting or removing electronic states relative to the unaltered structure through doping yields either a lower or higher bandgap (the energy difference between the lowest laying excited state and the highest laying valence state in a crystalline material). In this way, textbook cases of quantum confinement of electrons can be produced, allowing for sensitive engineering of diverse materials for an extremely wide array of applications [28]. Electrons injected into the diode laser are in the higher-lying conduction band initially when travelling into the device. By injecting electrons into a material with a slightly lower bandgap relative to the surrounding layers, one can force the electron to radiate energy to recombine into

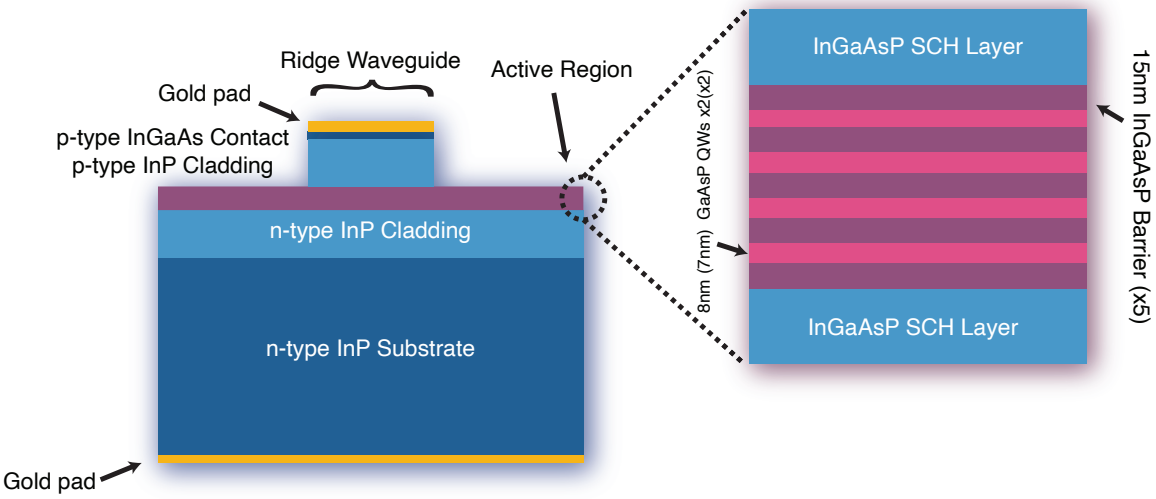

Figure 5.10: A depiction of the laser diodes characterized and used for spectroscopy in this thesis.

the valance band and be drawn out of the structure to maintain a continuous flow of current [28]. Thus, by injecting a large number of electrons into the quantum well gain structure, one will create a population inversion in the quantum well in steady state if $\tau_l >> \tau_{inj}$, with τ_{sch} depicted in Figure 5.9.

Lasing is induced when one reaches a threshold injection current, above which a population inversion is achieved and the number of spontaneously emitted photons is enough to induce a sustained avalanche of stimulated emission. It should be noted that the laser diode structure also forms the lasing cavity, because the index of refraction of the diode material is often considerably larger than that of air. Laser diodes are also constructed such that the index mismatch between the structure and air in the vertical and horizontal directions is such that the electric field mode is confined within the structure spatially. Such a construction is known as a *waveguide*, and will provide a spatial mode profile for the field confined within the cavity.

Suppose we have a diode laser as depicted in Figure 5.10 with x and y being the transverse coordinates and z being the direction of mode propagation. For the sake of argument, suppose that the laser is operating at a steady-state power in one mode,

such that the intracavity electric field $E(x, y, z, t)$ can be decomposed into a spatial mode shape $A(x, y, z)$ and an oscillatory part $E(z, t)$. $E(x, y, z, t)$ must be a solution to the paraxial wave equation within the diode, and thus separable. We write

$$\vec{E}(x, y, z) = A(x, y, z)E(z, t)\vec{\epsilon} \tag{5.41}$$

where $\vec{\epsilon}$ is the polarization of the laser field. Although the actual electric field dynamics will be a bit more complex, let's just examine a few modes in the cavity to illustrate how one may think about locking the phases of multiple cavity modes together. To satisfy the Fabry-Pérot condition, we must have that $E(z, t)$ can be decomposed into leftward and rightward travelling modes such that

$$E(z, t) = E_+(z, t) + E_-(z, t) = E_0[e^{(-ik_{m,z}z - i\omega_m t)} - e^{(ik_{m,z}z + i\omega_m t)}] \tag{5.42}$$

with $k_{z,x} = \frac{\pi m}{L}$ and $\omega = \frac{\pi mnc}{L}$ with m being the mode number and n being the index of refraction within the active structure of the laser diode. Let's briefly neglect cavity losses, which is a bad approximation in a laser diode, but we are interested only in sketching the intensity of the lasing field confined within the diode $I_x(x)$ which is

$$\begin{aligned} I_z(z, t) &= E^*(z, t)E(z, t) \\ &= 2|E_0|^2 \sin^2(k_z z + \omega_m t). \end{aligned} \tag{5.43}$$

If we look at a snapshot of the intensity profile in the z direction of some possible m-th mode and its adjacent modes in the diode we see that there are areas of overlapping intensity. If we have just the m-th mode of the laser emitting light at some time, its intensity profile will be a standing wave within the cavity. This means that it will grow in intensity until it uses all available gain at its intensity maxima. In other words, the power of mode m will grow until at each intensity maxima of the standing

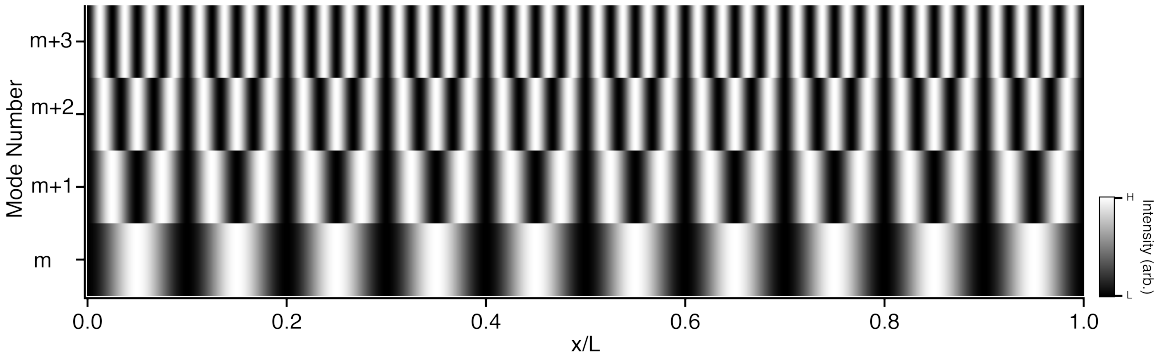

Figure 5.11: The intensity profile of several different standing wave modes in a laser cavity.

wave, single-frequency lasing depletes the population inversion of electrons. Figure 5.11 depicts this situation for several modes confined within the cavity. It should be noted that, if one wants many modes to emit light, summing many in-phase modes within the cavity is not ideal. The situation depicted above, in which a cavity mode depletes gain in a spatially dependant way is called *spatial hole burning*. In this case, gain competition between modes is maximized and the laser will not support multi-mode lasing without an external modelocking mechanism. For overlapping intensity maxima, the maximum gain possible for a number of lasing modes with the same maximum in the structure decreases in proportion to the number of modes which are attempting to lase, making comb formation impossible.

However, combs in semiconductor structures *do* form by simply powering on our semiconductor combs [29]. To lock the modes together of such a comb in the face of gain competition between modes, one can actually take advantage of the spatial hole burning to force the electric field modes be out of phase with each other as they propagate through the laser structure. This has been shown in a few contexts. By numerically simulating the carrier dynamics of the semiconductor laser structure, it can be shown that the spatial hole burning within a diode laser will actually act to reinforce comb generation in the case that the electrons within the laser diode are not able to diffuse very far [23]. My colleague on this project conducted extensive

simulation work to this effect, demonstrating that in the case of short average diffusion lengths for the electrons, gain competition between modes cannot wash out multi-mode lasing. This happens because if the electrons are slowed spatially, a more uniform gain profile is available across the entire diode. This actually makes multi-mode, modelocked lasing the most energetically favorable operation condition in such a laser.

Recgognizing this fact, there has been a recent push to demonstrate the development of frequency-modulated frequency combs in different parts of the electromagnetic spectrum. The physics of chaotic electron tunneling in quantum cascade lasers, whose operating regime is from the mid-infrared down to terahertz energy scales [30, 31], are particularly amenable to comb generation of this nature. In such a laser, electrons are injected into the structure and then tunnel between a descending cascade of quantum wells embedded in the structure, at each point giving off low-energy photons into the diode. Frequency-modulated modelocking of these combs ensues naturally because the electron tunneling timescales are long relative to the frequency of the laser operation such that single-mode lasing can be disfavorable. In other systems, like quantum dash and quantum dot lasers in which the gain medium confines electrons in either all three or two of three spatial dimensions, the same phenomena arises: electrons cannot diffuse quickly enough through the structure for one lasing mode to dominate the gain competition [15]. It was not until our work that single-section diode lasers in the telecommunications window of the optical spectrum were seen to produce frequency combs. Here, too the same phenomena arises: the electron diffusion length is much shorter than the lasing wavelength, and the resulting multi-mode output is a frequency-modulated (FM) frequency comb [29, 32].

Such FM combs were difficult to characterize fully until recent theoretical work (reference [25]) pulled all detailed effects on the electric field dynamics within a semiconductor laser together into one ‘master equation’ description analogous to the Haus

master equation. It was recently demonstrated that the key nonlinearity in semiconductor laser cavities that locks the phases of the different modes together is called *cross-steepening* where, when the electric field has a large disctontinuity (which can happen near a poorly reflecting mirror), the forward propagating field will experience different dispersion than the backward propagating field. This difference will act as a phase gradient, stabilized by nonlinear mixing between the forward and backward propagating electric field discontinuities in the cavity. Another way of looking at this is by stating that the *poorness* of the cavity (semiconductor cavities have typical mirror reflectivities of roughly 50%) combined with high in-cavity powers acts to reinforce nonlinear mixing between cavity modes such that the most stable operating conditions are when adjacent modes are *out of phase with each other*, and in fact the total electric field will follow a piece-wise parabolic phase gradient in the cavity as a result of this inter-mode mixing.

In this formalism, we can decompose the field within the cavity as $E(z,t) = K(z)F(z,t)$ where we let $K(z) := (P(z)/P_0)^{1/2}$ be the spatially varying gain envelope where P_0 is the average output power, and $P(z)$ is the spatially varying gain within the cavity. Then it can be shown that

$$\frac{\partial F(z,t)}{\partial T} = -\frac{\beta \partial^2 F(z,t)}{2\partial z^2} + \gamma |F(z,t)|^2 \tilde{\phi} F(z,t) - il(|F(z,t)|^2 - P_0)F(z,t) \qquad (5.44)$$

where γ is the phase cross-steepening, β is the group-velocity dispersion within the diode, $\tilde{\phi} = \langle arg(F(z,t))\rangle - arg(F(z,t))$ is a phase potential proportional to the four-wave mixing term acting to drive the fields of adjacent modes out of phase and l is the round-trip cavity loss.

It is more difficult to obtain an intuitive picture in this case. However we can make some inroads: much like in the Haus master equation the interplay between gain and dispersion must be balanced for stable operation. In this case, γ can be

understood to contain both the phase nonlinearity and the power gain. In fact, this term can be defined simply as

$$\gamma = i(\gamma_1 - \gamma_2)\frac{\Delta P}{4L_c P_0} \tag{5.45}$$

where γ_1 and γ_2 are the changes in phase as a function of unit distance for the forward and backward propogating waves respectively, L_c is the cavity length, assumed to be short enough such that ΔP represents the linear change in gain per round-trip assumed to be dominant, and P_0 is being average intracavity power. While the exact form of γ and the phase behavior of the four-wave mixing term outlined above depend on the dispersion and gain profile of each cavity, this representation captures the essential features: the increased gain for the total field in the laser depends on the phases of each individual mode being forced out of phase such that multi-mode lasing can be supported without being destroyed by spatial-hole burning.

The above master equation admits solutions of the form

$$F(z,t) = A_0 \mathrm{Exp}\Big[i\gamma\frac{|A_0|^2}{2\beta}\Big(z^2 - \frac{L_c^2\gamma|A_0|^2 t}{3}\Big)\Big] \tag{5.46}$$

where A_0 is taken to be the amplitude of F(z,t). In this case, you see both a parabolic dependance of the phase on position within the cavity *and* a linear phase ramp with increasing time in the output. **The twin observation of these effects can be considered the 'smoking gun' signature of a true FM comb**. As we shall see, it is incredibly difficult to actually prove that a frequency comb is an FM comb, but if you can show that the frequency increases linearly in the time domain, and the phase has a parabolic shape in frequency domain, this constitutes a direct confirmation that one has an FM comb as opposed to an un-modelocked laser. Figure 5.12 depicts the output of two combs with the same spectrum, one in-phase modelocked, and one with out-of-phase FM modelocking ensuring the coherence between the different

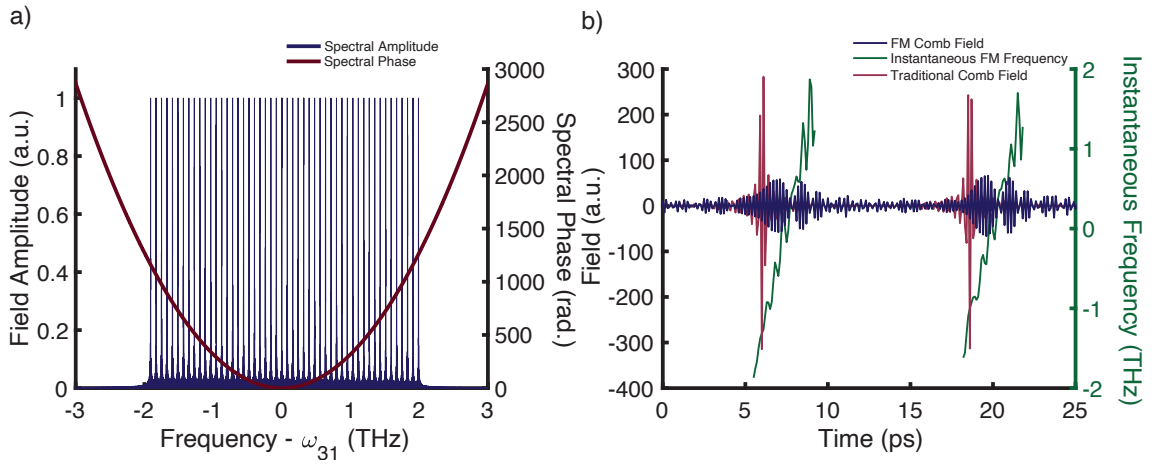

Figure 5.12: (a) The frequency-domain spectrum used in this comparison between modelocking mechanisms with the characteristic parabolic FM spectral phase. (b) The time-domain output of both cases. The in-phase modelocked comb has a clear pulse structure, whereas the FM modelocked comb has an elongated, quasi-continuous wave profile with a linear ramp in instantaneous frequency.

modes. In the FM modelocking case, we've also plotted both the spectral phase and the instantaneous frequency to demonstrate what the distinctive FM signatures are: a linearly increasing phase in the time domain and a parabolic spectral phase in the frequency domain. Depending on the spectral envelope, there may be some amplitude modulation components in the comb as well.

5.5 Conclusion

The coherent frequency comb forms the bedrock of much of modern spectroscopy. However, in-phase modelocked combs are typically quite bulky and not practical for implementation in applications requiring low space, weight, and power consumption profiles, such as remote timing transfer [33], remote rapid gas concentration measurements [34], or in space-borne precision measurements for tests of fundamental physics [35] and novel clock-based gravitational wave spectrometers [33]. In the next section, we showcase our work demonstrating a simple, diode-based frequency comb which is poised to excel in future applications with such stringent requirements.

References

(1) Ye, J.; Cundiff, S. T. ., *Femtosecond Optical Frequency Comb : Principle , Operation , and Applications*, 2004.

(2) Diddams, S. A.; Vahala, K.; Udem, T. *Science* **2020**, *369*, DOI: 10.1126/science.aay3676.

(3) Schnatz, H.; Lipphardt, B.; Helmcke, J.; Riehle, F.; Zinner, G. *Phys. Rev. Lett.* **1996**, *76*, 18–21.

(4) Rosenband, T. et al. *Science* **2008**, *319*, 1808–1812.

(5) Brewer, S. M.; Chen, J. S.; Hankin, A. M.; Clements, E. R.; Chou, C. W.; Wineland, D. J.; Hume, D. B.; Leibrandt, D. R. *Phys. Rev. Lett.* **2019**, *123*, 33201.

(6) Jones, D. J.; Diddams, S. A.; Ranka, J. K.; Stentz, A.; Windeler, R. S.; Hall, J. L.; Cundiff, S. T. *Science* **2000**, *288*, 635–639.

(7) Hall, J. L. *Reviews of Modern Physics* **2006**, *78*, 1279–1295.

(8) Udem, T.; Holzwarth, R.; Hänsch, T. W. *Nature* **2002**, *416*, 233–237.

(9) Beyer, A.; Maisenbacher, L.; Matveev, A.; Pohl, R.; Khabarova, K.; Grinin, A.; Lamour, T.; Yost, D. C.; Hänsch, T. W.; Kolachevsky, N.; Udem, T. *Science* **2017**, *358*, 79–85.

(10) Ludlow, A. D.; Boyd, M. M.; Ye, J.; Peik, E.; Schmidt, P. O. *Rev. Mod. Phys.* **2015**, *87*, 637–701.

(11) Coddington, I. R.; Newbury, N. R.; Swann, W. C. *Optica* **2016**, *3*, DOI: 10.1364/OPN.28.1.000032.

(12) Cossel, K. C.; Waxman, E. M.; Giorgetta, F. R.; Cermak, M.; Coddington, I. R.; Hesselius, D.; Ruben, S.; Swann, W. C.; Truong, G.-W.; Rieker, G. B.; Newbury, N. R. *Optica* **2017**, *4*, 724–728.

(13) Lomsadze, B.; Cundiff, S. T. *Phys. Rev. Lett.* **2018**, *120*, 233401.

(14) Suh, M.-G.; Yang, Q.-F.; Yang, K. Y.; Yi, X.; Vahala, K. J. *Science* **2016**, *354*, 600–603.

(15) Hillbrand, J.; Auth, D.; Piccardo, M.; Opačak, N.; Gornik, E.; Strasser, G.; Capasso, F.; Breuer, S.; Schwarz, B. *Phys. Rev. Lett.* **2020**, *124*, 1–6.

(16) Joshi, S.; Calò, C.; Chimot, N.; Radziunas, M.; Arkhipov, R.; Barbet, S.; Accard, A.; Ramdane, A.; Lelarge, F. *Opt. Express* **2014**, *22*, 11254–11266.

(17) Weiner, A. M. **2009**.

(18) Pedrotti, F. L.; Pedrotti, L. S.; Pedrotti, L. M. **2007**.

(19) Sakurai, J. J.; Napolitano, J. **2017**, DOI: 10.1017/9781108499996.

(20) Brabec, T.; Spielmann, C.; Curley, P. F.; Krausz, F. *Opt. Lett.* **1992**, *17*, 1292–1294.

(21) Haus, H. A.; Fujimoto, J. G.; Ippen, E. P. *J. Opt. Soc. Am. B* **1991**, *8*, 2068–2076.

(22) Delfyett, P. J.; Florez, L. T.; Stoffel, N.; Gmitter, T.; Andreadakis, N. C.; Silberberg, Y.; Heritage, J. P.; Alphonse, G. A. *IEEE Journal of Quantum Electronics* **1992**, *28*, 2203–2219.

(23) Dong, M. Frequency Comb Generation From Stimulated Brillouin Scattering and Semiconductor Laser Diodes, Ph.D. Thesis, 2018.

(24) Dong, M.; Cundiff, S. T.; Winful, H. G. *Phys. Rev. A* **2018**, *97*, 053822.

(25) Burghoff, D. *Optica* **2020**, *7*, 1781.

(26) Sun, C.; Dong, M.; Mangan, N. M.; Winful, H. G.; Cundiff, S. T.; Kutz, J. N. *IEEE Journal of Quantum Electronics* **2020**, *56*, 1–9.

(27) Ashcroft, N. W.; Mermin, N. D. **1976**.

(28) Zory, P. S. **1993**.

(29) Dong, M.; Day, M. W.; Winful, H. G.; Cundiff, S. T. *Opt. Express* **2020**, *28*, 21825–21834.

(30) Faist, J.; Capasso, F.; Sivco, D. L.; Sirtori, C.; Hutchinson, A. L.; Cho, A. Y. *Science* **1994**, *264*, 553–556.

(31) Burghoff, D.; Kao, T.-Y.; Han, N.; Chan, C. W. I.; Cai, X.; Yang, Y.; Hayton, D. J.; Gao, J.-R.; Reno, J. L.; Hu, Q. *Nature Photonics* **2014**, *8*, 462–467.

(32) Day, M. W.; Dong, M.; Smith, B. C.; Owen, R. C.; Kerber, G. C.; Ma, T.; Winful, H. G.; Cundiff, S. T. *APL Photonics* **2020**, *5*, 121303.

(33) Giorgetta, F. R.; Swann, W. C.; Sinclair, L. C.; Baumann, E.; Coddington, I.; Newbury, N. R. *Nature Photonics* **2013**, *7*, 434–438.

(34) Coburn, S.; Alden, C. B.; Wright, R.; Cossel, K.; Baumann, E.; Truong, G. W.; Giorgetta, F.; Sweeney, C.; Newbury, N. R.; Prasad, K.; Coddington, I.; Rieker, G. B. *Optica* **2017**, *5*.

(35) Lezius, M. et al. *Optica* **2016**, *3*, 1381–1387.

CHAPTER VI

Showcasing the Next Generation of Frequency Combs

6.1 Introduction

This chapter details our demonstration that semiconductor diode frequency combs (DFCs) using quantum wells as a gain medium satisfy all five requirements outlined in the introduction of chapter V. These criteria are that, in order for a frequency comb to be considered truly portable, it must be (i) compact, (ii) its output must be coherent, it must be (iii) battery operable, (iv) tunable, and have (v) demonstrated use in dual-comb spectroscopy measurements. Criteria (ii) and (v) are the most challenging to demonstrate, so a bulk of the following work will be detailing our assertion that DFCs surpass these challenges, though we shall address the fulfillment of each criterion in turn.

Many of the required milestones have been met in other devices, for instance dual-comb spectra have been acquired using coherent micro-ring resonator combs [1] which can also be battery-powered [2, 3]. Furthermore, combs generated by quantum-dot [4, 5], quantum-dash [6, 7], and by quantum well diode lasers in different spectral regions [8] have shown promise. Our DFCs, however, have the advantage of simplicity over every other current comb source in generalizability and ease of construction; we

lightly tweaked an off-the-shelf quarternary diode comb recipe to lower the diffusion lengths for carriers within the semiconductor structure, allowing for the nonlinear phase-gradient dependent frequency modulated (FM) modelocking to occur [9–13], pointing the way toward low-cost development and integration of similar DFCs.

This chapter will be structured such that a brief section will be devoted to DFC basics, demonstrating that they are compact, battery operable, and tunable. Then, considerable space will be devoted to our demonstration of mutual coherence between the teeth of a DFC comb, a notoriously difficult prospect [14]. Finally, this chapter will conclude with the demonstration of practical dual-comb spectroscopy enabled by compact DFCs, showcasing their ability to launch DFC measurements from the lab out into the field.

6.2 Diode Size, Battery Operation, and Tunability

One advantage of using quantum well lasers to produce frequency combs directly is that they are, by nature, compact. They are simple ridge waveguide Fabry-Pérot cavity diodes, depicted in Figure 5.10 from the previous chapter. Though the details of their fabrication can be found in Refs. [10] and [12], their construction was (in order, from the bottom-most layer to the top) an n-type InP substrate, grown to be 350 μm thick, on top of which was grown an n-type InP cladding layer, on top of which was grown a quarternary InGaAsP spatial confinement layer, and then four InGaAsP 8 nm wide quantum wells with eight 15 nm-wide barriers separating the wells. The top of this active layer was another InGaAsP confinement layer with a p-type InP cladding and then a p-type InGaAs contact on top. This contact was etched into a narrow ridge to confine the electric field horizontally, while the vertical confinement was provided by the cladding/active layer/cladding index of refraction grating.

This construction allows roughly two dozen DFCs to fit into the device pictured

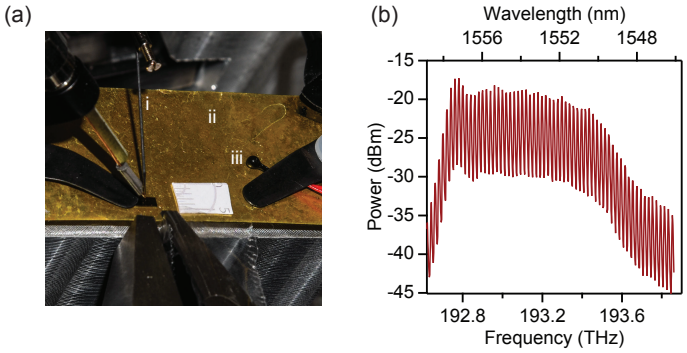

Figure 6.1: (a) A depiction of a chip containing twenty one DFCs. The power supplies (i) injected current through the probes connected to the contact on the ridge waveguide while the platform (ii) provided a current return to each power supply, while a temperature controller operated to keep the platform at a stable temperature with a measurement taken using a stock 10 kΩ thermistor for feedback control. (b) A depiction of a typical DFC output spectrum.

in Figure 6.1(a), with a typical output spectrum shown in Figure 6.1(b). DFCs are extremely simple to operate. We inject current into the top contacts with tungsten probe tips using a pair of stock, adjustable laser diode power supplies. The platform upon which the DFCs were placed is temperature controlled with a Peltier cooler directly under the gold current return depicted in Figure 6.1(a)(iii). The combs produce a stable comb-like output upon the applied current exceeding the lasing threshold current by roughly 10-20%.

We can also tune comb properties using both the platform temperature and injection current, which should roughly map to tuning the repetition rate by changing the diode length and offset frequency by modifying the number of free carriers in the cavity and thus its local index of refraction. However, these two control knobs are not necessarily independent, because an increase or decrease in injection current can change the diode temperature due to a change in ohmic heating. The result of fixing either temperature or injection current and then adjusting the other parameter are shown in Figures 6.2 and 6.3. Although not decoupled entirely, changes in the temperature and injection current cause a roughly linear shift in the comb lines, with the frequency of each comb line red-shifting as a function of increasing temperature

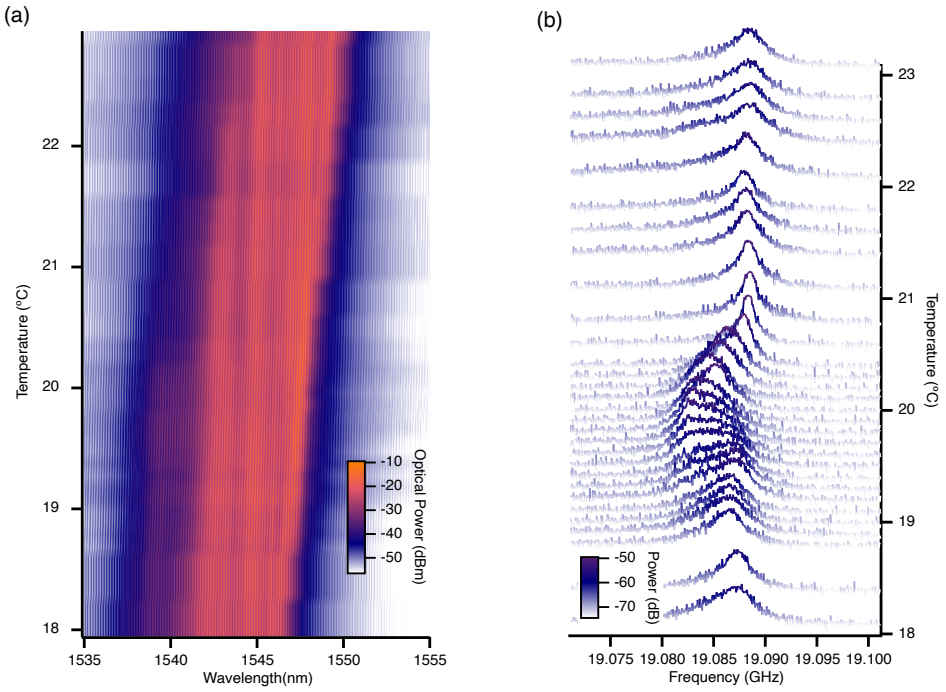

Figure 6.2: (a) Comb spectra taken by fixing the injection current and varying the platform temperature for one DFC. (b) The repetition rate beatnote of the DFC device while the platform temperature is varied. The vertical stripes in every horizontal trace are individual comb teeth.

and current.

As can be seen, the repetition rate does not necessarily change monotonically in the temperature-dependent data, whereas it changes more monotonically as the current is increased. Both these datasets demonstrate that DFCs *can* be tuned monotonically by either an increase or decrease in platform temperature and injection current, although the extent to which each variation is due to either the repetition rate or the offset frequency varying requires more inquiry.

Primarily, the fact that the repetition changes relatively chaotically in both cases, even in the presence of monotonic, well-behaved changes in the envelope of the DFC spectrum is interesting. This suggests that, although the length of the diode may change, the repetition rate is not simply dependent on the round-trip time of the waveform in the cavity. This, in conjunction with recent theoretical results [15], suggests that, though the repetition rate is likely *set* by the cavity, it can vary around

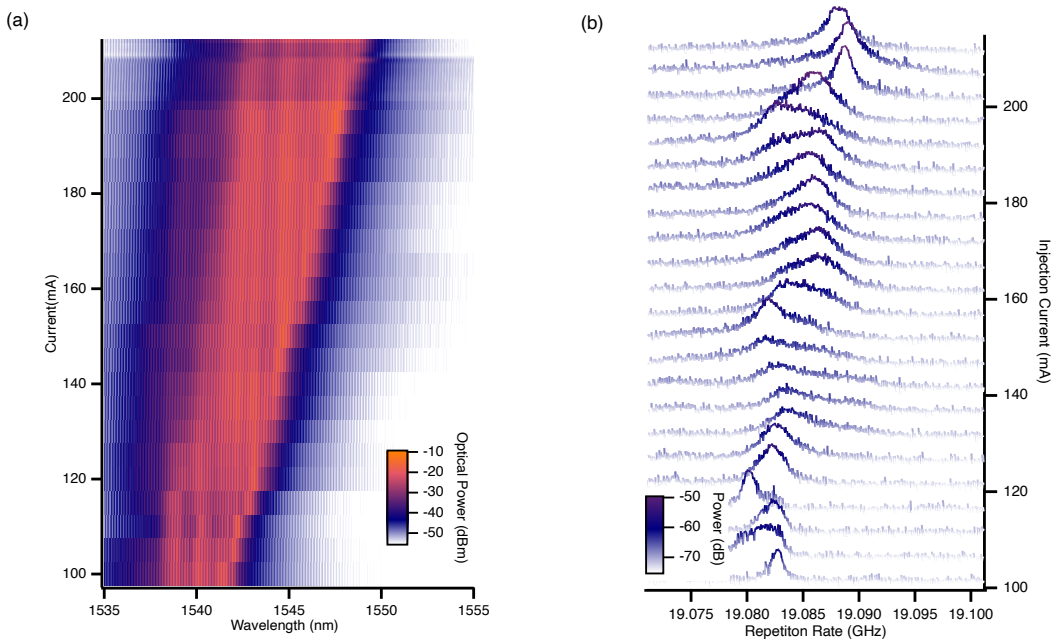

Figure 6.3: (a) Comb spectra taken by fixing the platform temperature and varying the injection current for one DFC. (b) The repetition rate beatnote of the DFC device while the injection current is varied.

this value due to rapid changes on the phase-steepening dynamics within the cavity, and points to the fact that potential future precision control over the repetition rate could be established by carefully (but rapidly) varying the intra-cavity intensity over time to provide feedback and control over the repetition rate. This could potentially be done by modulating the injection current, or through optical feedback by electro-optically modulating the phase of a portion of the comb output and re-directing that light back into the comb cavity, amongst other options [2, 16]. The net result of the current and temperature tuning, summarized in Figure 6.4, is that by tuning these parameters separately, we can change the frequency of individual comb teeth by greater than the spacing between teeth, a key requirement for their application in precision measurement and spectroscopy applications.

Furthermore, we show that DFCs can be battery powered using battery power supply which draws power from household AA batteries and delivers it to the same current injection probes used over the rest of these reported measurements. Figure

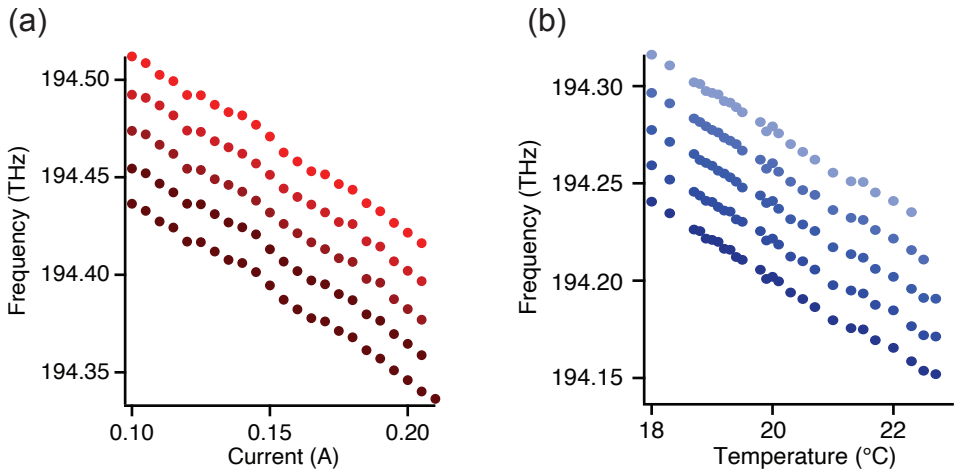

Figure 6.4: (a) The variation of four comb teeth tracked as a function of increasing diode current. (b) The variation of four comb teeth as a function of increasing diode temperature. Both figures show monotonic change in the center frequency of each tooth, pointing the way to combining these two tuning parameters to obtain full, precise control over the comb spectrum.

6.5 summarizes this result. The power supply was a basic current divider used to tune the injection current to roughly 200 mA through the diode. The output spectrum of a battery-powered DFC is shown in Figure 6.5(c). The power consumption of a single DFC was roughly 0.3 W at this injection current, meaning that a single household AA battery can power a DFC for roughly half an hour.

The sum of these results is that DFCs are compact, tunable, and battery operable. These three 'portability' requirements were easily fulfilled by DFCs, eclipsing the progress made by competing frequency comb sources in record time. We now turn our attention to demonstrating that DFCs output *coherent, FM modelocked combs*.

6.3 Measuring the Coherence of a Diode Frequency Comb

There are essentially two ways one can show that a frequency comb is coherent. The easiest is to direct the output of a frequency comb onto a fast photodiode and measure the beatnote at the RF frequency corresponding to the repetition rate of the comb [2, 12, 17]. This is a measure of the second-order coherence function of the

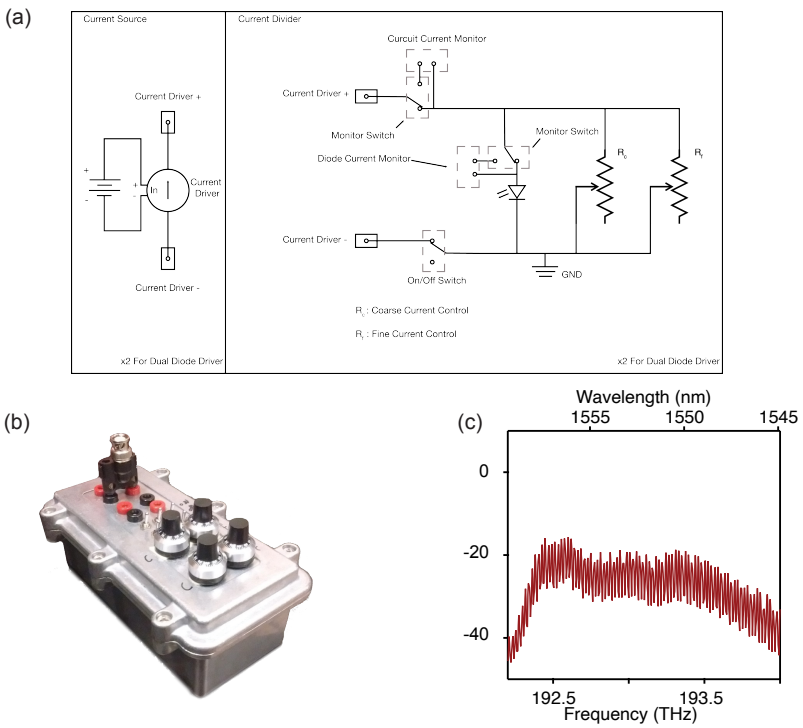

Figure 6.5: (a) The circuit for the battery power pack powering the DFC devices. A simple, two potentiometer voltage divider was constructed to split and control the current from the batteries to power up to two diodes separately. At different places in the circuit, the current through the power supply could be monitored. (b)The battery power supply box, containing up to six AA batteries. (c)The output of a battery operable DFC, showing that the DFC is spectrally stable on macroscopic timescales.

comb's time domain output (see Chapter VII). However, this method does not tell you *how* a comb is modelocked. That is, if one only observes a beatnote in the RF domain at the repetition rate of the comb, that just demonstrates that adjacent comb teeth *do* share coherence between them, but it does not yield a direct demonstration of either frequency-modulated or in-phase modelocking. In order to show that our DFCs are indeed passively FM modelocked, we must actually measure the electric field output by the frequency comb and compare its spectral phase to the qualitative behavior we would expect from an FM-modelocked comb. In other words, we must measure the output spectral phase, and if we are correct about DFCs being both *coherent* combs and *FM-modelocked* combs, we will observe a parabolic spectral phase and

a linear carrier-frequency ramp in the time domain. Those are the 'smoking gun' signatures of FM modelocking as detailed in Chapter V. Showing that these combs are FM-modelocked is important because it both confirms their coherent nature and shows that we are taking advantage of all gain avaliable within the diode in the most efficient possible way.

6.3.1 Methodology

Measuring the electric field output by a laser is no easy task [14, 18]. The two most popular techniques use a method of self-correlation to retrieve both the amplitude and phase structure of an arbitrary 'pulse' structure. The most common, and therefore the most widespread technique to do so is known as the Frequency Resolved Optical Grating, or FROG [14]. To use FROG, one splits a laser pulse in two, then impinges the replicas onto a frequency doubling crystal, collecting the spectrum of the frequency-doubled output as a function of the delay between the two pulse replicas. Through careful alignment, and careful phase matching within the thin frequency doubling crystal, one can use the resulting two-dimensional spectrogram to retrieve the full intensity and phase profile of a laser pulse [14].

Another common electric field characterization technique, and one which has been used in devices similar to DFCs is known as SWIFTS, or Shifted Wave Interference Fourier Transform Spectroscopy [9]. In this technique, one takes a coherent light source with some arbitrary repetition rate and shines its output directly onto a fast photodiode to obtain the repetition rate beatnote. Then one uses this beatnote as the reference signal for a lock-in amplifier. By then splitting the output of the lightsource in question in two and scanning the two pulse replicas with respect to each other at a separate, signal photodiode (while lock-in detecting the signal at the coherent beat frequency), the full spectrum and phase profile of the electric field output by the original lightsource can be obtained.

Both of these techniques are not suitable for our case. We want to characterize the electric field of a quasi continuous wave, FM comb. We therefore will not be able to use FROG because it requires a nonlinear, second-harmonic generation step; something likely not achievable with an FM comb given the low peak power of its output. Furthermore, SWIFTS requires that the electric field is stable over the timescale of a minute or so as a delay stage is scanned by several millimeters to a centimeter and an interferogram is recorded. There is no *a priori* guarantee that the electric field of our DFCs is so stable.

We therefore use a technique derived from dual-comb spectroscopy to characterize the spectrum of our DFCs [19]. This technique is very simple: we cross-correlate the pulse train of a well-known frequency comb with the output of the DFC. We use a Menlo Systems AC1550 frequency comb with a repetition rate of 250 MHz as our characterization pulse, meaning that, when we cross-correlate the pulse train from the Menlo comb with that of our DFC (with a repetition rate of roughly 25 GHz), there will be one hundred Menlo comb teeth between every DFC tooth in the frequency domain. Furthermore, according to the manufacturer, the pulse train is well compressed, meaning that its phase is flat in the time and frequency domains. Therefore, if there is a way to map the beating between the DFC and the characterization comb into the RF domain, then the resulting RF comb will carry only the spectral phase information from the DFC. We deem this DFC characterization technique cross-correlation dual comb (XCDC) spectroscopy because we are performing a first-order cross-correlation between the reference comb and our DFC pulse trains. Figure 6.6 is a depiction of the experimental implementation of XCDC.

To implement the XCDC characterization of the DFC output, we combine the output of our Menlo laser and a DFC on a beamsplitter. The two output ports of this beamsplitter are directed simultaneously to an optical spectrum analyzer (OSA) and to a fast photodiode. The OSA possesses sufficient resolution to resolve the absolute

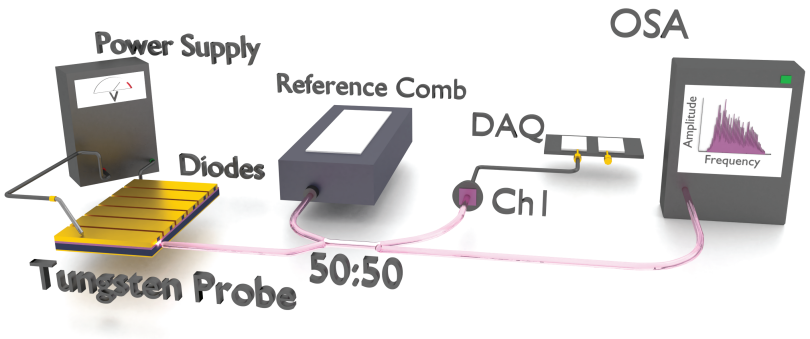

Figure 6.6: A depiction of the XCDC experiment used to characterize the electric field of our DFC sources. The output of a DFC is combined with that of a reference comb on a beam splitter. The resulting composite pulse train is directed simultaneously to a fast photodiode and an optical spectrum analyzer to up-convert the RF data to the optical domain.

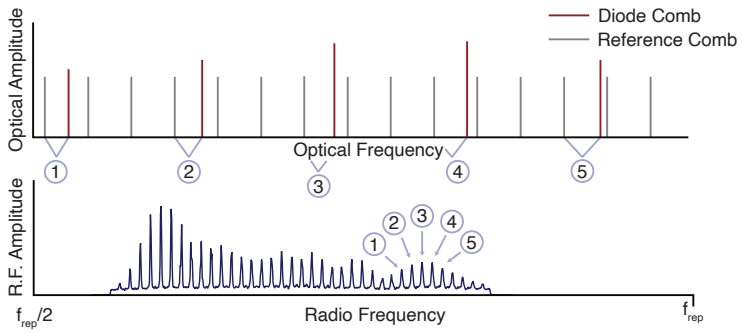

Figure 6.7: A depiction of the XCDC technique in the (a) optical and (b) RF frequency domains. The RF comb teeth, marked 1-5 in (b) are the result of separate diode comb teeth in (a) beating with adjacent reference comb teeth. As long as a *harmonic* the reference comb repetition rate is nearly commensurate with the DFC comb repetition rate, a useable RF comb will form.

frequency of individual comb teeth, which allows us to map the RF information back into the optical domain. On the fast photodiode, the two combs interfere. Each DFC tooth beats with an adjacent comb tooth of the Menlo comb, but there are one hundred Menlo teeth separating each DFC tooth. Figure 6.7 shows the frequency-domain concept of this technique.

Although the Menlo comb and the DFC have highly incommensurate repetition rates, what is important is that the 100th harmonic of the repetition rate of the Menlo comb and the DFC repetition rate are *nearly* commensurate. To see how an RF comb

could result from such a repetition rate mismatch, suppose we have two frequency combs A and B with electric fields

$$E_a(\omega) = \sum_n \mathrm{Exp}(-in\omega_{rep,a}t - i\omega_{ceo,a}t) \tag{6.1}$$

and

$$E_b(\omega) = \sum_m \mathrm{Exp}(-im\omega_{rep,b}t - i\omega_{ceo,b}t) \tag{6.2}$$

where $\omega_{rep,a}$ and $\omega_{rep,b}$ are the repetition rates of combs A and B respectively, and the summation indices $n \in [n_{min}, n_{max}], \mathrm{and} m \in [m_{min}, m_{max}]$ run over the mode numbers with finite spectral weight, while $\omega_{ceo,a}$ and $\omega_{ceo,b}$ are the carrier-envelope offset frequencies of combs A and B. Let's assume that $\omega_{rep,a} = d\omega_{rep,b} + \delta$ where δ is small in comparison to both $\omega_{rep,a}$ and $\omega_{rep,b}$, and d is some large integer on the order of 100. Now, let's examine the intensity spectrum in the RF domain

$$I_{beat} \propto \mathrm{Exp}(-i\Delta\omega_{ceo}t) \sum_{m,n} \mathrm{Exp}[-i(n\omega_{rep,a} - m\omega_{rep,b})t)] + c.c. \tag{6.3}$$

where $\Delta\omega_{ceo} = \omega_{ceo,a} - \omega_{ceo,b}$. Since $\omega_{rep,a} = d\omega_{rep,b} + \delta$, we can rewrite the frequency argument to read

$$n\omega_{rep,a} - m\omega_{rep,b} = (nd - m + n\delta)\omega_{rep,b}. \tag{6.4}$$

We note that the lowest frequency beatnotes will occur when

$$nd - m = 0 \tag{6.5}$$

or when

$$m_{min} = n_{min}d. \tag{6.6}$$

The lowest-frequency replica RF spectrum will be

$$I_{beat} \propto \mathrm{Exp}(-i\Delta\omega_{ceo}t)\sum_n \mathrm{Exp}[-in\delta t] + c.c.. \tag{6.7}$$

where $n \in [n_{min}, n_{max}]$ without loss of generality. In other words, when two frequency combs beat together with one comb having a near-integer multiple of the other's rep-rate, one can still perform dual-comb spectroscopy with these two combs.

Furthermore, the temporal phase behavior of our comb in question also maps easily into this measurement. Suppose that one of our combs is weakly chirped such that its instantaneous frequency changes linearly in time and its spectrum can be written

$$E_a(t) = \sum_n \mathrm{Exp}(-in\omega_{rep,a}t - i\omega_{ceo,a}t - i\phi(t)) \tag{6.8}$$

with temporal phase profile $\phi(t)$ describing a pulse with arbitrary time-dependent phase. Then, in this case we will measure the following at our detector

$$I_{beat}(t) \propto \mathrm{Exp}(-i\Delta\omega_{ceo}t)\sum_n \mathrm{Exp}[-in\delta t - i\phi(t)] + c.c.. \tag{6.9}$$

Thus, if one comb is unchirped, and the other is chirped, the XCDC signal can be used to directly retrieve the phase profile of the unknown, chirped field.

6.3.2 Results and Discussion

We take advantage of the fact that any spectral phase information will map into the XCDC measurement to confirm that our DFCs exhibit the 'smoking gun' behavior of FM modelocking: a chirped time- and frequency-domain spectrum. To do so, we operate one DFC at a platform temperature of 10.020 °C and current of 152.42 mA. Current (36 mA) was run through the adjacent device to provide fine temperature control. The XCDC spectrum was taken in the time-domain with a data acquisition

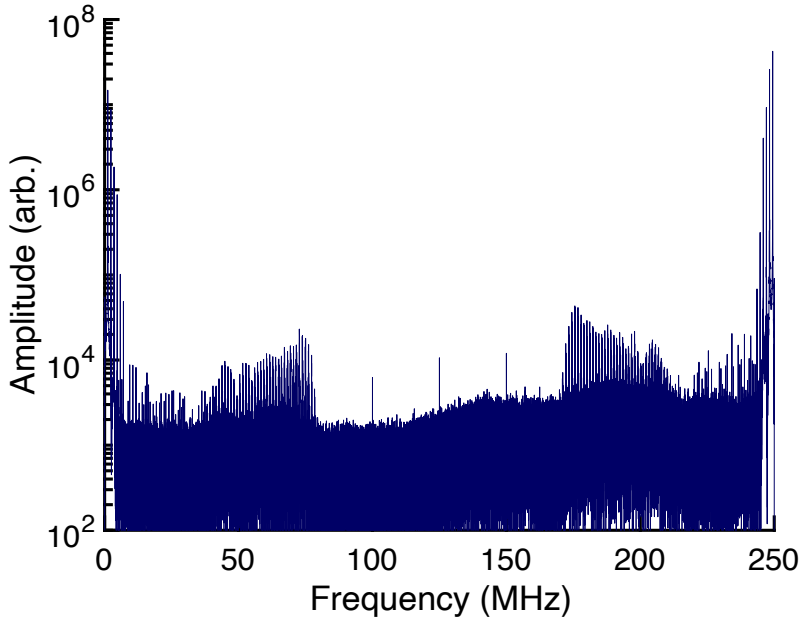

Figure 6.8: The raw XCDC data containing a dual-comb spectrum (and its replica) between the DFC and the Menlo comb. The two periodic RF combs centered about 60 MHz and 190 MHz are the XCDC data. All other spikes are spurious noise or digital aliasing of other RF signals within the experiment.

board (DAQ) sampling at 500 MSamples/s for 700 μs (350 kSamples per data record).

Figure 6.8 is the raw, frequency domain XCDC data. There are two XCDC replica RF combs, reflected about $f_{rep,ref}/2 = 125$ MHz. This is because, for every DFC comb tooth, there is a nearest and next-nearest neighbor comb tooth from the reference comb nearby. Therefore, we capture both sets of beatnotes in the RF domain. Due to the placement of the lowest frequency (first) DFC comb tooth relative to those from the reference comb, the higher frequency replica is the correct XCDC data, and will be the data we choose to analyze, as confirmed by the appearance of the frequency comb spectrum on the OSA, with the highest amplitude teeth falling at the lower end of the frequency domain output of the DFC. We acquire the data in the time domain and Hilbert transform the dataset, obtaining the full analytic RF signal. The RF signal consists of 'bursts' corresponding to the reference comb pulses sweeping through the DFC pulses on the detector.

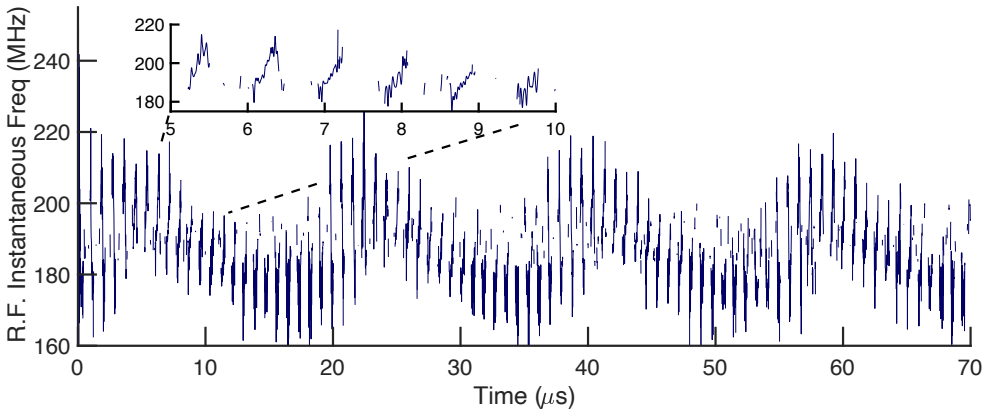

Figure 6.9: A snapshot of 70 μs of the instantaneous frequency of the RF XCDC time-domain data. The slope and center frequency of the dataset oscillate with a roughly twenty-burst period

This data contained significant noise which required careful processing to extract the true time- and frequency-domain phase profile of the DFC emission. First, the data was band-pass filtered to capture only the XCDC signal which lay between roughly 170 MHz and 220 MHz. The noise still present in this data can be easily seen by examining the instantaneous frequency of the filtered data, shown in Figure 6.9.

This noise is due to self-mixing of the strong RF signal in the DAQ board, as it did not change in character or frequency for other data sets when the parameters of the XCDC experiment changed (such as the difference in repetition rate of the DFC device and the reference comb), so this noise was not reflective of the DFC output. Luckily, because both the slope and central frequency of the data set oscillated with the same frequency (roughly once every twenty bursts), there is a straightforward and well-known technique to rid its effect from our data.

This technique, known as coherent averaging [20], is ideal to remove periodic phase fluctuations in dual-comb data. To perform this averaging, we take the time-domain data and chop it into forty frames corresponding to one noise period, or roughly twenty bursts. We then take each frame and align the burst envelopes in the time domain, being sure to carefully symmeterize the eventual data set about the central pixel to

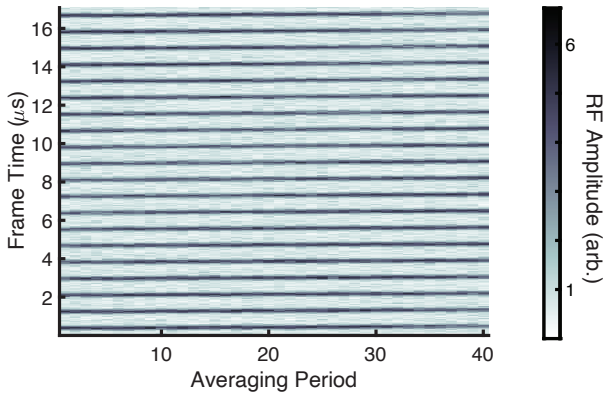

Figure 6.10: The data frames constituting the coherent averaging process, stacked horizontally. After the correct first burst is selected, each successive sequence of twenty bursts is carefully aligned with its companions in neighboring frames, and then the frames are averaged together (corresponding to averaging in the x-direction of this figure). The resulting twenty-burst dataset is free from the pollution induced by the phase noise in the DAQ.

not introduce any artefacts. Following this careful symmeterization and alignment process, we average the complex-valued frames together, producing one twenty-burst frame of averaged data. The aligned data frames are shown in Figure 6.10.

There is an incredibly important detail to keep in mind when conducting this process, because the frequency domain phase profile is highly sensitive to any data processing oversights. This detail is the selection of the 'correct' first burst in the data set. This is determined by the discrete Fourier-transform conventions of whichever analysis software package is used and needs to be done carefully to avoid adding a frequency domain linear phase ramp that would reflect a timing error resulting from any incorrect selection. To do this we selected the correct first burst by repeatedly coherently averaging the data set with different 'first' bursts and choosing the burst which, when Fourier transformed, resulted in no linear phase ramp being added to the spectral phase data. The correct first burst also corresponded to the correct concavity of the spectral phase, as determined by examining the spectral phase of the full data record (whose phase concavity is not sensitive to the noise we are trying to remove), and which resulted in a spectral phase profile symmetric about the DFC

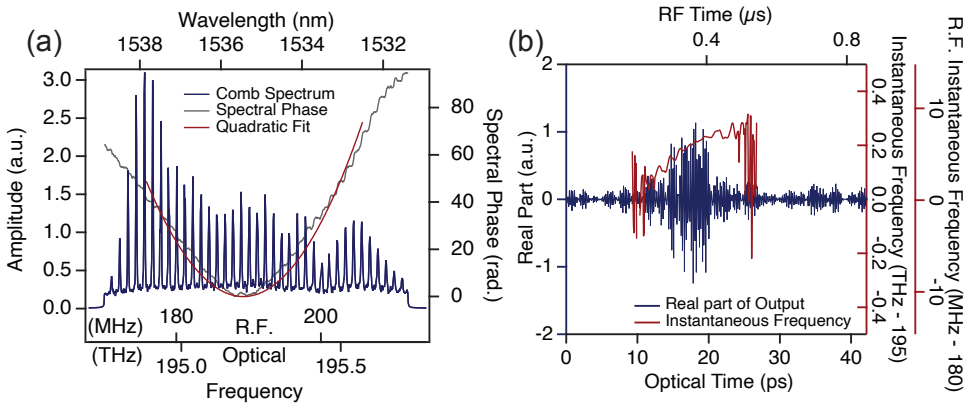

Figure 6.11: The final XCDC measurement in the frequency- and time-domains showing the spectral phase profile and temporal phase ramp typical of an FM modelocked comb.

carrier frequency, found by taking the comb tooth at the geometric center of the DFC spectrum. Following the averaging process, the spectral phase was unwrapped in both the time and frequency domains using a MATLAB phase unwrapping algorithm that corrects for phase jumps of $\pm 2\pi$ inherent in the way time- and frequency-domain phase is defined.

As stated before, because the spectral phase of the reference comb was flat, any variation in the spectral phase of the XCDC signal is due to the DFC. Furthermore, MATLAB's discrete Fourier transform uses a positive-definite frequency kernel and an anti-symmetric sine-transform convention, and therefore both time-domain chirp and the concavity of the frequency-domain parabola are positive, though by typical convention a positive time-domain chirp corresponds to a negative GDD coefficient in the frequency domain.

The results of this data processing algorithm are depicted in Figure 6.11, where we fit the RF data to the concurrently acquired OSA spectrum to up-convert time-domain RF data to the optical frequency domain. We clearly see the 'smoking-gun' signature of FM modelocking: a parabolic spectral phase in the frequency domain and

a dominantly linear frequency ramp in the time-domain corresponding to a chirped, quasi continuous-wave output as expected for an FM-modelocked comb [10–12, 15]. We fit the parabolic phase data in the frequency domain, taking care to remember that, due to the difference between MATLAB discrete Fourier transform conventions and typical analytic Fourier conventions, that a positive-concavity parabola corresponds to a negative group-delay-dispersion (GDD) coefficient [14]. We fit the phase profile to obtain a GDD coefficient of -4.3 ps^2, agreeing well with our characterization of this light source as a 'quasi-continuous wave' laser, though there could be some weak higher-order chirp present in the DFC output due to higher-order nonlinearities present in the cavity.

6.3.3 Conclusion

Our XCDC measurements clearly demonstrate that DFCs are *coherent*, *FM modelocked* frequency combs. This is a crucial fact because as seen in Chapter VII, the *coherence* of the whole comb spectrum is the key fact undergirding its usefulness as a light source. Furthermore, this XCDC measurement constitutes the first direct measurement of the full time- and frequency-domain output of a quantum well-based frequency comb operating in the 1.5μm window. With this measurement, we have now shown that DFCs fulfill four of five portability requirements. The only demonstration left is to show that DFCs are capable of being mutually coherent with other DFCs and that they can be used in a practical demonstration of dual-comb spectroscopy.

6.4 Demonstrating Practical Dual-Comb Spectroscopy with Diode Frequency Combs

In the previous section, we showed that DFCs could be coherent with other comb sources, and that they were FM modelocked combs as expected. In this section,

we will show that DFCs can be used in practical dual-comb spectroscopy (DCS) applications. We will first discuss how we acquire our spectra, then how we error-correct the RF comb to ensure that we accurately capture the optical absorption profile of our gas cell, and then provide some concluding remarks by way of discussing the future applicability of our devices and possible next steps for the DFC project.

6.4.1 Methodology

The gas cell used in the DCS measurement was purchased from Wavelength References and was a 300 Torr version of their HCN gas cell (part description HCN-13-H(16.5)-300-FCAPC). The datasheet accompanying the calibration cell gives a 16 pm (68 pm) FWHM linewidth for the P8 line for the 25 Torr (100 Torr) version of the cell, so linearly extrapolating to a pressure of 300 Torr, the linewidth of the transitions should be roughly 200 pm or 25GHz at 1550nm, or commensurate roughly with the repetition rate of our DFCs. We therefore expect for our DCS spectrum to capture the absorption profile of the cell with roughly one tooth per absorption peak.

We want to show that our DCS spectrum matches the correct absorption profile of the gas cell, so we began by acquiring the absorption spectrum. We do this by using the Menlo comb as a white light source and taking its spectrum with and without the HCN cell using the OSA. Then we use Beer's Law to calculate the absorption spectrum of the cell to which we are going to compare our DCS measurement. This control measurement is presented in figure 6.12, and was chosen to be in the rough spectral window of the DFC output.

Following this basic characterization, we used the setup depicted in Figure 6.13 to acquire DCS data. We powered two combs on the chip depicted in Figure 6.1 using two tungsten probes contacting each comb, with 210 mA and 195 mA of current. Once the combs were powered, we collected their light using two lensed fiber tips and then combined the output of two combs using a 50:50 in-fiber beamsplitter. We

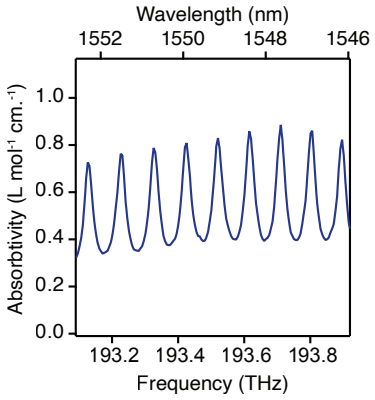

Figure 6.12: The simple Absorbtion spectrum of the HCN test cell taken using just the OSA spectrometer.

used two polarization controllers to ensure the proper overlap of the polarization states of the two combs. Subsequently, 50% of the dual-comb light was sent to a photodetector before the gas cell (labelled Ch1 in Figure 6.13) and 50% of the dual-comb light was sent through the cell. Then, 90% of the remaining light was sent to a photodetector (labelled Ch1 in Figure 6.13) and the dual comb traces before and after the sample cell were collected in the time domain using the same DAQ card as the XCDC measurements. The remaining 10% of the dual-comb light was sent to the OSA and used to resolve the dual-comb spectrum in the optical domain so that up-conversion between the RF and optical domains could occur.

6.4.2 Results and Error Correction

The raw DCS data is shown in Figure 6.14. We collected a data record with length 10 μs and a sampling rate of 2GS/s. The difference in repetition rate between the two combs in the optical domain was 8.92 MHz, which corresponds to f_{rep} of the RF spectrum. First, the dataset was bandpass filtered to isolate the DCS signal in the frequency domain. The next, and potentially the most important step was to correct for the fact that Channels 1 and 2 had different detectors with different bandwidths and collection efficiencies. To perform this correction, a separate DCS spectrum

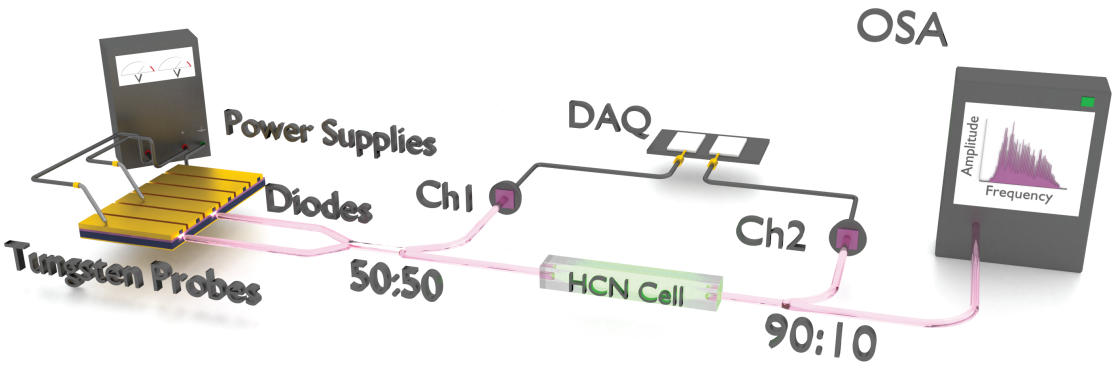

Figure 6.13: The DCS setup. Two power supplies power two DFCs whose light is collected. Half of that light is sent to a detector before the cell marked Ch1, then half through the cell, where the light is split again to collect both the RF (using Ch2) and optical signals simultaneously to convert the DFC DCS spectrum from the RF domain to the optical frequency domain.

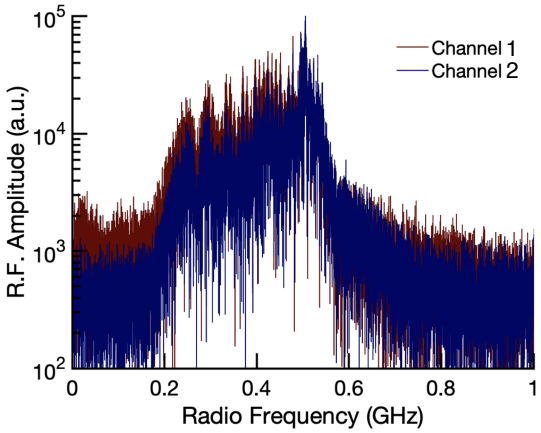

Figure 6.14: The raw dual-comb spectra acquired before (Channel 1) and after (Channel 2) the gas cell.

without the cell was collected where the two combs were tuned such that their RF DCS spectrum spanned the entire 1 GHz frequency window. Then the spectrum was downsampled such that only the RF envelope of the DCS signal remained for each channel. The ratio between the RF envelope for the two channels was calculated and the raw DCS data from the absorption measurement was then amplitude corrected using this ratio in the frequency domain such that the two channels could be directly compared.

The next remaining sources of noise were the repetition and offset frequency noise

of the RF comb which required two separate correction methods to recover the noisless RF comb. The offset frequency correction we implement is simple. We filter out a comb tooth in the RF frequency spectrum for each channel and mix the complex conjugate of that tooth with the raw data. This 'perfectly' corrects only one comb tooth by self-mixing all noise out from just that tooth. This process serves to remove offset frequency noise from the whole DCS spectrum, because any noise in the offset frequency will cause all comb teeth to shift together. However, this process mixes repetition rate noise into each comb tooth as an integer function of its distance from the 'perfect tooth.'

Explicitly, the uncorrected noise in the frequency of the n-th tooth of the RF comb is

$$f_n(t) = nf_{rep} + f_{os} + n\delta f_{rep}(t) + \delta f_{os}(t) \tag{6.10}$$

where $\delta f_{rep}(t)$ and $\delta f_{os}(t)$ are the noise in the repetition rate and offset frequency of the RF comb respectively. If we mix this comb tooth with itself, we will have

$$f_n(t) - f_n(t) = 0 \tag{6.11}$$

leaving a 'perfectly' corrected comb tooth at zero frequency as stated above. However, the result of this mixing process on a neighbor tooth is

$$f_{n+1}(t) - f_n(t) = f_{rep} + \delta f_{rep}(t) \tag{6.12}$$

and also on the next-nearest-neighbor tooth:

$$f_{n+2}(t) - f_n(t) = 2f_{rep} + 2\delta f_{rep}(t). \tag{6.13}$$

By mixing the whole comb with our selected tooth, we remove $\delta f_{os}(t)$ from each tooth but add $\delta f_{rep}(t)$ as a function of the relative tooth spacing. The data after this

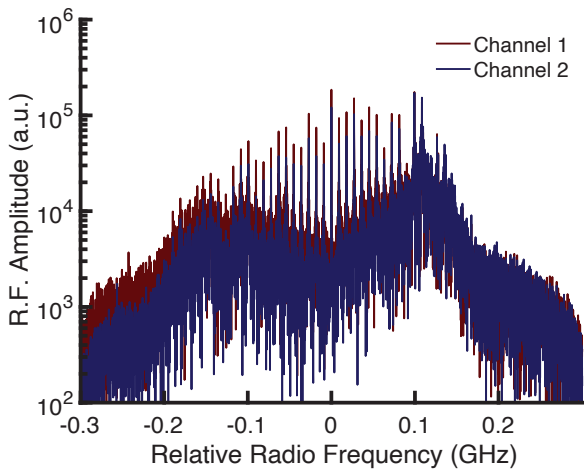

Figure 6.15: The pair of offset-corrected combs upon mixing each channel with the 'perfect tooth' chosen arbitrarily. This process mixed in repetition rate noise to each RF comb as can be seen by the linearly ascending noise floor as a function of comb tooth away from the central frequency.

correction is depicted in figure 6.15 where zero frequency is set relative to the chosen 'perfect tooth' in each channel after mixing with each RF comb.

We then needed to correct both the ambient repetition rate fluctuations *and* those that we mixed in during the offset-frequency correction step. We performed a technique known as digital-difference frequency generation (DDFG) to self-mix the combs in each channel to isolate f_{rep} and its noise term $\delta f_{rep}(t)$. For this correction, we take the time-domain data streams for both channels and mix them with their complex conjugate and Fourier transform the result. This is an auto-correlation between each channel's RF comb spectrum. This procedure leaves RF teeth at integer multiples of the repetition rate, whose widths correspond to the Fourier transform of $\delta f_{rep}(t)$. The DDFG signal for channel 1 is depicted in figure 6.16.

We use the lowest frequency DDFG tooth as a 'clock' by which to resample the dataset in the time domain. To do so, we filtered out the lowest frequency DDFG tooth and inverse Fourier transformed it into the time domain. The phase of this signal was then unwrapped to obtain a phase ramp whose slope centered around f_{rep}. The beginning and end phases of this ramp were used to redefine a target phase ramp

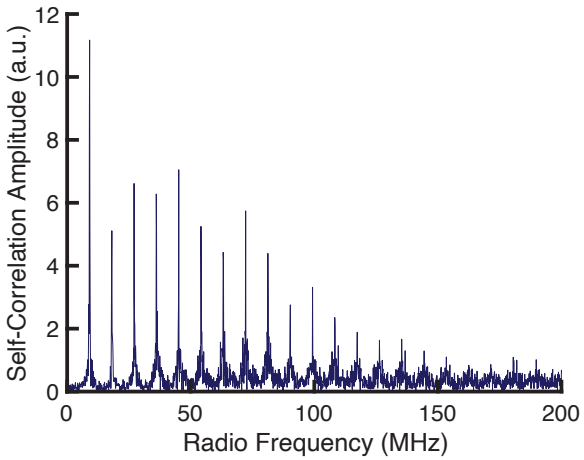

Figure 6.16: The DDCS spectrum derived from channel 1. Peaks in this spectrum correspond to harmonics of f_{rep} and the width of each tooth corresponds to the spectral width of $\delta f_{rep}(t)$.

for the whole dataset. Each point in the old time-domain datasets (for both channels) is resampled to this new clock such that the parts of the time-domain data that evolve at the old clock frequency (defined by the uncorrected phase ramp) have no frequency fluctuations about the new clock. This method of correcting the timing errors in the data cancels noise in the time domain for waveforms that evolve at multiples of the original clock frequency (i.e. each tooth of the RF comb). Furthermore, because this method corrects noise at multiples of the original clock frequency, it serves to remove the extra $\delta f_{rep}(t)$ mixed into each comb tooth as described above. To get a sense of the noise in f_{rep}, figure 6.17 shows the instantaneous repetition rate of the RF dataset, found by unwrapping the phase of the first DDFG tooth in the time-domain and calculating

$$f_{rep}(t) = \frac{d\phi(t)}{dt}. \tag{6.14}$$

This method only works well in the case of an RF comb with already high signal-to-noise (roughly 10dB for our dataset) such that a single tooth can be isolated for mixing with the whole spectrum and such that f_{rep} and its harmonics are well defined

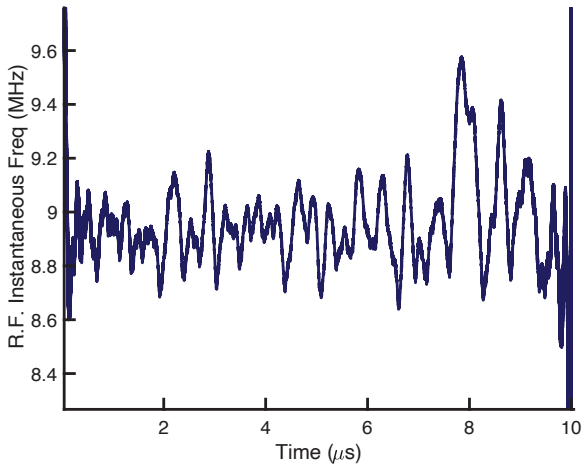

Figure 6.17: The instantaneous repetition rate of the RF comb showing slight variations about the central value of 8.98 MHz.

in the DDFG dataset. We found that this two-step process for error correction failed if the width of the first harmonic tooth in the DDFG spectrum was larger than 1/20 times the RF f_{rep}. In this dataset, the width of the first harmonic of the DDFG tooth was 240kHz full-width half max, roughly 37 times smaller than the difference in the optical repetition rate between the two combs (or the RF f_{rep}) which was 8.98 MHz. The advantage of our method is that, in principle, it could be applied to datasets in real-time, acquired and processed digitally using a field-programmable gate array. However, if the signal-to-noise ratio is small for a given dataset, other error correction methods would be more appropriate.

After performing this noise correction process for both channels, we took the amplitude of each tooth in the frequency domain from each channel and then did the same Beer's law calculation to obtain the final DCS absorption spectrum. We then used the OSA spectrum to convert the RF frequency of each tooth into the optical domain by fitting two RF teeth to two OSA teeth and using the result to calculate the appropriate optical frequency axis. The final result, shown in figure 6.18 shows good agreement with the traditional absorption measurement obtained initially.

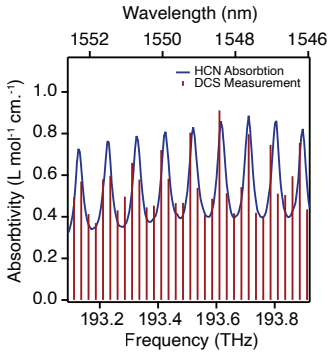

Figure 6.18: A comparison between the absorption spectra obtained using DCS and traditional absorption spectroscopy with the OSA acting as the grating spectrometer.

6.5 Conclusion

Throughout this chapter, we have demonstrated conclusively that DFCs are ready for application because they fulfill all portability criteria. They are compact, tunable, efficient, coherent, and have proven use in practical dual-comb spectroscopic measurements. Furthermore, DFCs provide FM modelocked combs, in agreement with theory [10, 11, 15].

In the future DFCs could be rapidly deployed to conduct in-field gas assays by simply combining the light of two combs in free-space and directing the light over an open optical path to a detector, similar to work done using in-fiber combs [21]. DFCs would have the advantage over this work, however, of consuming orders of magnitude less power, and easy commercially replicability relative to the specialty fiber laser oscillators required to do this work today. Furthermore, DFCs are ripe for application in environments where low space, weight, and power (SWAP) use are required, such as multi-comb distance ranging between spacecraft in orbit, or in orbital frequency-comb based atomic clocks which would be useful for all manner of gravitometric studies [22].

Finally, there is (in principle) no fundamental restriction on the operating wavelength of an FM-modelocked comb, so long as the wavelength of the comb spectrum is

within the window of light currently producible with semiconductor heterostructures, ranging from THz frequencies to ultraviolet wavelengths. This has *enormous* potential implications. As useful as optical frequency combs currently are, if structures taking advantage of FM modelocking can be developed to widen comb bandwidths and explore different wavelength regions than those currently shown in the literature, ubiquitous, cheap, and rapid precision optical spectroscopy can be proliferated, opening new possibilities in precision gas detection and measurement and even paving the way for comb-based spectrometers to be easily incorporated in handheld electronic devices. With DFCs, the dream of ubiquitous, portable precision spectroscopy is achievable.

References

(1) Suh, M.-G.; Yang, Q.-F.; Yang, K. Y.; Yi, X.; Vahala, K. J. *Science* **2016**, *354*, 600–603.

(2) Shen, B. et al. *Nature* **2020**, *582*, 365–369.

(3) Stern, B.; Ji, X.; Okawachi, Y.; Gaeta, A. L.; Lipson, M. *Nature* **2018**, *562*, 401–405.

(4) Hillbrand, J.; Auth, D.; Piccardo, M.; Opačak, N.; Gornik, E.; Strasser, G.; Capasso, F.; Breuer, S.; Schwarz, B. *Phys. Rev. Lett.* **2020**, *124*, 1–6.

(5) Mao, Y.; Liu, J.; Lu, Z.; Song, C.; Poole, P. J. *2019 Optical Fiber Communications Conference and Exhibition, OFC 2019 - Proceedings* **2019**, *25*, DOI: 10.1109/jstqe.2019.2916840.

(6) Joshi, S.; Calò, C.; Chimot, N.; Radziunas, M.; Arkhipov, R.; Barbet, S.; Accard, A.; Ramdane, A.; Lelarge, F. *Opt. Express* **2014**, *22*, 11254–11266.

(7) Rosales, R.; Murdoch, S. G.; Watts, R.; Merghem, K.; Martinez, A.; Lelarge, F.; Accard, A.; Barry, L. P.; Ramdane, A. *Optics Express* **2012**, *20*, 8649.

(8) Frez, C.; Forouhar, S.; Burghoff, D. *photonics* **2020**, *076111*, DOI: 10.1063/5.0009761.

(9) Burghoff, D.; Kao, T.-Y.; Han, N.; Chan, C. W. I.; Cai, X.; Yang, Y.; Hayton, D. J.; Gao, J.-R.; Reno, J. L.; Hu, Q. *Nature Photonics* **2014**, *8*, 462–467.

(10) Dong, M. Frequency Comb Generation From Stimulated Brillouin Scattering and Semiconductor Laser Diodes, Ph.D. Thesis, 2018.

(11) Dong, M.; Cundiff, S. T.; Winful, H. G. *Phys. Rev. A* **2018**, *97*, 053822.

(12) Dong, M.; Day, M. W.; Winful, H. G.; Cundiff, S. T. *Opt. Express* **2020**, *28*, 21825–21834.

(13) Sun, C.; Dong, M.; Mangan, N. M.; Winful, H. G.; Cundiff, S. T.; Kutz, J. N. **2019**, 1–9.

(14) Trebino, R. Frequency-Resolved Optical Gating : The Measurement of Ultrashort Laser Pulses, English, Boston, 2012.

(15) Burghoff, D. *Optica* **2020**, *7*, 1781.

(16) Asghar, H.; Wei, W.; Kumar, P.; Sooudi, E.; McInerney, J. G. *Optics Express* **2018**, *26*, 4581.

(17) Delfyett, P. J.; Florez, L. T.; Stoffel, N.; Gmitter, T.; Andreadakis, N. C.; Silberberg, Y.; Heritage, J. P.; Alphonse, G. A. *IEEE Journal of Quantum Electronics* **1992**, *28*, 2203–2219.

(18) Jones, D. J.; Diddams, S. A.; Ranka, J. K.; Stentz, A.; Windeler, R. S.; Hall, J. L.; Cundiff, S. T. *Science* **2000**, *288*, 635–639.

(19) *Journal of Lightwave Technology* **2011**, *29*, 3091–3098.

(20) Coddington, I.; Swann, W. C.; Newbury, N. R. *Physical Review A - Atomic, Molecular, and Optical Physics* **2010**, *82*, 1–13.

(21) Coburn, S.; Alden, C. B.; Wright, R.; Cossel, K.; Baumann, E.; Truong, G. W.; Giorgetta, F.; Sweeney, C.; Newbury, N. R.; Prasad, K.; Coddington, I.; Rieker, G. B. *Optica* **2017**, *5*.

(22) Lezius, M. et al. *Optica* **2016**, *3*, 1381–1387.

CHAPTER VII

Detailing the Role of Coherence in Optical Frequency Comb Measurements

7.1 Introduction

Often, when new sources of frequency combs are demonstrated, little care is taken to show that the combs are, in fact, coherent. Furthermore, due to the difficulty of measuring the optical phase of some given electric field, even fewer demonstrations of new comb sources bother with trying to sort out the modelocking physics in their devices. This chapter exists to rectify this by showing *why* the mutual coherence is absolutely crucial to the experimental application of frequency combs. Furthermore, we will provide necessary and sufficient conditions for showing that a comb is coherent.

We realistically model a frequency comb and contrast its properties with an incoherent light source with a 'comb-like' structure, created by filtering a broadband incoherent source through a Fabry-Pérot cavity. We first compare the first- and second-order coherence of the two light sources, showing that, although one can construct a filtered light source which will have the same first-order coherence properties as a frequency comb (and the same optical power spectrum), its higher-order coherence will be dramatically different from that of a coherent comb. We then illustrate the crucial importance of the coherent nature of comb output by simulating the out-

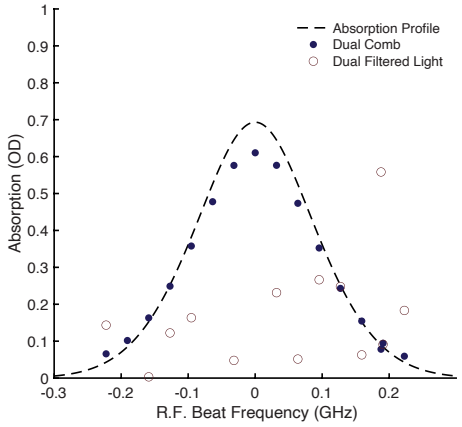

Figure 7.1: A comparison between calculated dual-comb absorption profiles using either a pair of incoherent light sources (open circles) or a pair of frequency combs (closed circles). The two pairs of light sources have identical optical spectra to each other, but the fact that the comb teeth are coherent with each other is what makes the frequency combs useful in a DCS experiment.

come of a dual-comb spectroscopy (DCS) measurement and a frequency-metrology experiment conducted with both types of light sources, representing perhaps the most common uses of frequency combs. Past theoretical investigations have started with perfectly periodic fields and added noise perturbations [1–4], but the theory we present here is more general and can be used to model both technical and quantum noise present in frequency combs generated by a wide variety of light sources.

To showcase the importance of this discussion at the beginning of this chapter(and point out that it is not a simple issue of semantics), Figure 7.1 summarizes the difference that coherence between comb teeth makes in a practical DCS measurement. In brief: one must show that a light source is coherent before it can be a feasible frequency comb source.

7.2 Building the Analysis Toolbox

In this section we will assemble the analysis tools required to compare two different light sources with identical spectra: the mode-locked (but noisy) frequency comb and

the Fabry-Perót filtered incoherent lightsource.

7.2.1 The First-Order Coherence and power spectrum of a Single Mode

We begin by considering a noisy, single-frequency, electric field mode. Here we model the intrinsic noise as a stochastically varying, time-dependent phase, $\phi_s(t)$. We will calculate the power spectrum of this mode to establish the framework in which we describe phase noise in general. In all summations, it should be assumed that the relevant summation index runs over cavity mode numbers with finite spectral weight.

The field of this mode can be written in the time domain

$$E_s(t) = a_s e^{-i\omega_0 t + i\phi_s(t)} \ . \tag{7.1}$$

Here, we take the Fourier transform to be symmetric with a positive-definite frequency kernel, so that

$$E_s(\omega) = \frac{1}{\sqrt{2\pi}} \int_{-\infty}^{\infty} dt' E_s(t') e^{i\omega t'} \ . \tag{7.2}$$

Therefore, the power spectrum of this mode can be written via the Weiner-Khinchin theorem as

$$P_s^{(1)}(\omega) = |E_s(\omega)|^2 = \frac{1}{2\pi} \int_{-\infty}^{\infty} d\tau \langle E_s^*(t) E_s(t+\tau) \rangle e^{i\omega\tau} \tag{7.3}$$

where the braces denote the time-average. While the exact nature of this time-average depends on the physical system, we will utilize a result used to describe a typical phase diffusion process [5, 6]. We assume that the phase noise term is statistically stationary and Markovian in nature [7], thus allowing us to define Γ_s as a fixed rate of decoherence events whose occurrence follows a Poissonian distribution for the random

phase $\phi_s(t)$. Under these assumptions we find the time-average is

$$\langle e^{i(\phi_s(t+\tau)-\phi_s(t)} \rangle = e^{-\Gamma_s|\tau|} \ . \tag{7.4}$$

These assumptions are valid for most realistic light sources, and we note that providing a microscopic description of all possible decoherence mechanisms for a light source is not salient to our goal here, though this theory could be readily extended to incorporate various other spectral lineshapes which result from a variety of non-Markovian dephasing processes in a laser. We define the "coherence time" of this mode as $\tau_c = 1/\Gamma_s$, and with this in mind, we find that the final power spectrum is a Lorentzian of the form

$$P_s^{(1)}(\omega) = \frac{|a_s|^2}{\pi} \frac{1}{(\omega - \omega_0)^2 + \Gamma_s^2} \ . \tag{7.5}$$

7.2.2 First-Order Coherence of a Frequency Comb

To quantify the effect of phase noise in the frequency comb field, we perform an analysis of its first order coherence. For simplicity, we will assume the amplitude is time independent and equal for all modes, though incorporating a time-varying amplitude would simply impose a spectral envelope on the output of each light source.

The electric field of our generic frequency comb can be written

$$E_{comb}(t) = \sum_n a_0 e^{-i\omega_n t + \phi_n(t)} \tag{7.6}$$

with the frequency of each mode written in terms of the repetition rate in the carrier-envelope offset frequency, $\omega_n = n\omega_r + \omega_{ceo}$, and with $\phi_n(t)$ the time-dependent phase noise term for each tooth. Additionally, each mode will have two components in its noise diffusion term. One term is common to all modes and corresponds to noise associated with ω_{ceo}, which could be due to thermal fluctuations in the lasing medium or

spontaneously emitted photons within the cavity leading to time-dependent changes in total cavity dispersion, for instance. The other noise term is due to fluctuations in ω_r and can be associated with mechanical and thermal noise in the shape, size, or alignment of the cavity. Additionally, pump intensity fluctuations resulting from a number of sources can contribute to both common and repetition-rate phase noise [8]. Explicitly, for a frequency comb we rewrite the phase noise parameter to represent these fluctuations and obtain

$$\phi_n(t) = \theta(t) + n\psi(t) \tag{7.7}$$

where $\theta(t)$ is a noise term detailing the fluctuations common to all teeth and $\psi(t)$ is the phase noise in the relative spacing between teeth.

As a result, we can rewrite the total comb field to read

$$E_{comb}(t) = a_0 e^{-i\omega_{ceo}t + i\theta(t)} \sum_n e^{-in\omega_r t + in\psi(t)} \ . \tag{7.8}$$

One can model the noise in the repetition rate in two ways. For a generic frequency comb, if quantum effects dominate the noise profile of a given light source, then one can re-index equation 7.8 such that the n = 0 mode will be the optical carrier frequency and one would thus replace ω_{ceo} with the carrier frequency in the following analysis. Here, we will limit our scope to modelling technical noise (as opposed to quantum noise) only (which should typically dominate in a noisy frequency comb), such that the n^{th} mode is ω_{ceo}. To calculate the power spectrum of the comb, $P(\omega) = |E_{comb}(\omega)|^2$, we need to first calculate the first-order coherence of the comb field

$$g^{(1)}(\tau) = \langle E^*(t)E(t+\tau)\rangle = \int_{-\infty}^{\infty} \mathrm{dt}\ E^*(t)E(t+\tau)\ . \tag{7.9}$$

We will use the un-normalized forms of coherence functions to simplify the general-

ization of our calculation. We find that

$$\begin{aligned}\langle E^*_{comb}(t)E_{comb}(t+\tau)\rangle &= \sum_{m,n}\langle E^*_n(t)E_m(t+\tau)\rangle \\ &= \sum_n \langle E^*_n(t)E_n(t+\tau)\rangle\end{aligned} \tag{7.10}$$

where we have used the fact that $\langle E^*_n(t)E_m(t+\tau)\rangle = \langle E^*_n(t)E_m(t+\tau)\rangle\delta_{mn}$ since the time-average of the fields will only be non-zero when $n = m$. Assuming that the phase noise correlations are of the same type as in Equation 7.4, we have

$$\begin{aligned}\langle E^*_{comb}(t)E_{comb}(t+\tau)\rangle &= |a_0|^2 e^{-i\omega_{ceo}\tau-\Gamma_\theta|\tau|} \\ &\quad\times\sum_n e^{-in\omega_r\tau-n\Gamma_\psi|\tau|}\end{aligned} \tag{7.11}$$

where Γ_θ and Γ_ψ are the decoherence rates in the phase common to each mode and between modes respectively. The power spectrum of $g^{(1)}(\tau)$ is therefore

$$P^{(1)}_{comb}(\omega) = \frac{|a_0|^2}{\pi}\sum_n \frac{1}{(\omega-\omega_n)^2+(\Gamma_\theta+n\Gamma_\psi)^2} \tag{7.12}$$

This result is illustrative because for a single frequency comb mode (with a coherence time of $\tau_c = 1/(\Gamma_\theta + n\Gamma_\psi)$), there is no difference in linewidth between its first-order correlation and a generic electric field mode with the same coherence lifetime. Therein lies the subtlety of this analysis: when simply comparing the power spectra of a frequency comb and, say, an incoherent assembly of modes with the same center frequencies as the frequency comb and the same coherence times for each mode, one cannot immediately distinguish between the two. In the development of novel frequency comb sources, it is therefore not simply enough to show that a device emits a 'comb-like' spectrum. Great care must be taken to demonstrate mutual coherence between the electric field modes. As we shall see, this mutual coherence is the crucial advantage that a frequency comb provides over other light sources.

7.2.3 Second-Order Coherence of a Frequency Comb

To separate the common noise and the repetition rate noise, we need to perform a second-order coherence calculation. The (unnormalized) second order coherence is measured by the auto-correlation of the intensity and can be written

$$g^{(2)}(\tau) = \langle I(t)I(t+\tau)\rangle = \int_{-\infty}^{\infty} \mathrm{dt}\ I(t)I(t+\tau). \tag{7.13}$$

We are particularly interested in the coherence of the interference between the various modes, because the common noise will mix out of the auto-correlation, but the repetition rate noise will remain. Using Equation 7.6 with noise defined by Equation 7.7, the intensity of a comb can be written

$$I_{comb}(t) = |a_0|^2 \sum_n \sum_m e^{-i(n-m)\omega_r t} e^{i(n-m)\psi(t)}. \tag{7.14}$$

Here, we introduce a new summation integer $k = n - m$, such that

$$-\left(\max(n) - \min(n)\right) < k < \left(\max(n) - \min(n)\right)\ . \tag{7.15}$$

This allows us to rewrite the double summation as a single summation over k. Thus the intensity correlation of a frequency comb is written

$$\langle I_{comb}(t)I_{comb}(t+\tau)\rangle \sim |a_0|^4 \sum_k \sum_{k'} e^{-ik'\omega_r\tau} \langle e^{-i(k+k')\omega_r t} e^{i(k\psi(t)+k'\psi(t+\tau)}\rangle. \tag{7.16}$$

The presence of the exponential $e^{-i(k+k')\omega_r t}$ in the time average will produce a Kronecker delta $\delta_{-k,k'}$, allowing us to sum over k' to obtain

$$\langle I_{comb}(t)I_{comb}(t+\tau)\rangle \sim |a_0|^4 \sum_k e^{-ik\omega_r\tau} \langle e^{ik(\psi(t+\tau)-\psi(t))}\rangle. \tag{7.17}$$

Assuming again that $\psi(t)$ has the same decoherence characteristics as in Equation 7.4, we find the the second-order coherence to be

$$\langle I_{comb}(t) I_{comb}(t+\tau) \rangle \sim |a_0|^4 \sum_k e^{-ik\omega_r \tau - k\Gamma_\psi |\tau|} \ . \tag{7.18}$$

Then, taking the Fourier transform of the intensity beatnote to obtain its power spectrum, we have (omitting the DC term)

$$P^{(2)}_{comb}(\omega) = \frac{|a_0|^4}{\pi} \sum_k \frac{k\Gamma_\psi}{(\omega - k\omega_r)^2 + (k\Gamma_\psi)^2}. \tag{7.19}$$

The linewidth of the lowest frequency intensity beatnote is solely due to decoherence from repetition rate fluctuations. The common noise term has cancelled out, and we can now therefore separately quantify it in principle, by comparing the linewidths of the power spectra of $g^{(1)}(\tau)$ for the nth and $g^{(2)}(\tau)$ of the lowest frequency beatnote. To quantify the repetition rate noise, a portion of the comb output is directed to a photodetector (which effectively performs an intensity auto-correlation in the time-domain). The width of this beatnote corresponds to the time-domain fluctuations of ω_{rep}. To quantify the noise in ω_{ceo}, a portion of the comb is sent into an f to $2f$ interferometer, quantifying ω_{os} and its noise [9].

7.2.4 Filtering a White Light Source Through a Fabry-Pérot Cavity

In order to examine the experimental advantages that a frequency comb provides over a filtered, incoherent light source, we turn to discuss the properties of a white light source filtered through a high-Q Fabry-Pérot cavity. Such a lightsource could mimic the spectrum of a frequency comb, and is *a priori* a possible output for many comb-like light sources without a mechanism to ensure modelocking bewteen the

phasese of each mode. We will start with an incoherent input field of the form

$$E_{in}(t) = a_0 e^{i\phi(t)} \tag{7.20}$$

where the phase $\phi(t)$ is the total noise term with a decoherence rate of Γ_w such that

$$\langle e^{i\phi(t+\tau)-\phi(t)} \rangle = e^{-\Gamma_w|\tau|}. \tag{7.21}$$

We filter the input cavity with the half-width at half maximum linewidth γ and equally spaced center frequencies at integer multiples of ω_r. The filtered electric field is now

$$E_f(t) = \sum_n a_0 \gamma \int_{-\infty}^{t} \mathrm{dt'} e^{i\phi(t')-in\omega_r(t-t')-\gamma(t-t')}. \tag{7.22}$$

Due to the nature of $\phi(t)$ the phase fluctuations emerging at each center frequency $n\omega_r$ will not be correlated with each other. The coherence of the filtered field is a convolution of the individual coherences, yielding

$$\begin{aligned} \langle E_f^*(t) E_f(t+\tau) \rangle = \frac{1}{2\pi} \sum_n \int_{-\infty}^{\infty} d\tau' \langle E_{in}^*(t) E_{in}(t+\tau) \rangle \\ \times \langle L_n(t)^*(t) L_n(t+\tau-\tau') \rangle \end{aligned} \tag{7.23}$$

where $L_n(t)$ is the time domain representation of a single Lorentzian in the Fabry-Pérot cavity,

$$L_n(t) = \gamma e^{-in\omega_r t-\gamma t}. \tag{7.24}$$

The first-order coherence for the nth filtered field is then

$$g_{f,n}^{(1)}(\tau) = \frac{\Gamma_w + \gamma}{2} e^{-in\omega_r\tau} \left[\frac{e^{-\gamma|\tau|} + e^{-\Gamma_w|\tau|}}{\Gamma_w + \gamma} + \frac{e^{-\Gamma_w|\tau|} - e^{-\gamma|\tau|}}{\gamma - \Gamma_w} \right]. \tag{7.25}$$

Here, we can make the generalization that $\Gamma_w >> \gamma$ for the case in which white light is filtered through a narrow linewidth Fabry-Pérot cavity, so the coherence in this approximation reduces to

$$g^{(1)}_{f,n}(\tau) \approx e^{-in\omega_r\tau-\gamma\tau}, \tag{7.26}$$

the same as that of our Lorentzian filter. Here it is important to emphasize that, though the coherence time has lengthened significantly due to the filtering, the actual field for a single mode is

$$E_{f,n}(t) = a_0\gamma e^{-in\omega_r t-\gamma t}\int_{-\infty}^{t} dt' e^{i\phi(t')+in\omega_r t'+\gamma t'}, \tag{7.27}$$

which retains the incoherent phases in the original white light source around the peak center frequencies, $n\omega_r$. Thus, the resulting filtered fields will not have good mutual coherence or retain periodicity in the time domain.

We have reached a point in our analysis where we can start to differentiate a frequency comb from an incoherent light source. To do this, we compare the power spectrum obtained in Equation 7.19 with that obtained from a filtered white light source. For the sake of comparison, we will assume that they both have the same coherence time as the nth comb tooth $\tau_c = 1/(\Gamma_\theta + n\Gamma_\psi)$ (as to be indistinguishable in the first-order measurement). We thus rewrite the filtered white light field (Equation 7.22) as approximately a sum of uncorrelated modes with first-order coherence $\gamma = 1/\tau_c$ such that

$$E_f(t) \sim E_w(t) = a_0\sum_n e^{-in\omega_r t+i\phi_n(t)}\ , \tag{7.28}$$

where the random phase noise of $\phi_n(t)$ has the property $\langle e^{i\phi_n(t+\tau)-\phi_n(t)}\rangle = e^{-\gamma|\tau|}$ as in Section 7.2.1. Following the same steps as in the frequency comb case in section

7.2.3, the intensity correlation of a filtered white light source is

$$\langle I_w(t) I_w(t+\tau)\rangle \sim |a_0|^4 \sum_k e^{-ik\omega_r\tau} \langle e^{i(\phi_n(t)-\phi(t+\tau))} e^{-i(\phi_m(t)-\phi_m(t+\tau))}\rangle \ , \tag{7.29}$$

which simplifies to

$$\langle I_w(t) I_w(t+\tau)\rangle \sim |a_0|^4 \sum_k e^{-ik\omega_r\tau - 2\gamma|\tau|} \ , \tag{7.30}$$

with $k = n - m$. We have used the fact that the modes have phase variations are uncorrelated and statistically stationary. The power spectrum is then found to be

$$P_w^{(2)}(\omega) = \frac{|a_0|^4}{\pi} \sum_k \frac{2\gamma}{(\omega - k\omega_r)^2 + 4\gamma^2} \ . \tag{7.31}$$

Substituting the fact that $\gamma = 1/\tau_c$,

$$P_w^{(2)}(\omega) = \frac{|a_0|^4}{\pi} \sum_k \frac{2(\Gamma_\theta + n\Gamma_\psi)}{(\omega - k\omega_r)^2 + 4(\Gamma_\theta + n\Gamma_\psi)^2} \ , \tag{7.32}$$

we can compare the power spectrum of the intensity beatnotes to that of a frequency comb. We see now a major difference between the beating of two frequency comb lines versus the beating of two incoherent sources with the same coherence time – while the first-order coherence is the same for both sources, the second-order calculation shows that noise in the comb parameters can sometimes cancel due to the correlations between field modes. The incoherent sources would not have any correlated noise by definition, so their second-order coherence times add when performing an experiment whose observable is an intensity cross-correlation. We also note that, while the linewidth of frequency comb modes changes with mode k, a filtered white light source has a constant linewidth for all modes.

7.3 Numerical Comparison Between a Frequency Comb and Filtered White Light

To demonstrate the crucial difference that phase coherence makes in a light source outputting periodically-spaced spectral modes, we numerically simulate a noisy frequency comb and a filtered white light source based upon the models given in Section 7.2.4. We then compare the results for two different experimental observables. The first will be a comparison between the first-order coherence of the fields for each light source, showing graphically the fact that a first-order coherence measurement of a field is not enough to establish phase coherence between modes. The second is a calculation of the intensity auto-correlation, demonstrating that the mutual coherence in the comb teeth lead the RF beat spectra to be dramatically different between the two light sources. We will also demonstrate the practical difference phase coherence between modes makes between teeth in a dual-comb spectroscopy experiment. Strictly speaking, we demonstrated that the noise present in the RF comb generated by beating two frequency combs together is 'correctable' and the noise present in the RF comb generated by beating two filtered white light sources is not. Finally, we simulate a simple frequency metrology experiment, wherein we beat two optical frequencies with each of our simulated comb and white light sources. This demonstration shows that the mutual coherence present between comb teeth allows for a nearly resolution-limited measurement of the frequency difference between the two light sources, while the same measurement conducted with the filtered white light is not possible. We choose to simulate dual-comb spectroscopy and frequency metrology conducted with each light source because they are the two most ubiquitous comb applications which *require* coherence between modes, and because they form the basis of a wide array of comb-based measurement techniques [10, 11].

7.3.1 First- and Second-Order Coherences of a Frequency Comb and Filtered White Light

To numerically simulate the filtered white-noise spectrum, we first generate a field of the form presented in equation 7.1 with decoherence events occcurring at an average rate of $\Gamma_s = 2$ ps^{-1}. We simulate decoherence events in the white light spectrum by random jumps in the value of $\phi_s(t)$ uniformly distributed over the interval $\Delta\phi_s(t) \in [0, 2\pi]$. We use picoseconds as a reference unit, but the time- and frequency-domain resolution and bandwidths our simulated spectra are arbitrary and the results are therefore generally applicable to the outputs of generic comb and filtered white light sources. We then filter the white light through a Fabry-Pérot cavity with a half-width, half maximum linewidth $\gamma = 0.8/(2\pi)$ GHz by multiplying the white light spectrum by a series of fifteen Lorentzian modes in the frequency domain, spaced by $\omega_r = 0.2$ rad. $\cdot$THz.

To generate the comb spectrum, we simulate a field of the form presented in equation 7.8 with fifteen comb 'teeth.' For comparison's sake, we choose a comb decoherence rate of $\Gamma_c = .01$ ps^{-1}. We then generate simulated phase noise $\theta(t)$ and $\psi(t)$ by generating a series of random dephasing events (occurring randomly) at an average rate of Γ_c with phase jumps in the intervals $\delta\theta(t) \in [0, 0.005\pi]$ and $\delta\psi(t) \in [0, 0.0022\pi]$. These are chosen such that the linewidth of the central comb tooth is identical to that of the filtered white-light spectrum, while retaining realistic and independent noise characteristics for both the repetition rate and offset frequency of the comb. The smaller phase jumps in the comb spectrum are justified by the fact that the main sources of noise in a comb occur either on a much slower timescale (cavity fluctuations) or cause much less relative phase noise (spontaneous emission of a photon into a given mode) when compared to a white light spectrum.

Figure 7.2 is a summary and comparison of the basic properties of each simulated field. This figure demonstrates the *prima facie* subtle difference between observable

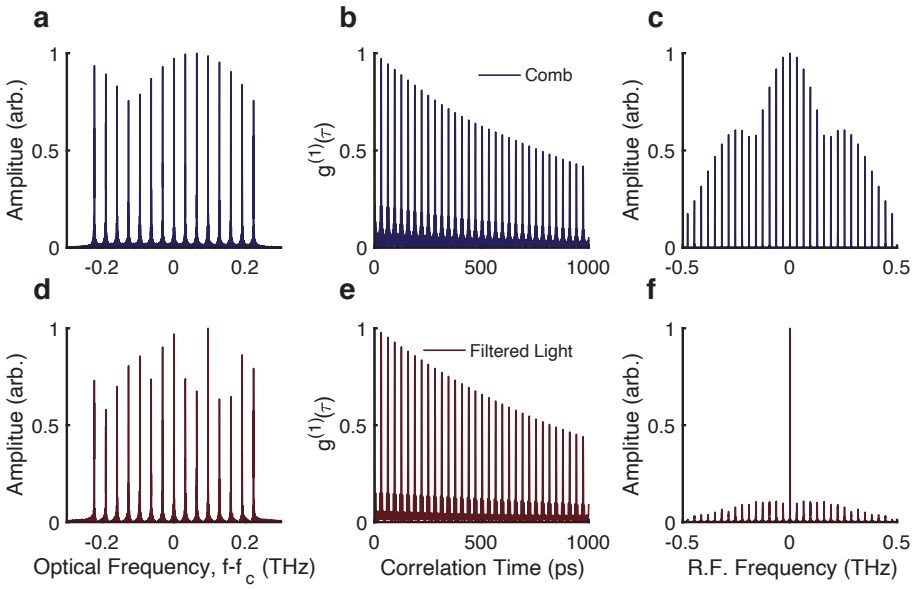

Figure 7.2: A comparison between features of a coherent frequency comb and filtered white light with the same spectral properties. (a) The optical spectrum, (b) first-order field correlation, and (c) RF intensity auto-correlation of the frequency comb output. (d-f) The same numerical results for a filtered white light source. Though the numerically calculated first-order coherence of the two sources are indistinguishable, the auto-correlation demonstrates the dramatic difference between the coherent comb and the incoherent, filtered white light.

characteristics of the two fields. In Figure 7.2 (a)and (d), we compare the optical spectra of the generated comb and filtered white light sources. The linewidths of the modes are all nearly identical, and although the spectral amplitudes of the white light modes are less uniform, this is simply a numerical artifact and not applicable to generally distinguishing between a coherent and incoherent source in practice. In Figure 7.2(b) and (e), we show the calculated first-order coherence $g^{(1)}(\tau)$ of each field. As demonstrated in our analytical results, the first-order coherence of the fields are nearly identical. It is not simply enough to show that a field is first-order coherent if one is demonstrating that a light source is a frequency comb. Only in a higher-order coherence measurement, such as the RF intensity beat spectrum (Figure 7.2 (c) and (f)) does the effect of the mutual coherence between modes become apparent. In the case of a frequency comb, this beat spectrum should show a series of teeth separated by $\omega_r/(2\pi)$ whose amplitudes are comparable with the zero frequency comb tooth (which corresponds to self-beating of each tooth), and whose widths correspond directly to the rep-rate noise $\psi(t)$. In the case of the filtered white light, however, the RF beat spectrum takes on a distinctly different shape. The zero-frequency tooth dominates the spectrum because each 'tooth' is coherent with itself but not with the other modes present in the field. The higher-frequency beatnotes, if detectable, will be suppressed by an order of magnitude or more due to the lack of mutual coherence between the modes.

7.3.2 The Importance of Phase Coherence in Dual-Comb Spectroscopy

Dual-comb and multi-comb spectroscopy have become ubiquitous methods for conducting rapid, extremely high-resolution time- and frequency-domain studies on an enormous array of systems [10, 12]. Furthermore, the principles of multi-comb spectroscopy have been employed in precision distance ranging and rapid distance metrology applications. Because of the wide-spread use of these techniques, it is

important to underscore the essential role that mutual coherence between the comb teeth in a frequency comb plays in these experiments.

To see the crucial nature that the mutual coherence between the comb teeth plays in a practical experiment, we will first analytically calculate, numerically simulate, and attempt to noise-correct symmetric RF spectra generated with each type of light source. Suppose we have two comb fields,

$$E_a(t) = e^{-i\omega_{ceo,a}t+i\theta_a(t)} \sum_n a_n e^{-in\omega_{rep,a}t+in\psi_a(t)} \tag{7.33}$$

and

$$E_b(t) = e^{-i\omega_{ceo,b}t+i\theta_b(t)} \sum_m b_m e^{-im\omega_{r,b}t+im\psi_b(t)} \ . \tag{7.34}$$

We then combine the fields and send the combined dual-comb signal to a detector. If we neglect the D.C. terms (typical for an RF measurement), and ensure that $\omega_{ceo,a} \neq \omega_{ceo,b}$, then the dual comb total intensity is

$$I_{ab}(t) \propto E_a^*(t)E_b(t) + E_a(t)E_b^*(t). \tag{7.35}$$

We therefore have that

$$I_{ab}(t) \propto e^{-i\Delta\omega_{ceo}t+i\theta_a(t)-i\theta_b(t)} \times \sum_{n,m} a_n b_m^* e^{-in\omega_{r,a}+im\omega_{r,b}+in\psi_a(t)-im\psi_b(t)} + c.c. \ . \tag{7.36}$$

If both combs have phase noise parameters which carry the aforementioned Poissonian properties, their sums and differences will also be of the same character. We can therefore define $\Delta\theta(t) = \theta_a(t) - \theta_b(t)$ as the joint carrier-offset phase noise of the RF comb. We examine the kth term in the double summation where $n = m = k$ in

equation 7.36 and define $\Delta\omega_r = \omega_{r,b} - \omega_{r,a}$

$$I_{ab}(t) \propto e^{-i\Delta\omega_{ceo}t+i\Delta\theta(t)}\Bigg(\sum_k a_k b_k^* e^{-ik\Delta\omega_r t+ik\Delta\psi(t)}+ \sum_{m,n,n\neq m,} a_n b_m^* e^{-in\omega_{r,a}+im\omega_{r,b}+in\psi_a(t)-im\psi_b(t)}\Bigg) + c.c.. \quad (7.37)$$

where $\Delta\psi(t) = \psi_a(t) - \psi_b(t)$. For a detector of finite bandwidth, we can ignore all higher-order RF replicas, as long as $\max(k\Delta\omega_r) < \max(\omega_{r,a}, \omega_{r,b})/2$ such that the RF comb teeth do not wrap into higher- and lower-order replicas. Discarding the higher-order replicas, we have

$$I_{ab}(t) \propto e^{-i\Delta\omega_{ceo}t+i\Delta\theta(t)} \sum_k a_k b_k^* e^{-ik\Delta\omega_r t+ik\Delta\psi(t)} + c.c. \; . \quad (7.38)$$

Comparing Equation 7.38 to Equation 7.6, it is clear we have a comb-like structure in the intensity of the dual-comb beat. We can now define new variables $c_k = a_k b_k^*$ as the complex amplitude, $\omega_k = \Delta\omega_{ceo} + k\Delta\omega_r$ as the central frequency and $\psi_k(t) = \Delta\theta(t) + k\Delta\psi(t)$ as the phase noise of each mode. The dual-comb intensity of the lowest-order replica is now written

$$I_{ab}(t) \propto \sum_k c_k e^{-i\omega_k t+i\psi_k(t)} + c.c. \; . \quad (7.39)$$

Rewriting slightly, we have

$$I_{ab}(t) \propto \sum_k 2|c_k| \cos(\omega_k t + \psi_k(t) + \theta_{k0}) \quad (7.40)$$

where θ_{k0} is a constant phase stemming from the amplitudes c_k.

To calculate the intensity power spectrum of the two combs a and b, we evaluate

the integral

$$P_{ab}^{(2)}(\omega) = \frac{1}{\sqrt{2\pi}} \int_{-\infty}^{\infty} d\tau \langle I_{ab}(t) I_{ab}(t+\tau) \rangle e^{i\omega\tau} \ . \tag{7.41}$$

The time-averaged intensity can be written

$$\begin{aligned} \langle I_{ab}(t) I_{ab}(t+\tau) \rangle \propto & \sum_k \sum_{k'} |c_k||c_{k'}| \\ & \times \langle \cos(\omega_k t + \psi_k(t) + \theta_{k0}) \cos(\omega_{k'}(t+\tau) + \psi_{k'}(t+\tau) - \theta_{k'0}) \rangle \end{aligned} \tag{7.42}$$

Utilizing the cosine product-to-sum identity and noting the following relations

$$\langle \cos((\omega_{k'} + \omega_k)t + ...) \rangle = 0 \tag{7.43}$$

and

$$\langle \cos((\omega_{k'} - \omega_k)t + ...) \rangle = \delta_{kk'} \langle \cos((\omega_{k'} - \omega_k)t + ...) \rangle, \tag{7.44}$$

we sum over k' to obtain a simplified time-average

$$\langle I_{ab}(t) I_{ab}(t+\tau) \rangle \propto \sum_k |c_k|^2 \langle \cos(\omega_k \tau + \psi_k(t+\tau) - \psi_k(t)) \rangle \tag{7.45}$$

Now, we need to treat the noise terms delicately in the time-average; we can rewrite the previous result

$$\langle I_{ab}(t) I_{ab}(t+\tau) \rangle \propto \frac{1}{2} \sum_k |c_k|^2 (e^{-i\omega_k \tau} \langle e^{i(\psi_k(t) - \psi_k(t+\tau))} \rangle + c.c.) \ . \tag{7.46}$$

We have now

$$\langle e^{i(\psi_k(t) - \psi_k(t+\tau))} \rangle = \langle e^{ik(\Delta\psi(t) - \Delta\psi(t+\tau))} \rangle \langle e^{i(\Delta\theta(t) - \Delta\theta(t+\tau))} \rangle \ . \tag{7.47}$$

Since $\Delta\theta(t) = \theta_a(t) - \theta_b(t)$ and $\Delta\psi(t) = \psi_a(t) - \psi_b(t)$, we have

$$\langle e^{ik(\Delta\psi(t)-\Delta\psi(t+\tau))}\rangle = \langle e^{ik[(\psi_a(t)-\psi_a(t+\tau))+(\psi_b(t)-\psi_b(t+\tau))]}\rangle \tag{7.48}$$

and

$$\langle e^{ik(\Delta\theta(t)-\Delta\theta(t+\tau))}\rangle = \langle e^{i[(\theta_a(t)-\theta_a(t+\tau))+(\theta_b(t)-\theta_b(t+\tau))]}\rangle \ . \tag{7.49}$$

If we assume that the noise of both combs is uncorrelated, then

$$\langle e^{i(\psi_k(t)-\psi_k(t+\tau))}\rangle = e^{-k(\Gamma_\psi,a+\Gamma_\psi,b)|\tau|-(\Gamma_\theta,a+\Gamma_\theta,b)|\tau|} \tag{7.50}$$

We define $\Gamma_{j,k} = k(\Gamma_{\psi,a} + \Gamma_{\psi,b}) + (\Gamma_{\theta,a} + \Gamma_{\theta,b})$ as the joint dephasing rate between the two beating modes, then

$$\langle I_{ab}(t) I_{ab}(t+\tau)\rangle \propto \frac{1}{2}\sum_k |c_k|^2 (e^{-i\omega_k\tau - \Gamma_{j,k}|\tau|} + c.c.) \ . \tag{7.51}$$

Finally, we can write

$$P_{ab}^{(2)}(\omega) \propto \frac{1}{\sqrt{2\pi}}\sum_k |c_k|^2 \int_{-\infty}^{\infty} d\tau \ e^{i\omega\tau - \Gamma_{j,k}|\tau|} \ \cos(\omega_k\tau) \tag{7.52}$$

and evaluate the integral to obtain

$$P_{ab}^{(2)}(\omega) \propto \sqrt{\frac{2}{\pi}}\sum_k \frac{|c_k|^2}{(\omega-\omega_k)^2 + \Gamma_{j,k}^2} \ . \tag{7.53}$$

where we take the positive-frequency only replica of this spectrum, as is done experimentaly. Prior to doing any numerical simulations, it is important to point out the following: because the two combs were self-coherent to begin with, their beating produces a *coherent* RF comb. Strictly speaking, the total RF comb (including replicas) is a surjective mapping of two sets of comb teeth onto a corresponding set of sum-

and difference-frequency beatings.

If, instead, we were beating two filtered white light sources together with slightly different mode spacings, we would have (assuming fields of the form in Equation 7.27 and equal linewidths γ)

$$I_{ab,f}(t) \sim \sum_k d_k e^{-ik\Delta\omega_r t - 2\gamma t} \times \int_{-\infty}^{t} dt' e^{i\phi(t') + ik\omega_{ra}t' + \gamma t'} \int_{-\infty}^{t} dt'' e^{i\phi(t'') + ik\omega_{rb}t'' + \gamma t''} + \langle c.c. \rangle \ . \quad (7.54)$$

In contrast to the case of beating frequency combs, there remain highly uncorrelated phase fluctuations through the filtering of white light through cavities a and b. By definition, the phase noise in the vicinity of $k\omega_{ra}$ would have no correlation with the noise in vicinity either $(k+1)\omega_{ra}$ or $k\omega_{rb}$, thus retaining the incoherence present between the modes in the original filtered sources.

To illustrate the importance of mutual coherence between the electric field modes in a frequency comb light source, we shift to a numerical simulation of dual-comb spectroscopy, both with coherent combs and filtered white light. We generate two sets of combs and filtered sources with the same dephasing properties of the sources in Figure 7.2. We use the same mode spacing for each light source, with $\omega_{r,a} = 0.2$ rad.·THz and $\omega_{r,b} = 0.21$ rad. · THz so that $\Delta\omega_r = 0.01$ rad.·THz. We again simulate sources with 15 modes. In Figure 7.3 we show two intensity spectra calculated by beating two combs and two filtered white light sources together. We will concern ourselves only with the positive-frequency beat term in the dual-comb spectrum, $E_a^*(t)E_b(t)$, because in a real dual-comb experiment one would apply a nonzero $\Delta\omega_{ceo}$ frequency to separate the positive and negative-frequency replicas of the RF signal.

It is not *a priori* possible to tell the difference between these two light sources simply from the frequency-domain RF spectra because the linewidths of each beat-

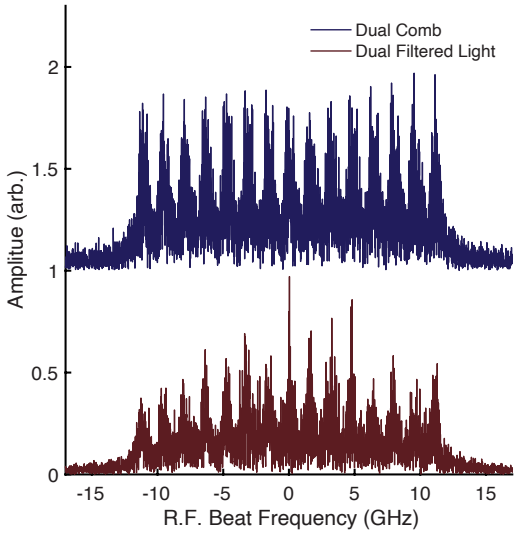

Figure 7.3: A comparison between the RF spectra generated by beating either two combs or two filtered white light sources together. Note that their linewidths are nearly identical.

ing mode simply add when beating together. However, there is a crucial difference between the noise in these spectra that render the dual-comb RF far more useful. Because the comb teeth are mutually coherent and the noise is correlated from tooth to tooth, it is relatively straightforward to correct noisy DCS signals. In the case of an incoherent light source, this is not true.

To demonstrate this, we apply a very simple noise correction algorithm to the data in Figure 7.3. We first select, conjugate, and mix the central tooth with the entire comb, thereby cancelling the common noise for all teeth in the comb. We then perform a digital self-correlation to measure the repetition rate noise, and re-sample the data to cancel it and all attendant harmonics as a function of tooth number [13]. The result of doing this can be seen in Figure 7.4. For the DCS signal, the simple correction has resulted in pixel-wide comb teeth with little remaining noise. In the case of the incoherent RF comb, it is impossible to identify the second-order RF autocorrelation in the resampling process due to the lack of coherence, and therefore it is not possible to correct the noise in the incoherent RF spectrum. This is evident by

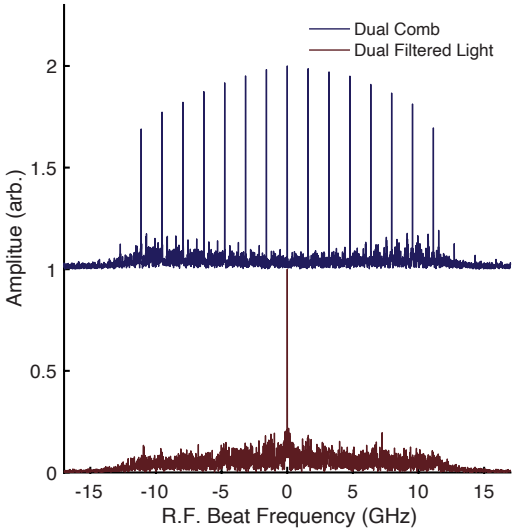

Figure 7.4: A comparison between the corrected RF spectra generated by beating either two combs or two filtered white light sources together.

the fact that the result of the noise removal scheme is that the central tooth becomes well corrected (because it is coherent with itself), but the remaining spectrum is far more noisy than the original RF comb, to the extent that it is extremely difficult to identify other 'teeth.'

To further demonstrate why this difference in coherence is important, we generate a mock DCS spectrum by duplicating the pairs of optical spectra and filtering them through a Gaussian 'absorption' profile. It is commonplace to take the amplitudes of the DCS teeth and generate a Beer's Law absorption profile with them, something that is not experimentally feasible if they are not coherent. We use the same noise correction algorithm outlined above and attempt to take the teeth of each corrected RF comb and calculate the mock absorption profile. The results of this process are presented in Figure 7.5. The dramatic contrast between results obtained with a coherent light source and those obtained with the filtered incoherent light source demonstrates the crucial nature that the correlation between modes present in a coherent light source plays in a practical application. In other words, in the search for suitable combs for DCS applications, it is not simply enough to show a comb-

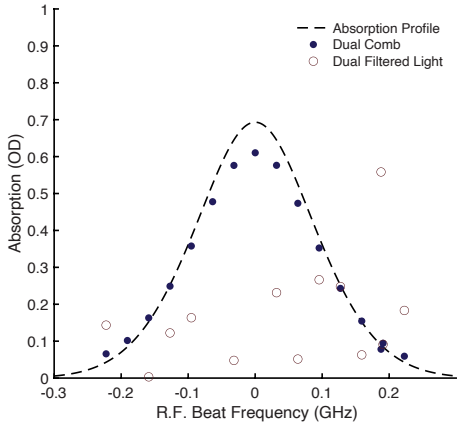

Figure 7.5: A comparison between calculated absorption profiles using each light source.

like spectrum. It is *also* not simply enough to demonstrate an RF beat spectrum generated by beating two comb-like optical spectra. One must show that a light source is coherent first before it can be a feasible DCS platform.

Our simple noise correction algorithm is not perfect, however. It does not quite capture the modulation depth induced by the Gaussian filter, but that is simply because the offset frequency noise inherent in the comb teeth cause a small amount of numerical averaging as the tooth instantaneously sweeps through each region of the feature causing its amplitude to be slightly averaged about the neighborhood of points in frequency space near line center. In a practical experiment, this can be corrected by using as short of a data record with as high of a sampling rate as possible or by more complex noise retrieval and removal schemes [14].

7.3.3 The Importance of Phase Coherence in Frequency Metrology

Another area in which frequency combs have found wide application, and indeed their first and arguably most important use, is in frequency metrology experiments [9]. The basic principle is as follows. One has a laser at some frequency ω_l and an absolute frequency reference (for instance an optical or RF atomic clock) at a second frequency ω_{ref}. The frequency comb is then used to measure the absolute

frequency difference between the two frequencies. Without loss of generality, assume that $\omega_l > \omega_{ref}$ and we write the laser field as

$$E_l(t) = a_l e^{i\omega_l t + i\phi_l(t)} \tag{7.55}$$

where $\phi_l(t)$ is the phase noise in the laser field, and

$$E_{ref}(t) = a_{ref} e^{i\omega_{ref} t + i\phi_{ref}(t)} \tag{7.56}$$

where $\phi_{ref}(t)$ and is the phase noise in the reference field. We want to measure the difference frequency $\omega_{diff} = \omega_l - \omega_{ref}$ between the two fields. If the difference frequency is large (say on the order of terahertz), it is not feasible to directly beat the two fields together as this pushes past the limits of electronic detector signals. Instead, a comb is used to provide a 'gear' to step-down the frequency differences into something measurable by a typical photodetector - this happens by taking the comb and beating it with both $E_l(t)$ and $E_{ref}(t)$, and then mixing those two beatnotes together. Suppose our frequency comb is of the same form as before

$$E_{comb}(t) = e^{-i\omega_{ceo} t + i\theta(t)} \sum_n a_n e^{-in\omega_r t + in\psi(t)} \ . \tag{7.57}$$

then we can write $\omega_l = \omega_n + \delta\omega_l$ and $\omega_{ref} = \omega_m + \delta\omega_{ref}$ where $\omega_n = n\omega_r + \omega_{ceo}$ and $\omega_m = m\omega_r + \omega_{ceo}$ such that $\omega_{diff} = (n-m)\omega_r + (\delta\omega_l - \delta\omega_{ref})$. Then the beatnotes between the two fields and the combs (ignoring DC terms) will be at $\omega_{beat} = (\delta\omega_l - \delta\omega_{ref})$. Since it is not experimentally challenging to obtain both m and n indices and hence the comb frequencies ω_m and ω_n (for instance, by using a wavemeter to measure ω_l and locking the comb in some way to ω_{ref}), one obtains the difference frequency between the frequency of interest and the reference with extremely high precision (easily better than 1 part in 10^{14}). Importantly, because mth and nth teeth are mutually coherent,

the mixing process cancels much of the noise present in the initial comb teeth, leaving a much lower uncertainty in the eventual RF line center than is present when using just a filtered white light source as the 'gear' between the laser and the reference. It should be noted that optical frequency synthesis (constituting a third major comb-based application) is essentially the reverse of the above process, so the following discussion is applicable to that case as well.

As in the previous sections, we will analyze this procedure in detail and derive the RF linewidth of the eventual difference frequency beatnote and then demonstrate the advantage that a coherent frequency comb offers in this case by replicating a simple frequency metrology experiment with our numerically simulated spectra.

Utilizing the fields in Equations 7.55, 7.56, and 7.57, the RF intensities of the lowest order beatnotes, that is beating between the CW lasers and the closest comb tooth to each frequency (neglecting the D.C. terms) can be written

$$RF_l(t) = a_{l,RF} e^{i(n\omega_r + \omega_{ceo} - \omega_l)t + i(\phi_l(t) + \theta(t) - n\psi(t))} + c.c. \tag{7.58}$$

for the laser field and

$$RF_{ref}(t) = a_{r,RF} e^{i(m\omega_r + \omega_{ceo} - \omega_{ref})t + i(\phi_{ref}(t) + \theta(t) - m\psi(t))} + c.c. \tag{7.59}$$

for the reference field, where $\theta(t)$ and $\psi(t)$ are the comb noise parameters from section 7.2.2 and $a_{l,RF} = a_l a_n^*$ and $a_{r,RF} = a_{ref} a_m^*$. Now mixing the two intensity signals together, we have

$$RF_{beat}(t) = |RF_{ref}(t)|^2 + |RF_l(t)|^2 + 2RF_l(t)RF_{ref}(t) \ . \tag{7.60}$$

We concentrate on the third term, which is typically isolated experimentally with an RF band-pass filter because this term contains the correct frequency beatnote

we would like to measure. Let $A = (n\omega_r + \omega_{ceo} - \omega_l)t + (\phi_l(t) + \theta(t) - n\psi(t))$ and $B = (m\omega_r + \omega_{ceo} - \omega_{ref})t + (\phi_{ref}(t) + \theta(t) - m\psi(t))$ so that

$$2RF_l(t)RF_{ref}(t) = 2(a_{l,RF}a_{r,RF}e^{i(A+B)} + a_{l,RF}a^*_{r,RF}e^{i(A-B)} + a^*_{l,RF}a_{r,RF}e^{i(B-A)} + a^*_{l,RF}a^*_{r,RF}e^{-i(A+B)}) \ . \quad (7.61)$$

Note the first and fourth terms will be at a frequency of $\omega_{RF,sum} = \pm((n+m)\omega_r + \omega_{ceo} - (\omega_l + \omega_{ref})$ which will be outside of a given detection bandwidth if $n, m \sim 10^4 - 10^7$ as is true in a typical comb-based experiment. The most useful terms to us are the middle two terms. Examining the terms of interest, we have

$$RF_{meas}(t) \sim a_j e^{i(A-B)} + c.c. \quad (7.62)$$

where $a_j = a_{l,RF}a^*_{r,RF}$. When calculating $A - B$, we note that

$$A - B = [(n-m)\omega_r - (\omega_l - \omega_{ref})]t + (\phi_l(t) - \phi_{ref}(t) - (n-m)\psi(t)) \ . \quad (7.63)$$

We see that the common phase noise between comb teeth has cancelled entirely and the repetition-rate phase noise has been reduced significantly: in a typical comb, $n - m$ will be orders of magnitude smaller than either n or m alone. Since $\omega_l = n\omega_r + \omega_{ceo} + \delta\omega_l$ and $\omega_{ref} = m\omega_r + \omega_{ceo} + \delta\omega_{ref}$, then

$$(n-m)\omega_r - (\omega_l - \omega_{ref}) = (\delta\omega_l - \delta\omega_{ref}) = -\omega_{beat} \quad (7.64)$$

which is the beatnote at our desired frequency. Finally, if we assume that $\phi_l(t)$ and $\phi_{ref}(t)$ have the same statistically stationary and random properties as the noise

discussed in Section 7.2.1, with dephasing rates Γ_l and Γ_{ref} we will have

$$\langle RF_{meas}(\tau)RF_{meas}(t+\tau)\rangle \propto a_j^2 e^{-i\omega_{beat}\tau-\Gamma_j|\tau|} + c.c. \tag{7.65}$$

where $\Gamma_j = \Gamma_l+\Gamma_{ref}+(n-m)\Gamma_\psi$. We will therefore have that the RF power spectrum of the beatnote we desire is

$$P^{(2)}(\omega) \propto \sqrt{\frac{2}{\pi}}\frac{a_j}{(\omega-\omega_{beat})^2+\Gamma_j^2}. \tag{7.66}$$

For the sake of comparison, we note that in the case of a filtered white light source, the form of the beatnote spectrum will be similar. Explicitly, Equation 7.63 is instead

$$A - B = [(n-m)\omega_r - (\omega_l - \omega_{ref})]t + (\phi_l(t) - \phi_{ref}(t) - \phi_n(t) - \phi_m(t)) \tag{7.67}$$

where $\phi_n(t)$ and $\phi_m(t)$ have the same properties as discussed in Section 7.2.1 such that the power spectrum of the desired beatnote is

$$P_w^{(2)}(\omega) \propto \sqrt{\frac{2}{\pi}}\frac{2a_j\gamma}{(\omega\pm\omega_{beat})^2+4\gamma^2}. \tag{7.68}$$

which is significantly more broad than the measurement conducted with the comb since $\gamma = \Gamma_\theta + n\Gamma_\psi$ as before. In the white light source, because the 'teeth' are not coherent, we have a half width half maximum linewidth which is just sum of the individual line widths for the filtered modes and each of ω_l and ω_{ref}, leading to a far less precise measurement.

Now we again present a numerical simulation, this time of the aforementioned frequency metrology measurement, both with a coherent comb and filtered white light. We use the same simulated frequency comb and filtered light sources as before, now with parameters $\omega_{ref} = -1.18$ rad.·THz and $\omega_l = 1.28$ rad.· THz where we are

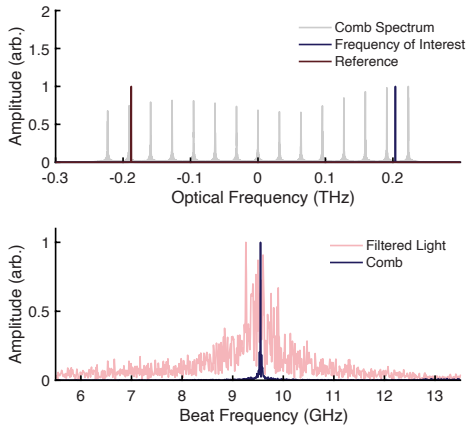

Figure 7.6: A frequency metrology measurement conducted with each kind of light source. In (a), we have the comb spectrum along with the two light sources we are trying to reference against each other. (b) A comparison between the results obtained using either the filtered white light or the comb as the 'gear' between our lasers of interest. The width of each RF beatnote is the uncertainty in the frequency measurement.

measuring frequency relative to the central comb tooth. We set $n-m = 12$, and since $\omega_r = 0.2$ rad.·THz and $\omega_{diff} = 2.46$ rad.·THz, the beatnote $\omega_{beat} = 0.06$ rad.·THz so $f_{beat} = \omega_{beat}/(2\pi) = 9.55$ GHz. Figure 7.6 is a summary of this simulation. In panel (a), we show the comb spectrum with the two single-frequency spectra. We note that the generated single-frequency spectra are such that the CW laser and reference are perfect single frequencies to simply directly compare the results obtained with each lightsource. In panel (b), we show the end result of the mixing process, which leaves the beatnote at f_{beat}. It is clear that the beatnote resulting from frequency metrology conducted with the frequency comb is far more narrow. The mutual coherence between the teeth has resulted in a cancellation of most of the noise present in the measurement as expected. The beatnote resulting from conducting the same experiment with a filtered white light source, on the other hand, is much less defined, with enhanced uncertainty about the peak center. In a practical implementation, the result obtained using filtered incoherent light is not useful.

7.4 Conclusion

In this work, we have examined the subtle nature and important role that the mutual coherence between comb teeth plays in frequency comb applications. Besides being the defining feature of a frequency comb, the mutual coherence between teeth enables one to conduct high-resolution and high-precision frequency measurements in a way not possible with a similar, but incoherent light source. When searching for new comb sources, particularly miniaturized frequency combs, it is not simply enough to show that a spectrum is comb-like. It is also not simply enough to take a first-order auto-correlation of the electric field. Rather, to show that a light source is indeed a frequency comb, one must conduct a higher order coherence measurement, measure the spectral phase of the teeth to show they are related, or show that the RF DCS spectra are correctable in some way.

References

(1) Von der Linde, D. *Applied Physics B Photophysics and Laser Chemistry* **1986**, DOI: 10.1007/BF00697487.

(2) Menyuk, C. R.; Wahlstrand, J. K.; Willits, J.; Smith, R. P.; Schibli, T. R.; Cundiff, S. T. *Optics Express* **2007**, *15*, 6677.

(3) Wahlstrand, J. K.; Willits, J. T.; Menyuk, C. R.; Cundiff, S. T. *Optics Express* **2008**, *16*, 18624.

(4) Bao, C.; Funk, A. C.; Yang, C.; Cundiff, S. T. *Conference on Lasers and Electro-Optics Europe - Technical Digest* **2014**, *2014-January*, 3266–3269.

(5) Berman, P. R.; Malinovsky, V. S., *Principles of laser spectroscopy and quantum optics*, 2010.

(6) Kubo, R. *Adv. Chem. Phys.* **1969**, *15*, 101–127.

(7) Mandel, L.; Wolf, E., *Optical Coherence and Quantum Optics*; Cambridge University Press: New York, 1995.

(8) Holman, K. W.; Jones, R. J.; Marian, A.; Cundiff, S. T.; Ye, J. *OSA Trends in Optics and Photonics Series* **2003**, *88*, 1908–1910.

(9) Jones, D. J.; Diddams, S. A.; Ranka, J. K.; Stentz, A.; Windeler, R. S.; Hall, J. L.; Cundiff, S. T. *Science* **2000**, *288*, 635–639.

(10) Coddington, I. R.; Newbury, N. R.; Swann, W. C. *Optica* **2016**, *3*, DOI: 10.1364/OPN.28.1.000032.

(11) Udem, T.; Holzwarth, R.; Hänsch, T. W. *Nature* **2002**, *416*, 233–237.

(12) Lomsadze, B.; Cundiff, S. T. *Phys. Rev. Lett.* **2018**, *120*, 233401.

(13) Sterczewski, L. A.; Westberg, J.; Wysocki, G. *Optics Express* **2019**, *27*, 23875.

(14) Burghoff, D.; Han, N.; Shin, J. H. *Optics Letters* **2019**, *44*, 2966.

CHAPTER VIII

Conclusion and Outlook

8.1 The Future of Multidimensional Studies of Color Centers in Diamond

Though many of the dynamical parameters of the SiV color center were known prior to our work [1–4], we were able to leverage the ability of MDCS to separate single object dynamics in an inhomogeneously broadened ensemble to add to a large and growing body of work characterizing the optical properties of SiV centers in diamond, and group-IV color centers more broadly. By comparing one-quantum MDCS spectra of the total nonlinear polarization with those of the spectrum of just the luminous color centers within a dense ensemble, we showed that the large population of 'dark color centers' which do not re-emit light upon absorption was present in our sample. We posited that the mechanism behind this dramatic difference between MDCS spectra taken using the two different acquisition methods was due to strain-induced coupling to an energetically proximate dark state [5]. The extended coherence times exhibited by the dark centers (roughly an order of magnitude longer than the bright centers) suggest that the storage time of a particular excitation could potentially be elongated by tuning the net strain experienced by individual centers.

We studied the same color center ensemble with double-quantum MDCS to show

that pairwise excitation-dependent electronic dipole-dipole interactions exist. We posited that these interactions could be strong enough to cause the observed inhomogeneity in our sample and, further, that the interaction strength can be optically modified. This result has important ramifications: magnetic dipole-dipole interactions are currently used to transfer information between electronic and nuclear spins in color center systems [6]. Conceivably, quantum information protocols utilising a combination of electronic and magnetic dipole dipole interactions can be employed to transfer optically prepared quantum states between distinct color centers in an ensemble.

In the future, MDCS studies of color centers in diamond could provide useful insight into a number of areas. Primarily, the density of color centers in our sample was approximately 10^18 centers/cm^3. This is far higher than that used in single-center studies. To bridge the gap between our results and results obtained by studying the linear PL spectra of single color centers, MDCS spectra taken on ensembles of varying density could reveal useful insights into the source of the strain causing the hidden centers to not emit light. Namely, by comparing MDCS spectra acquired on the same sample with a varying color center density, we can understand the relationship between implantation density and strain.

Additionally, by combining novel photon-counting realizations of MDCS [7] with lower-density samples, we can begin to explore the nonlinear quantum-optical properties of single color centers. This could open new frontiers in understanding the quantum interactions between distant color centers and between color centers and their environment, extending the promising MDCS studies of this class of quantum emitter.

Finally, since color centers have proven to be useful nano-probes of their environment, we may be able to apply the capabilities of MDCS to resolve intrinsic linewidths and peak centers in the presence of inhomogeneity in sparsely populated ensembles

whose optical spectra are modified by some extrinsic potential [8]. Work related to this thesis has already shown that MDCS can help separate orientation groups of color centers in an ensemble, allowing for the full bulk strain tensor to be characterized [8]. Likewise, one could imagine employing lower density ensembles of color centers, in combination with either MDCS or optical-density magnetic resonance [9] to precisely image the strength and direction of external magnetic fields, allowing for precision imaging of current flows in novel materials [10]. These outlined directions are just some of the many fruitful research lines to be explored with color centers in diamond.

8.2 The Future of Miniaturized Diode Frequency Combs

In the second half of this thesis, we detailed results demonstrating that DFCs output coherent, useful frequency combs. They're efficient, and can be battery powered, paving the way for wide adoption. However, there is much work to be done to improve the properties of their optical output.

Primarily, the results reported herein were obtained with no attempt to stabilize the output amplitude, offset frequency, or repetition rate of the DFCs. To employ DFCs in any form of precision measurement, one must be able to establish and maintain simultaneous control over both the repetition rate and offset frequency [11]. Future work detailing methods to establish precision control could start by examining stabilization efforts in THz quantum cascade combs, similar in operation principle and structure to DFCs. The most promising techniques entail self-injection locking of the DFC spectrum by reflecting the comb spectrum back into the laser structure, or by using a second frequency comb source to ensure that the appropriate coherent spectrum is maintained (either another DFC or a stabilized, mode-locked lasr) [12]. Furthermore, rapid current modulation has been shown to stabilize the repetition rate of THz quantum cascade combs, a potentially useful stabilization method for DFCs

[13].

As with mode-locked lasers, however, measuring and controlling the offset frequency is more challenging. The most straightforward way to do so is called f-2f interferometery, first pioneered in 2000 [11]. To take advantage of this technique, however, the DFC output power must be increased, the pulses shortened, or both. Currently, these devices output a maximum of 1 mW of optical power; due to the quasi-CW nature of DFC output, this is not nearly enough power to drive nonlinearities required for f-2f interferometery. Alternatively, the absolute offset frequency can be stabilized (but not measured) if a beatnote between an optical reference frequency and a nearby comb tooth is measured and corrected for using slow current or temperature variations, provided the relative comb tooth spacing is strictly set by rapid (25 GHz) current modulations to stabilize the repetition rate [13]. Provided that the output spectra of diode frequency combs can be more easily controlled, we are confident that they can provide a next-generation platform to launch precision dual-comb spectroscopy from the lab to wide application.

References

(1) Zhang, J. L.; Lagoudakis, K. G.; Tzeng, Y.-K.; Dory, C.; Radulaski, M.; Kelaita, Y.; Fischer, K. A.; Sun, S.; Shen, Z.-X.; Melosh, N. A.; Chu, S.; Vučković, J. *Optica* **2017**, *4*, 1317–1321.

(2) Becker, J. N.; Görlitz, J.; Arend, C.; Markham, M.; Becher, C. *Nat. Commun.* **2016**, *7*, 13512.

(3) Pingault, B.; Jarausch, D. D.; Hepp, C.; Klintberg, L.; Becker, J. N.; Markham, M.; Becher, C.; Atatüre, M. *Nature Communications* **2017**, *8*, DOI: 10.1038/ncomms15579.

(4) Becker, J. N.; Becher, C. *Physica Status Solidi (A) Applications and Materials Science* **2017**, *214*, 1–11.

(5) Gali, A.; Maze, J. R. *Phys. Rev. B* **2013**, *88*, 235205.

(6) Dutt, M. V. G.; Childress, L.; Jiang, L.; Togan, E.; Maze, J.; Jelezko, F.; Zibrov, A. S.; Hemmer, P. R.; Lukin, M. D. *Science* **2007**, *316*, 1312–1316.

(7) Tamimi, A.; Landes, T.; Lavoie, J.; Raymer, M. G.; Marcus, A. H. *Optics Express* **2020**, *28*, 25194.

(8) Bates, K. M.; Day, M. W.; Smallwood, C. L.; Owen, R. C.; Ulbricht, R.; Schröder, T.; Bielejec, E.; Cundiff, S. T. **2021**.

(9) Kazi, Z.; Shelby, I. M.; Watanabe, H.; Itoh, K. M.; Shutthanandan, V.; Wiggins, P. A.; Fu, K.-M. C. *Phys. Rev. Applied* **2021**, *15*, 054032.

(10) Ku, M. J. H. et al. *Nature* **2020**, *583*, 537–541.

(11) Jones, D. J.; Diddams, S. A.; Ranka, J. K.; Stentz, A.; Windeler, R. S.; Hall, J. L.; Cundiff, S. T. *Science* **2000**, *288*, 635–639.

(12) Hillbrand, J.; Andrews, A. M.; Detz, H.; Strasser, G.; Schwarz, B. **2019**, *13*, 101–104.

(13) Consolino, L.; Nafa, M.; Cappelli, F.; Garrasi, K.; Mezzapesa, F. P.; Li, L.; Davies, A. G.; Linfield, E. H.; Vitiello, M. S.; De Natale, P.; Bartalini, S. *Nature Communications* **2019**, *10*, 2938.

APPENDICES

APPENDIX A

A Short Foray into Spectral lineshapes

To derive the lineshape of the gain bandwidth (or just a general resonance lineshape, as pointed to multiple times in this Thesis), and therefore the range of frequencies a frequency comb can support, we will follow Kubo's stochasic theory of lineshapes [1–4] and discuss two separate cases: one in which the gain medium is homogeneously broadended, and one in which the gain medium is inhomogeneously broadened. These two cases lead to two different spectra and thus two different laser behaviors. The gain bandwidth of our simple three-level system is given by examining the time-dependent behavior of the energy of photons spontaneously emitted from level 3 as they are allowed to fluctuate due to interactions of electrons in state $|3\rangle$ with their environment.

To see how fluctuations in energy level $|3\rangle$ in Figure 2.16 lead to a finite gain bandwidth, we will assume that the energy of photons emitted from level 3 fluctuate about their average value in time

$$E_3(t) = \hbar\omega_3(t) = \hbar(\omega_{3,0} + \delta\omega_3(t)) \tag{A.1}$$

and that $\delta\omega_3(t)$ is some function of time with an average value of zero, or $\langle\delta\omega(t)\rangle = 0$.

Furthermore, to make the problem tractable, we will assume that the behavior of $E_3(t)$ follows that of the simple harmonic oscillator with stochastic changes in frequency such that

$$\dot{E}_3(t) = i\ \omega(t) E_3(t). \tag{A.2}$$

Now, following Kubo's analysis for the stochastically varying quantity $E_3(t)$ [1, 2], we know that

$$E_3(t) = E_3(0)\ \exp\Big(i \int_0^t \omega(t')dt'\Big). \tag{A.3}$$

is a solution to equation A.2. After a time t, the correlation between the initial condition $E_3(0)$, and the instantaneous $E_3(t)$ is

$$\langle E_3(t)E_3(0)\rangle = \langle |E_3(0)|^2\rangle \langle \exp\Big(i \int_0^t \omega(t')dt'\Big)\rangle. \tag{A.4}$$

Now, since we can write $\omega_3(t) = E_3(t)/\hbar = \omega_{3,0} + \delta\omega_3(t)$, this becomes

$$\langle E_3(t)E_3^*(0)\rangle = \langle |E_3(0)|^2\rangle\ \exp(i\omega_{3,0})\psi(t) \tag{A.5}$$

where $\psi(t)$ is variously as either the *correlation* or *relaxation* function for the fluctuation of $\delta\omega_3(t)$. We will solve for $\psi(t)$ which will then give us the frequency-domain form of our lineshape and a general framework for analyzing the 'perfect' pulse from our frequency comb.

$$\psi(t) = \langle \exp\Big[i \int_0^t dt\ \delta\omega_3(t)\Big]\rangle. \tag{A.6}$$

Using the cumulant expansion, we can write $\psi(t)$ as

$$\psi(t) = \exp\Big[\sum_{n=1}^{\infty} \int_0^t \mathrm{dt}_1 \int_0^{t_1} \mathrm{dt}_2 ... \int_0^{t_{n-1}} \mathrm{dt}_n \langle \delta\omega_3(t_1)...\delta\omega_3(t_n)\rangle\Big]. \tag{A.7}$$

We can explicitly expand $\psi(t)$:

$$\psi(t) = \exp\Big[\int_0^t \mathrm{dt}_1 \langle \delta\omega_3(t_1)\rangle + \int_0^t \mathrm{dt}_1 \int_0^{t_1} \mathrm{dt}_2 \langle \delta\omega_3(t_1)\delta\omega_3(t_2)\rangle + ...\Big]. \tag{A.8}$$

Since $\langle \delta\omega(t)\rangle = 0$ to ensure that $E_3(t)$ fluctuates only about its average, the first term is zero. Furthermore, we can inspect equation A.3 and recognize that it provides a perturbative expansion for $\psi(t)$. In one case, in which the frequency-space spectral density of $\delta\omega_3(\omega')$ is taken to be a Gaussian normal distribution, all of the higher-order moments of the expansion vanish and then it *is* appropriate to take only the lowest order terms. In our case, we will assume a Gaussian distribution for our fluctuations to obtain an analytic expression for the behavior of $\psi(t)$, which is appropriate for many, but not nearly all cases [3, 4]. We will furthermore that the two-point correlation function between our fluctuations, $\langle \delta\omega_3(t)\delta\omega_3(0)\rangle$, has a Poisson distribution such that

$$\psi(t) = \exp\Big[\int_0^t \mathrm{dt}_1 \int_0^{t_1} \mathrm{dt}_2 \ \delta^2 \ e^{-t_2/\tau_c}\Big]. \tag{A.9}$$

where δ^2 is the amplitude of fluctuations, and τ_c is the characteristic time of fluctuations in $E_3(t)$. We integrate once to obtain

$$\psi(t) = \exp\big[\delta^2 \int_0^t \mathrm{dt}_1(\tau_c - \tau_c e^{-t_1/t_c})\big] \tag{A.10}$$

and finally

$$\psi(t) = \exp\big[-\delta^2\tau_c^2(e^{-t/\tau_c} + t/\tau_c - 1)\big]. \tag{A.11}$$

We can now use $\psi(t)$ to calculate the bandwidth of our gain medium.

Typically in statistical lineshape analyses, two different fluctuation limits are explored: the 'fast' and 'slow' fluctuation limits. The object of this rather lengthy exercise is to demonstrate the necessary requirements for a frequency comb to be

able to support a broad spectrum of frequencies, so we must be careful about what we mean by 'fast' and 'slow' here. For the purpose of our analysis, we consider 'fast' and 'slow' fluctuations to be measured relative to the frequency of the photons emitted from energy level 3.

In any case, we can write that the spectral shape of the gain available from state $|3\rangle$ in figure 5.4 can be found from the Fourier transform of equation A.3 [1, 2]:

$$G_3(\omega) = \frac{1}{2\pi} \int_{-\infty}^{\infty} \mathrm{d}t e^{-i\omega t} e^{i\omega_{3,0} t} \ \psi(t). \tag{A.12}$$

In the case of 'slow' fluctuations of state $|3\rangle$ as related to the lifetime of an electron in state $|3\rangle$ (expressed mathematically as $t/\tau_c << 1$), we expand the term in the exponential to second order to obtain

$$\psi(t) \approx \exp\big[-\delta^2 \tau_c^2 (1 - \frac{t}{\tau_c} + \frac{t^2}{2\tau_c^2} + O(t^3) - 1 + \frac{t}{\tau_c}) \big] = \exp\big[-\delta^2 t^2 \big] \tag{A.13}$$

We then Fourier transform this expression by plugging this approximation into equation A.12 to obtain

$$G_3(\omega) = \frac{1}{2\sqrt{\pi\delta^2}} \ \exp[\frac{-(\omega - \omega_3)^2}{(2\delta)^2}]. \tag{A.14}$$

In the opposite limit, where the fluctuations of state $|3\rangle$'s energy as related to the lifetime of an electron in state $|3\rangle$ are 'fast,' we have

$$\psi(t) \approx \exp\big[-\frac{\delta^2}{\tau_c} t \big]. \tag{A.15}$$

The intensity spectrum of emitted photons is therefore

$$I_{em} \sim \frac{1}{(\omega - \omega_3)^2 + \frac{\delta^4}{\tau_c^2}} \ . \tag{A.16}$$

References

(1) Kubo, R. *Journal of Mathematical Physics* **1963**, *4*, 174–183.

(2) Kubo, R. *Adv. Chem. Phys.* **1969**, *15*, 101–127.

(3) Mukamel, S., *Principles of nonlinear optical spectroscopy*; Oxford series in optical and imaging sciences; Oxford University Press: New York, 1995.

(4) Abramavicius, D.; Palmieri, B.; Voronine, D. V.; Šanda, F.; Mukamel, S. *Chemical Reviews* **2009**, *109*, 2350–2408.

APPENDIX B

A Detour about Spatially Inhomogeneous Rabi Oscillations

One detail not treated in the main text that is important to the overall interpretation of our DQ2D fit is the following: the pump spot size is the same as that of the four-wave mixing probe beams. One might think that this completely destroys the possibility that *any* Rabi-like behavior wold be observed. This is simply untrue. What *does* happen is that the spatial inhomogenaiety of the field translates to an apparent reduction in overall Rabi frequency and reduced fringe visibility with increasing pulse area. Figure B.1 is a simulation of this phenomena detailing what happens to the apparent Rabi oscillations in the case of similar pump and probe spot sizes.

To create this simulation, we generated a distribution of Rabi frequencies which depended on the pump intensity profile which was measured to be roughly Gaussian with $\sigma_{pump} = 1.33$ μm while the four-wave-mixing probe beams were collinear and also roughly Gaussian with $\sigma_{FWM} = 1.6$ μm. This may look like a hopeless situation for observing Rabi-like behavior, but because the flopping behavior depends on the field and the four-wave-mixing signal depends on the square of the intensity, the signal comes from a spatially more confined spot. We populate the pump spot with

a distribution of dipole moments scaled to the pump field, and then calculate the 'effective population fraction' as the fraction of centers in the excited state as a function of pulse area *as seen by the four-wave-mixing probe*. The results of this simulation are presented in B.1.

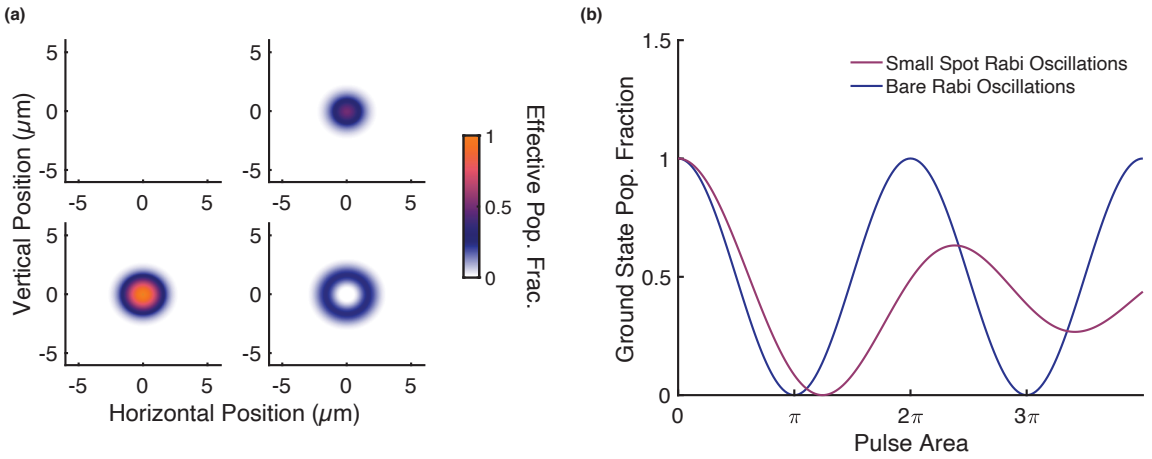

Figure B.1: The simulated ground state population at a pulse area of $0,\pi/2,\pi$, and 2π showing the spatial inhomogenaiety of the at-center pump field.

What is apparent from figure B.1(a) is that,as the pulse area increases, the Rabi flopping behavior spreads in an annular ring centered around the pump intensity maximum. As this happens, the apparent Rabi frequency is reduced as the center and wings of the distribution become more out of synch with eachother. However, the flopping behavior overall is not washed out. If we fit the simulated small-spot curve in figure B.1(b), we find an apparent reduction in the Rabi frequency such that $\Omega_{apparent} = \mathrm{b}\Omega_{real}$ with b = 0.81 estimated using the first minimum of the numerical simulation in B.1(d), or b = 0.83 for a fit of the first three cycles of the numerical simulation to a damped oscillation with a finite offset. We will use the 'worse' value of b = 0.81 for our remaining calculation of $P_{\pi,thy}$.